

# Cellular Fronthauling for Data Capacity Increase in Underserved Spaces

Présentée le 17 juin 2022

Faculté des sciences et techniques de l'ingénieur  
Laboratoire de circuits pour télécommunications  
Programme doctoral en génie électrique

pour l'obtention du grade de Docteur ès Sciences

par

**Adrian SCHUMACHER**

Acceptée sur proposition du jury

Prof. R. C. R. Fleury, président du jury  
Prof. A. P. Burg, Dr R. Merz, directeurs de thèse  
Prof. S. Pollin, rapporteuse  
Dr H. Lehmann, rapporteur  
Prof. A. Skrivervik, rapporteuse



*To my wife and son*



# Acknowledgements

First, I would like to express my deepest appreciation to my doctoral advisor Prof. Andreas Burg and thank him for his guidance and continued support throughout my PhD study. I am grateful to him for believing in my potential, the always fruitful discussions, and his well-versed and pertinent comments. He has the gift of immediately grasping the essence of what is being discussed. If there were problems, he quickly encircled them and contributed with a results-oriented spirit. After every discussion we had, I always felt full of motivation.

Next, I would also like to express my gratitude to my co-advisor, Dr. Ruben Merz, for supporting me, the guidance in my PhD and my professional life, his invaluable advice, and our friendship.

Further, I would like to thank Prof. Sofie Pollin (KU Leuven), Prof. Anja Skrivervik (Microwaves and Antennas Group, EPFL), and Dr. Hugo Lehmann (METAS) for agreeing to review this thesis and serving as examiners on the thesis committee. I also thank Prof. Romain Fleury (Laboratory of Wave Engineering, EPFL) for acting as the president of my PhD jury.

Going back in time, I want to express my sincere gratitude to my MSc thesis advisor, the late Prof. Peter Händel (KTH), who believed in me, knew my interests, and kept supporting me in starting a PhD.

This thesis resulted from joint activities started at the innovation department of Swisscom (Switzerland) Ltd. and the Telecommunications Circuits Laboratory (TCL) at EPFL. I would like to thank Hugo Lehmann and Rico Schwendener for making such an industrial PhD possible. Furthermore, I would like to extend my thanks to my colleagues at Swisscom, whom I cannot list all. Special thanks go to Patrick Weibel for his support and for making it possible that I could pursue this PhD in the organization, and to those who supported me and my work in one way or another (in alphabetical order): Guillermo Barrenetxea, Pavle Belanovic, Carine Genoud, Cornelius Heckrott, Nima Jamaly, Roger Jegerlehner, Stefan Mauron, Thomas Pinegger, Matthias Rohrer, Tim Rüegg, Damiano Scanferla, Olaf Schleusing, Daniel Wenger, Erich Zimmermann, and my interns and trainees Francesco Gallo, Samuel Mettler, and Cedar Urwyler. Thanks should also go to Reto Schoch (Schoch Technik), László Szűcs and Alessandro Giorio (Ericsson), and Christian Patry (Enkom) for their contributions during measurement campaigns.

Although I was an external PhD student at the Telecommunications Circuits Laboratory (TCL), I visited the lab whenever possible and had the chance to meet great people for fruitful and enjoyable discussions. With a few, I even had the opportunity to work on joint projects,

## Acknowledgements

---

which I enjoyed a lot. In alphabetical order, I would like to thank: Orion Afisiadis, Alexios Balatsoukas-Stimming, Andrea Bonetti, Reza Ghanaatian, Pascal Giard, Robert Giterman, Andreas Kristensen, Sitian Li, Christoph Müller, Joachim Tapparel, Ning Xu. I also thank Ioanna Paniara for her help with administrative tasks.

Furthermore, I want to thank Jochen Giese for the inspiring friendship over the years since KTH, our delightful discussions, and especially for reviewing my thesis.

I am endlessly grateful to my parents, Ernst and Elsbeth, and my brother Roman, for supporting me in different ways over all the years of education and for giving me the flexibility to choose my path.

Finally and most importantly, I want to express my deepest gratitude to my wife Rahel for her unconditional love and support in all dimensions and my son Nils for curiously asking questions, frankly commenting on everything, and reminding me of what is important in life.

*Konolfingen, May 29<sup>th</sup>, 2022*

Adrian Schumacher

# Abstract

The increase in wireless data traffic continues and is a product of several factors. First, new technologies and capabilities enable new use cases for which new products emerge. Then, with the growing user adoption over time, the data traffic is further increased. As a result, the actual growth numbers vary year over year, but the trend is sustained. People nowadays also expect ubiquitous availability of mobile connectivity and use cloud services or stream music and video. Moreover, an increasing number of machines are being connected too. While mobile network operators (MNOs) deploy outdoor cellular networks, a significant portion of the mobile data traffic is consumed or originates indoors or while traveling in trains. To this end, MNOs constantly upgrade their networks to satisfy the capacity demand. Additionally, new and wider frequency bands are made available by regulators. However, the mid-band frequencies between 3 GHz and 6 GHz poorly enter buildings, and outdoor cells on millimeter-wave (mmWave) frequencies (24 GHz to 100 GHz) are practically unusable indoors and inside modern railways with their metallic hull and coated windows acting as Faraday cages. The increasing network densification with local cell sites (also inside shielded structures) can provide a partial solution. However, the required fiber and roll-out process is very costly and takes time. Moreover, providing sufficient capacity for the increasing data traffic demand inside buildings and trains is difficult where an optical fiber backhaul is too costly or impossible.

State-of-the-art solutions are analyzed for solving the indoor capacity challenge. However, we found that these rely on or impact the existing outdoor cellular network and thus cannot provide additional capacity to the network that is used indoors. As a solution, we propose the mmWave bridge, an amplify-and-forward out-of-band repeater concept. It is a radio access technology (RAT) transparent and cost-efficient method to fronthaul mobile cells. Moreover, it provides wireless data capacity inside buildings, vehicles, or concealed areas outdoors, where low signal levels drastically limit the achievable capacity or prevent communication with distant base stations. The cellular signal of a base station is fronthauled over newly available mmWave frequencies outdoor without interfering with the existing cellular network. Mid-band frequencies are used indoors to provide sufficient coverage beyond rooms and, at the same time, benefit from the outdoor-to-indoor attenuation reducing possible interference.

The benefits of the mmWave bridge are described, and we discuss the corresponding challenges and solutions. Moreover, a hardware prototype was developed based on commercial off-the-shelf components. We have tested our prototype in three use cases to demonstrate

## Abstract

---

the functionality and compatibility with commercial infrastructure and mobile terminals and present the measurement results. We can show that the entire capacity of a mobile cell can be fronthauled over distances in relation to the mmWave frequency propagation and signal power. Finally, the amplify-and-forward out-of-band repeater concept is generalized regarding the fronthaul carrier frequency. The use of beamforming antennas on RAT-transparent repeaters without access to in-band beam control is investigated, and a solution with a minimal impact of a few percent in throughput reduction is presented.

Key words: millimeter wave communications, mmWave, wireless communications, cellular networks, beamforming, amplify-and-forward, out-of-band, repeater, relay node, prototype

## Résumé

L'augmentation du trafic de données sans fil est le résultat de plusieurs facteurs. Les nouvelles technologies permettent de nouvelles applications pour lesquelles de nouveaux produits sont créés. Avec leur adoption croissante, le trafic de données continue d'augmenter. Et une disponibilité omniprésente d'Internet est aujourd'hui attendue. De plus en plus d'appareils et de machines sont également connectés. Alors que les opérateurs de réseaux mobiles déploient leurs réseaux à l'extérieur, une part importante du trafic de données mobiles est générée en intérieur ou lors de trajets en train. Pour répondre à cette demande croissante, les opérateurs améliorent constamment leurs réseaux. De plus, les régulateurs mettent à disposition de nouvelles bandes de fréquences plus larges. Cependant, les fréquences de bande moyenne entre 3 GHz et 6 GHz pénètrent mal dans les bâtiments, et les cellules extérieures aux fréquences d'ondes millimétriques (mmWave) (24 GHz à 100 GHz) sont pratiquement inutilisables à l'intérieur et dans les trains modernes. La densification du réseau mobile avec plus de sites cellulaires est très coûteuse et prend du temps à construire. Il est également difficile de fournir une capacité suffisante pour le trafic croissant dans les bâtiments et les trains où le backhaul de fibre est trop coûteux ou impossible.

Pour résoudre les problèmes de capacité en intérieur, nous avons analysé les solutions de pointe. Nous avons constaté qu'elles s'appuient sur le réseau cellulaire existant, ce qui limite la capacité et ne peut donc pas fournir de capacité supplémentaire à l'intérieur. La solution que nous proposons est le pont mmWave, un concept d'amplification et de retransmission basé sur des répéteurs hors bande pour une retransmission (fronthaul) économique et neutre en termes de technologie radio. Il fournit une capacité de données sans fil à l'intérieur des bâtiments, des véhicules ou des zones extérieures couvertes par de faibles niveaux de signal limitant considérablement la capacité disponible ou empêchant la communication avec des stations de base distantes. Le signal cellulaire d'une station de base est transmis à l'extérieur via des fréquences mmWave nouvellement disponibles sans interférer avec le réseau cellulaire existant. Les fréquences de bande moyenne sont utilisées à l'intérieur pour fournir une couverture suffisante au-delà des pièces, tout en bénéficiant de l'atténuation entre l'extérieur et l'intérieur, ce qui réduit les interférences potentielles.

Nous décrivons les avantages du pont mmWave et discutons les défis de la solution et la manière dont nous les avons résolus. De plus, un prototype matériel a été développé sur la base de composants commerciaux disponibles sur le marché. Nous avons testé notre prototype dans trois cas d'utilisation pour démontrer la fonctionnalité et la compatibilité avec

## Abstract

---

l'infrastructure commerciale et les appareils mobiles, et nous présentons les résultats des mesures. Nous pouvons montrer que toute la capacité d'une cellule mobile peut être transmise sur des distances en fonction de la propagation de la fréquence des ondes millimétriques et de la puissance d'émission. Enfin, nous étudions l'utilisation d'antennes à faisceaux sur des répéteurs indépendants de la technologie radio, sans accès au contrôle des faisceaux intra bande, et présentons une solution ayant un impact minimal de quelques pour cent sur le débit de données.

Mots clefs : communications par ondes millimétriques, mmWave, communications sans fil, réseau cellulaire, formation de faisceaux, amplifier et transmettre, hors bande, répéteur, relais, prototype

# Zusammenfassung

Die kontinuierliche Zunahme des drahtlosen Datenverkehrs ist das Ergebnis mehrerer Faktoren. Neue Technologien ermöglichen neue Anwendungsfälle, für die neue Produkte entstehen. Mit deren zunehmenden Akzeptanz steigt der Datenverkehr weiter. Heutzutage erwarten die Leute eine allgegenwärtige Verfügbarkeit des Internets und nutzen Cloud-Dienste oder streamen Musik und Videos. Auch werden immer mehr Geräte und Maschinen vernetzt. Während Mobilfunknetzbetreiber ihre Netze im Freien bereitstellen, wird ein erheblicher Teil des mobilen Datenverkehrs in Innenräumen oder während der Fahrt in Zügen verursacht. Um den steigenden Kapazitätsbedarf zu decken, rüsten die Betreiber ihre Netze ständig auf. Zusätzlich stellen Regulierungsbehörden neue und breitere Frequenzbänder zur Verfügung. Die Mittelband-Frequenzen zwischen 3 GHz und 6 GHz dringen jedoch nur schlecht in Gebäude ein, und Aussenzellen auf Millimeterwellen-Frequenzen (mmWellen) (24 GHz bis 100 GHz) sind in Innenräumen und in modernen Zügen, deren metallische Hülle und beschichtete Fenster wie ein Faraday'scher Käfig wirken, praktisch unbrauchbar. Die Verdichtung des Mobilfunknetzes mit mehr Zellenstandorten ist sehr kostspielig und braucht Zeit für den Aufbau. Ausserdem ist es schwierig, ausreichend Kapazität für den steigenden Datenverkehr in Gebäuden und Zügen bereitzustellen, wo ein Glasfaser-Backhaul zu kostspielig oder unmöglich ist.

Um die Kapazitätsprobleme in Innenräumen zu lösen, haben wir die Lösungen auf dem neuesten Stand der Technik analysiert. Jedoch haben wir festgestellt, dass sie sich auf das bestehende Mobilfunknetz stützen, dessen Kapazität belasten, und daher keine zusätzliche Kapazität in Innenräumen bereitstellen können. Als Lösung schlagen wir die mmWellen-Brücke vor, ein Verstärkungs- und Weiterleitungskonzept basierend auf Ausserband-Signalverstärker zur kosteneffizienten und Funktechnologie-neutralen Weiterleitung (Fronthaul) von Mobilfunkzellen. Es bietet drahtlose Datenkapazität innerhalb von Gebäuden, Fahrzeugen oder verborgenen Bereichen im Freien, wo niedrige Signalpegel die erreichbare Kapazität drastisch einschränken oder die Kommunikation mit weit entfernten Basisstationen verhindern. Das Mobilfunksignal einer Basisstation wird über neu verfügbare mmWellen-Frequenzen im Freien übertragen, ohne das bestehende Mobilfunknetz zu stören. Mittelband-Frequenzen werden in Innenräumen verwendet, um eine ausreichende Abdeckung über Räume hinaus bereitzustellen und gleichzeitig von der Dämpfung zwischen Aussen- und Innenräumen zu profitieren, wodurch mögliche Interferenzen reduziert werden.

Wir beschreiben die Vorteile der mmWellen-Brücke und erörtern die Herausforderungen der Lösung und wie wir sie gelöst haben. Ausserdem wurde ein Hardware-Prototyp basie-

## Abstract

---

rend auf handelsüblichen Komponenten entwickelt. Wir haben unseren Prototypen in drei Anwendungsfällen getestet, um die Funktionalität und Kompatibilität mit kommerzieller Infrastruktur und mobilen Endgeräten zu demonstrieren, und präsentieren die Messergebnisse. Wir können zeigen, dass die gesamte Kapazität einer Mobilfunkzelle über Distanzen in Abhängigkeit von der mmWellen-Frequenzausbreitung und der Sendeleistung übertragen werden kann. Schliesslich wird die Verwendung von Strahlenbündelungs-Antennen auf Funktechnologie-unabhängigen Signalverstärkern ohne Zugang zur Innerband-Strahlsteuerung untersucht, und eine Lösung mit einer minimalen Auswirkung von wenigen Prozent auf den Datendurchsatz vorgestellt.

Stichwörter: Millimeterwellenkommunikation, mmWellen, drahtlose Kommunikation, zelluläre Netzwerke, Strahlenbündelung, verstärken-und-weiterleiten, ausserband, Signalverstärker, Relaisknoten, Prototyp

# Contents

<b>Acknowledgements</b>	<b>i</b>
<b>Abstract (English/Français/Deutsch)</b>	<b>iii</b>
<b>1 Introduction</b>	<b>1</b>
1.1 Motivation . . . . .	2
1.2 Contributions . . . . .	3
1.3 Thesis Outline . . . . .	4
1.4 Third-Party Contributions . . . . .	5
1.5 Notation . . . . .	6
<b>2 Wireless Capacity Increase: Measurements and State of the Art</b>	<b>7</b>
2.1 Path Losses in 5G Mid-Band Spectrum (3.5 GHz) . . . . .	8
2.1.1 Related Work on Path Loss Estimation at 3.5 GHz . . . . .	9
2.1.2 Overview of Empirical Path Loss Models . . . . .	11
2.1.3 Measurement Setup and Environment . . . . .	12
2.1.3.1 Measurement Method . . . . .	12
2.1.3.2 5G Testbed . . . . .	12
2.1.3.3 Reference Measurements in Legacy Frequency Bands With 4G . . . . .	15
2.1.3.4 Rural Area Environment . . . . .	16
2.1.3.5 Suburban Area Environment . . . . .	16
2.1.3.6 Urban Area Environment . . . . .	17
2.1.3.7 Outdoor-to-Indoor Scenario . . . . .	17
2.1.4 Measurement Results . . . . .	18
2.1.4.1 Rural Environment . . . . .	18
2.1.4.2 Suburban Environment . . . . .	19
2.1.4.3 Urban Environment . . . . .	21
2.1.4.4 Outdoor-to-Indoor Scenario . . . . .	22
2.1.5 Measurement Conclusions . . . . .	23
2.2 State of the Art . . . . .	24
2.2.1 Deployment Options to Increase Indoor Capacity . . . . .	26
2.2.1.1 Small Cells . . . . .	26
2.2.1.2 Relays . . . . .	26
2.2.1.3 Repeaters . . . . .	27

2.2.2	Out-of-Band Repeater Using mmWave Frequencies . . . . .	28
2.2.3	Cellular Corridor for Railways . . . . .	29
2.2.4	Energy Efficiency for Cellular Railway Corridors . . . . .	30
2.2.5	Beam Control and Selection for Layer-1 Repeaters . . . . .	30
2.3	Summary . . . . .	31
<b>3</b>	<b>The mmWave Bridge</b>	<b>33</b>
3.1	Proposed mmWave Bridge Solution . . . . .	34
3.2	Deployment Objective and Use Cases . . . . .	36
3.2.1	Advantages of the mmWave Bridge . . . . .	36
3.2.2	Disadvantages of the mmWave Bridge . . . . .	36
3.2.3	Fixed Wireless Access . . . . .	36
3.2.4	Cellular Corridor for Railways . . . . .	37
3.2.5	Temporary Cell Deployment or Extreme Terrain . . . . .	37
3.3	Architecture Overview . . . . .	38
3.3.1	Beamforming . . . . .	39
3.3.2	Donor Link Multiple Access . . . . .	39
3.3.3	Duplexing Models . . . . .	40
3.4	Comparison of State of the Art with the mmWave Bridge . . . . .	40
3.4.1	Scenarios and Configurations . . . . .	40
3.4.2	Signal Paths . . . . .	41
3.4.3	General Aspects and Assumptions . . . . .	43
3.4.4	System Models . . . . .	44
3.4.4.1	Outdoor Macro Network . . . . .	44
3.4.4.2	Small Cell Model . . . . .	45
3.4.4.3	Repeater Model . . . . .	45
3.4.4.4	Layer-3 Relay Model . . . . .	47
3.4.4.5	mmWave Bridge Model . . . . .	47
3.4.4.6	Capacity Estimation . . . . .	48
3.4.5	Results and Discussion . . . . .	48
3.5	Summary . . . . .	52
<b>4</b>	<b>mmWave Bridge Prototype</b>	<b>55</b>
4.1	Prototype Architecture . . . . .	56
4.1.1	Up-/Downconversion and Filtering . . . . .	58
4.1.2	Local Oscillator . . . . .	58
4.1.3	Synchronization . . . . .	59
4.1.4	Duplexing . . . . .	59
4.1.5	mmWave Antennas . . . . .	60
4.1.6	Control and Signal Processing . . . . .	61
4.2	Prototype Characterization . . . . .	61
4.2.1	Link Budget . . . . .	61
4.2.2	Frequency Selectivity . . . . .	62

4.2.3	Phase Noise . . . . .	63
4.2.4	Error Vector Magnitude . . . . .	64
4.3	Validation Measurements . . . . .	65
4.3.1	4G LTE FDD . . . . .	65
4.3.2	5G NR TDD . . . . .	65
4.3.3	Beamforming Antenna . . . . .	66
4.4	Summary . . . . .	67
<b>5</b>	<b>mmWave Bridge for Fixed Wireless Access</b>	<b>69</b>
5.1	Fixed Wireless Access in Rural Areas . . . . .	70
5.1.1	Measurement Environment, Setup, and Methodology . . . . .	70
5.1.2	Measurement Results and Discussion . . . . .	71
5.2	Small Cell Fronthaul . . . . .	73
5.2.1	Measurement Environment and Setup . . . . .	73
5.2.2	Measurement Results . . . . .	74
5.2.2.1	Path Loss and Link Budget . . . . .	74
5.2.2.2	5G Throughput Measurements . . . . .	75
5.3	Summary . . . . .	75
<b>6</b>	<b>mmWave Bridge for Cellular Corridors for Railways</b>	<b>77</b>
6.1	Improving Railway Track Coverage . . . . .	78
6.1.1	mmWave Bridge for Cellular Railway Corridors . . . . .	80
6.1.2	Trial Infrastructure . . . . .	81
6.1.2.1	Macro Site . . . . .	81
6.1.2.2	mmWave Bridge Installation . . . . .	82
6.1.3	Measurement Methodology . . . . .	83
6.1.4	Results and Discussion . . . . .	83
6.1.4.1	Coverage for Macro Antenna (Baseline) . . . . .	84
6.1.4.2	mmWave Bridge Coverage Increase . . . . .	85
6.1.4.3	Doppler Measurements . . . . .	88
6.1.4.4	Stretching the Macro Inter-Site Distance . . . . .	90
6.2	Increasing Cellular Network Energy Efficiency . . . . .	92
6.2.1	System Architecture for Low Power Consumption . . . . .	93
6.2.1.1	Railway Track Capacity Model with Bridge Nodes . . . . .	93
6.2.1.2	Radio Unit Power Model . . . . .	95
6.2.2	Energy Autonomous Bridge Nodes . . . . .	96
6.2.2.1	Solar Power Model . . . . .	97
6.2.2.2	Geographical Setting . . . . .	97
6.2.3	Numerical Results and Discussion . . . . .	98
6.2.3.1	Grid Powered Operation . . . . .	98
6.2.3.2	Energy-Autonomous Bridge Operation . . . . .	99
6.3	Summary . . . . .	100

<b>7</b>	<b>Beam Control for Layer-1 Repeaters</b>	<b>103</b>
7.1	System Overview . . . . .	104
7.1.1	Out-of-Band Repeater . . . . .	104
7.1.2	In-Band Repeater . . . . .	104
7.1.3	Beamforming Antenna and Control . . . . .	105
7.2	Cell-Search and Initial Access Link . . . . .	105
7.2.1	Systematic Scan . . . . .	105
7.2.2	Scan with Prior Information . . . . .	106
7.2.3	Results Using Outdoor Measurements . . . . .	107
7.3	Beam Measurement Process and Impact . . . . .	109
7.3.1	3GPP Link Failure Protocol Mechanism . . . . .	109
7.3.2	Beam Measurement Impact Results . . . . .	110
7.4	Beam Management and Tracking . . . . .	112
7.4.1	Algorithm Choices for Beam Tracking . . . . .	112
7.4.1.1	Random Beam Selection . . . . .	113
7.4.1.2	Nearest Neighbor Selection . . . . .	113
7.4.1.3	Simple Multi-Armed Bandit . . . . .	113
7.4.1.4	Contextual Bandit with Nearest Neighbor Selection . . . . .	114
7.4.2	Performance Evaluation with Measurements . . . . .	114
7.5	Summary . . . . .	116
<b>8</b>	<b>Conclusion and Outlook</b>	<b>117</b>
<b>A</b>	<b>Appendix</b>	<b>121</b>
A.1	Coordinate Transformation to Beam Angles . . . . .	121
A.1.1	Coordinate Frames . . . . .	121
A.1.1.1	Earth-Centered Earth-Fixed Frame (ECEF, <i>e</i> -frame) . . . . .	121
A.1.1.2	Local Tangent Plane/Frame ( <i>t</i> -frame) . . . . .	121
A.1.1.3	Body Frame ( <i>b</i> -frame) . . . . .	122
A.1.2	Transformation from Coordinates to Beam Angles . . . . .	122
	<b>Bibliography</b>	<b>136</b>
	<b>List of Acronyms</b>	<b>137</b>
	<b>List of Figures</b>	<b>141</b>
	<b>List of Tables</b>	<b>147</b>
	<b>Curriculum Vitae</b>	<b>149</b>
	<b>List of Publications</b>	<b>151</b>

# 1 Introduction

Since the beginning of mobile wireless communications in the early 1980s, a new generation of technology was introduced roughly every ten years. Each new generation brings further evolution, higher efficiency, and more features enabling new use cases and services. The radio access technologies (RATs) used in the first two generations were numerous, and countries followed their own standards incompatible with others. Therefore, the International Telecommunication Union Radiocommunication Sector (ITU-R) in 1990 defined requirements for International Mobile Telecommunications (IMT) to harmonize the implementation of RATs and enable worldwide interoperability. After IMT-2000 for the 3rd generation (3G) of mobile networks and IMT-Advanced for the 4th generation (4G), we currently use the 5th generation (5G) as specified by the requirements in IMT-2020. The ubiquitous and reliable availability of mobile communications led to the rapid adoption of new capabilities. The number of connections and the amount of mobile network data traffic have been growing, and this trend is predicted to continue [1] as also shown in Fig. 1.1. Therefore, the ITU-R also defines and harmonizes additional frequency spectrum to support the communication device and traffic growth. The new spectrum introduced with 5G lies in the so-called *mid-band* around 3.5 GHz and in millimeter wave (mmWave) frequencies roughly between 24 GHz and 100 GHz.

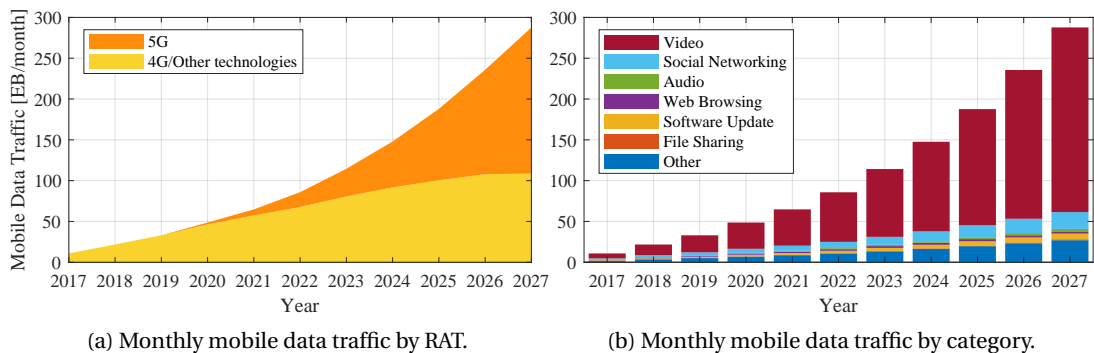


Figure 1.1: Monthly mobile data traffic development since the year 2017 and prediction until the year 2027 [1].

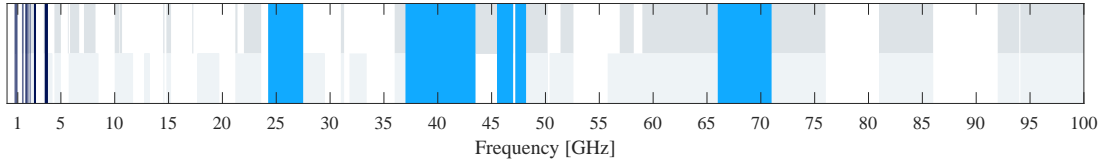


Figure 1.2: Frequency allocation for fixed and mobile use (grey shades). Licensed frequency bands in use for mobile communications in Switzerland (dark blue), frequency bands for mmWave mobile communications (light blue). (Source: Swiss OFCOM)

However, the use of these frequencies is not new. The mid-band spectrum has or still is used for Worldwide Interoperability for Microwave Access (WiMAX) and 4G Long Term Evolution (LTE) mobile services. The mmWave frequencies are used for fixed point-to-point links, but some bands are refarmed for mobile communication allowing carrier bandwidth of several 100 MHz, see Fig. 1.2.

Nowadays, people communicate and access the Internet with their mobile devices not only en route, but also at home, in offices, and inside other buildings. Statistics from studies such as [2] and our estimates on the Swisscom network show that around 80 % of the mobile data traffic originates or terminates indoors. Moreover, particular circumstances like the COVID-19 lockdowns in 2020 [3] and the trend to more remote working from home reinforce the indoor use.

### 1.1 Motivation

Mobile network operators (MNOs) deploy most of their cellular network sites outdoor. With strategic planning of outdoor sites, it is much easier and more economical to cover large areas and many buildings simultaneously than building and installing indoor cells everywhere. To keep up with the demand for higher data capacity, evolving wireless communication standards have introduced measures to improve the spectral efficiency, such as multiple input multiple output (MIMO) systems and means to reduce inter-cell interference. Unfortunately, these measures alone are insufficient. Adding cells on additional frequency bands on existing cell sites may be an option where unused licensed spectrum is available, and the regulatory electromagnetic field (EMF) limits allow it. However, the power budget dictated by regulations often is almost exhausted, hindering the installation of additional cells or only allowing a limited transmit power. Thus, new cells only reach a minimal coverage area due to the combination of low transmit power and wider cell bandwidths. Considering indoor users as well as train passengers, the new frequency bands available with 5G have the disadvantage of a higher propagation attenuation, particularly when penetrating buildings [4]. Commonly used low-emissivity (Low-E) coated glass windows for thermal isolation also strongly attenuate radio frequency (RF) signals. Therefore, indoor users and train passengers cannot immediately benefit from adding high-capacity cells in mid-band or mmWave frequencies to existing mobile network outdoor sites. Densifying the network with additional cell sites takes time and is costly because of the site acquisition, obtaining the construction permissions, and the civil infrastructure construction itself.

The first objective of this thesis is in line with quotes from several renowned researchers<sup>1</sup> mentioned by Larry Greenstein [5]: “*Before we can build a new radio system, we have to understand the propagation.*” Hence, we conduct measurements in the field to learn more about the propagation characteristics in specific situations. Our second objective is to densify cellular networks to increase the area capacity. The third objective is to find a method to increase the data capacity for users inside shielded structures such as buildings or trains. Finally, we develop a working prototype to demonstrate the feasibility of our chosen method.

## 1.2 Contributions

The main contribution of this thesis is the conceptualization of a method to bring more data capacity to users inside buildings or railway carriages and develop and demonstrate a prototype for an economically attractive mobile network capacity extension in different scenarios.

The detailed contributions are listed in the following:

- We conducted extensive measurement campaigns at 3.5 GHz with a 5G beamforming testbed in typical rural, suburban, and urban areas, both outdoor and indoor [6]. The beamforming antenna measurement data obtained in the measurement campaigns are made publicly available under: <https://c4science.ch/source/bfmeasdata3500mhz/>.
- We show that empirical path loss models for 3.5 GHz tend to overestimate the path loss for 5G outdoor macro cells with beamforming MIMO antennas. We also show that the possible gigabit capacity cannot be achieved inside buildings.
- We propose and design the *mmWave Bridge*, an out-of-band amplify-and-forward repeater. Advantages and limitations are described.
- We show how to fronthaul the data capacity from macro cell sites into buildings.
- We develop high-level analytical models to compute the achievable indoor data capacity for several methods: conventional macro outdoor-to-indoor (baseline), layer-1 repeater, layer-3 relay, indoor small cell, and the bridge using mmWave frequencies for the fronthaul [7].
- We develop and implement our mmWave bridge as a hardware prototype to demonstrate the practical feasibility. In addition, signal power and throughput measurements with commercial off-the-shelf (COTS) smartphones are performed to validate the concept [8].
- We show that a mmWave bridge can be used to ease the deployment of a cellular corridor for railways, requiring fewer macro sites at an extended inter-site distance with mmWave bridge nodes in-between to maintain the high data capacity inside railway carriages [9].

---

<sup>1</sup>Don Cox (Bell Labs), Andy Viterbi (Qualcomm), Fumiyuki Adachi (NTT DoCoMo), Dick Frenkiel (WINLAB), David Goodman (NYU-Poly), and Larry Greenstein (Bell Labs, AT&T Labs, Rutgers University)

- We calculate the overall normalized energy consumption for a cellular corridor along railway tracks and show that our mmWave bridge helps save a significant amount of power and energy, reducing the carbon footprint of mobile communications [10].
- We propose a beam scanning and tracking method for amplify-and-forward repeater nodes without access to beam control. The impact on the user capacity is measured, and the relation to the beam measurement duration and interval is characterized [11].

### 1.3 Thesis Outline

The content of each chapter of this thesis is briefly outlined and summarized in the following.

**Chapter 2, Wireless Capacity Increase: Measurements and State of the Art**, introduces the challenges of increasing mobile network data capacity. Measurements at the 5G mid-band spectrum (3.5 GHz) are described, and the outdoor and outdoor-to-indoor propagation results are discussed. Finally, the state of the art for improving data capacity for indoor and railway passengers are listed, and related works regarding all topics visited in this thesis are discussed.

In **Chapter 3, The mmWave Bridge**, we build on the findings of the previous chapter and introduce the mmWave bridge concept as a method to provide higher data capacity in buildings using the new frequency spectrum made available by 5G. MmWave frequencies allow for compact high-gain antennas and avoid disturbing the cellular network on sub-6 GHz frequencies. Deployment use cases for the mmWave bridge and the system architecture are described. Finally, we develop analytical models for the numerical evaluation of the data capacity performance. Using the results, we can compare our mmWave bridge to other state-of-the-art solutions for providing indoor capacity.

In **Chapter 4, mmWave Bridge Prototype**, the concept from the previous chapter is transformed into hardware. The prototype is used to validate the concept and demonstrate the feasibility. Furthermore, the prototype allows us to perform measurements, study the mmWave propagation aspects and the use cases, and test the concept in realistic conditions. First, we detail the prototype hardware architecture and describe the sub-components. Then, we characterize the prototype regarding RF signal and quality parameters. To conclude the chapter, the functional verification is described, and the achievable performance is evaluated.

A first application is described in **Chapter 5, mmWave Bridge for Fixed Wireless Access**. It defines a wireless link between fixed communication nodes, where one is located, e.g., on an existing cell site, and one or more are typically installed at buildings (on the roof, window, or outer wall), providing the user access for broadband Internet connectivity. Fixed wireless access can also be used in a more general sense to provide backhaul or fronthaul connectivity to, e.g., small cells. Next, we describe field measurements conducted to assess the maximum coverage range and the impact on the performance. Finally, the obtained results are presented and discussed.

A second application is described in **Chapter 6, mmWave Bridge for Cellular Corridors for Railways**. This application is a specifically relevant case related to efforts undertaken to improve the data capacity for train passengers. We describe the challenges and how the mmWave bridge helps to solve them. We detail a measurement campaign that was conducted and present the results. An additional angle is taken, looking at the energy efficiency of a cellular corridor for railways. We show how the mmWave bridge can be optimized and how it contributes to increasing the overall energy efficiency of a cellular corridor.

In **Chapter 7, Beam Control for Layer-1 Repeaters**, we generalize the mmWave bridge regarding the fronthaul carrier frequency. This generalization leads to an amplify-and-forward (AF) repeater node with an electronically controllable beamforming antenna. Typically, such beamforming antennas are used and controlled based on in-band information and signaling control channels. However, the operation of AF repeaters should ideally be fully transparent for signals and still allow the means to control the beam and beam measurements. We show how an AF repeater can efficiently and quickly establish an initial access link. The impact on the communication performance is estimated numerically and analyzed with measurements, and several beam tracking methods are presented and compared using measured data from Chapter 2.

## 1.4 Third-Party Contributions

For the field measurements reported in Chapter 2, involving mobile network infrastructure equipment, the installation on existing cell sites, and conducting the measurements, multiple people supported the logistics. My role was the overall lead, planning the measurements and resources, preparing, conducting, and finally, post-processing and analyzing the measurement results.

The mmWave RF frontend hardware for simplex operation was assembled by Erich Zimmermann from Swisscom. The hardware architecture and component selection were jointly made. The evolution of the initial hardware to the mmWave bridge prototype described in Chapter 4 for duplex communication was done by myself.

The mmWave prototype incorporates field programmable gate arrays (FPGAs) for control and processing. The firmware for these FPGAs was developed together with Reza Ghanaatian Jahromi from EPFL and implemented by him.

The field measurements reported in Chapter 6 were only possible because the infrastructure, equipment, and train setups were in place for measurements that are not part of this thesis. My effort was planning the measurements, installing the mmWave bridge equipment and antennas, conducting, processing, and analyzing the results.

### 1.5 Notation

In this work, bold lowercase letters represent vectors and bold uppercase letters represent matrices. The discretized probability density function (PDF) over a two-dimensional angle space is denoted by  $f(\phi, \theta)$ , where  $\phi$  and  $\theta$  denote azimuth and elevation angles, respectively. Furthermore, equations involving signal or noise power, signal-to-noise ratio, gain, or attenuation are typically given in linear domain unless indicated with [dB]. However, associated values are given in logarithmic domain.

## 2 Wireless Capacity Increase: Measurements and State of the Art

The worldwide data traffic is bound to increase, as seen in Chapter 1 and Fig. 1.1. Therefore, mobile network operators continuously have to upgrade their infrastructure to provide sufficient data capacity and prevent data congestion. New evolving RATs are needed to increase spectral and energy efficiency, but wider carrier bandwidths are also required. Because bandwidth in frequencies below the traditionally used 3 GHz is scarce, the solution is to resort to higher frequencies, e.g., the mid-band spectrum or the mmWave frequencies depicted in Fig. 1.2.

The 3rd Generation Partnership Project (3GPP) is the standardization body that developed Universal Mobile Telecommunications System (UMTS) for 3G, LTE for 4G, then New Radio (NR) for 5G, and is currently working on the future evolution 5G-Advanced and 6th generation (6G) of mobile networks. 3GPP organizes the technical evolution of their standards in releases. UMTS started with Release 99, followed by Release 4 and increasing. LTE was introduced with Release 8 and evolves further. NR was introduced with Release 15, and the latest published version is Release 17. 5G-Advanced is planned to be introduced with Release 18 at the end of 2023. Basic 6G features are expected with Release 21 earliest in 2028. While the RATs up until 3G only supported carrier frequencies below 3 GHz, 4G can use higher frequencies but still below 6 GHz (sub-6 GHz). 5G is designed for multiple frequency ranges. The low- and mid-band spectrum is covered by frequency range 1 (FR1), and the mmWave frequency spectrum between 24.25 GHz and 52.6 GHz is covered by frequency range 2 (FR2). These frequency ranges are illustrated in Fig. 2.1, along with other ranges covering all frequencies up to 114.25 GHz. Even higher frequency bands are studied for 6G that may use the range up to 1 THz.

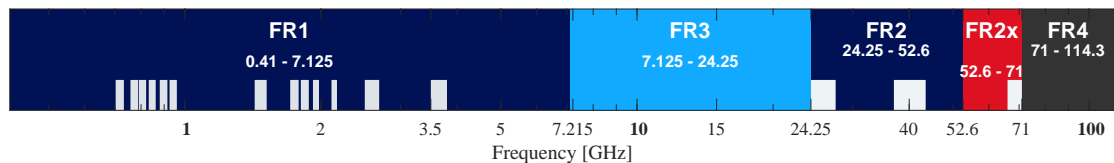


Figure 2.1: 5G NR frequency ranges (FR) and harmonized frequency allocations (light gray). FR1 and FR2 are supported with the first release of 5G NR (Rel. 15).

However, even the higher frequencies cannot solve the capacity challenge of indoor users. Capabilities such as multiple transmission and reception point (mTRP) [12] and centralized/cloud-RAN (C-RAN) provide the foundations for massive densification of cell sites. Eventually, the concept of cell-free networks [13] may be possible to realize. Unfortunately, the construction of new sites and their optical fiber provisioning is costly. Therefore, we focus on near- to mid-term possibilities that can be beneficial already in the following years but should be forward compatible with future RAT evolutions.

This chapter starts with an analysis of path loss measurements at 3.5 GHz for typical urban, suburban, and rural areas and is related to the work published in [6]. Then, the results are compared with empirical path loss models, and the findings regarding indoor users are presented. In conclusion, we learn that the newly available frequency band at 3.5 GHz (allowing carrier bandwidths of up to 100 MHz) is poorly suited for providing outdoor-to-indoor capacity. Therefore, we continue this chapter by listing state-of-the-art solutions to increase indoor data capacity for buildings with a considerable building entry loss (BEL). Finally, an overview of the related work is provided concerning the topics of this thesis.

### 2.1 Path Losses in 5G Mid-Band Spectrum (3.5 GHz)

The global demand for higher-capacity mobile Internet services drives the continuous evolution of mobile (cellular) technologies. Before 5G NR, only frequency bands up to around 2.7 GHz have been used (with a few exceptions in some countries [14]). More bandwidth in a higher frequency spectrum is needed to carry the required increase in data capacity. CEPT/ECC identified<sup>1</sup> several frequency bands to be harmonized in Europe for 5G usage: 3400–3800 MHz in the sub-6 GHz spectrum and for mmWave communications, the 24.25–27.5 GHz frequency band. In most countries, national regulators have already made the 3.4–3.8 GHz (referred to as 3.5 GHz) band available for mobile network operators. An auction for 3.5–3.8 GHz was conducted in Switzerland during the first quarter of 2019. 5G NR is frequency band agnostic and could be deployed on sub-6 GHz bands and in the mmWave spectrum. As a compromise to having reasonably good propagation properties and wider carrier bandwidths, the 3.5 GHz band is particularly interesting among the sub-6 GHz bands. Propagation channels for mobile use in the 3.5 GHz band and above have mainly been studied in the context of WiMAX, and with less carrier bandwidth than 5G will be able to use (up to 100 MHz carrier bandwidth for sub-6 GHz frequencies). It also needs to be considered that an increase in bandwidth requires the same factor for a power increase to maintain the same coverage area.

Propagation models are used for radio network planning, categorized into deterministic, stochastic, empirical, and standardized models [15, Chapter 4]. While deterministic models (e.g., ray tracing) may yield accurate results, they require a high degree of detailed description and calibration of the environment and are computationally expensive. Stochastic models (e.g., COST 207) employ random variables that do not require much information about the

---

<sup>1</sup><https://www.cept.org/ecc/topics/spectrum-for-wireless-broadband-5g>

environment; however, they cannot provide high-accuracy path loss predictions. Empirical (e.g., Hata-Okumura) and standardized models are based on measurements and have been widely adopted to predict a mean path loss as a function of distance, frequency, and some additional parameters specific to the environment or infrastructure. They also require only a few parameters and can provide an acceptable prediction accuracy, better than the very general and simplified path loss model (2.1). For these reasons, radio network planners often use empirical path loss models for network planning simulations.

### 2.1.1 Related Work on Path Loss Estimation at 3.5 GHz

Before 5G, there was already an interest in the 3.5 GHz band in the early 2000s for WiMAX, the radio access technology primarily for fixed wireless access. Hence, several measurement results are available for the frequency range 3.4–3.8 GHz. In [16], path loss measurement results obtained with a WiMAX system for urban, suburban, and rural environments from Cambridge, UK, are presented and compared to the COST 231 Hata, SUI, and ECC-33 models. The measured user equipment (UE) heights were 6 m and 10 m, which are considerably higher than what is typical for mobile phone users. In [17], path loss results using a continuous wave (CW) signal in multiple cities in the UK have been presented in the form of the simplified model according to (2.1). Further results using a CW signal are available in [18] from a suburban office park area in Ghent, Belgium. A comparison with models showed that their measured path loss was higher than what the Erceg model predicts and lower than COST 231 WI and COST 231 Hata. Moreover, the estimated path loss exponent from the measurements is higher than what all models provide. The authors assumed that these models consider US houses mostly built of wood, while European houses are mostly brick or concrete. Measurements in a flat rural area surrounded by mountains in the Piedmont area in Italy are reported in [19]. The authors used a WiMAX system and compared the obtained results with empirical prediction models. The authors in [20] conducted measurements with a CW signal in a suburban environment in Shanghai, China. The obtained results were fitted to the generic path loss according to (2.1) but not compared with any other model.

Common to these former measurement campaigns was that they either used a WiMAX system with a bandwidth of only 3.5 MHz or a CW signal. Therefore, no conclusions can be drawn confidently for a wide bandwidth such as 100 MHz that can be used for 5G. Furthermore, the base station (BS) antenna height varied between 15–36 m, while the UE antenna height varied between 2–10 m above ground. Comparisons have been done with the models Erceg, COST 231 WI, COST 231 Hata, SUI, and ECC-33, but none with the 3GPP path loss models. All publications calculated a path loss exponent  $\gamma$  and standard deviation  $\sigma_\gamma$  according to the simplified path loss model from (2.1), summarized in Table 2.1 (only the lowest UE height is considered in the table). The variations in these parameters (e.g.,  $\gamma$  for a suburban terrain ranges from 2.13 to 4.9 and for urban terrain from 2.3 to 4.3) indicate that there are many influences on the propagation channel that may depend on the geographic region, construction material, and vegetation which in parts has also been confirmed in [21].

Table 2.1: Comparison of path loss parameters for (2.1) at 3.5 GHz

Terrain	Location	Signal	UE Height [m]	Distance [m]	$\gamma$	$\sigma_\chi$ [dB]
Rural	Cambridge, UK [16]	WiMAX	6	250–2000	2.7	10
Rural	Piemonte, Italy [19]	WiMAX	2	1000–10000	2.5	8.9
Suburban	Cambridge, UK [16]	WiMAX	6	250–2000	2.13	11.1
Suburban	Ghent, Belgium [18]	CW	2.5	30–1500	4.9	7.7
Suburban	Shanghai, China [20]	CW	3	300–1800	3.6	9.5
Urban	Cambridge, UK [16]	WiMAX	6	250–2000	2.3	11.7
Urban	United Kingdom [17]	CW	2.5	100–2000	4.3	7.5

In summary, [16] suggests the ECC-33 model for urban and the SUI (terrain B) for suburban environments. [18] concludes that the Erceg (terrain C) best fits suburban environments, but underpredicts the measured path loss. For rural environments, [19] and [16] show that the best fitting models SUI (terrain B & C) and COST 231 Hata overestimate the measured path loss. Because the path loss model with the lowest prediction error varies, it is challenging to decide on a specific model for network planning purposes.

Regarding outdoor-to-indoor propagation, CW measurements were presented in [22], along with a few outdoor measurements. A difference of only 10 dB more attenuation was found for a modern building compared to an old building, which results from different wall thicknesses and building materials, according to the authors. Because Low-E coated windows typically add 20–30 dB attenuation, we conclude that the modern building may not be equipped with Low-E windows. In [23], the authors used a WiMAX system and measured an average BEL in the range of 7.5–12 dB through windows and 13–17.5 dB through walls. It is also highlighted that the angle-dependent loss increases with the carrier frequency and is about 2 dB higher compared to 1.8 GHz. Additionally, the authors note that the effect of indoor furniture may start playing a role at 3.5 GHz. Outdoor-to-indoor coverage using a 5G testbed was measured and presented in [24]. A window penetration loss of 21 dB has been measured, but a direct comparison of the outdoor to the indoor received power levels is not available.

The related works listed above show that the path loss characteristics (path loss exponent  $\gamma$ , fading standard deviation  $\sigma_\chi$ ) vary greatly depending on the environment. An overview of relevant empirical path loss models is given in Section 2.1.2. To have a local reference and decide on a model for network planning, we conducted extensive measurements in Switzerland in a rural, suburban, and urban environment. The measurement setup and environments are described in Section 2.1.3. Contrary to most prior works, a beamforming BS antenna was used, parallel measurements on a live network in legacy frequency bands were conducted for comparison and validation, and more realistic UE antenna heights for mobile cellular applications were used. The obtained results are compared against the 3GPP, WINNER II, and SUI path loss models and are described in Section 2.1.4. The model ITU-R P.1411-9 was excluded due to its specificity to environments requiring information on line-of-

Table 2.2: Selected empirical path loss models

Name	Frequency Range	Distance Range
Hata-Okumura	150 – 1500 MHz	1 – 20 km
COST 231 Hata	1500 – 2000 MHz	1 – 20 km
COST 231 Walfish-Ikegami	800 – 2000 MHz	0.02 – 5 km
Erceg	≈ 2000 MHz	0.1 – 8 km
SUI IEEE 802.16	1 – 4 GHz	0.1 – 8 km
ECC-33	3.4 – 3.8 GHz	1 – 10 km
WINNER II	2 – 6 GHz	0.05 – 5 km
ITU-R P.1411-9	0.3 – 100 GHz	0.055 – 1.2 km
3GPP	0.5 – 100 GHz	0.01 – 5* km

\* 10 km for RMa LOS

sight (LOS) and non-line-of-sight (NLOS), BEL, multipath models for both environments of street canyon and over roof-tops, number of signal components, polarization characteristics, and fading characteristics.

### 2.1.2 Overview of Empirical Path Loss Models

Because most mobile communications applications have been using frequencies up to around 2 GHz, the empirical path loss models were optimized to cover only these frequencies. Examples are (see also Table 2.2): Hata-Okumura [25], COST 231 Hata [26], COST 231 Walfish-Ikegami (COST 231 WI) [26], and Erceg [27]. Path loss models valid for the 3.5 GHz band are the *Stanford University Interim (SUI)* IEEE 802.16 model [28], which is an extension to the Erceg model, the *ECC-33* model [29], which extrapolates the Hata-Okumura model, the *WINNER II* models [30], the *ITU-R P1411-9* models [31], as well as the *3GPP* models described in [32].

When designing wireless networks, it is evident that underestimating the path loss can lead to coverage holes. Likewise, overestimating the path loss is undesirable because this leads to severe inter-cell interference (ICI) issues. For an accurate prediction, existing models need to be evaluated for the environments in which they shall be used and adjusted if necessary. Additionally, penetration of signals from outdoor-to-indoor depends heavily on the building materials and varies a lot, even within the same cell coverage area. While wooden and older houses—Rec. ITU-R P.2109-0 [33] refers to ‘traditional buildings’—tend to have a small penetration loss, modern ‘thermally-efficient’ buildings with infrared reflecting Low-E coated glass windows impose high losses.

The path loss (in dB) can generally be expressed according to the simplified model in [15, eq. (1.12)]:

$$L_P(d) = A_0 + 10\gamma \log_{10} \left( \frac{d}{d_0} \right) + \chi \quad d > d_0, \quad (2.1)$$

where  $A_0 = 20 \log_{10}(4\pi d_0 / \lambda)$  represents the deterministic path loss component at the reference distance  $d_0$  in meters and where  $\lambda$  is the signal wavelength. The path loss exponent is denoted by  $\gamma$ , and  $d$  is the distance in meters between BS and UE. Finally,  $\chi$  is the stochastic shadow fading component in dB with a zero-mean log-normal distribution and standard deviation  $\sigma_\chi$ . The above-mentioned empirical models can also be expressed according to (2.1) with additional terms depending on, e.g., the operating frequency, BS, and UE antenna height [19, eqs. (3)–(12)].

### 2.1.3 Measurement Setup and Environment

Before presenting the measurement results, we describe the methodology and provide information on the equipment, antennas, and signal used. Because we want to compare the measurements with empirical path loss models for rural, suburban, urban, and indoor environments, the specifics of the environments where the various measurement campaigns were conducted are described.

#### 2.1.3.1 Measurement Method

To compare path losses, we first need to obtain the RF propagation path loss based on a defined power emitted by a transmitter (the beamforming antenna of the BS), and the measured power at a receiver antenna (the UE). Therefore, the propagation path loss in the downlink is defined as the RF attenuation  $L_P$  in dB of a transmitted BS signal when it arrives at the UE receiver:

$$L_P = P_T + G_T(\phi, \theta) + G_R - P_R \quad [\text{dB}], \quad (2.2)$$

where  $P_T$  is the BS transmitted power in dBm, and  $G_T(\phi, \theta)$  is the transmitter antenna gain in dB as a function of azimuth angle  $\phi$  and elevation angle  $\theta$ . Because the UE antenna is omnidirectional, we can simplify the receiver antenna gain as a constant  $G_R$  in dB. Finally,  $P_R$  is the local mean received power in dBm.

All measurement parameters were geographically binned in a two-dimensional square 5 m-grid for the analysis, thus removing fast fading effects according to the Lee sampling criterion [34]. The local averaging further prevents a bias from temporal influences due to, e.g., stops at red traffic lights. For each bin, the median value was computed. In addition, the median value was also calculated for each 5 m distance bin for the log-distance path loss plots.

#### 2.1.3.2 5G Testbed

For conducting measurements as close as possible to a typical 5G scenario, we had the unique opportunity to employ one of the few available 5G testbeds (similar to [24]) worldwide. This setup consisted of a BS unit, an active antenna system (AAS) connected via fiber to the BS, and in our case, two UEs (see Fig. 2.2a for a picture of the AAS and one UE). The center frequency

## 2.1 Path Losses in 5G Mid-Band Spectrum (3.5 GHz)

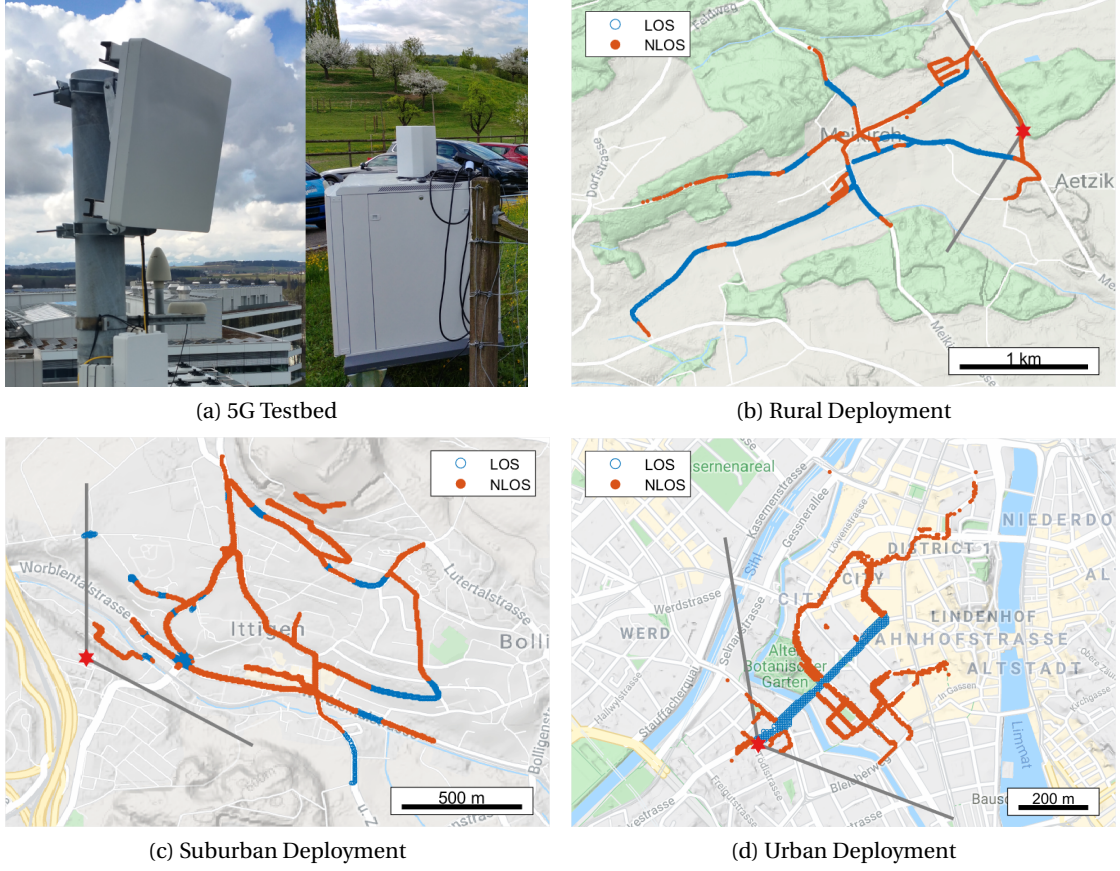


Figure 2.2: (a) Shows the 5G testbed AAS on a mast and the UE in the field, (b) the map of the rural deployment with a red star indicating the AAS location with the 120° sector, and the LOS/NLOS classification. Similarly, (c) and (d) show the map of the suburban and urban deployments, respectively.

for which test licenses were available was 3.55 GHz. The time division multiplexing (TDD) orthogonal frequency division multiplexing (OFDM) signal effectively occupied a bandwidth of 80 MHz. Further details can be found in [24, Tab. 1] and the references therein. Contrary to the beam grid described in [24], we used a configuration with the 48 different dual-polarized beams arranged in a grid of three rows with 16 beams each (visible in Fig. 2.3a). The antenna gain and the resulting coverage remain approximately the same as with the configuration described in [24], with 27 dBi, and 120° in azimuth and 30° in elevation, respectively. The two identical UEs have eight antenna ports connected to an eight-element omnidirectional cross-polarized antenna, each element with a gain of 6 dBi.

As in [24], the mobility reference signal received power (MRSRP) for each of the 48 beams has been logged and used for the analysis. The mobility reference signal (MRS) is a pilot signal used for subframe synchronization and identification of downlink beams. It is transmitted every 5 ms and cycles through all 48 beams over 20 ms. Although there are significant differences,

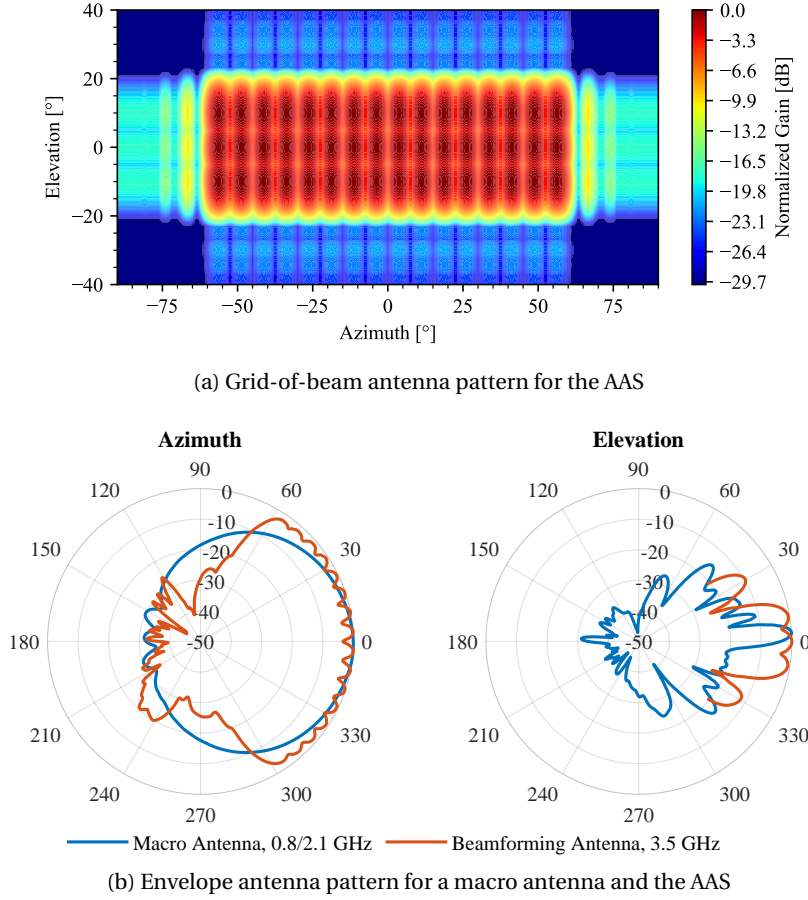


Figure 2.3: Antenna patterns used for the macro antennas (conventional sector and AAS).

such as the subcarrier bandwidth, it can be used similarly to the LTE reference signal received power (RSRP). The highest of the 48 MRSRP values is used as  $P_R$  for each period. The cable loss in the UE between the RF frontend and the antenna can be considered part of the constant  $G_R$ , which becomes 4 dB. We can directly use the configured power  $P_T$  of the AAS on the transmitter side because the radio chains and power amplifiers are directly connected to the antenna elements. However, depending on where the UE is located with respect to the AAS, a directive antenna gain  $G_T(\phi, \theta)$  is considered. For the grid-of-beam beamforming antenna, an artificial envelope pattern can be calculated by cycling through all beams sequentially, then virtually overlaying them, and taking the maximum at each angle, see Fig. 2.3b. The total measurement uncertainty is 6.25 dB considering the tolerances of cable losses and deviations from the typical antenna gains.

The UE has been moved around with a van and pushed by hand in places where driving was not possible. A picture of the measurement van with one UE inside and its antennas on the roof of the van is shown in Fig. 2.4. Behind the van, a second UE is shown, pushed by hand in pedestrian areas and indoors. When using the van, the UE and scanner antennas were mounted 16 cm over the roof of the vehicle to limit its influence on the antenna characteristic,



Figure 2.4: Measurement van with a UE inside and its antennas installed at the back on the roof. A second UE on wheels is shown behind the van.

which resulted in a height of 2.1 m above ground. When manually pushing the UE around, the antennas were at 1.4 m above ground, corresponding to the approximate height at which an adult usually holds a smartphone. In all cases, we ensured that no people, vehicles, or other non-stationary obstacles were in the proximity of the UE.

### 2.1.3.3 Reference Measurements in Legacy Frequency Bands With 4G

For the analysis of the 5G cell signal propagation at 3.5 GHz, it is helpful to have a comparable 4G (LTE) cell available in a frequency band where more measurement data and experience exist. Additionally, 5G is first introduced in a non-standalone (NSA) mode, where a 4G anchor carrier is required. Thus, the test deployments were chosen to have an existing macro site antenna mast to install the 5G AAS and a live LTE signal on a legacy frequency band.

For the measurements, a mobile network scanner (Rohde & Schwarz TSMW) with a laptop running Nemo Outdoor has been used for logging propagation channel metrics based on the LTE downlink signal. The RF was locked to one frequency band (800 MHz or 2.1 GHz), and all RSRP values per cell were recorded. For the analysis, only the values of the cells of interest were used. The 2×2 MIMO antennas (Rohde & Schwarz TSMW-Z8), which were used, emulate omnidirectional smartphone antennas to give realistic results. Together with the cable losses, their gain is considered with  $-3$  dBi each<sup>2</sup>. The transmit power is corrected with the feeder cable losses on the LTE base station side to have the transmit power  $P_T$  at the antenna ports. Again, a directive antenna gain  $G_T(\phi, \theta)$  is considered (see Fig. 2.3), depending on the relative location of the testbed UE to the LTE BS antenna. Based on the tolerances of the used components, the total measurement uncertainty is 4.5 dB. The network scanner has been fitted inside the 5G testbed UE, and the 2×2 MIMO antennas could also be mounted close to the 5G antennas of the UE without shielding them.

<sup>2</sup>Smartphone antennas are usually integrated and partially covered, resulting in negative antenna gains



Figure 2.5: The installation of the base station rack (left picture) and the AAS on the live macro site mast (right picture).

### 2.1.3.4 Rural Area Environment

The rural deployment was located close to a village (Meikirch) northwest of Bern, Switzerland. The selected live macro site only had an LTE 800 MHz cell with a 10 MHz carrier directed over flat open fields towards a village at a 1–1.5 km distance. The 5G AAS was installed right below the existing live macro antenna at the height of 12.4 m above ground, with the same azimuth angle as the macro antenna, see Fig. 2.5. The vertical separation of the macro antenna to the testbed AAS was 2.1 m, which resulted in a mean elevation angle difference of  $0.22^\circ$  seen from the UE antenna over all measurement sample locations. The maximum used transmitted power for 3.5 GHz was  $1560 W_{ERP}$ .

The measurements took place in mid-July 2018 during a sunny and clear week with an air temperature of around  $22^\circ\text{C}$ .

### 2.1.3.5 Suburban Area Environment

The suburban deployment was done in Ittigen, just northeast of Bern, Switzerland, situated on a slightly ascending slope, see Fig. 2.6. For comparison, the signal from an existing LTE macro site at 2.1 GHz with a 20 MHz carrier was used. The testbed AAS has been mounted on a smaller extra mast next to the existing LTE macro site mast due to space limitations on the latter. The height of the AAS was 24.5 m above ground. The horizontal separation between the antennas was 3.8 m, while the vertical separation was 8.5 m. The mean angular separation of both antennas seen from the UE over all measurement sample locations is  $0.232^\circ$  in azimuth and  $0.819^\circ$  in elevation and is regarded as negligible. The maximum transmitted power for 3.5 GHz had to be limited due to stringent non-ionizing radiation (NIR) regulations in Switzerland. Without lowering the transmitted power on the live macro cells, the permitted maximum transmit power for 3.5 GHz was  $384 W_{ERP}$ .



Figure 2.6: View of a part of the suburban measurement area from the AAS.

The measurements took place at the end of April and the beginning of May 2018, with sunny and also overcast days but no rain. The air temperature was around 15–20 °C.

### 2.1.3.6 Urban Area Environment

For an urban deployment, a suitable and existing live macro site was selected in Zurich, Switzerland. The AAS has been mounted just below an existing macro sector antenna on the same mast at the height of 29.4 m above ground, overlooking a flat part of the city. Unfortunately, due to technical issues, no measurements of an LTE legacy band could be taken for this scenario. Again, the NIR regulations required that we lower the maximum transmit power. We could use the same maximum 384 W<sub>ERP</sub> for the 3.5 GHz 5G cell as in the suburban deployment by slightly reducing the power on a few live macro cells on this site.

The measurements took place middle of August 2018 during a sunny week with an air temperature of around 25 °C.

### 2.1.3.7 Outdoor-to-Indoor Scenario

We collected indoor measurements at six buildings of the suburban deployment and two buildings of the urban deployment to assess the BEL for frequencies above 3 GHz. Unfortunately, no connection to the base station could be established in two suburban buildings, coincidentally, where there was no room with view towards the 5G AAS. In all cases, the measurements were started inside, just behind a window with line-of-sight to the 5G AAS. The UE was then slowly and steadily moved further inside the building, either until the connection dropped or the backside of the building was reached. Outdoor reference measurements were taken just in front of the building or on a terrace on top of the building.

Table 2.3: Estimated Path Loss Model Parameters for (2.1)

Frequency	Rural LOS/NLOS		Suburban		Urban	
	$\gamma$	$\sigma_\chi$ [dB]	$\gamma$	$\sigma_\chi$ [dB]	$\gamma$	$\sigma_\chi$ [dB]
3.55 GHz	2.3 / 3.1	5.1 / 9.4	2.9	6.9	4.8	7.1
2.1 GHz	–	–	3.7	7.0	–	–
800 MHz	2.8 / 3.4	5.9 / 7.5	–	–	–	–

### 2.1.4 Measurement Results

For all environments described in the previous section, a total of 267 data sets were analyzed. Each site deployment was analyzed separately, and the path loss was obtained according to (2.2). With a least squares (LS) regression, the path loss exponent  $\gamma$  is estimated with the reference distance  $d_0$  at 100 m, and the standard deviation  $\sigma_\chi$  is calculated according to the model (2.1). The estimated values are listed in Table 2.3. A comparison with the models SUI IEEE 802.16 (A, B, C), ECC-33, WINNER II (C1, C2, D1), and 3GPP (RMa, UMa) was performed. In general, the ECC-33 model overestimates the path loss and is not well suited because it was derived by fitting curves for distances of 1 to 10 km. Prediction error statistics have been computed for the few models that agree the most with the respective measurements. The mean prediction error  $\mu_e$  indicates an over- (positive value) or under-prediction (negative value) with standard deviation  $\sigma_e$ , and the root mean square error (RMSE) of the prediction represents the general metric for comparison of how well the models fit the measurements. These were calculated in log-domain [dB].

#### 2.1.4.1 Rural Environment

As expected, this environment provides a good share of LOS opportunities; in fact, 42 % of the measurement samples are estimated to be in LOS condition. The large share of LOS makes it necessary to analyze LOS and NLOS separately. The classification for LOS/NLOS has been done by manually defining five coordinate polygons. All measurement samples within these five polygons were categorized as LOS, the others as NLOS. The measured path loss for 3.5 GHz is shown in Fig. 2.7 (LOS marked with circles) with predictions from the models 3GPP Rural Macro (RMa) NLOS and the WINNER II D1 (rural macro) NLOS. The free space path loss (FSPL) according to Friis is also shown as a reference. Variations in the path loss from 600 m to 2 km (see shaded area) show the changes between LOS and NLOS environments. All error statistics are listed in Table 2.4. Both models overestimate the path loss by 14.9 dB and 9.8 dB, respectively, and the WINNER II D1 rural NLOS models fit best, although the measurements are often well outside of their 8 dB standard deviation. The shadow fading distribution is shown in Fig. 2.8 in the top two distributions for LOS and NLOS.

Because 5G NSA requires a 4G anchor carrier, it is vital to know the differences in the path losses at the frequencies used. For comparison, the measured path loss for the 800 MHz LTE signal is also shown in Fig. 2.7, with the corresponding FSPL as a reference. Furthermore,

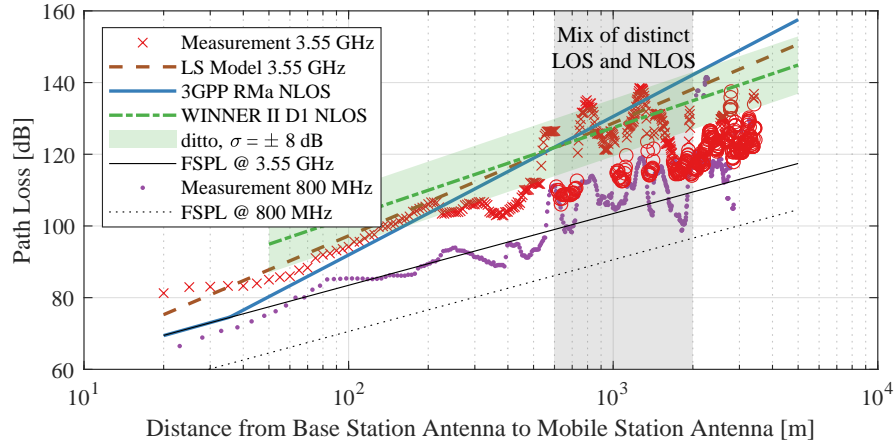


Figure 2.7: Rural environment measurements compared to models.

for each 5 m measurement grid location, both path losses are plotted in Fig. 2.9. If only a frequency-dependent offset is assumed, a line with a slope of 10 dB/10 dB can be fitted. This offset is in theory  $20 \log_{10}(3.5 \text{ GHz}/0.8 \text{ GHz}) = 12.8 \text{ dB}$ , but measurements show 15 dB with a standard deviation of 8.3 dB. The 2.2 dB residual is within the measurement uncertainty.

### 2.1.4.2 Suburban Environment

As explained in Section 2.1.3.5, parallel measurements at 2.1 GHz have been conducted for this campaign. In this case, two anomalies were corrected during the data validation: the first was caused by a loss of connectivity because of a large apartment complex affecting signal propagation. The affected street segment was excluded from the analysis; the second originated from the local geography, resulting in a much higher than expected signal strength. Fitting the data to a two-ray model [35] using the delay spread information from the network scanner allowed us to explain this anomaly. The corrected overall path loss versus distance is shown in Fig. 2.10. The environment does not offer many LOS opportunities. Therefore, we could categorize LOS areas by manually defining coordinate polygons that were visually validated with pictures on site. As a result, 14 % of all samples fall into such LOS polygons.

Comparing empirical models with the measurements at 3.5 GHz shows the best agreement with the SUI Terrain C model (RMSE = 4.87 dB) and the 3GPP RMa NLOS (RMSE = 5.29 dB) model. Both models overestimate the path loss by 2.11 dB and 3.83 dB, respectively. These results are also listed in Table 2.4. The shadow fading with a close to normal distribution is shown in Fig. 2.8 on the third row.

The available measurement data and the estimated path loss on 2.1 GHz (also shown in Fig. 2.10) allow the comparison with 3.5 GHz, as shown in Fig. 2.9. Fitting a slope of 10 dB/10 dB results in an offset of 5.8 dB with a standard deviation of 8.1 dB. In theory, this frequency-dependent offset is  $20 \log_{10}(3.5 \text{ GHz}/2.1 \text{ GHz}) = 4.4 \text{ dB}$ . The 1.4 dB residual is within the measurement uncertainty.

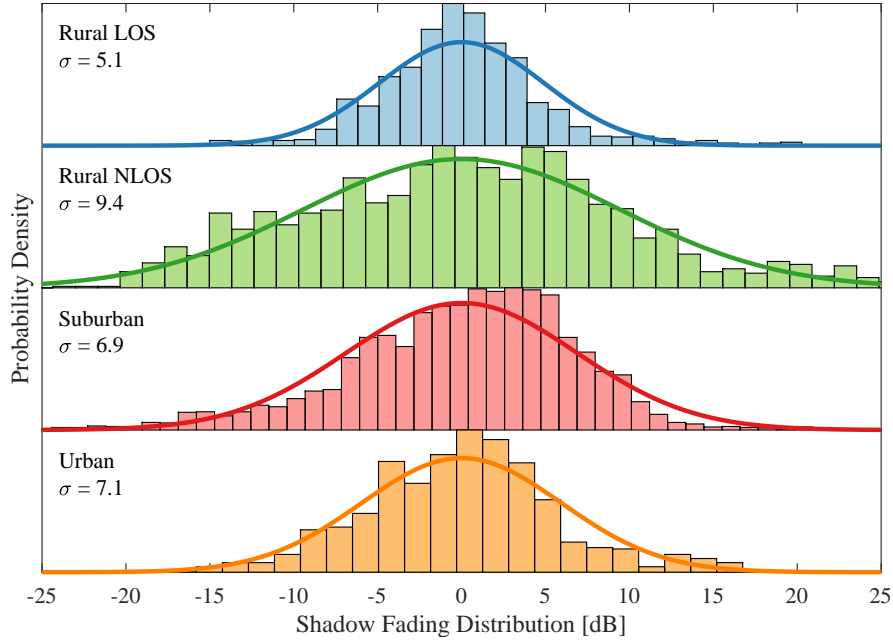


Figure 2.8: Distribution of the measured shadow fading components. The solid curve represents the Gaussian fit for each distribution and is an indication if the shadow fading has a log-normal distribution.

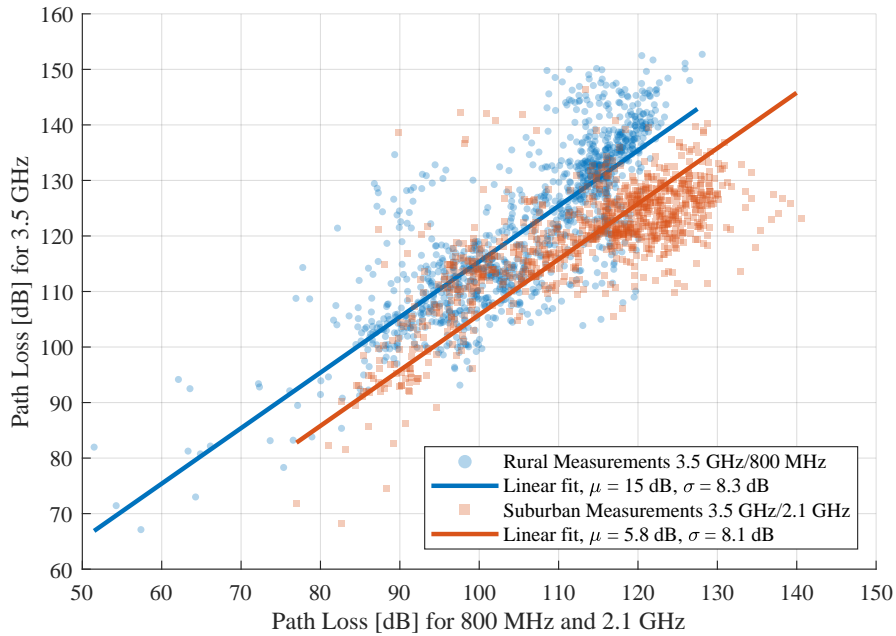


Figure 2.9: Path loss for 3.5 GHz vs. 800 MHz and 2.1 GHz in the rural and suburban measurement area; validating the theory of 12.8 dB and 4.4 dB path loss difference.

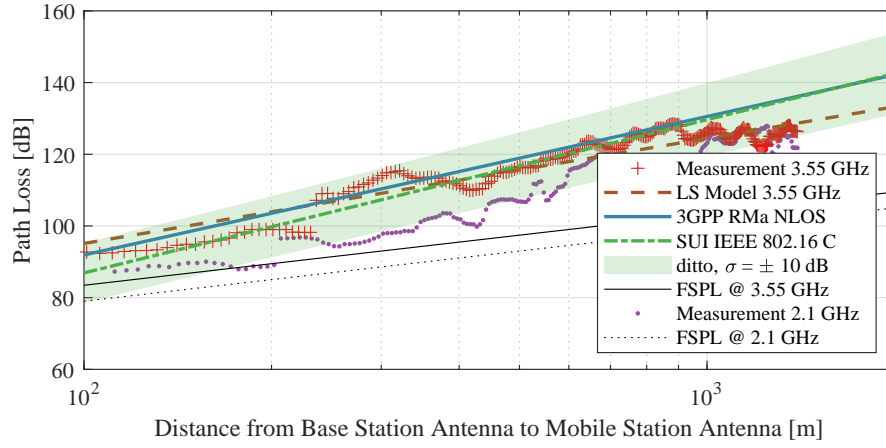


Figure 2.10: Suburban environment measurements compared to models.

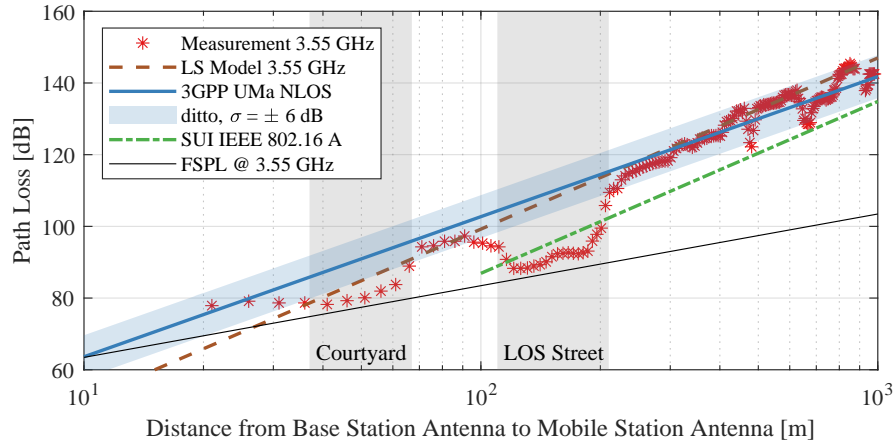


Figure 2.11: Urban environment measurements compared to models.

### 2.1.4.3 Urban Environment

In our measurement data from the urban deployment, we have 27 % of the samples in LOS conditions. This share may seem a lot, but considering a dense deployment with inter-site distances of a few hundred meters and only considering outdoor coverage, this is actually reasonable. The main LOS contributions come from one long street at the azimuth angle of the antenna, between 110-210 m (see the gray-shaded area in Fig. 2.11). Another area with close to LOS path loss has been identified as the courtyard of the city block on which the antenna was mounted (southwest corner, overlooking the city block towards northeast). Regarding the comparison with empirical models, the two that fit the best are the 3GPP Urban Macro (UMa) NLOS (RMSE = 6.84 dB) and the SUI Terrain A (RMSE = 9.78 dB). The 3GPP UMa model slightly overestimates the path loss by 2.1 dB, and the SUI Terrain A model underestimates the path loss by -8.3 dB. Also, these results are listed in Table 2.4. The shadow fading distribution is shown at the bottom of Fig. 2.8 and conforms to the normal distribution.

Table 2.4: Path loss model prediction error statistics

Environment Model	Rural		Suburban		Urban	
	RMa	WINNER2	RMa	SUI C	UMa	SUI A
$\mu_e$ [dB]	14.9	9.82	3.83	2.11	2.07	−8.3
$\sigma_e$ [dB]	10.8	7.53	3.66	4.4	6.54	5.18
RMSE	18.4	12.4	5.29	4.87	6.84	9.78

Table 2.5: Outdoor-to-indoor comparison at 3.5 GHz

Building, Number	RSRP [dBm]		SINR [dB]		Throughput ratio inside*
	outside	inside	outside	inside	
Traditional, 2	−94.2	−98.0	37.2	31.4	79.3 %
Modern Low-E, 3	−74.6	−107.0	34.9	23.9	77.8 %

\* Throughput achieved inside, normalized by throughput achieved outside.

### 2.1.4.4 Outdoor-to-Indoor Scenario

The indoor RSRP measurements are normalized with the corresponding reference outdoor RSRP, and the empirical cumulative distribution function (ECDF) is shown in Fig. 2.12. Buildings 1–4 are from the suburban deployment, the buildings 5 & 6 are from the urban deployment. The measurements clearly show which buildings are modern with coated Low-E windows and which ones use regular windows:

**Building 1** is an older office building with regular double-glazing windows.

**Building 2** is a retirement home with uncoated double-glazing windows.

**Building 3** is a new apartment house with triple-glazing Low-E windows, causing around 30 dB of additional loss.

**Building 4** is a newer office building with triple-glazing windows and one coated layer.

**Building 5** is a renovated 14-floor office building. The measurements from the ground floor behind large single layer shop-windows show lower attenuation than behind multiple glazing Low-E windows on the 13th floor.

**Building 6** is a 12-floor renovated office building with Low-E windows. The measurements from the 6th- and 12th-floor show about the same attenuation, only walls inside the building cause different variations in the path loss.

In general, we can conclude that newer or renovated buildings with coated Low-E windows add 10–30 dB of additional penetration loss compared to buildings with traditional regular windows. Besides, it is crucial for the available indoor capacity what RSRP levels and resulting signal-to-interference-and-noise ratios (SINRs) are available. Two representative examples are listed in Table 2.5. While we have a similar SINR available outdoor (2.3 dB difference) in both cases, the indoor SINRs differ more (7.5 dB). If the outdoor RSRP is lower than in these two cases, the impact on the SINR and achievable capacity is much more substantial. Finally, there was no communication link and, therefore, no capacity available in rooms without LOS to the BS antenna.

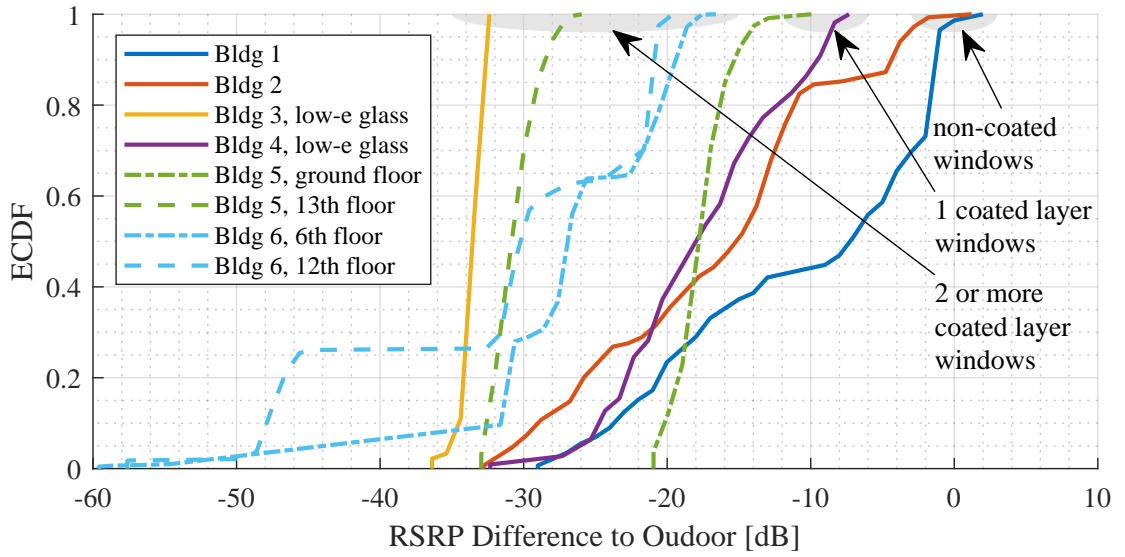


Figure 2.12: Outdoor-to-indoor penetration loss shown as ECDF of the received power difference from indoor compared to outdoor.

### 2.1.5 Measurement Conclusions

Measurements from rural, suburban, and urban measurement campaigns with a 5G testbed operating in the 3.5 GHz band have been analyzed and compared with predictions from empirical path loss models (3GPP, WINNER II, SU1). Almost all models tend to overestimate the path loss. Even though no model gives the least error in all environments, the 3GPP group of models are consistently ranked among the top two, with an over prediction of 2.1 dB and 3.8 dB for the urban and suburban scenario and 14.9 dB for the rural scenario. The path loss exponents are slightly lower with a beamforming antenna at 3.5 GHz compared to a conventional macro antenna at 2.1 GHz and 800 MHz. Although 3.5 GHz does exhibit an increased path loss of 5.8 dB compared to 2.1 GHz and 15 dB compared to 800 MHz, the outdoor signal coverage is still good. However, indoor coverage and capacity were only available in rooms with windows facing the BS antenna. Finally, the excessive attenuation of around 10 dB per coating layer of Low-E windows impacts outdoor-to-indoor penetration significantly. This issue is particularly concerning as the number of newly built and renovated houses grows.

### 2.2 State of the Art

The reason for low to inexistent data capacity inside buildings or railway carriages is often a highly shielding hull causing a significant penetration loss. Two possibilities exist to increase capacity: (1) the penetration loss is reduced; (2) dedicated wireless connectivity is deployed inside.

Modern buildings and railway carriages are equipped with coated Low-E windowpanes for thermal isolation. Unfortunately, these windows also strongly attenuate RF signals, thus limiting the data capacity. The solution for (1) is to reduce the penetration loss by replacing or treating windows. Structured windows—also known as frequency selective surfaces (FSSs)—are Low-E windowpanes treated with Laser to engrave a pattern into the coating [36]. Such treated windows reduce the RF attenuation from around 20–30 dB to 1–3 dB [37].

Option (2) to install active equipment in buildings or railway carriages can be further distinguished. The communication layers provide a systematic way for categorization:

**Layer-1 relay:** amplify-and-forward (AF) type, called (signal) booster or repeater

**Layer-2 relay:** decode-and-forward (DF) type, same cell identification

**Layer-3 relay:** functions of a base station, own cell identification

**Small cell/wireless router:** typically provides a mobile cell or wireless local area network (WLAN) backhauled over cable or wireless, e.g., 4G or 5G

Further details with characteristics, advantages, and disadvantages of layer-1 to layer-3 relays are discussed in [38]. Another, more specific categorization is provided in the LTE standard with relay type 2 (layer-2 relay) and type 1 (layer-3 relay), which is further split into type 1a (out-of-band) and type 1b (in-band). However, we consider only the following three categories for our study: layer-1 relay/repeater, layer-3 relay, and small cell/wireless router. The layer-2 relay is omitted because it suffers from the same potential interference from an outdoor donor cell to an indoor service cell if the outdoor-to-indoor isolation is not sufficiently large. The three methods considered are depicted in Fig. 2.13:

- (a) the indoor **small cell** (or WLAN access point) backhauled by fiber-optical cable providing full capacity independent of the outdoor network load;
- (b) a layer-3 **relay** installed at the building or railway carriage providing a cellular access different from the outdoor network, but because of the wireless backhauling the available indoor capacity depends on the outdoor capacity shared with the outdoor users;
- (c) a layer-1 **repeater** installed at the building or railway carriage that amplifies the wireless communication signals, thus providing an extension of the outdoor network to the inside also sharing the outdoor network capacity.

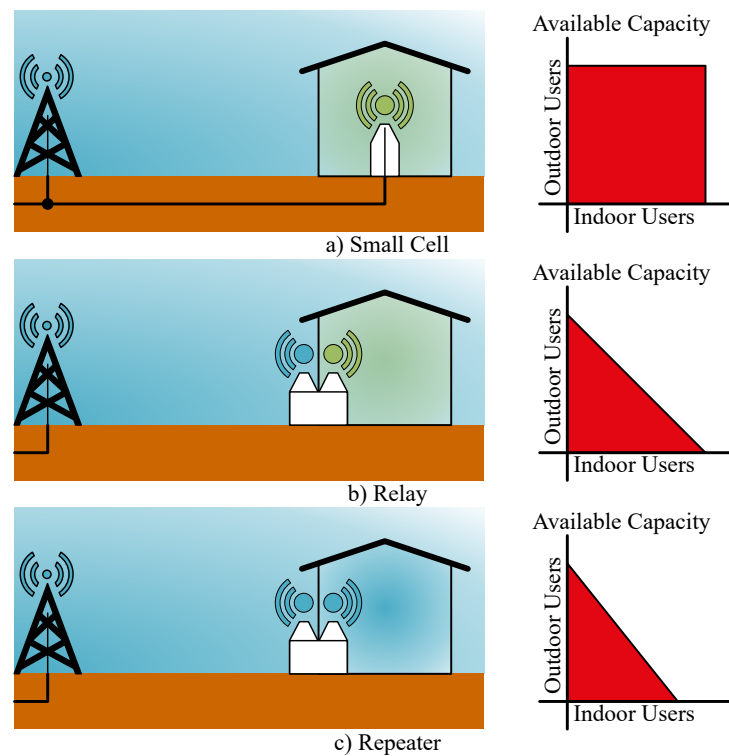


Figure 2.13: Methods to increase indoor data capacity.

Besides the methods mentioned above, there are further emerging technologies that may contribute to an indoor capacity increase:

**Integrated Access and Backhaul (IAB)** is a feature specified in 3GPP NR Release 16 as a method for base stations to use the wireless access network for backhauling [39–41]. An IAB can be categorized as a relay (b) in Fig. 2.13. The advantage is that (new) cell sites can be deployed using the access network also for backhauling. The MNOs have more flexibility with their spectrum pool and can decide which carrier frequencies they use for what. The disadvantages are the additional latency introduced because of protocol processing and the higher complexity of the required hardware compared to a repeater. An IAB node acts itself as a base station, possibly requiring different radio hardware if the backhaul and access are in different frequency spectra.

**Reconfigurable Intelligent Surface (RIS)** describes a technology based on passive electromagnetic surfaces (metasurfaces) that can be electronically controlled [42–44]. The integrated electronics can influence the scattering, absorption, reflection, and diffraction properties of the RIS and thereby control its impact on signal propagation in software. The use of RISs in a wireless network environment with a software-based reconfiguration platform to optimize the connectivity and propagation is called a “smart radio environment”. The advantages are that RISs are nearly passive and ideally do not need any dedicated energy source. They can be deployed, e.g., on walls, ceilings, windows, or billboards, and can take almost any two-dimensional shape and size. Furthermore,

as an RIS does not actively amplify, it does not introduce noise in the reflected signal. The disadvantages are the complexity of sensing and controlling the radio environment and the relative technological infancy compared to other methods. The absence of amplification may also limit the use cases of an RIS.

### 2.2.1 Deployment Options to Increase Indoor Capacity

This section describes the three major solutions introduced above and listed in Fig. 2.13 in more detail, along with related work, and discusses their advantages and disadvantages.

#### 2.2.1.1 Small Cells

The ideal solution to provide high data capacity in buildings is to install small cells. Note that we use this term as an umbrella term for various forms of small cells, including picocells and femtocells. A small cell provides a dedicated mobile network independent of the outdoor network, thus adding the full capacity of an isolated cell to the overall network capacity. Smaller buildings may be equipped with just one small cell, but bigger buildings may require multiple small cells. Because these cells all need an appropriate backhaul connection to provide the high data rates, an expensive, large-scale deployment of fiber to the home (FTTH) is required. While efforts in this direction are ongoing, it is economically not feasible to achieve FTTH deployments for close to 100 % of the buildings within the next couple of years. Especially in larger countries, it might take decades if the vision is not discarded altogether. Another disadvantage of small cells may be the residual interference between the outdoor mobile network and the indoor small cell if they use the same frequency bands [45]. Furthermore, even reduced complexity small cells require complex hardware, which is costly and require regular maintenance and updates to follow the evolution of standards.

#### 2.2.1.2 Relays

A method that does not require a wired backhaul is the installation of relays that operate on layer-2 or layer-3. The layer-2 relay decodes the received signal, reencodes it (decode-and-forward), and sends it again amplified on the same frequency, ideally clean of noise and interference [46, 47]. The layer-3 relay not only decodes the received signal but also creates a new cell with its own cell identification on either the same or on a different carrier frequency. It also performs user data concatenation, segmentation, reassembly, and ciphering. However, if the received signal level or quality on the donor link is too low, the decoding may fail, and the relay fails to transmit the cell signal. Therefore, careful planning and installation of the donor antenna are required. A disadvantage of the relay is the substantial delay from decoding and reencoding the signal. In addition, if the service cell carrier frequency overlaps with a cell carrier frequency used outdoor, a high isolation between the outdoor (donor) and indoor (service) cells is required to prevent interference from the direct path (see Fig. 2.14). However,

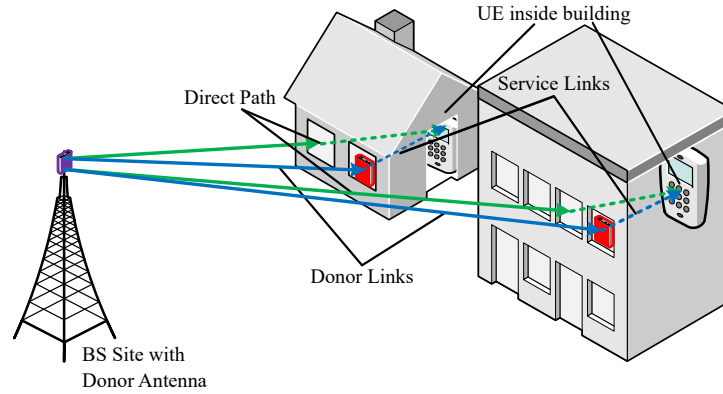


Figure 2.14: Base station transmitting to mobile stations inside buildings. Direct signal path in green, relayed/repeated signal path in blue.

if the link operates in mmWave spectrum, the high BELs help to reduce such interference. While a layer-2 relay needs radio control functions for the communication between the donor base station and the relay, a layer-3 relay has less impact on the standard but requires the functionality of a base station itself, much like a small cell. Therefore, relays suffer from similar complexity and maintenance issues as small cells. Unlike small cells that require a wired backhaul, relays can also be used onboard trains. In a more informal and general sense, but technically incorrect, a WLAN (Wi-Fi) access point with a cellular backhaul (cellular WLAN router) could also be considered a relay.

### 2.2.1.3 Repeaters

Layer-1 AF in-band repeaters are a widely deployed, inexpensive method to extend the coverage and bring data capacity to remote areas and into buildings or trains where the outdoor macro network cannot reach. A repeater (red box in Fig. 2.14) receives the donor base station signal through a (directional) antenna, filters the signal, and retransmits it amplified through the service antenna in the same frequency band as the donor cell. Therefore, its operation is transparent for the base station and the UE, which reduces hardware and integration complexity and maintenance costs. Regarding the data capacity, two MIMO layers have been standard since the introduction of LTE, and with 5G NR, even four MIMO layers may become common, especially indoors. However, to support multiple layers requires the installation of multiple donor and service antennas with the same number of repeater amplifier chains [48].

The major disadvantage of repeaters is the additional noise added to the repeated signal due to the amplifier. If multiple repeater systems are deployed in a cell, they add considerable noise in the uplink of the common donor cell [49]. The signal delay through a repeater can be critical if the power level difference between the outdoor donor cell and the indoor service cell is not sufficiently high. If we consider the downlink path and denote the donor link signal outside at the repeater donor antenna with  $x(t)$ , the service link signal  $y(t)$  at the UE can be calculated according to (2.3). For simplicity, we only consider the instantaneous power and

assume one-tap propagation channels, i.e., without multipath.  $G_R$  denotes the repeater gain,  $L_P$  the propagation loss inside the building or railcar from the transmitter of the repeater to the receiver of a UE.  $L_I$  represents the building or railcar isolation<sup>3</sup> and is larger than  $L_W$ , which represents the penetration loss (or BEL) of a signal from outside through the window to the UE inside. The signal delay of the repeater is represented by  $\tau$ .

$$|y(t)|^2 = \underbrace{\frac{G_R}{L_P} |x(t - \tau)|^2}_{\text{main component}} + \underbrace{\frac{G_R}{L_P} \sum_{k=2}^{\infty} \left(\frac{G_R}{L_I}\right)^{k-1} |x(t - k\tau)|^2}_{\text{self-interference}} + \underbrace{\frac{x(t)}{L_W}}_{\text{direct interference}} \quad (2.3)$$

The main component is the desired outside donor signal amplified by the repeater experiencing the path loss inside the building or railcar. If the signal delay  $\tau$  is not sufficiently small<sup>4</sup>, the outside donor signal coming straight through the windows to the UE ( $\tau$  earlier than the signal through the repeater) causes intersymbol interference (ISI). We refer to this type of interference as direct interference. Finally, the self-interference is caused by the signal amplified from a feedback loop<sup>5</sup>. While there are signal processing techniques to minimize self-interference, they require significant memory depending on  $\tau$  and are often based on decoding the relayed signal, which partially annihilates the advantage of a repeater. From 2.3, we can see that the ratio  $G_R/L_I$  is fundamental for driving the self-interference term to negligible values. Ideally, we want the gain  $G_R$  to be high to compensate for  $L_P$ , which shows that  $L_I$  needs to be even larger ( $L_{I,\text{dB}} - G_{R,\text{dB}}$  should typically be  $> 15$  dB). It is now apparent that the achievable SINR with a repeater depends on the repeater gain to isolation ratio  $G_R/L_I$  and the penetration loss  $(\frac{G_R}{L_I})/L_W$ . While the window penetration loss  $L_W$  is fixed, the isolation loss  $L_I$  can sometimes be improved, e.g., by increasing the distance from the outside donor antenna to the inside service antenna. Furthermore, the inside propagation loss  $L_P$  can also be minimized with an appropriate choice of antennas or radiating cables.

### 2.2.2 Out-of-Band Repeater Using mmWave Frequencies

A low-cost amplify-and-forward relay node is described in [50], aiming to counteract limited spatial diversity in outdoor-to-indoor scenarios. To this end, spatially multiplexed massive MIMO signals from an outdoor donor cell in a sub-3 GHz frequency band are translated to frequency multiplexed service signals at mmWave frequencies. Compared to legacy repeaters, this concept promises high capacity gains thanks to a higher MIMO channel rank and multi-user MIMO if deployed in large numbers inside buildings. However, it relies on a low BEL and many uncorrelated MIMO paths. A further disadvantage is the incompatibility with existing standard-compliant equipment. The BS and UE need to incorporate special RAT protocol

<sup>3</sup>The isolation corresponds to the path loss between the indoor service antenna and the outdoor repeater antenna that picks up the donor link signal.

<sup>4</sup>In LTE a cyclic prefix of an OFDM symbol has a duration of  $4.7 \mu\text{s}$ . To prevent inter-symbol interference,  $\tau$  needs to be smaller than that.

<sup>5</sup>Imagine a microphone, an audio amplifier, and a loudspeaker: if the microphone is too close to the loudspeaker (insufficient isolation), oscillating screeching sound appears.

stacks in their chipsets, either based on IEEE 802.11ad or special functions for this type of relay, which are not part of 3GPP 4G or 5G standards. Furthermore, it is envisaged in [50] that the nodes shall be low-cost and intended for customer self-installation. Without high-quality hardware and without installation planning and guidance, this approach may not always provide the expected high capacity.

Another concept that translates sub-3 GHz signals to mmWave frequencies and back is described in [51]. The goal is also to increase the channel capacity by providing a high MIMO channel rank inside a building. Instead of relying on sub-3 GHz signals to penetrate into buildings, an outdoor unit uses mmWave frequencies for the donor link and the unlicensed 2.4 GHz band for the service link. At the donor cell, the baseband signal is “time-space-coded”<sup>6</sup>, and the multiple MIMO layers are allocated on different frequency sub-bands resulting in a single input single output (SISO) signal with a larger bandwidth. The complete block of sub-bands is upconverted to mmWave frequencies and transmitted to the relay unit at a building, where the sub-bands are downconverted and “time-space-decoded”<sup>6</sup> before the signal is sent into the building and to the UEs. Unfortunately, the mentioned time-space-coder and a time-space-decoder that are required as an integral part inside the BS serving the relays are not part of existing standards. Furthermore, the design relies on outdoor units with signals in frequency bands that easily penetrate buildings but may also cause interference around the building with outdoor mobile networks in the same frequency band. Additionally, the 2.4 GHz band is often crowded because of the many WLAN access points, Bluetooth devices, and other applications using this unlicensed band. Finally, this concept also suffers from the so-called keyhole effect [50] leading to a MIMO channel rank reduction.

### 2.2.3 Cellular Corridor for Railways

An application related to increasing indoor capacity is the increase of capacity for railway passengers. The solution is the deployment of a cellular trackside corridor for railways. Such a corridor is described, e.g., in [52]. An optical fiber ring distribution network connects base stations from a central location to remote antenna units (RAUs). An adaptation with fewer base stations is described in [53, 54]. Instead of installing one base station per RAU in the central station, a distributed antenna system (DAS) is deployed that yields longer cells and fewer handovers. In [55], a further adaptation is presented that uses mmWave frequencies for the access link to the train. The authors of [56] extend the concepts mentioned above by introducing a dual-hop system. The trackside RAUs use mmWave frequencies to provide a high-capacity backhaul link to train antenna units that operate as moving relay nodes. After the frequency conversion, a media converter is employed to create the access network, based, e.g., on WLAN, for the in-train network. Common to all these solutions is the required optical fiber network for supplying the radio signal to the trackside radio units. However, cable or fiber-based solutions are not attractive due to the associated installation cost for civil work. Furthermore, any installation on board trains cause a conflict between the long life cycles

<sup>6</sup>The wording corresponds to what the authors in [51] specifically use.

of the railway industry for servicing or upgrading the onboard equipment and the rapid evolution in telecommunications [54]. This conflict leads to a constant lag of the technology used onboard trains compared to what is available in the mobile network and the UEs.

### 2.2.4 Energy Efficiency for Cellular Railway Corridors

The energy efficiency of urban heterogeneous mobile networks has been studied in [57]. Their results suggest that an existing macro network with additional low-power pico nodes improves energy efficiency compared to a conventional network with only large cell sites because users may be served from nearby pico nodes, saving energy in the macro nodes. A similar conclusion can be drawn from [58], where the authors found that the deployment of small cells within a macro network significantly reduces the required base station transmit power while the capacity is increased. In contrast to the former papers, which focus on additional small cells, [59] studied if an increased macro cell sectorization could also decrease the overall energy consumption of a cellular network. The authors compared the increased sectorization with network densification and found that additional small cells are still more energy efficient. Those methods only improve the energy efficiency normalized by the provided capacity based on a given number of high-power macro cell sites. However, reducing the number of high-power sites while maintaining the capacity and the specific needs of cellular railway corridors has not been studied.

The evaluation of the above-described impact of additional small cells on the overall power consumption of the mobile network requires sophisticated system models. For this, the work described in [60] shows how the power consumption of radio access network (RAN) equipment can be described accurately in a simple and handy model. Using this model, the authors also present a case study for the energy efficiency of LTE. An additional parameter to the mentioned model is added in [61], taking the cell load as a fractional value into account. The authors in [62] also studied and applied the previously mentioned model for 5G NR with updated parameters. Finally, [63] describes a more complex power model that may be better suited for 5G and 6G, but it requires many more parameters, which are hard or impossible to obtain for commercial products.

### 2.2.5 Beam Control and Selection for Layer-1 Repeaters

Layer-1 repeaters commonly do not use beamforming antennas because of the lack of in-band beam control in line with the signal transparency. However, assuming the impediment of control is solved, repeaters can benefit from analog beamforming antennas to minimize the path loss or track a user or donor node. For efficiency reasons, not the whole beam space is scanned, but a subset of beams is measured.

The context information in the form of a mobile or base station location is used in [64] and [65] to minimize the beam search delay for analog beamforming antennas. The authors assume

that the instantaneous location information is available, and a beam pointing in that direction can be selected, which is often not possible in practice.

The problem of aligning beams without in-band measurements is addressed in [66]. Measurements at a sub-6 GHz frequency are used to infer the best beams at a mmWave frequency. However, the required additional radio frontends and antenna arrays increase the complexity, size, weight, power consumption, and cost (SWaP-C). In [67], a deep neural network is trained to associate the best beam based on the received signal strength from a subset of beams. Besides the user location, signal strength measurements are also required, which may not cover the entire geographical area. A method to determine the best beam alignment in a logarithmic number of measurements is described in [68]. The authors assume that multiple arbitrarily hashed beams can be measured simultaneously. Unfortunately, if analog beamforming antennas do not allow the simultaneous use of multiple beams, the enormous speed advantage disappears. The authors in [69] formulate the alignment of analog beamforming antenna beams as a multi-armed bandit (MAB) model. Contextual information regarding beam misalignment and received energy is exploited to reduce the search space and minimize the overall regret. However, the system model assumes a beam alignment phase followed by a communication phase and only considers a stationary scenario for the evaluation. If the user location and environment keep changing, such an approach cannot be used.

## 2.3 Summary

With 5G, new and higher frequency bands can be used, and much wider carrier bandwidths are possible than with any RAT before. We conducted extensive measurement campaigns in rural, suburban, and urban environments using a pre-commercial 5G testbed operating in the 3.5 GHz band. The measurements have been analyzed regarding the path loss and compared with predictions from empirical path loss models. We found that the models tend to overestimate the path loss for outdoor scenarios. However, the maximum allowed effective isotropic radiated power (EIRP) of a cell is unchanged. Thus, the wider cell bandwidth possible above 3 GHz lowers the power density. Additionally, the higher propagation loss of the higher carrier frequency leads to a combined difference in the order of  $-10$  dB in received power on the UE side compared to a 4G cell signal on a lower legacy frequency band. Furthermore, modern buildings with Low-E windows dramatically impact the BEL with an excessive attenuation of 10–30 dB. Therefore, with the limited outdoor-to-indoor coverage, only a fraction of the high capacity of a 100 MHz cell at 3.6 GHz can be used inside buildings in rooms with windows facing the BS antenna. Moreover, no communication link could be established in rooms without LOS to the BS antenna. A similar issue appears in modern trains with a wagon penetration loss of 20–30 dB. In conclusion, the data capacity potential offered by 5G cannot be materialized with the new and higher frequency bands for outdoor-to-indoor coverage and other related scenarios. Many approaches to remedy the problem have been presented in related works by others, but they all still have deficiencies, and more work is needed.



## 3 The mmWave Bridge

The measurements in the previous chapter showed that the capacity potential of 5G in the 3.5 GHz mid-band and at mmWave frequencies can barely propagate into buildings. Thus, solving the capacity problem indoors and also outdoors in areas with poor coverage requires additional small cells to be deployed (cell densification). Unfortunately, the fiber backhaul of small cells is costly, and obtaining the required permissions takes time. Therefore, we propose and describe a bridge as paired out-of-band repeaters employed to fronthaul sub-6 GHz cell signals from existing cell sites to where the local small cell needs to provide the additional capacity. The bridge concept does not rely on a specific fronthaul carrier frequency. However, due to the dense deployment of all available legacy frequency bands below 3 GHz, almost no bandwidth is available without the risk of interference. The 3.5 GHz band offers several hundred MHz shared among several MNOs, leaving around 100 MHz carrier bandwidth per operator, depending on its acquired license. Nevertheless, the mmWave frequency bands offer up to a few GHz of spectrum, which has become available with the decisions taken at the World Radiocommunication Conference in 2019 [70]. Therefore, to fronthaul a 3.5 GHz TDD cell signal with 100 MHz of bandwidth or a sub-3 GHz frequency division multiplexing (FDD) cell signal with a bandwidth of two times 20 MHz and its inherent duplex spacing of, e.g., 45 to 190 MHz, the available bandwidth in the mmWave frequency spectrum can easily accommodate multiple such carriers. A further advantage of using mmWave frequencies for fronthauling is the smaller antenna dimensions because of the smaller wavelength. Finally, while the higher propagation loss may be detrimental, this higher loss can also be considered an advantage for interference management: obstacles blocking the propagation can be used to limit the coverage and restrain or prevent interference with other cell signals or fronthaul links.

In this chapter, we first describe further the concept of the mmWave bridge and illustrate the high-level functionality. We then describe the deployment objectives and advantages and list typical use cases. The mmWave bridge system architecture is presented next, detailing several functional aspects. After that, we developed a simulation with detailed link budget models to numerically evaluate the performance of the mmWave bridge compared to other

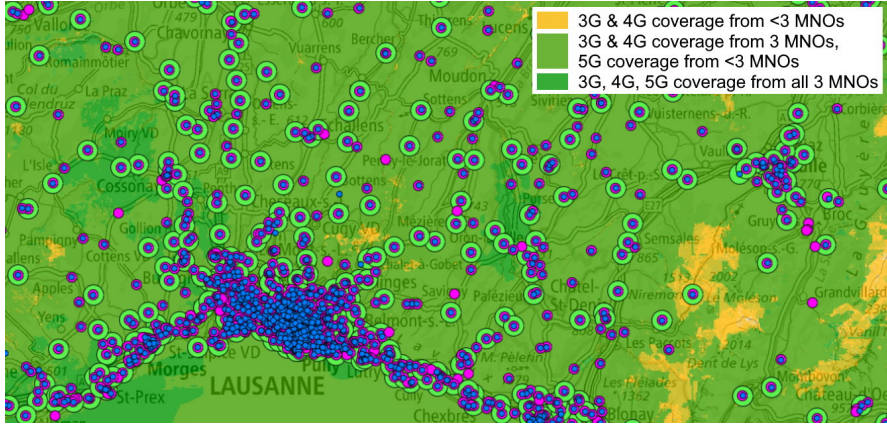


Figure 3.1: Exemplary mobile coverage map showing mobile sites from all MNOs as circles and the availability of 3G, 4G, and 5G service with transparent tiles. (Source: Swisstopo [71]).

state-of-the-art solutions to increase indoor capacity for a fixed wireless access (FWA) use case. Finally, the results from the performance comparison are discussed. The work presented in this chapter has partially been published in [7] and [8].

### 3.1 Proposed mmWave Bridge Solution

Because of the popularity of video streaming and social networking (see Fig. 1.1b), mobile network data traffic has been growing in the last decade, and this trend is predicted to continue [1], as discussed in Chapter 1. Thanks to the convenience and reliability, people access the Internet with their cellular devices everywhere, especially also inside buildings. However, the mobile networks are typically deployed outdoors for the larger area and population coverage. Often, almost all available frequency bands are used to provide the required mobile capacity. The publicly available coverage map in Fig. 3.1 [71] shows the availability of 3G, 4G, and 5G services with transparent tiles and illustrates the dense network. Adding cells using newly available mmWave frequencies to existing cell sites provides considerable additional outdoor capacity. However, this advantage vanishes for outdoor-to-indoor coverage: while the attenuation of certain building materials such as wood, plasterboard, and drywall does not change much with an increasing frequency, it can significantly increase for brick and concrete walls (from 17.7 dB at <3 GHz to 175 dB at 40 GHz) [4, 72]. Therefore, indoor users cannot immediately benefit from high-capacity outdoor cells at mmWave frequencies.

Deploying additional regular cell sites closer to or inside buildings is very costly. For example, the capital expenditure (CAPEX) for a macro base station site with three carriers amounts to US\$ 120,000 [73] or even 175,000 [74]. Furthermore, the required time for site acquisition, the legal and regulatory approval processes, and the civil construction processes are lengthy.

The best solution to provide significant data capacity indoors is to deploy the wireless network inside buildings using *small cells* (we include all forms with this term, like picocells and

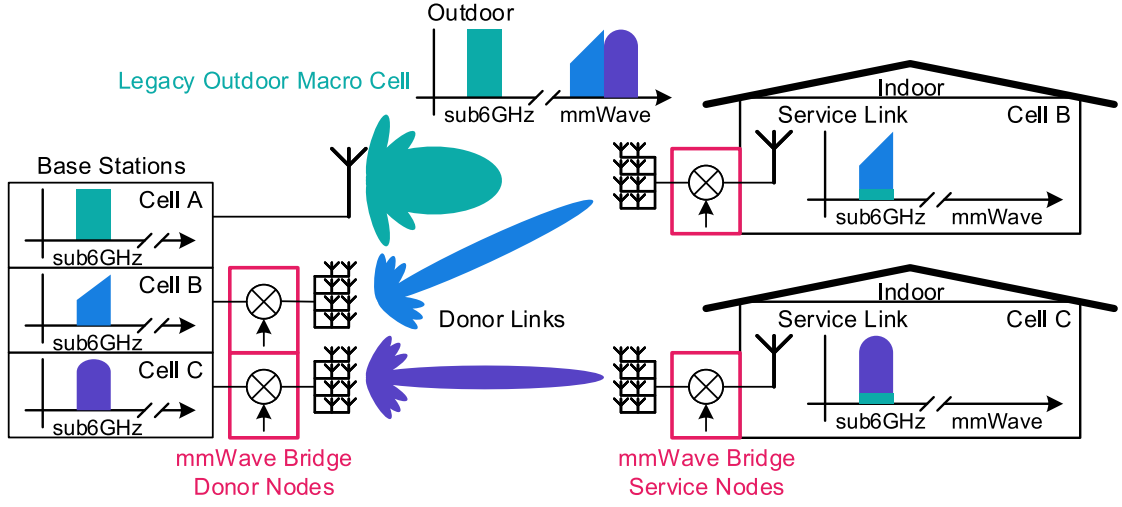


Figure 3.2: Two sub-6 GHz cells (B and C) are upconverted to mmWave, transmitted to buildings where they are downconverted, and re-transmitted inside on their original carrier frequency. Indoor users are offloaded from the legacy outdoor cell A to either cell B or C.

femtocells). Despite the advantages of small cells, such as reduced ICI, better uplink capacity due to lower path losses, and improved macro cell reliability [75], small cell infrastructure is often costly to deploy. Specifically, meeting the stringent backhaul latency and data rate requirements ( $>1$  Gbps) is difficult and expensive [76], especially when new optical fiber connections are required that are not already installed. In Section 2.2, we have already explained further solutions for providing better mobile network capacity indoors, such as DF relays or AF repeaters. However, the capacity that these solutions add indoors is shared with outdoor users.

To alleviate the issues described above, we propose a mmWave bridge that provides sub-6 GHz mobile network cells inside buildings or in areas with poor coverage, without the need for costly optical fiber links. Instead of relying on optical fiber backhaul for an additional small cell, the RF signals are transported to and from the buildings or remote cell sites over mmWave frequencies. Our mmWave bridge consists of two complementing nodes, a **donor node** typically installed on an existing cell mast (or where a fiber backhaul already exists) and cabled to a (small) cell BS; see Fig. 3.2 on the left side. The BS provides an RF cell signal (donor cell) at a sub-6 GHz frequency, which is upconverted to a given mmWave frequency and relayed to the mmWave bridge **service node**, also known as the customer premises equipment (CPE). The CPE downconverts the cell signal to the original sub-6 GHz frequency, which is then fed into the building and transmitted to the UE, as shown on the right in Fig. 3.2. The uplink operates in reverse direction. In essence, this can be seen as an analog RF fronthaul over paired out-of-band AF repeater nodes.

A mmWave bridge can be deployed to provide additional wireless capacity and coverage for a fixed wireless access (FWA) service if the cells on sub-6 GHz frequency bands are already loaded and the allowed transmit power budget is exhausted or if the customer needs a dedicated mobile cell and it is too expensive or impossible to provide dedicated optical fiber connections

for on-site small cells. The bridge can also fronthaul cell signals from existing cell sites to distributed short-range relays, for example, along railway tracks. The analog signal up- and downconversion ensure transparent operation regarding the used radio access technology and readily integrates with existing BSs and UEs without new proprietary hardware or changes to wireless communication standards.

### 3.2 Deployment Objective and Use Cases

Our primary objective is to provide local coverage through small cells where it is impossible or too costly to deploy optical fiber connections at the same time. Interference with existing cellular networks has to be avoided, and their available capacity must be maintained.

#### 3.2.1 Advantages of the mmWave Bridge

The proposed mmWave bridge concept has many operational advantages over the existing alternative methods. First and foremost, it does not require any changes in the existing and well-operating outdoor macro networks, nor does it have any adverse impact. Second, it readily works with standard base stations and UEs already used by customers. Third, its simple up-/downconversion can be fully implemented in the analog RF domain, minimizing the signal delays. Fourth, its transparent AF functionality is independent of the RAT and is forward-compatible with the evolution in 4G, 5G, or future technologies (e.g., 6G). Fifth, the deployment of such a mmWave bridge is cheaper than deploying optical fiber and small cells or additional sub-6 GHz cells. Finally, self-installation by customers is possible if the CPE is carefully engineered and simple-to-follow instructions are given.

#### 3.2.2 Disadvantages of the mmWave Bridge

Unfortunately, there are also disadvantages to the mmWave bridge. One is the donor link range related to the path loss of its link frequency (i.e., mmWave frequency) and allowed transmit power, and the limitation to LOS or NLOS with a strong reflection. However, this limitation may be less relevant depending on the use case explained below. Another disadvantage is the need for additional bandwidth tied to the out-of-band repeater concept. Although using mmWave frequencies for the donor link alleviates this disadvantage, which will be explained in Section 3.3. Furthermore, the use of high-precision mmWave RF components induces higher costs compared to sub-6 GHz RF components. Finally, there are always at least two nodes necessary, i.e., a service node always needs to be served by a donor node.

#### 3.2.3 Fixed Wireless Access

A first use case of the mmWave bridge is to provide FWA service into buildings to which the outdoor network poorly penetrates, see Fig. 3.3a and Fig. 3.3b. A mmWave bridge donor

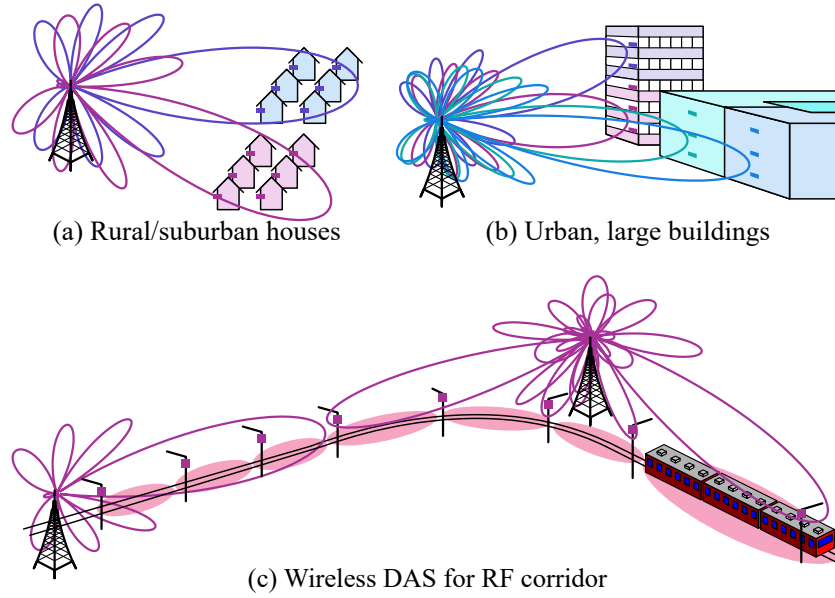


Figure 3.3: Deployment examples for a mmWave bridge for FWA service to houses (a) or large buildings (b) and as a fronthaul for an RF corridor along a railway track (c).

node typically serves multiple buildings in its vicinity. The BS is shared among the users in the buildings covered by the donor link. Dependent on the environment and to cover larger densely built-up areas, multiple donor links concurrently serve groups of buildings. Nevertheless, a donor link distance of up to, e.g., 1 km is sufficient to serve a considerable number of buildings in an urban or suburban area.

### 3.2.4 Cellular Corridor for Railways

A second use case is to provide Internet connectivity and additional capacity to trains employing an RF corridor along railway tracks realized with a distributed antenna system (DAS) [54]. The costly fiber fronthaul links and installation of the DAS are replaced with the mmWave bridge. A donor node serves multiple mmWave bridge service nodes installed at regular distance intervals, e.g., on catenary masts along the railway track, to create the dedicated corridor cell, see Fig. 3.3c. The macro sites for the corridor are installed at regular distances with LOS to the railway tracks (catenary masts) by design, facilitating the use of mmWave frequency links.

### 3.2.5 Temporary Cell Deployment or Extreme Terrain

Further use cases are the temporary deployment of cells where a fiber installation cannot be justified for the short time of use. The mmWave bridge can also serve fronthaul links from sites with optical fiber access to multiple locations to which it is challenging to deploy fiber, e.g., in mountainous terrain.

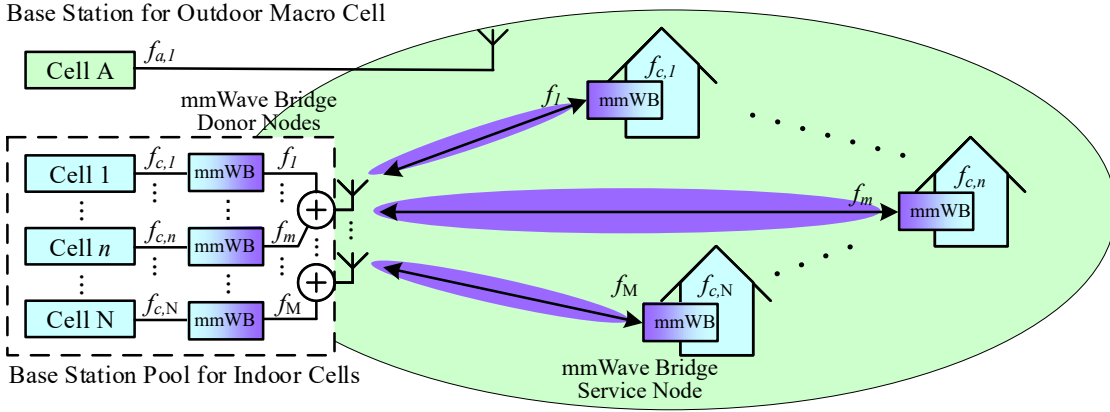


Figure 3.4: Multiple indoor cells (blue) fronthauled over mmWave bridges (mmWB) in the coverage area of a macro cell (large green circle).

### 3.3 Architecture Overview

As a solution to the costly deployment of fiber and small cells, our proposed mmWave bridge allows installing an additional sub-6 GHz cell on existing cell sites where fiber backhaul is available. A donor node also installed at the cell site connects to the RF ports of the radio unit (RU) to replace the passive antenna of the cell to be fronthauled, see Fig. 3.4. The bridge donor node upconverts the downlink (DL) cell signals on the sub-6 GHz frequency, designated with  $f_{c,n}$ , where  $n$  denotes the cell  $[1, N]$ , to the mmWave frequencies  $f_m$ , where  $m = [1, M]$ , for transmission over the donor link. The large bandwidth (several 100 MHz) in the mmWave spectrum allows for frequency-multiplexing of many sub-6 GHz cells with bandwidths of 20-100 MHz. High-gain (analog) beamforming antennas are used to transmit the cells to the bridge service node, which is known as the CPE. Thanks to the directionality of the high gain beamforming antennas, the mmWave carrier frequencies can also be reused depending on the angular spread; thus,  $M \leq N$ . The CPE consists of an outdoor and indoor unit. The outdoor unit is installed on a window, building wall, or roof, ideally with LOS to the antenna of the bridge donor node. Depending on the size of the building and the required data capacity, one CPE may be sufficient, or multiple CPEs may be installed to cover multiple floors or building sections. The indoor unit of the CPE reradiates the downconverted DL cell signal on its original sub-6 GHz frequency. For the uplink (UL), the CPE picks up the UL signal, upconverts it to the corresponding mmWave frequency, and transmits it to the bridge donor node, where the signal is downconverted and fed to the base station. One donor cell connected to one mmWave bridge donor node can serve one or multiple bridge service nodes located in the coverage area of the donor node, allowing to share or dynamically move the cell capacity between service nodes.

An overview block diagram of our proposed mmWave bridge is provided in Fig. 3.5. The donor node and the service node both operate similarly: they upconvert the received sub-6 GHz signal to a mmWave carrier frequency for transmission over the donor link; the received mmWave signal is downconverted to sub-6 GHz for retransmission to the BS or UE. Immediate

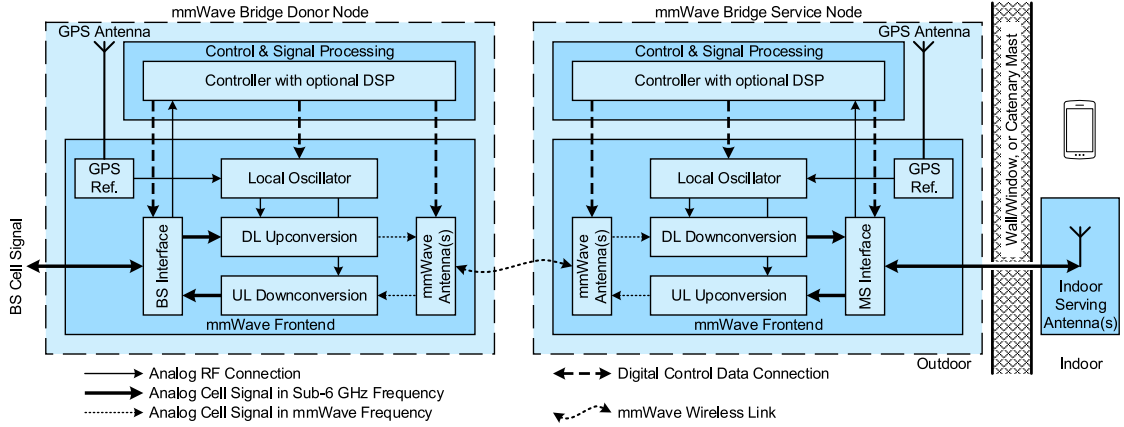


Figure 3.5: Block diagram of the mmWave bridge donor node and service node. The serving antenna for the user access link is placed indoors.

deployment and compatibility with wireless standard compliant cells as well as UEs are ensured as our proposed mmWave bridge operates fully transparent to the RAT by keeping the cell signal in the analog domain. Only for system management, a digital control and signal processing block is required.

### 3.3.1 Beamforming

For compensating the higher path loss in mmWave frequencies, while keeping the antenna dimensions compact and proportional to the wavelength, high-gain mmWave beamforming antennas are required. Static scenarios allow for a fixed deployment in which mmWave beams are adjusted once during installation. However, there are use cases where the donor node switches between multiple service nodes over time. Examples are a cell following a train by always serving the fixed installed mmWave bridge service nodes closest to the train, or FWA service where capacity can be moved between office buildings and residential buildings depending on, e.g., the hourly demand or changes to the environment. In these cases, an adjustment to the beams between the donor and service nodes may be required. For such more agile deployments, an antenna with an electronically steerable beam is employed to ensure a stable link that minimizes the path loss between the nodes.

### 3.3.2 Donor Link Multiple Access

When more capacity needs to be deployed, e.g., in densely built areas, multiple donor cells need to be relayed over mmWave bridges. The large available bandwidth at mmWave frequencies is used for multiplexing several sub-6 GHz cells supporting frequency division multiple access (FDMA) ( $f_{1...M}$  in Fig. 3.4). Additionally, mmWave beamforming antennas with a narrow beam pattern allow multiplexing different cells in different directions providing spatial division multiple access (SDMA) ( $N$  different beams/directions in Fig. 3.4). The same mmWave frequency on the donor link can then be shared for multiple cells.

### 3.3.3 Duplexing Models

Most cellular signals in the frequency bands below 3 GHz operate in FDD, while cellular signals above 3 GHz operate in TDD. Therefore, different hardware configurations are required to use a single antenna for both transmission (TX) and reception (RX), supporting FDD and TDD. For FDD, duplexers [77] are used to separate TX and RX paths at the BS interface and mobile station (MS) interface (see Fig. 3.5). Because corresponding bandpass filters are challenging to design at mmWave frequencies providing the required sharp passbands, separate mmWave antennas may be used for DL and UL paths. For TDD, solid-state RF switches [77] are used to switch the BS and MS interface and the mmWave antennas between TX and RX.

## 3.4 Comparison of State of the Art with the mmWave Bridge

Simulations can be done to analyze and compare different concepts for providing wireless capacity inside buildings to determine which ones are most suitable and learn about potential trade-offs. While simulation tools and environments already exist, such as ns3 [78], they require a lot of contextual information and may produce artifacts due to too specific implementations, like scheduling. Because our interest is in the underlying channel, namely the link budget and the resulting signal-to-noise ratio (SNR), an outdoor-to-indoor simulation has been developed in MATLAB that allows considering differently parameterized scenarios.

The simulation setup considers a BS antenna communicating with UEs inside buildings. For each UE, the signal path can go directly through one or multiple windows or penetrate through walls, doors, the roof, or other structures, which is considered the baseline and represents the status quo. Additionally, active equipment is installed, e.g., at the window or wall, relaying the signal between an outdoor and an indoor antenna. The small cell is a special case with a wired backhaul, i.e., without a wireless outdoor signal path. The following cases have been considered for comparison:

**Baseline:** mobile station inside a building served by an outdoor macro network

**Small Cell:** a small cell with wired backhaul, no dependency on an outdoor network

**Repeater:** layer-1 in-band relay, filtering and amplifying signals

**Relay:** layer-2 or layer-3 relay, operating in- and out-of-band

**Bridge:** fronthauling of a sub-6GHz cell using mmWave frequencies

### 3.4.1 Scenarios and Configurations

The simulation consists of a testbench containing one or several scenarios to run, see Fig. 3.6. Each scenario consists of an environment defining the BS location with a permitted maximum

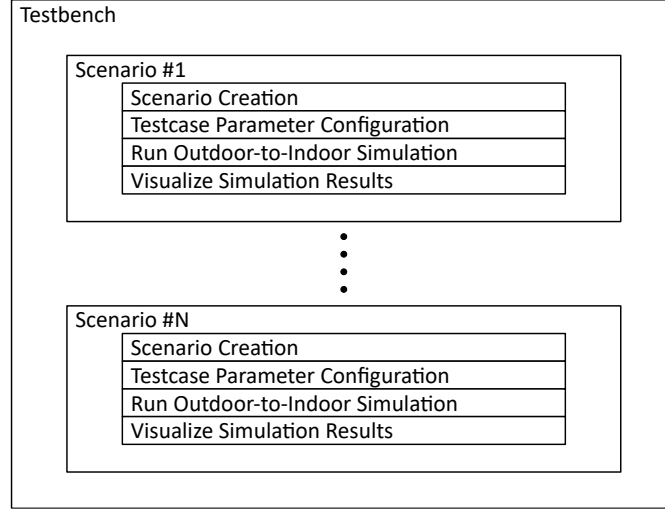


Figure 3.6: Simulation block diagram: multiple scenarios can be configured and run.

transmit power and geographically distributed buildings with or without Low-E windows and some UEs inside. If a real environment is selected, the location and number of UEs are distributed according to the population statistics. Example scenarios are shown in Fig. 3.7.

The testcase parameter configuration defines the carrier frequencies, cell bandwidth, number of MIMO layers, noise figures, antenna gains, signal delays, and others. A complete list of parameters is listed in Table 3.1. With all configurations and parameters defined, the link budget is computed for all UEs, and the resulting SINR for DL and UL are stored. Additionally, the link and cell capacity are estimated using the obtained results. Finally, the results are visualized with plots.

#### 3.4.2 Signal Paths

The signal path for the link budget and SINR analysis can be abstracted, as shown in Fig. 3.8. The cell signal propagates from the BS antenna to the building through the air, attenuated by an outdoor propagation loss that can be modeled as either FSPL or considering additional effects, e.g., empirical path loss models. At the building, there is always one path going through the windows, walls, or other parts of the building shell, directly to the mobile station. This penetration loss can also be modeled with, e.g., an empirical BEL model such as [33]. An additional path may go through a relay, experiencing effects such as delay and, in some cases, an increase in noise, and finally also arrive at the UE after some short indoor propagation path (again using empirical path loss models). Finally, the SINR is computed inside the UE receiver. The same is calculated in the uplink direction to complete the duplex link. Measured parameters are shown in blue-colored text in Fig. 3.8.

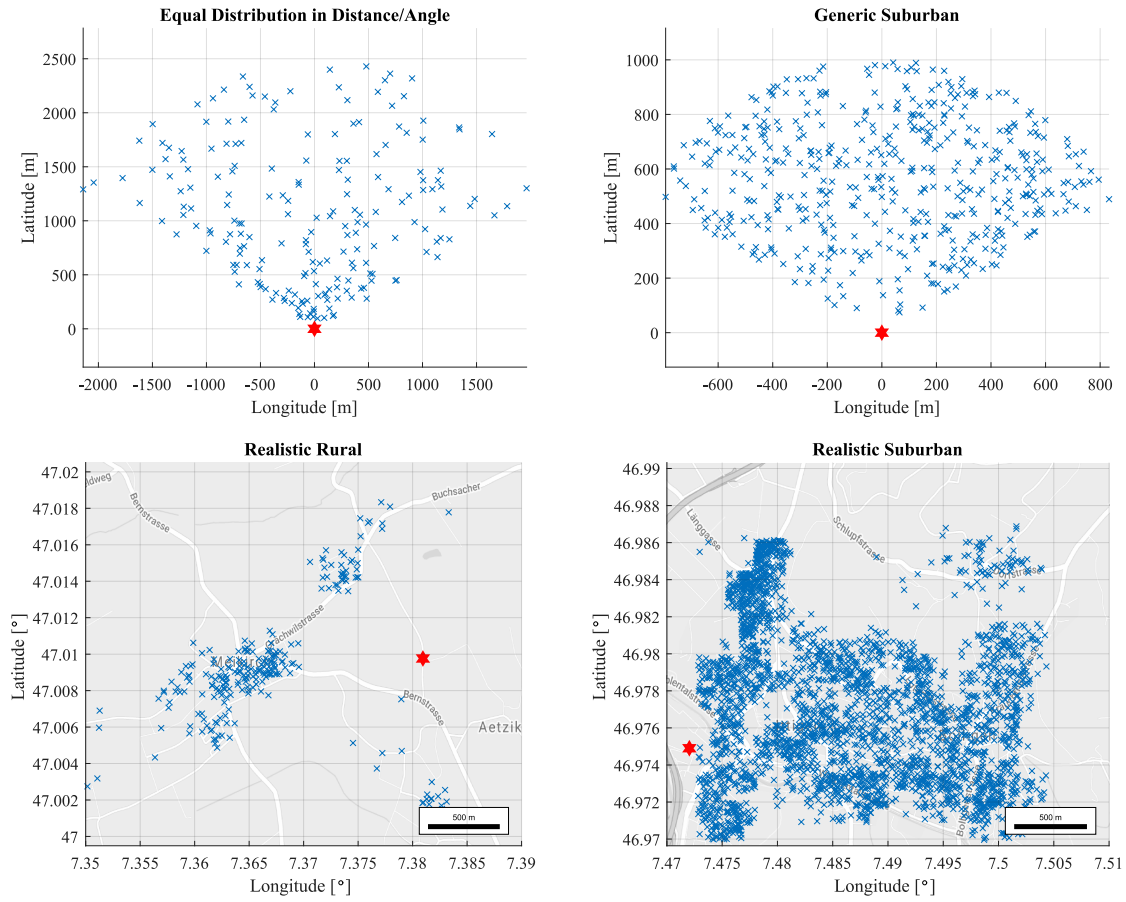


Figure 3.7: Examples of scenario environments that can be generated.

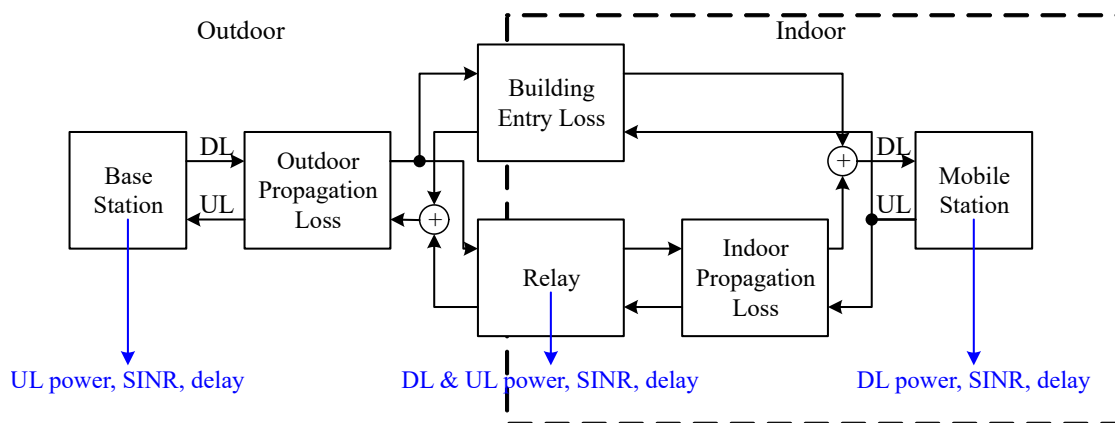


Figure 3.8: Abstracted signal path from a base station to an indoor mobile station.

#### 3.4.3 General Aspects and Assumptions

The performance of our proposed mmWave bridge is evaluated against the competing methods discussed in Section 2.2.1 and an outdoor macro network as a baseline. For the sake of brevity, we only consider a 5G NR carrier at 3.6 GHz with 100 MHz of bandwidth and one at 26 GHz<sup>1</sup> with 400 MHz of bandwidth. The standard cross-polarized antennas allow for  $2 \times 2$  MIMO transmissions, either using spatial multiplexing in high SINR or diversity in low SINR, providing a capacity increase of up to two times under ideal channel conditions compared to a SISO transmission.

The scenario consists of  $N_B$  individual buildings scattered across a sector of  $120^\circ$  at uniformly distributed distances<sup>2</sup> from the base station (a 5th generation node B (gNB)). The cell radius, with the considered frequencies and transmit powers, is limited to several hundreds of meters, over which the terrain usually does not change much. Therefore a flat terrain is assumed. For simplicity, buildings occupy a square area, all face the gNB, and all have the same height. If an outdoor donor antenna of a service node at a specific height above ground on the building wall (or window) is shadowed by another building, NLOS condition is assumed, otherwise LOS. As we have seen in Chapter 2, the 3GPP empirical path loss models [32] are best suited for central European areas and are thus used to compute the outdoor propagation loss  $L_{\text{out}}$  up to the building wall. For methods with an indoor service antenna, LOS is assumed for a uniformly distributed distance  $d$  between 2 m and 10 m (e.g., in a living room, office, shop), and the FSPL model (based on the Friis transmission equation) is used to model the indoor path loss  $L_{\text{in}}$ .

Simulation parameters are summarized in Table 3.1. Transmit powers are specified as EIRP and therefore include the antenna gain and feeder losses. Equations are given for the DL direction. The UL experiences the same path losses, and the equations can be derived analogously. The noise components are neglected in the following equations if they are orders of magnitude below the thermal noise floor. However, the noise components are accurately computed in the simulations.

Interference from neighboring macro cells has not been considered, which would mainly degrade the performance of the macro outdoor-to-indoor, layer-1 repeater, and layer-3 relay methods in the sub-6 GHz spectrum. In the mmWave spectrum, neighbor cell interference is lower thanks to beamforming and the higher path loss. Perfect synchronization and channel estimation are assumed. Fading effects are also neglected due to the static links, mainly with LOS conditions and the wide bandwidth of the cell signals.

---

<sup>1</sup>26 GHz is a 5G mmWave band for Europe

<sup>2</sup>Analysis of building location statistics around existing base stations show a close to uniform distribution, i.e., the farther away from a base station, the sparser the building density

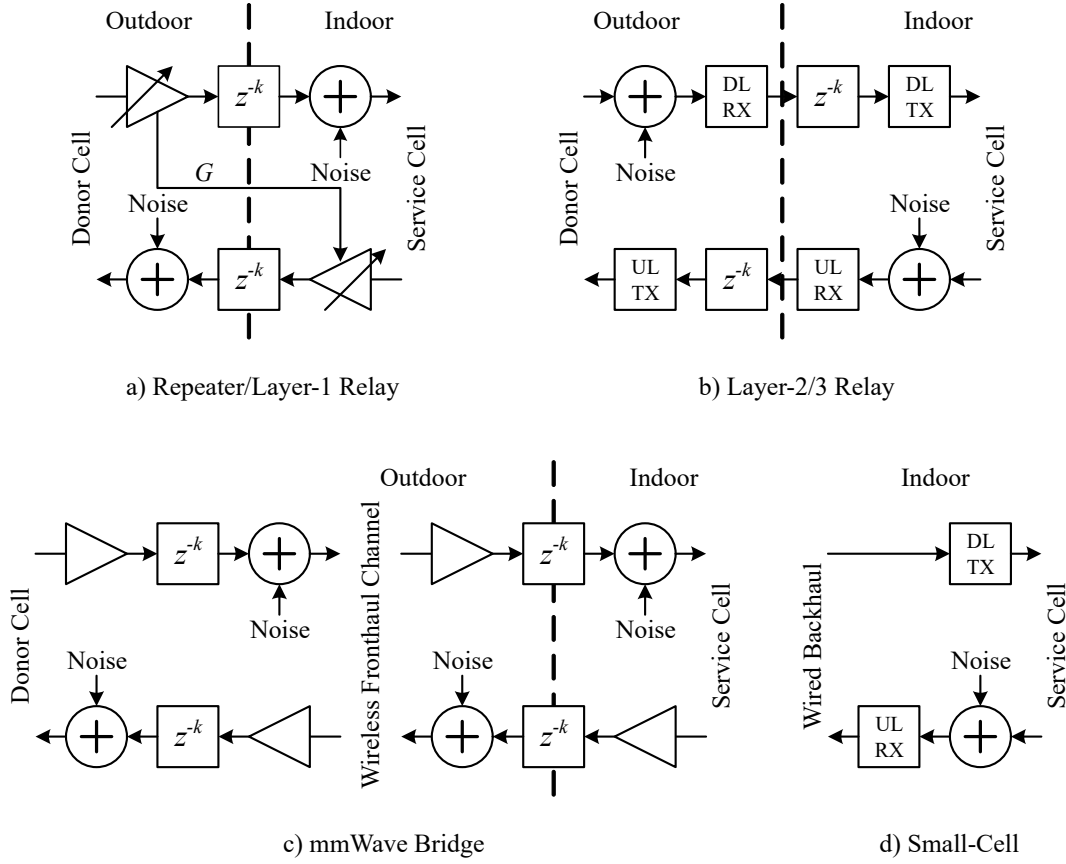


Figure 3.9: Block diagrams of the simulation models for the four active equipment. The added noise components depend on the noise figures of the active sub-components of the respective signal path and the thermal noise.

### 3.4.4 System Models

The system models for the baseline (outdoor macro network propagating indoor) and for each of the four solutions with active equipment are described next. The high-level components and effects, such as amplifiers, noise, and delay elements, are shown in Fig. 3.9 for the four solutions. Using the signal power instead of the amplitude and phase is justified with the wide signal bandwidth of 20 MHz to 100 MHz.

#### 3.4.4.1 Outdoor Macro Network

The first case represents the baseline with an outdoor macro network serving indoor users. The BEL from outdoor-to-indoor is computed according to the model ITU-R P.2109 [33] and denoted with  $L_{O2I}$ . This model allows the calculation of a BEL for frequencies of 80 MHz up to 100 GHz. Besides the carrier frequency, additional parameters to the model are the elevation angle of the signal path at the building facade, a probability with which the loss is not exceeded, and the building class ('traditional' or 'thermally-efficient'). For the elevation angle, we assume

a horizontal propagation (thus  $0^\circ$ ), a median building entry loss (0.5), and finally, ‘traditional’ buildings, i.e., without thermally efficient and highly attenuating building materials such as metallic-coated glass windowpanes. Note that this BEL model already accounts for the indoor propagation loss and atmospheric gas attenuation; therefore, the received power for the UE becomes

$$P_{\text{UE,rx}}^{\text{MN}} = \frac{P_{\text{BS,tx}} G_{\text{UE,ant}}}{L_{\text{out}} L_{\text{OI}}}, \quad (3.1)$$

with  $P_{\text{BS,tx}}$  denoting the constant base station transmit power and  $G_{\text{UE,ant}}$  the UE antenna gain.

#### 3.4.4.2 Small Cell Model

The small cell represents the ideal case where each building provides optical fiber connectivity and is equipped with a small cell. The received power for a UE becomes

$$P_{\text{UE,rx}}^{\text{SC}} = \frac{P_{\text{SC,tx}} G_{\text{UE,ant}}}{L_{\text{in}}}, \quad (3.2)$$

with  $P_{\text{SC,tx}}$  denoting the constant small cell transmit power. The only performance impact for this method is the interference from the outdoor macro cell that is assumed to operate also on the same frequency as the indoor small cell. Therefore, the interference power becomes  $P_{\text{UE,if}}^{\text{SC}} = P_{\text{UE,rx}}^{\text{MN}}$ .

#### 3.4.4.3 Repeater Model

The layer-1 repeater is modeled as an in-band AF relay. We assume that one repeater is installed at each building, serving the indoor users with an amplified signal from outside the same building. The repeater model consists of an amplifier with a limited maximum output power  $P_{\text{LIR,tx,max}}$ , additive noise, and a signal delay  $\tau$  caused by filter group delays that can cause ISI if it exceeds the OFDM cyclic prefix (CP) duration  $T_{\text{CP}}$ , as explained in Section 2.2.1.3. Donor and service antenna gains are denoted with  $G_{\text{LIR,D}}$  and  $G_{\text{LIR,S}}$ , respectively. The total repeater gain  $G_{\text{LIR}}$  includes the antenna gains and the repeater amplification gain  $G_{\text{R}}$ . The received power at the repeater donor antenna is  $P_{\text{LIR,rx}}$ , while  $P_{\text{LIR,UE}}$  denotes the power of the signal from the repeater at the UE antenna (excluding the UE antenna gain  $G_{\text{UE,ant}}$ ). The received power for the UE is:

$$P_{\text{LIR,rx}} = \frac{P_{\text{BS,tx}}}{L_{\text{out}}} \quad (3.3)$$

$$G_{\text{R}} = \min(G_{\text{R,max}}, P_{\text{LIR,tx,max}} - P_{\text{LIR,rx}} G_{\text{LIR,D}}) \quad (3.4)$$

$$G_{\text{LIR}} = G_{\text{LIR,D}} G_{\text{R}} G_{\text{LIR,S}} \quad (3.5)$$

$$P_{\text{LIR,UE}} = \frac{P_{\text{LIR,rx}} G_{\text{LIR}}}{L_{\text{in}}} \left[ 1 + \sum_{k=1}^{K_{\text{CP}}} \left( \frac{G_{\text{LIR}}}{L_{\text{iso}}} \right)^k \right] \quad \text{with} \quad K_{\text{CP}} = \left\lfloor \frac{T_{\text{CP}}}{\tau} \right\rfloor \quad (3.6)$$

Finally, we obtain the total signal power received by the UE as

$$P_{\text{UE,rx}}^{\text{LIR}} = \begin{cases} (P_{\text{LIR,UE}} + P_{\text{UE,rx}}^{\text{MN}}) G_{\text{UE,ant}} & : \tau < T_{\text{CP}} \\ P_{\text{LIR,UE}} G_{\text{UE,ant}} & : \tau \geq T_{\text{CP}} \end{cases}. \quad (3.7)$$

The consideration of noise levels is essential in repeaters. Besides the noise from amplifiers, there may also be noise from self-interference, as explained in Section 2.2.1.3. Self-interference depends on the repeater gain to antenna isolation ratio and the signal delay  $\tau$  through the repeater. The resulting power at the repeater output (service antenna) can be written as:

$$P_{\text{LIR,tx}} = P_{\text{LIR,rx}} G_{\text{LIR}} \sum_{k=1}^{\infty} \left( \frac{G_{\text{LIR}}}{L_{\text{iso}}} \right)^{k-1} \quad (3.8)$$

where  $L_{\text{iso}}$  represents the isolation loss between the indoor service antenna and the outdoor donor antenna of the repeater. For  $k \leq K_{\text{CP}}$ , the signal can be decoded without ISI. Only for  $k > K_{\text{CP}}$  do the delayed copies of the signal cause self-interference. Because the repeater gain is chosen for a stable operation, the infinite sum of the geometric series in (3.8) converges. From [79], we know

$$\sum_{k=1}^{\infty} ar^{k-1} = \frac{a}{1-r} \quad \text{if } |r| < 1. \quad (3.9)$$

By defining  $a = 1$  and  $r = G_{\text{LIR}}/L_{\text{iso}}$  and considering that the signal copies within the  $T_{\text{CP}}$  duration do not contribute to interference, we can use (3.8) to obtain the self-interference signal power as

$$P_{\text{if,tx}}^{\text{LIR}} = P_{\text{LIR,rx}} G_{\text{LIR}} \cdot \left[ \frac{L_{\text{iso}}}{L_{\text{iso}} - G_{\text{LIR}}} - \sum_{k=1}^{K_{\text{CP}}} \left( \frac{G_{\text{LIR}}}{L_{\text{iso}}} \right)^k \right]. \quad (3.10)$$

In practice, the repeater gain is often set at least 15 dB lower than the antenna isolation  $L_{\text{iso}}$ . The signal delay  $\tau$  can be designed slightly smaller than  $T_{\text{CP}}$ ; thus,  $K_{\text{CP}} = 1.2$  and the self-interference power becomes around 0.1 dB. Finally, the total interference power received by the UE becomes

$$P_{\text{UE,if}}^{\text{LIR}} = \frac{P_{\text{if,tx}}^{\text{LIR}}}{L_{\text{in}}} + P_{\text{UE,rx}}^{\text{MN}}, \quad (3.11)$$

The repeater noise power at the UE is computed according to

$$P_{\text{UE,N}}^{\text{LIR}} = \frac{N_0 F_{\text{LIR}}(G_{\text{R}}) B G_{\text{LIR,S}}}{L_{\text{in}}}, \quad (3.12)$$

where  $N_0$  denotes the thermal noise power spectral density (-174 dBm/Hz),  $F_{\text{LIR}}$  denotes the noise factor as a function of the repeater amplification gain,  $B$  is the signal bandwidth, and  $G_{\text{LIR,S}}$  is the service antenna gain.

#### 3.4.4.4 Layer-3 Relay Model

We only consider a layer-3 relay because it offers the out-of-band operation that a layer-2 relay does not support (on the link budget level considered here, a layer-2 relay performs very similarly to a layer-3 relay). Also here, it is assumed that one relay is installed at each building with an outdoor donor antenna facing the gNB and an indoor service antenna. The relay model consists of a low-noise amplifier with a specific noise figure and a constant output signal power. The equations for the power computation are analog to those for the small cell, with

$$P_{\text{UE,rx}}^{\text{L3R}} = \frac{P_{\text{L3R,tx}} G_{\text{UE}}}{L_{\text{in}}}, \quad (3.13)$$

and  $P_{\text{L3R,tx}}$  denoting the layer-3 relay transmit power. The signal processing delay is orders of magnitude larger than the CP duration  $T_{\text{CP}} = 2.35 \mu\text{s}$  of 5G NR at 3.6 GHz; therefore, an outdoor macro cell interferes with the indoor cell of the relay, depending on the BEL and if they both use the same frequency. In that case, the interference becomes  $P_{\text{UE,if}}^{\text{L3R}} = P_{\text{UE,rx}}^{\text{MN}}$  as for the small cell model.

#### 3.4.4.5 mmWave Bridge Model

For the mmWave bridge, we also assume that one CPE is installed at each building and served from the gNB location. Each amplifier in the bridge donor node, as well as the CPE, contributes to the noise in the overall link budget. Similar to the repeater, the amplifier gain is fixed but limited by the maximum specified output power  $P_{\text{mmWB,tx,max}}$ . A signal delay is also added, but there is no self-interference in the system thanks to the out-of-band operation (with FDD duplex filters or TDD DL/UL switches). First, the donor link power is computed from the donor node transmit power  $P_{\text{mmWB,D,tx}}$ , including the antenna gain and using the FSPL for a distance  $d$  and the wavelength  $\lambda$ :

$$P_{\text{mmWB,rx}} = P_{\text{mmWB,D,tx}} \left( \frac{\lambda}{4\pi d} \right)^2 \quad (3.14)$$

Then, the received power at the UE  $P_{\text{UE,rx}}^{\text{mmWB}}$  is computed from the CPE indoor transmit power  $P_{\text{mmWB,tx}}$  according to

$$G_{\text{mmWB}} = \min(G_{\text{mmWB,max}}, P_{\text{mmWB,tx,max}} - P_{\text{mmWB,rx}} G_{\text{mmWB,D}}) \quad (3.15)$$

$$P_{\text{mmWB,tx}} = P_{\text{mmWB,rx}} G_{\text{mmWB,D}} G_{\text{mmWB}} \quad (3.16)$$

$$P_{\text{UE,rx}}^{\text{mmWB}} = \frac{G_{\text{mmWB,S}} P_{\text{mmWB,tx}} G_{\text{UE}}}{L_{\text{out}} L_{\text{in}}} \quad (3.17)$$

$G_{\text{mmWB,D}}$  and  $G_{\text{mmWB,S}}$  represent the CPE donor and service antenna gains, respectively. As in all other methods, interference from an outdoor macro cell is considered on the same frequency as the indoor cell:  $P_{\text{UE,if}}^{\text{mmWB}} = P_{\text{UE,rx}}^{\text{MN}}$ . The output noise power from the mmWave

bridge received at the UE is computed according to

$$P_{N,tx}^{mmWB} = \frac{N_0 F_{mmWB}(G_{mmWB}) B G_{mmWB,S}}{L_{in}}, \quad (3.18)$$

where  $F_{mmWB}$  denotes the CPE noise factor as a function of the mmWave bridge gain.

#### 3.4.4.6 Capacity Estimation

For each method and simulated building, the SINR can be computed as:

$$\gamma = \frac{P_{UE,r}^{\bullet}}{N_0 \cdot B \cdot F_{UE} + P_N^{\bullet} + P_{UE,if}^{\bullet}}, \quad (3.19)$$

with  $F_{UE}$  representing the noise factor of the UE,  $P_N^{\bullet} = P_{N,tx}^{\bullet} L_{in} G_{UE}$  is the noise power received by the UE, and  $P_{UE,if}^{\bullet}$  is the interference power received by the UE. The SINR denoted with  $\gamma$  is then mapped to a SISO capacity value  $C$  in bit/s using the modified Shannon-Hartley theorem according to the 5G NR technical report [80, Sec. 5.2.7]:

$$C = \alpha B \log_2(1 + \gamma). \quad (3.20)$$

$B$  represents the channel bandwidth in Hertz, and  $\alpha$  is an attenuation factor representing implementation losses (0.6 for DL and 0.4 for UL). Also, according to [80], the capacity  $C$  is set to zero for  $\text{SINR} < -10$  dB. The equation in [81, Sec. 4.1.2] is used to compute the upper capacity limit for the supported maximum data rate. For TDD operation, one needs to also adjust for the DL to UL ratio, see Table 3.1. Note that the obtained capacity is valid for additive white gaussian noise (AWGN) channels.

#### 3.4.5 Results and Discussion

In Fig. 3.10, we present results for the rural and suburban environments from [6] as a case study. The outdoor SINR was calibrated at LOS locations with the measured SINR from [6]. Although neighboring cells and their interference were not considered, we assume that the same frequency used indoors is also used on the macro network for a different cell in the case of the mmWave bridge. The numerical evaluations are based on the population density per hectare (100×100 m) and the digital height model DHMS25/200 from the Swiss Federal Office of Topography (Swisstopo). The estimated indoor SINR available to users inside buildings (located in square tiles) is shown in Fig. 3.10 for the outdoor-to-indoor macro network baseline (left plots) and the cells fronthauled with the mmWave bridge to buildings with rooftop CPE antennas.

### 3.4 Comparison of State of the Art with the mmWave Bridge

Table 3.1: Simulation parameters and example values

Parameter	Values
Carrier frequency $f_c$	<b>3.6 GHz</b> <b>26 GHz</b>
Carrier bandwidth $B$	100 MHz 400 MHz
Subcarrier spacing	30 kHz 120 kHz
CP duration $T_{CP}$	$2.3 \mu s$ $0.6 \mu s$
TDD DL/UL ratio	4:1 4:1
gNB $P_{tx,EIRP}$	656 W 1000 W
gNB UL noise figure	3 dB 9 dB
gNB antenna gain	24 dBi 27 dBi
gNB $P_{0,nom,PUSCH}$	$-105$ dBm $-105$ dBm
UE max. TX power	23 dBm 23 dBm
UE DL noise figure	8 dB 9 dB
UE antenna gain	3 dBi 9 dBi
Outdoor propagation parameters values	path loss according to 3GPP RMa LOS/NLOS $h_{BS} = 30$ m, $h_{UT} = 2$ m, $W = 20$ m, $h = 10$ m
Building entry loss parameters values	according to ITU-R P.2109-0 $P = 0.5$ , traditional, $\theta = 0$
Small cell noise figure	$P_{max,EIRP} = 30$ dBm, $P_{0,nom,PUSCH} = -105$ dBm 7 dB 9 dB
antenna gain	6 dBi 24 dBi
L1 repeater	max. DL & UL gain = 60 dB, delay = $1 \mu s$
donor side	$P_{max,EIRP} = 40$ dBm, noise figure = 9 dB
service side	$P_{max,EIRP} = 30$ dBm, noise figure = 9 dB
donor antenna gain	6 dBi 24 dBi
service antenna gain	6 dBi 12 dBi
L3 relay	RX sensitivity $-125$ dBm (RSRP), delay = 10 ms
donor side	$P_{max,EIRP} = 40$ dBm, noise figure = 6 dB
service side	$P_{max,EIRP} = 30$ dBm, noise figure = 6 dB
donor antenna gain	6 dBi 24 dBi
service antenna gain	6 dBi 12 dBi
mmWave bridge	max. DL & UL gain = 60 dB, delay = $50 \mu s$
$P_{max,TX,EIRP}$	outdoor: 40 dBm, indoor: 30 dBm
noise figure	7 dB 9 dB
antenna gain	6 dBi 24 dBi

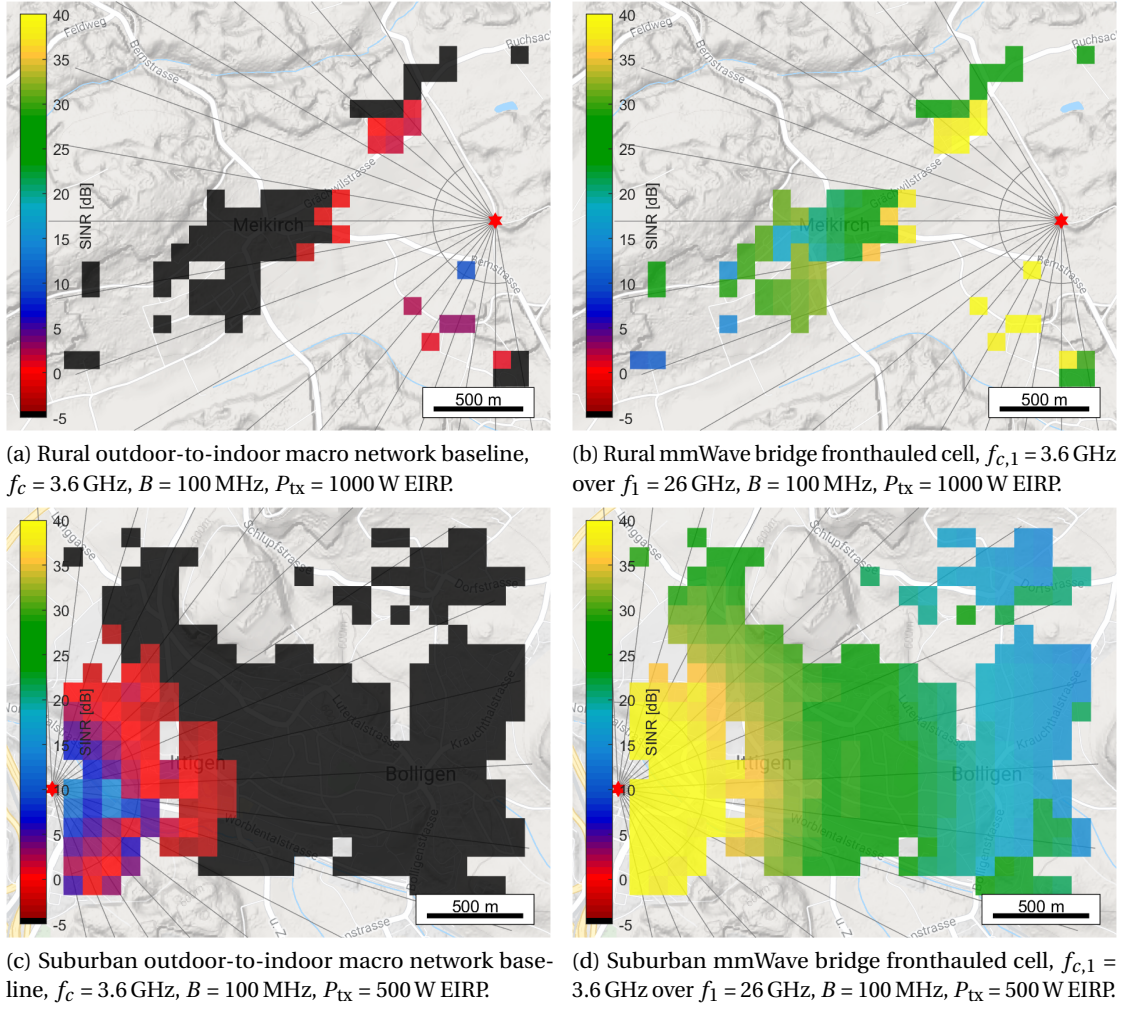


Figure 3.10: Indoor SINR coverage estimation for the outdoor-to-indoor macro network baseline (left plots) and with the mmWave bridge fronthauled cell with rooftop CPE antennas (right plots).

For a more general assessment than the two specific topographies evaluated in Fig. 3.10, Monte Carlo simulations are performed with  $N_{MC} = 100$  iterations for an equal distribution of  $N_B = 300$  buildings in a generic environment. The computed capacity for a single SISO link are shown in Fig. 3.11, with the boxes showing the 5%ile and 95%ile, the horizontal green lines inside the boxes the median, and the plus markers the mean values. For the mmWave bridge, only one result (for the 3.6 GHz carrier frequency) is shown, although it is assumed that 26 GHz is used as the fronthaul frequency. While it would technically be possible to fronthaul a mmWave cell signal, several advantages of the mmWave bridge would be lost (indoor propagation beyond a single room, backward compatibility, and operation with non-mmWave capable devices), and therefore, we omitted the option of using a mmWave cell frequency.

### 3.4 Comparison of State of the Art with the mmWave Bridge

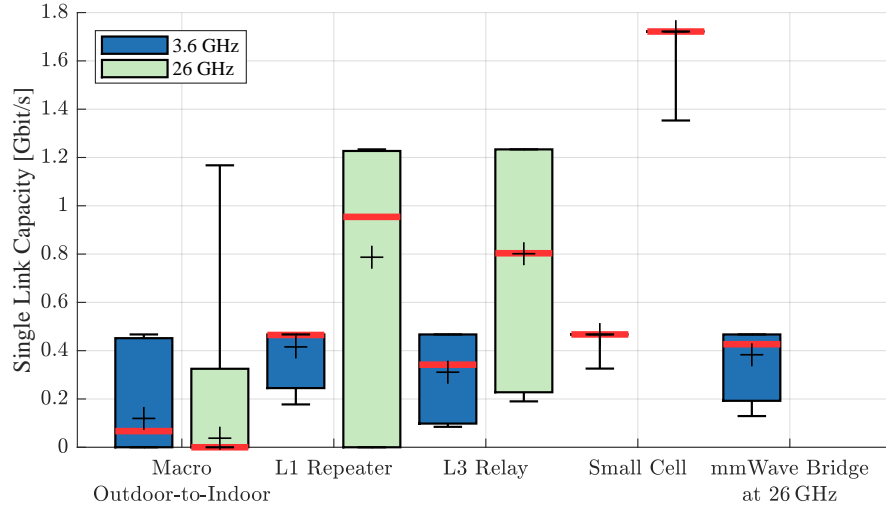


Figure 3.11: Single link SISO capacity comparison for the five discussed methods in two frequency bands, where applicable. The boxes show the 5%ile and 95%ile, the median (horizontal red line inside the box), and the mean value (+ marker)

The 5G NR standard supports multi-user MIMO (MU-MIMO) with up to four simultaneously scheduled UE. In a full-buffer scenario, we can assume an upper bound of four simultaneous links for the outdoor-to-indoor macro baseline, the layer-1 repeater, and the layer-3 relay. This ideal multi-user scheduling is also shown in Fig. 3.12, with the stacked bars representing co-scheduled users based on the mean link capacity. Note that the small cell case ideally scales the total capacity in the area with the number of installed small cells in the buildings. However, the mmWave bridge only scales depending on the number of available mmWave bridge links.

The mean SISO capacity that is available indoors from an outdoor macro network is relatively low for 3.6 GHz (119 Mbit/s) and close to zero for mmWave; see the left two boxes in Fig. 3.11. Adding a layer-1 repeater generally improves the capacity (416 Mbit/s for 3.6 GHz, 787 Mbit/s for 26 GHz), but it is crucial that the repeater delay is smaller than the CP length to prevent ISI. Due to the ICI, the layer-3 relay does not perform as well as a layer-1 repeater for buildings closer to the base station. However, for higher path losses, especially in mmWave, the layer-3 relay outperforms the layer-1 repeater. The mean SISO capacity with a layer-3 relay reaches 311 Mbit/s for 3.6 GHz and 801 Mbit/s for 26 GHz. An optimally placed small cell manages to deliver consistently high capacity for a user in the same room (467 Mbit/s for 3.6 GHz, 1.721 Gbit/s for 26 GHz). The only capacity-impacting factor is ICI from the outdoor macro cell. A mmWave bridge operating at 26 GHz can provide almost as much capacity as a layer-1 repeater (383 Mbit/s for the 3.6 GHz cell). The difference is that the mmWave bridge consists of more amplifiers and components that add more noise to the signal than a layer-1 repeater. But a mmWave bridge adds additional capacity, while the layer-1 repeater only amplifies the outdoor signal.

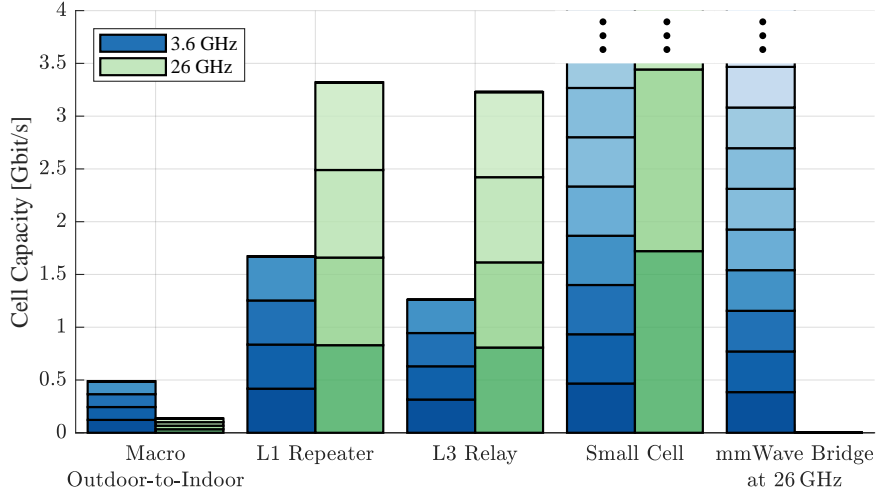


Figure 3.12: Cell capacity comparison based on simultaneously scheduled single SISO links (bar segments in different color shades) for the five discussed methods in two frequency bands, where applicable

Buildings are increasingly built or equipped with metallic coated Low-E windows. If the ITU-R P2109 model for ‘modern’ buildings instead of ‘traditional’ is used for the BEL, only the macro outdoor-to-indoor capacity results are affected: at mmWave frequencies, hardly any communication from inside a building is possible with an outdoor mmWave small- or macro cell; thus, outdoor mmWave cells would not cover the indoor UEs.

The large single-user capacity gains that the system proposed in [50] might provide cannot be reached with the mmWave bridge. However, the significant advantage of the mmWave bridge is that no changes in the deployed networks and at UE are required. Another advantage comes from the multiplexing of multiple links in the spatial and frequency domain. Assuming a mmWave antenna gain of 24 dBi, the half power beamwidth (HPBW) results to around  $10^\circ$ . For a cell sector with  $120^\circ$  in azimuth and minimal angular spread, up to 12 antennas can be used to cover the sector, scaling the capacity by a factor of 12, resulting in a 2.8-fold increase compared to the layer-1 repeater cell capacity. If four 100 MHz cells are frequency multiplexed in the 400 MHz mmWave bandwidth, the scaling factor even becomes 48, yielding an 11-fold increase compared to the layer-1 repeater cell capacity. Referring to Fig. 3.12, we note that a minimum of five mmWave bridge links already provide more cumulative cell area capacity than a single 5G NR gNB at 3.6 GHz. Furthermore, a minimum of nine mmWave bridge links outperform the available cell capacity when using repeaters or relays in the 26 GHz mmWave band.

### 3.5 Summary

In the previous chapter, we have seen that providing high data capacity indoors is challenging if optical fiber is unavailable and the outdoor cellular network is already loaded. Although

spectrum in higher frequency ranges allows for wider signal bandwidth and larger capacity, these signals do not (or not easily) penetrate buildings. Therefore, we proposed a mmWave bridge solution that transfers sub-6 GHz cell signals from a base station site to buildings or along railway tracks using mmWave frequencies and provides the original sub-6 GHz cell inside buildings or to the train. Such a mmWave bridge brings several advantages:

1. The mmWave bridge operates transparent to the cellular signals, readily working with existing base stations and UEs.
2. Using the newly available mmWave spectrum, no interference to existing outdoor cellular networks is added, nor are any changes in the existing network necessary.
3. The simple architecture can be fully implemented in analog circuits, which minimizes signal delays.
4. Its transparent AF architecture works independently of the RAT and is forward-compatible.
5. Using the large available bandwidth in the mmWave spectrum for frequency division multiple access and directive mmWave beamforming antennas for spatial division multiple access, many cells can be multiplexed for a high area capacity.

A simulation has been developed to assess the performance and compare the mmWave bridge with state-of-the-art solutions: macro network as a baseline, small cell, layer-1 in-band repeater, and layer-3 in- and out-of-band relay. The simulations have been performed under general assumptions representing average suburban areas. They show that a single mmWave bridge performs almost as well as an in-band layer-1 repeater but adds extra capacity, and the high spatial- and frequency-multiplexing gains allow for a many-fold (2.8 to 11 in the studied example) cell capacity increase compared to a layer-1 repeater or layer-3 relay deployment based on a 5G NR cell.



## 4 mmWave Bridge Prototype

The mmWave bridge concept was introduced in Chapter 3, and numerical link budget simulations showed that the idea could be used to fronthaul cells to other places. However, high-level simulations leave many relevant implementation aspects unanswered. For example, it is hard to decide which model will be used for each sub-component that eventually may not be available in the market due to supply chain problems. In addition, details such as the compatibility of sub-components with one another, a stable and clean power supply, changes in temperature, and others are to be considered in real hardware. Finally, the integration with a system such as 4G and 5G with complex configuration parameter sets and handling FDD and TDD is not immediately apparent.

We have developed a prototype of our proposed mmWave bridge using commercial off-the-shelf (COTS) components to validate the concept in practice and provide confidence in the solution. This prototype is also the basis for field trials that allow assessing the performance of the idea under real-world conditions, including all implementation losses. This chapter describes our prototype that verifies the feasibility of relaying sub-6 GHz standard-compliant cellular signals over mmWave frequencies while establishing a successful connection with a commercial carrier-grade BS and COTS UEs. The availability of mmWave beamforming antennas and the possibility of obtaining a test license from the Swiss Federal Office of Communications (OFCOM) dictated the frequency operating range of 38–40 GHz at the time of the prototype development. Both FDD and TDD cells should be relayed, but only SISO operation is supported for simplicity, which is a current limitation. Having in mind a commercial product, we wanted the prototype to perform well while keeping the cost low. Additionally, all typical sub-6 GHz frequency bands (1–4 GHz) should be supported, and an adjustable mmWave carrier frequency allows for maximum flexibility. Moreover, a solid and reliable setup facilitates field trials. The hardware architecture is explained in the following, and the sub-components are described. After that, the prototype is characterized in terms of link budget, frequency selectivity, phase noise, and error vector magnitude (EVM). Finally, several validation measurements were conducted to demonstrate the functionality of the working mmWave bridge prototype.

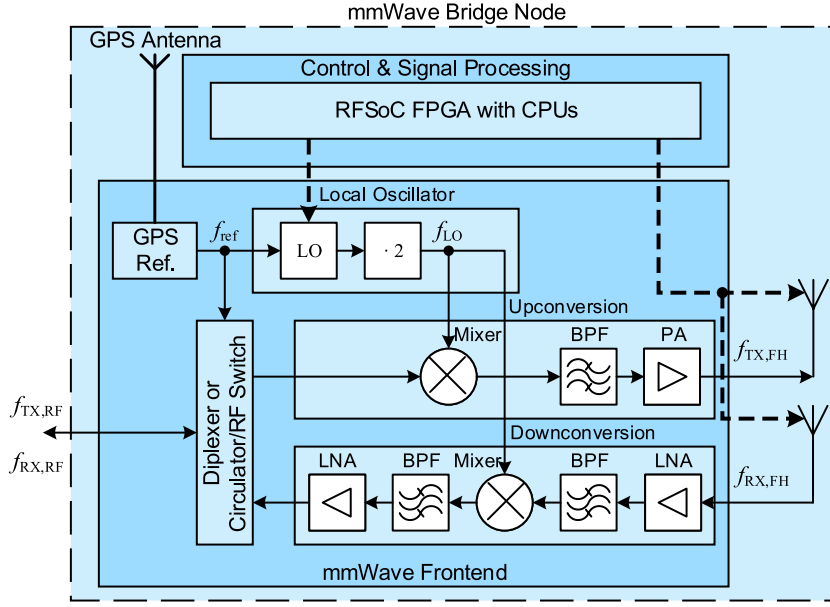


Figure 4.1: Block diagram of one mmWave bridge node (common for donor and service node)

## 4.1 Prototype Architecture

Because the mmWave bridge prototype is RAT agnostic, the goal is to demonstrate the fronthauling of signals relevant to an MNO. Specifically, we focus on 4G LTE and 5G NR for FDD and TDD cell signals in the frequency range of 1.7 GHz – 3.8 GHz.

The mmWave bridge consists of a donor node and a service node, as described in Section 3.3 and shown in Fig. 3.5. Both nodes can be identical to a large degree, which is also true for our prototype. The high-level block diagram of a mmWave bridge node is shown in Fig. 4.1. The sub-6 GHz signal input with carrier frequency  $f_{TX,RF}$  and output with carrier frequency  $f_{RX,RF}$  is shown on the left, while the mmWave signals are shown on the right ( $f_{TX,FH}$  and  $f_{RX,FH}$ ). The central part is the signal up- and downconversion and filtering, described in Section 4.1.1. Section 4.1.2 describes the local oscillator (LO) providing a CW signal with low phase noise for the frequency mixer. Because the donor and service nodes are spatially separated without a wired connection in-between, both nodes need to have provisions for wireless local oscillator synchronization to avoid large frequency offsets. Our prototype achieves synchronization with a Global Positioning System (GPS) reference, as explained in 4.1.3. Depending on the duplexing scheme and whether a BS or antenna is connected, either a duplex filter, a circulator, or RF switches are used to split or combine the DL and UL signal paths, as further described in Section 4.1.4. For our prototype, we use high-gain horn antennas as well as digitally controllable beamforming antennas described in Section 4.1.5. Finally, for the configuration and control of all components, such as the LO frequency and the beamforming antennas, and possible signal processing capabilities, an FPGA board is employed. Further details are explained in Section 4.1.6. A picture of the mmWave bridge donor node prototype is shown in Fig. 4.2.

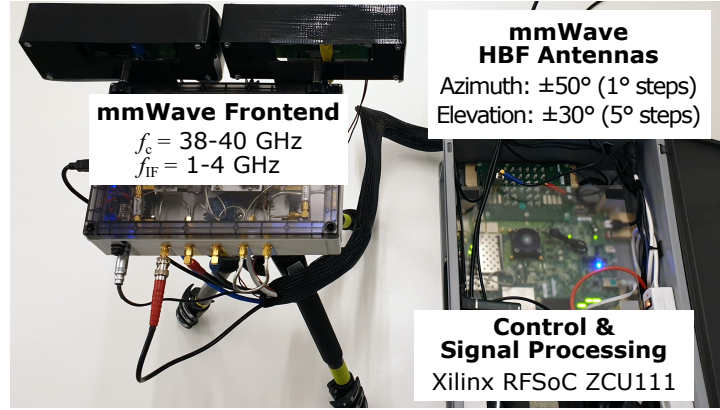


Figure 4.2: Picture of one frontend with the mmWave HBF antennas and the control and signal processing board.

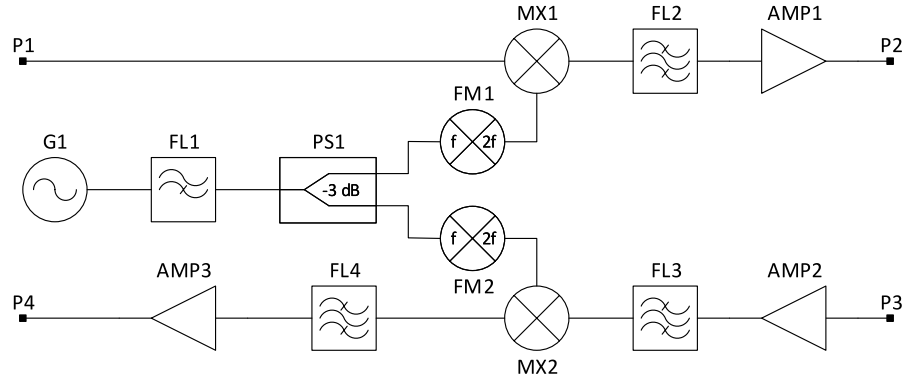


Figure 4.3: Schematic diagram of one mmWave bridge node frontend.

Table 4.1: Part list for one mmWave bridge node frontend in Fig. 4.3.

ID	Component	Part Name	Manufacturer	Details
AMP1	Amplifier	PE15A4050	Pasternack	26.5–40 GHz, 35 dB gain, 20 dBm P1dB
AMP2	Amplifier	AB038H1-14	Skyworks	36–41 GHz, 30 dB gain, 16 dBm P1dB
AMP3	Low-Noise Amp.	ZX60-63GLN+	Mini-Circuits	1.8–6 GHz, 29.6 dB gain, 14.6 dBm P1dB
FL1	Highpass Filter	custom	IB-FEMA	17 GHz high-pass filter
FL2	Bandpass Filter	PE-W28F002	Pasternack	38–40 GHz, WR-28
FL3	Bandpass Filter	PE-W28F002	Pasternack	38–40 GHz, WR-28
FL4	Bandpass Filter	PE87FL1013	Pasternack	2–4 GHz
FM1	Freq. Multiplier	HMC-C034	Analog Devices	$f_{out} = 32\text{--}46\text{ GHz}$ , $P_{out} = 13\text{ dBm}$
FM2	Freq. Multiplier	PE88X2002	Pasternack	$f_{out} = 32\text{--}46\text{ GHz}$ , $P_{out} = 8\text{ dBm}$
G1	Signal Generator	5019	Valon Technology	$f_{out} = 10\text{ MHz--}20\text{ GHz}$ , $P_{out} = 13\text{ dBm}$
MX1	Mixer	ML1-1850LS	Marki Microwave	LO 18–50 GHz, IF 0–24 GHz
MX2	Mixer	ML1-1850LS	Marki Microwave	LO 18–50 GHz, IF 0–24 GHz
P1	Connector	SMA-f	Huber+Suhner	SMA female connector
P2	Connector	2.92mm-K-f	Huber+Suhner	2.92 mm (K) female connector
P3	Connector	2.92mm-K-f	Huber+Suhner	2.92 mm (K) female connector
P4	Connector	SMA-f	Huber+Suhner	SMA female connector
PS1	Power Splitter	ZC2PD-K1844+	Mini-Circuits	18-40 GHz, 20 W, 0.8 dB insertion loss

### 4.1.1 Up-/Downconversion and Filtering

The mmWave bridge frontends for the RF signal up- and downconversion are implemented using COTS components. A schematic diagram is shown in Fig. 4.3 that is valid for both the donor and the service node, and the associated parts are listed in Table 4.1.

The CW signal from the LO (*GI*) is first high-pass filtered (*FL1*) to suppress leakage of sub-harmonics from the LO. The filtered signal is then split into two signals (*PS1*) before the frequency doubling in the frequency multipliers (*FM1*, *FM2*). This arrangement was chosen over doubling first and splitting next because the power of the signal fed to the mixer is 3.8 dB higher. Next, a bandpass filter (*FL2*, *FL3*) with a passband from 38–40 GHz suppresses the unwanted sideband right after the mixer (*MX1*) in the upconversion and the out-of-band signals right before the mixer (*MX2*) in the downconversion. On the mmWave side, the upconverted TX signal is amplified with a medium power amplifier (PA) (*AMP1*) providing 35 dB gain and a 20 dBm output power at the 1 dB gain compression point (P1dB) and a noise figure of 4.5 dB. For the downconversion, the received mmWave signal is amplified with an amplifier (*AMP2*) with 30 dB gain, 16 dBm P1dB output power, and a noise figure of 4 dB. The downconversion path has an additional bandpass filter (*FL4*) after the mixer to suppress unwanted mixer products outside the passband and an additional low noise amplifier (LNA) (*AMP3*) with about 30 dB gain, 14.6 dBm P1dB output power, and a noise figure of 0.9 dB. On the donor node, the BS is connected through the duplexer sub-component to the ports P1 for the DL and P4 for the UL. At the service node, a high-power amplifier (41.7 dBm/15 W P1dB) amplifies the DL signal from port P4, and another amplifier amplifies the received UL fed to port P1. A duplexer at the service node also ensures that no feedback loop impairs the communication link, and the same antenna can be used for TX and RX.

### 4.1.2 Local Oscillator

Based on the mmWave carrier frequency range and the sub-6 GHz intermediate frequency range, the mixer requires a CW signal with a tunable frequency between 34.2 GHz and 38.3 GHz. The effect of an LO signal with very high phase noise on an intermediate frequency (IF) carrier signal is visualized in Fig. 4.4. Because we want to transmit 4G LTE cell signals with 15 kHz subcarrier spacing (5G NR at 3.6 GHz has 30 kHz subcarrier spacing), it is critical that the LO provides a signal with low phase noise, as it would directly impair the communication signal. Unfortunately, reasonably priced high-quality signal generators for frequencies up to 40 GHz are rare. Therefore, we have decided to use a frequency doubler and an LO for frequencies up to 19–20 GHz. After a market analysis and evaluation of several configurable signal generators and synthesizers up to 20 GHz, two models were selected for their phase noise quality and cost: the APUASYN20 from AnaPico is used on the donor node, and the model 5019 from Valon Technology is used on the service node. This choice is in line with the thought of commercialization because fewer donor nodes are required, where a higher quality LO can be afforded, while the cost for service nodes (CPEs) is calculated tighter.

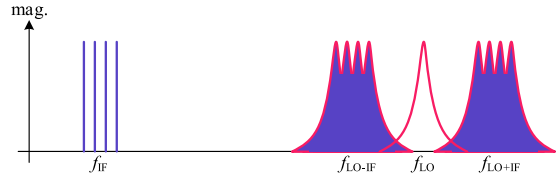


Figure 4.4: A multicarrier IF signal mixed with an LO with a given phase noise characteristic and the resulting mixer RF output signal as a combination of the IF and LO signals.

### 4.1.3 Synchronization

The donor and service nodes must operate on the same absolute carrier frequencies and without relative drift. Otherwise, the downconverted signal will not be on its original carrier frequency, and the communication link between the UE and the BS will fail. Therefore, we used a global navigation satellite system (GNSS) receiver as an accurate absolute time base. The Trimble Thunderbolt-E is a GPS disciplined oven-controlled crystal oscillator (DOCXO) that provides a stabilized 10 MHz reference signal fed to the LO. Additionally, a one pulse per second (1 PPS) signal can be used for absolute synchronization on seconds-boundaries.

### 4.1.4 Duplexing

A commercial RU of a BS provides one RF port per antenna. Therefore, the DL and UL signals must be split for fronthauling with our mmWave bridge. Similarly, a single antenna is used on the service node side, requiring the combination/separation for DL/UL signals, respectively. Duplexer filters are used for FDD operation. Two cavity filter duplexers are used with the goal to fronthaul 3GPP frequency bands 3 and 7 (1.8 GHz and 2.6 GHz). The insertion losses for bands 3 and 7 are 1.0 dB and 1.6 dB, and the band rejection is >95 dB and >60 dB, respectively, exceeding the minimum of 50 dB of isolation [82].

A dual-junction circulator (Pasternack, PE83CR1017) with 1 dB insertion loss and 40 dB isolation is used for TDD operation at the donor node. On the service node, solid-state RF switches (Mini-Circuits, ZFSWA2-63DR+) are used to switch DL and UL symbols. The switches have a 1.4 dB insertion loss, provide 65 dB of isolation, and switch within 35 ns, which is low enough for a sub-6 GHz 5G NR TDD signal. A 4G LTE or 5G NR TDD cell signal must be synchronized to Greenwich Mean Time (GMT). In most European countries<sup>1</sup>, the DL frame start is aligned with the seconds-boundary. The control of the switching time is achieved with an Arduino Due, and its timer counter is clocked with the 10 MHz reference signal from the DOCXO and reset with the 1 PPS pulses. The measured DL signal, the 1 PPS signal, and the RF switch control signal are shown in Fig. 4.5 with traces C1, C2, and C3, respectively.

<sup>1</sup>In Europe, currently only Italy uses a 2 ms offset to the seconds-boundary.

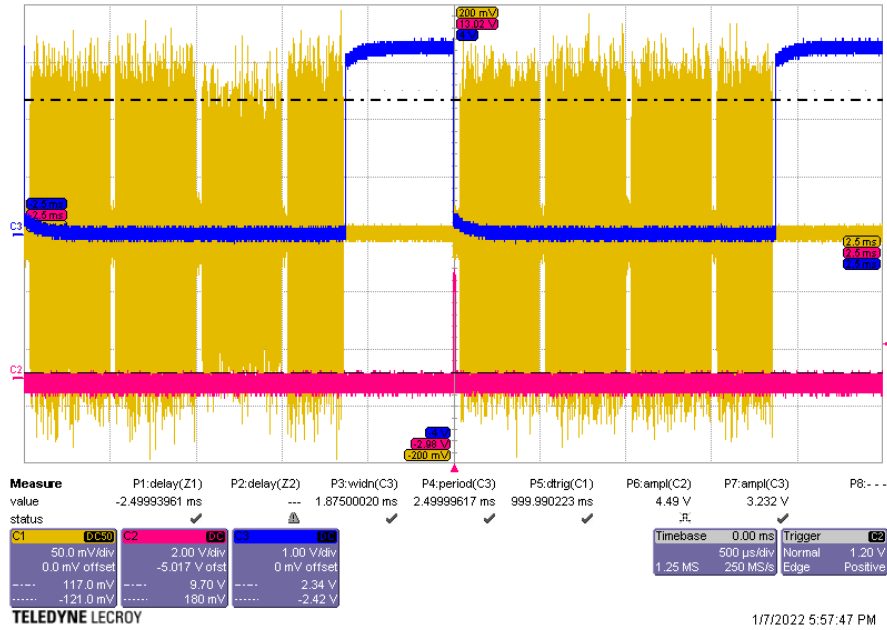


Figure 4.5: NR TDD DL signal (C1, yellow) and the DL/UL switch timing (C3, blue).

### 4.1.5 mmWave Antennas

In our prototype, we use separate mmWave antennas for DL (from the donor to the service node) and UL (inverse). Different antennas can be used depending on the application scenario. Specifically, we have conducted experiments with open waveguides with 6 dBi gain and horn antennas with 20 dBi and 25 dBi gain. Additionally, two electronically steerable beamforming antennas with 1313 configurable beams depicted in Fig. 4.6 have been used. These Holographic Beam Forming (HBF) [83] antennas from Pivotal Commware provide a gain of around 20 dBi and allow significant flexibility and speed in terms of beam steering. The single-polarization analog beamforming antennas are controlled over a USB interface.

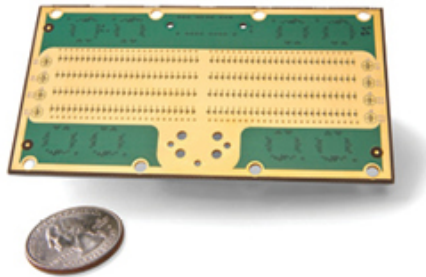


Figure 4.6: Pivotal Commware HBF antenna for 39 GHz (Source: Microwave Journal [84]).

### 4.1.6 Control and Signal Processing

For analyzing RX signals and controlling the beamforming antenna, the Xilinx radio frequency system-on-chip (RFSoc) evaluation board ZCU111 was chosen. This board provides RF input and output ports, an Ethernet port that we connected to a mobile router for remote access, a USB port, and two integrated processors. The larger quad-core processor in the device runs a Petalinux, and with PYNQ [85], it provides the possibility to use Python Jupyter notebooks for high-level control tasks. The received and downconverted UL signal is split and fed to the FPGA to be processed for beam control at the donor node. Upon initialization of the mmWave link, a beam control routine is run: the service node is configured to send a pilot signal while the donor node rapidly scans all configured beams; the receive and transmit antennas of the donor node are then configured to the beam providing the strongest signal. This procedure can be triggered periodically by sacrificing a short sub-6 GHz link interruption below the RAT connection reestablishment time, see Chapter 7.

## 4.2 Prototype Characterization

The mmWave bridge can be modeled as shown in Fig. 3.9c, consisting of an amplifier, additive noise, and a signal delay. Such a model is sufficient for link budget calculations, but further hardware impairments need to be considered for the data capacity performance. Most prominently, these are frequency selectivity, LO phase noise, and EVM due to non-linearities.

### 4.2.1 Link Budget

A link budget can be established based on values from datasheets. However, the resulting values may not precisely reflect the reality of a given hardware implementation, depending on the frequency selectivity of sub-components. The measured mmWave bridge node signal and noise power values and the resulting overall gains are listed in Table 4.2 and serve as limits to calibrate the link budget calculation listed in Table 4.3. Because of the peak-to-average power ratio (PAPR) of typically 10 dB for 5G NR and 4G LTE OFDM signals, the average composite signal input power should be around 10 dB below the maximum power specified in Table 4.2. Additionally, the noise power density from Table 4.2 must be adapted to the desired bandwidth. Therefore, for Table 4.3, we assume a 5G NR signal with 3276 subcarriers of 30 kHz each and add 79.9 dB to the noise power density of the thermal noise (-174 dBm/Hz) or measured noise. Note that the conversion loss of the mixer is higher than the nominal values in the datasheet because of the lower LO signal power.

The peak transmit power in Table 4.3 with a 25 dBi horn antenna results in a modest  $0.76 W_{\text{EIRP}}$  (28.8 dBm). For the example link budget in Table 4.3, we have assumed a nominal path loss of 118 dB corresponding to the free space path distance of 500 m. The resulting calculated SNR of 19.3 dB for a 100 MHz wide signal undoubtedly limits the link capacity. However, the peak 5G NR single layer capacity can be achieved by reducing the link distance to 250 m resulting in

Table 4.2: Measured mmWave bridge node prototype power and gain

Parameter	Donor Node				Service Node			
	TX		RX		TX		RX	
	2 GHz	3.5 GHz	2 GHz	3.5 GHz	2 GHz	3.5 GHz	2 GHz	3.5 GHz
Max. power in [dBm]	1.9	3.2	-25.1	-22.1	0.6	0.0	-28.4	-21.1
Gain [dB]	14.6	13.9	39.1	34.6	15.6	16.0	42.6	34.5
Power out [dBm]	16.5	17.1	14.0	12.5	16.2	16.0	14.2	13.4
Noise power out [dBm/Hz]	-127.8	-128.1	-121.1	-128.8	-107.1	-115.3	-120.6	-123.7

Table 4.3: mmWave bridge link budget for a 100 MHz 5G NR signal at the sub-component stages referenced in Fig. 4.3 for a nominal LOS distance of 500 m.

Value at stage	TX in (P1)	MX1 out	FL2 out	AMP1 out (P2)	TX ant. out	Path loss	RX ant. out (P3)	AMP2 out	FL3 out	MX2 out	FL4 out	AMP3 out (P4)
Component gain [dB]	-	-17	-1.5	34	25		25	30	-1.5	-10	-1.5	27
Connection loss [dB]	-	0.5	0.5	0.5	0.2	118	0.2	0.5	0.5	0.5	0.5	0.5
Signal power [dBm]	-10.0	-27.5	-29.5	4.0	28.8		-64.2	-34.7	-36.7	-47.2	-49.2	-22.7
Noise power [dBm]	-94.1	-80.8	-82.8	-48.0	-23.2		-94.1	-64.1	-66.1	-66.5	-68.5	-42.0
Resulting SNR [dB]	84.1	53.3	53.3	52.0	52.0		29.9	29.4	29.4	19.3	19.3	19.3

a 6 dB higher SNR. Also, if the signal bandwidth is reduced, e.g., if a 20 MHz LTE cell signal is transmitted (1200 subcarriers with 15 kHz), the SNR improves by  $10 \log_{10} \frac{3276 \cdot 30 \text{ kHz}}{1200 \cdot 15 \text{ kHz}} = 7.4 \text{ dB}$ , which is sufficient for the peak 4G LTE single layer capacity. Based on the maximum input power for the receiver (around -25 dBm), the minimum path loss is 89 dB, and the maximum path loss for a 0 dB SNR becomes 137 dB.

### 4.2.2 Frequency Selectivity

All sub-components used in hardware have their characteristic frequency selectivity: active components such as amplifiers, passive components such as filters, and RF connectors and cables. Such impairments are linear and can be considered part of the transmission channel that is corrected by the receivers of the RAT (UE, gNB) provided that losses are not excessive, leading to spectral nulls and excessive SNR loss in large parts of the spectrum. The measured overall transmission parameters S21 for the mmWave bridge nodes are shown in Fig. 4.7. We observe that signal losses from frequency selective behavior of the bridge components remain below 3 dB considering a signal bandwidth of 100 MHz.

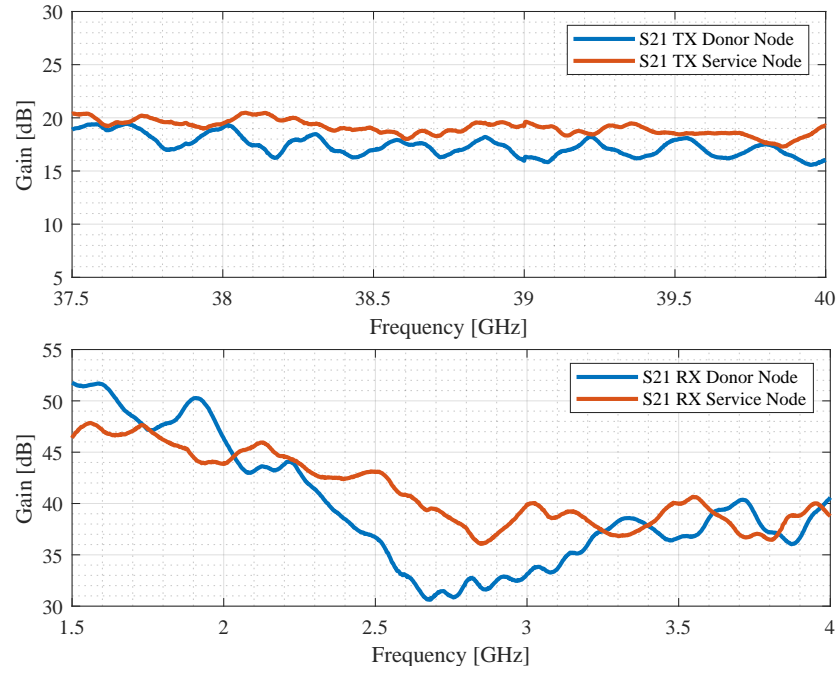


Figure 4.7: Measured transmission S21 of the respective paths.

### 4.2.3 Phase Noise

The most critical parameter for the mmWave bridge is the phase noise of the LO because it directly adds to the carrier signal noise in the mixer. Initially, a signal generator (R&S SMB100A 40 GHz) was used as an LO source. However, with the AnaPico APUASYN20 and the Valon Technology 5019, two smaller generators could be found that perform similarly, as shown in Fig. 4.8.

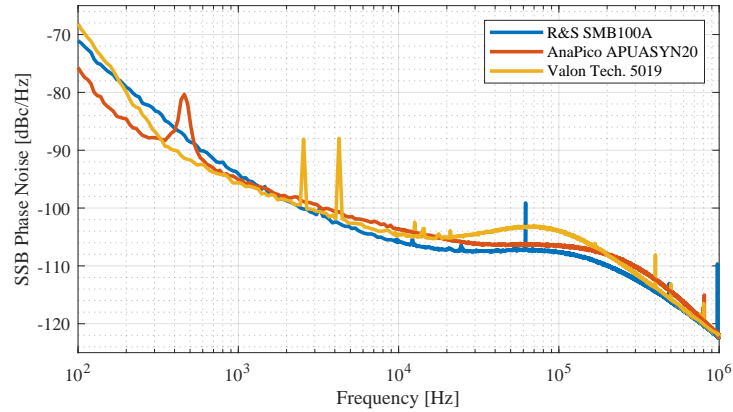


Figure 4.8: Measured phase noise at 18 GHz of three signal generators in comparison.

#### 4.2.4 Error Vector Magnitude

Finally, we have measured the EVM as an overall metric. A CW signal was sampled every quarter-wave at an offset of  $\pi/4$  to readily obtain a quadrature phase shift keying (QPSK) modulation and to assess the attainable signal quality. The root mean square (RMS) EVM  $EVM_{\text{RMS}}$  is computed according to (4.1) based on the measured QPSK constellation points  $S_{\text{meas},i}$  for  $i = 1 \dots N$  symbols and the  $k = 1 \dots M$  ideal constellation points  $S_{\text{ideal},k}$  ( $M = 4$  for QPSK).

$$EVM_{\text{RMS}} = \frac{\sqrt{\frac{1}{N} \sum_{i=1}^N |S_{\text{ideal},i} - S_{\text{meas},i}|^2}}{\sqrt{\frac{1}{M} \sum_{k=1}^M |S_{\text{ideal},k}|^2}} \quad (4.1)$$

The impact of the phase noise from the LO is the dominant source of impairments, which is clearly visible on the measured constellation points shown in Fig. 4.9. According to [86], the SNR can be computed from the EVM as:

$$\text{SNR} = -20 \log_{10} (EVM_{\text{RMS}}) . \quad (4.2)$$

The resulting SNR values according to (4.2) are 32.4 dB (donor TX), 24.9 dB (donor RX), 32.6 dB (service TX), and 28.5 dB (service RX). Although we only checked the EVM on QPSK signals, the results can be translated to other quadrature amplitude modulation (QAM) schemes. Because the QPSK constellation points have a constant magnitude, the RMS EVM equals the maximum EVM, which adopts the maximum constellation magnitude as its normalization factor [87]; hence,  $EVM_{\text{max}} = EVM_{\text{RMS}}^{\text{QPSK}}$ . The RMS EVM for an  $M$ -QAM signal is obtained from the maximum EVM according to (4.3) using the PAPR of the  $M$ -ary constellation [87]. The PAPRs for 16-, 64-, and 256-QAM are 1.324 (2.55 dB), 1.528 (3.68 dB), and 1.627 (4.23 dB), respectively.

$$EVM_{\text{RMS}} = EVM_{\text{max}} \cdot \text{PAPR} \quad (4.3)$$

Our lab measurements confirm the findings in [88] that an SNR of around 18 dB is required to achieve the maximum spectral efficiency with 64-QAM and an SNR of around 24 dB for 256-QAM. Therefore, considering 5G NR, our mmWave bridge nodes support 256-QAM as the maximum modulation and coding scheme (MCS) (code rate 948/1024) on the DL and 256-QAM with a reduced coding rate on the UL.

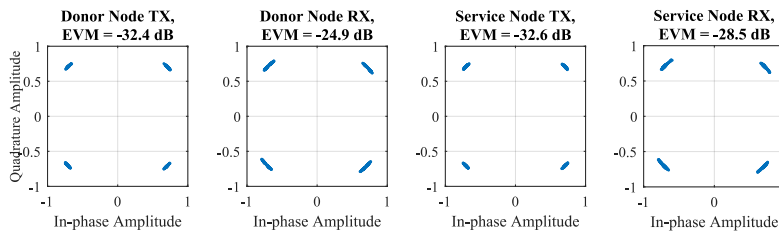


Figure 4.9: Measured constellation for the EVM calculation.

### 4.3 Validation Measurements

After basic characterization measurements, the completely assembled and integrated mmWave bridge was tested on a functional level. For a first measurement, an LTE cell with 20 MHz bandwidth was used to check signal quality metrics and achievable data throughput. Then, a 5G NR 100 MHz cell was used to measure the achievable throughput for broader bandwidth. Finally, the control of the beamforming antenna was tested in an outdoor LOS and an indoor NLOS scenario.

#### 4.3.1 4G LTE FDD

For the validation of FDD operation, we used a commercial base station providing a 4G LTE Release 15 FDD cell with 20 MHz of bandwidth. One antenna port of the RU in the lab was connected through a duplexer to the donor node of our mmWave bridge prototype. The mmWave bridge service node was set up in LOS to the donor node. The serving interface was also connected to a duplexer and was cabled to a small RF shielded Faraday box with an antenna and a UE inside. First, conducted measurements on the cable to the Faraday box were performed with a Rohde & Schwarz FSH8 spectrum analyzer with LTE downlink signal analysis functionality. With a DL RSRP of  $-44.8$  dBm fed to the Faraday box antenna, an overall EVM of 4.6 % and an SNR of 34.5 dB were measured on the cable. Next, data throughput tests were performed with iPerf3<sup>2</sup> and five parallel transmission control protocol (TCP) connections from a server close to the LTE core network to a single UE. Sequentially, two UEs were used for the tests. An LTE category 18 UE achieved a median throughput of 97.8 Mbps, and a category 20 UE achieved a median throughput of 96.7 Mbps. These results are close to the theoretical maximum data rate of 98 Mbps for a SISO link.

#### 4.3.2 5G NR TDD

5G NR provides wider cell bandwidth than LTE and, therefore, also higher data rates. A 5G NR standalone (SA) cell with 100 MHz bandwidth was provided by an Amarisoft Callbox Classic [89]. The cell was configured on the carrier frequency of 3.6 GHz. A state-of-the-art smartphone was used as UE that supports 5G SA and a peak DL throughput of 7.5 Gbps. However, with a SISO link with the configured TDD DL/UL pattern 4:1, a peak throughput of 387 Mbps is possible. The UE connected to the 5G cell fronthauled over the mmWave bridge achieved a peak throughput of 386 Mbps with an average MCS of 26.9 (27 is the highest possible MCS corresponding to 256-QAM).

---

<sup>2</sup>iPerf3 is a tool for throughput measurements: <https://iperf.fr/>

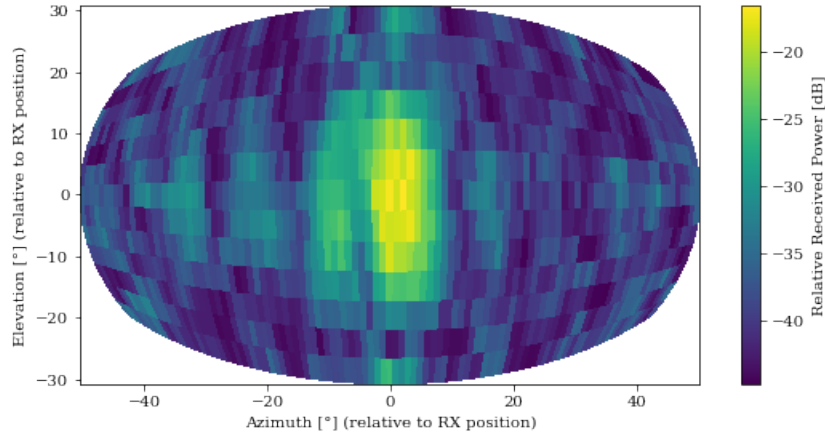


Figure 4.10: Angular RF power spectrum from a beam scan at the donor node in an outdoor scenario with LOS to the service node (maximum at  $2^\circ$  azimuth and  $0^\circ$  elevation).

### 4.3.3 Beamforming Antenna

The two mmWave beamforming antennas from Pivotal Commware provide a beam that is configurable from  $-50^\circ$  to  $50^\circ$  in azimuth (with  $1^\circ$ -steps) and from  $-30^\circ$  to  $30^\circ$  in elevation (with  $5^\circ$ -steps). Because the active beam can be switched quickly, beam measurements every millisecond are possible. A complete beam space scan with the prototype lasts around 1.4 s. In the first scenario, the mmWave bridge donor node and service node were placed outdoor at a given distance under LOS conditions with an antenna height of 2 m above ground. The measured angular RF power spectrum is shown in Fig. 4.10, with the artifacts of the beam pattern clearly visible.

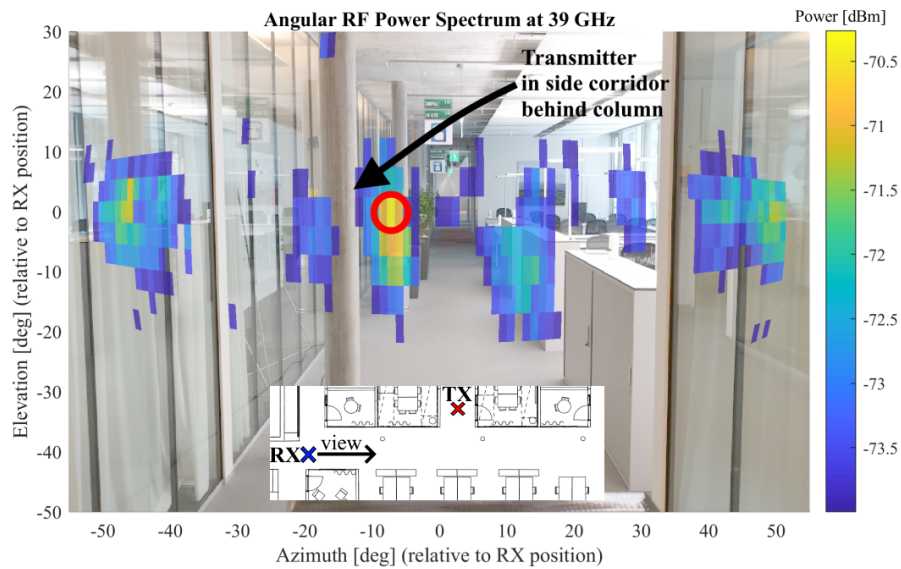


Figure 4.11: Angular RF power spectrum from a beam scan at the donor node in an indoor scenario with NLOS to the service node (maximum at  $-6^\circ$  azimuth and  $0^\circ$  elevation).

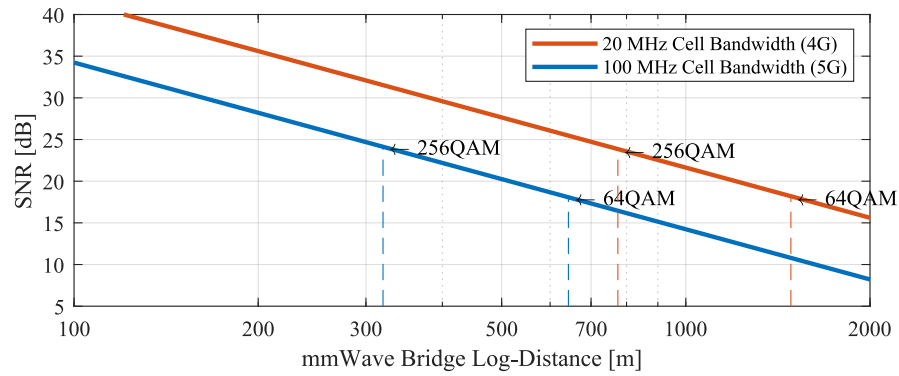


Figure 4.12: Estimated maximum link distance for the prototype at an output power of 30 dBm EIRP.

For a second scenario, the mmWave bridge nodes were set up indoors in an office space under NLOS conditions. The measured angular RF power spectrum is shown in Fig. 4.11, superimposed on a photo from the point of view of the beamforming antenna. For better visualization, beams with a received power below a threshold of  $-74$  dBm are not shown. In this particular example, four distinct reflection clusters can be identified. By holding large RF absorbing foam mats just in front of the reflecting surfaces, the exact position of these clusters could be verified as the signal disappeared into the noise. The red circle in the figure indicates the strongest reflection.

## 4.4 Summary

A prototype of a mmWave bridge has been built using COTS components. The two prototype nodes consist of analog frontends for signal up- and downconversion and related duplexing interfaces, mmWave beamforming antennas, and a control and signal processing board for estimating signal parameters, configuring the local oscillator frequencies, and steering the mmWave beams. A careful evaluation and selection of RF components were necessary, especially regarding the LO. The phase noise of the LOs has been identified as the limiting impairment. Nonetheless, an EVM between  $-32.6$  dB and  $-24.9$  dB can be achieved. With the limited output power of the TX mmWave amplifier (20 dBm P1dB saturation), but supported by the directive 20-25 dBi mmWave antennas, an EIRP of up to 1 W (30 dBm) can be realized. The functional lab tests validated that the mmWave bridge concept works, and almost the theoretical peak throughputs were achievable with COTS smartphones and 4G and 5G cells over the SISO link.

Based on the link budget for a transmit power of 30 dBm EIRP and the maximum achievable SNR for 64-QAM and 256-QAM, the plot in Fig. 4.12 can be drawn. It allows estimating the maximum achievable mmWave bridge prototype link distance for a given throughput target. For example, the approximate distance for a 20 MHz cell bandwidth to reach the peak capacity with 256-QAM is around 774 m and 1485 m with 64-QAM. A wider cell bandwidth at the same

total transmit power limits the distance because of the lower power density. With 100 MHz cell bandwidth, only about 320 m and 643 m can be covered to still reach the peak capacity with 256-QAM and 64-QAM, respectively. However, these limitations only come from the limited output power of the used PA. Longer link distances could be realized with a PA with increased output power.

Finally, the electronically controllable beamforming antennas were tested outdoor and indoors. The high beam resolution of  $1^\circ$  in azimuth and  $5^\circ$  in elevation allows for capturing a detailed view of signal reflections.

## 5 mmWave Bridge for Fixed Wireless Access

The concept of fixed wireless access (FWA) implies a static (non-mobile) wireless link. FWA provides broadband connectivity to places without fiber infrastructure or where an existing wired infrastructure does not provide a sufficiently high data capacity. Wired broadband connectivity is nowadays associated with data rates in the order of 100 Mbps. For example, the Swiss government is about to increase the minimum required data rate for the universal service<sup>1</sup> for broadband Internet to households from 10 Mbps to 80 Mbps [90]. However, not all buildings are equipped with FTTH, and the fiber upgrade of the last mile in the wired access network is costly and complex. Although 4G can provide such average data rates [91], higher data rates (several hundred megabits up to a few gigabits per second) are possible with multiple carriers or the wider cell bandwidths that 5G provides. Additionally, the lower latency of 5G can compete with the latency of wired Internet access. Therefore, 5G brings the prerequisites to enable FWA solutions. The convergent use of infrastructure for mobile broadband, Internet of Things (IoT)/machine-type communication (MTC), and FWA for broadband Internet service at home or small and medium-sized enterprises (SMEs) allows a cost-efficient use and a rapid rollout at scale [92].

An important question is the possible coverage range and how far FWA users can be supported. Example cell ranges are given in [92]. A range of up to 500 m is given for an outdoor wall-mounted antenna and a mmWave link with 200 MHz bandwidth at 28 GHz. According to [93], which describes the simulation in more detail, the BS transmit power was 35 dBm with a maximum BS antenna gain of 25 dBi, resulting in a maximum 1000 W EIRP for 2×2 MIMO. Our mmWave bridge prototype is designed for a transmit power of around 1 W EIRP, significantly limiting the achievable distances. Nonetheless, measurements can be conducted at reasonable distances, and results can be scaled to higher output power levels for a more extensive range.

In particular, in Section 5.1, we describe a measurement campaign with the mmWave bridge prototype in a rural environment. The results are analyzed, and the coverage potential and limitations are described. Another FWA use case is described in Section 5.2, where a small cell

---

<sup>1</sup>The universal service guarantees that basic telecommunications services are made available to all categories of the population and in all regions of the country.

is fronthauled to another location without the need for construction work to provide wireless connectivity inside an RF shielding structure, where no wired infrastructure is available. Again, the measurement results are discussed and highlight the potential of our mmWave bridge concept.

### 5.1 Fixed Wireless Access in Rural Areas

Deploying fiber in rural and, especially in sparsely populated areas, is costly and may not be feasible everywhere. However, FWA using mmWave frequencies is an option if the path loss allows it, i.e., the LOS distance between the BS antenna and the buildings is below 10 km or below 350 m in case of NLOS and clutter from vegetation [92]. Therefore, we conducted several measurements to validate the mmWave bridge concept for the FWA application and to test our prototype. Representative measurement examples are reported in the following.

#### 5.1.1 Measurement Environment, Setup, and Methodology

The mmWave range measurements have been conducted in a rural area that allows LOS on a straight track up to a distance of 1.3 km, as shown in Fig. 5.1a. A compact LTE Release 10 base station with an integrated evolved packet core (Nutaq PicoLTE) was used to provide the cellular network that is fronthauled with the mmWave bridge. The LTE Release 10 cell with a 20 MHz bandwidth in the 2.6 GHz frequency band allows a peak data rate of 75 Mbps for a SISO link. The base station RF signal was cabled to the mmWave bridge donor node with an antenna height of 2 m and installed at the position of the red pin in Fig. 5.1a. For the fronthaul donor link, the carrier frequency was configured to 39.75 GHz based on a test license from the Swiss Federal Office of Communications (OFCOM) [94]. The mmWave bridge service node with an antenna height of 1.75 m was cabled to an RF shielded Faraday box with a UE inside. With drive-test software, we logged various parameters from the smartphone, such as the SNR and throughput, while slowly moving the mmWave bridge service node away from the donor node. The measured parameters are filtered with a moving average filter over 5 m. Measurements are available for a distance of 50 m up to 1300 m. For validation and extrapolation beyond 1300 m, the SNR is calculated based on the FSPL model and the estimated noise floor from the measurements. The throughput is calculated using the obtained SNR with the model from [95, Sec. A.2]. In a second measurement for comparison with the fronthauled cell, the sub-6 GHz cell was transmitted directly over an antenna with the same transmit power available on the mmWave bridge node, which was 30 dBm EIRP.

The measurements were conducted on two days in November 2020. One day was sunny, and the other day was foggy, with a visibility of around 900 m, as shown in Fig. 5.1b.

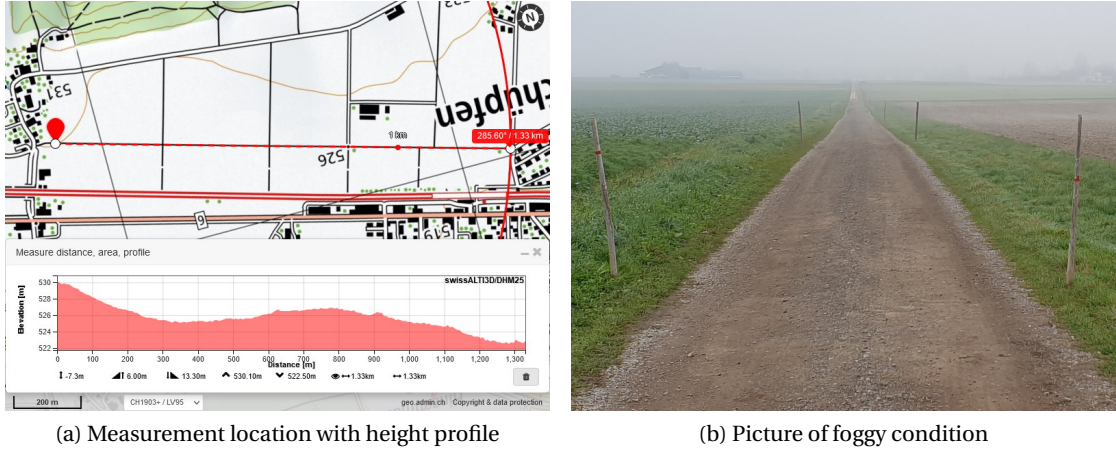


Figure 5.1: Map of the rural measurement location and weather condition on one of the measurement days (Map source: Swisstopo [96]).

### 5.1.2 Measurement Results and Discussion

Because the UE was fixed inside a Faraday box with a static channel to the mmWave bridge service node, the RSRP measured by the UE is proportional to the channel over the mmWave bridge fronthaul link, which had no gain control. However, the absolute RSRP values are not identical to the received power values on the mmWave frequency link because of amplification, filtering, and the downconversion mixer loss. Nonetheless, Fig. 5.2 shows the measured RSRP and the filtered RSRP. The strong signal at the short distance caused gain compression, which can be seen in the almost constant RSRP values for the first 75 m. A calculated signal power based on the FSPL model with an offset to match the measured RSRP validates the path loss exponent for LOS. Additionally, the two-ray path loss model [35] was computed for the mmWave donor link and is also shown in Fig. 5.2, indicating that the variations come from two-ray ground reflections.

The SNR and throughput are presented in Fig. 5.3 to show the achievable performance. Solid lines represent measured parameters from the UE connected to the cell relayed over the mmWave bridge. Dash-dot lines represent the measured parameters from a UE directly communicating with the sub-6 GHz cell. Dotted and dashed lines represent the calculated and extrapolated results for the mmWave bridge and direct sub-6 GHz cell, respectively. Note that certain UEs do not report SNR values  $>30$  dB showing a saturation effect. The calculated throughput (orange dotted and red dashed lines) also does not exceed the theoretical maximum of 75 Mbps. The measurements show that the displaced cell maintains its maximum throughput for a mmWave bridge donor link distance of up to 800 m. On the contrary, a direct sub-6 GHz connection to the UE maintains its maximum throughput up to 1100 m due to the lower propagation attenuation. Comparing the two scenarios (with and without a mmWave bridge), we note that the lower distance achieved through the bridge and to the UE can not be compared directly since, in practice, the UE would again be displaced further from the

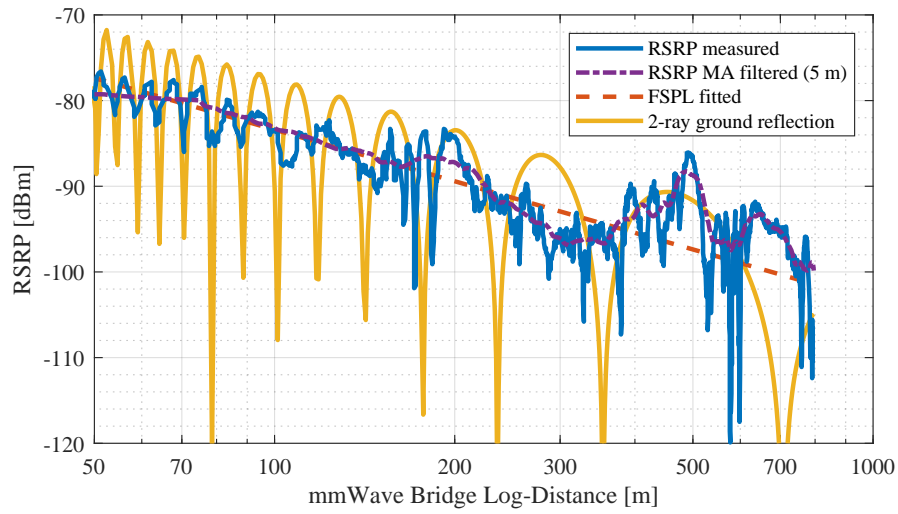


Figure 5.2: RSRP measurement agrees with the FSPL model, and variations come from two-ray ground reflections on the mmWave donor link.

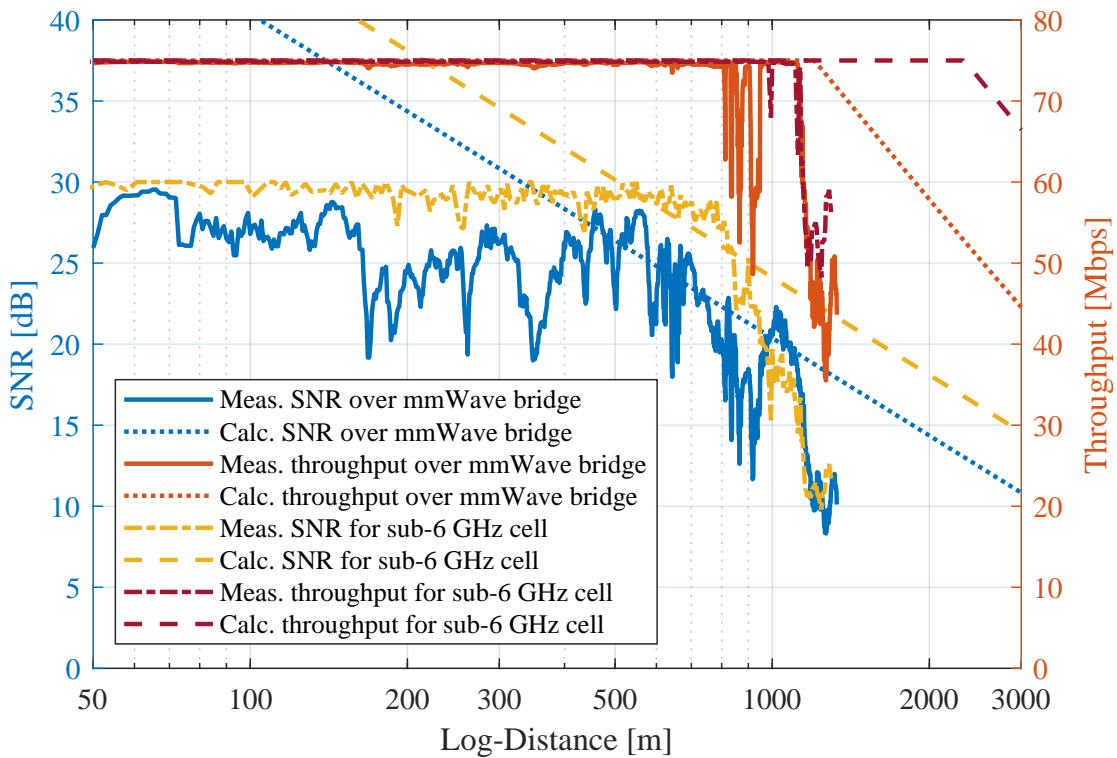


Figure 5.3: Measurement results for 50 m up to 1300 m and calculated results up to 3000 m for the UE connected over the mmWave bridge and, for comparison, directly to the sub-6 GHz cell.

service node. As the reemitted signal is amplified at the service node, the total range from the BS would be extended significantly by up to 800 m, thanks to the mmWave bridge. Note that additional effects from two-ray ground reflection have an impact also on the measured SNR. The calculated SNR in Fig. 4.12 roughly matches the trend of the measured SNR shown with the blue dotted line in Fig. 5.3.

For the FWA use case, we consider a 20 dB building entry loss resulting in a required sub-6 GHz transmit power of 50 dBm EIRP to reach the SNR and throughput shown in Fig. 5.3 inside a building at the given distance. Because the mmWave bridge service node is installed with the mmWave donor link antennas outside the building and the sub-6 GHz service link antennas inside, the mmWave bridge avoids the need to boost the outside cell power to compensate for the building entry loss. By creating a displaced and isolated cell inside the building without occupying the valuable sub-6 GHz spectrum outside for the connection, a reduction in the outdoor network capacity is avoided.

## 5.2 Small Cell Fronthaul

The mmWave bridge can also be used to fronthaul small cells in cases where additional or dedicated wireless connectivity is required, and a fiber deployment is impossible. An urgent availability of such a cell is another example where the lengthy fiber deployment process (planning, permissions, civil work) cannot meet the time requirements. Finally, a temporary need, e.g., for a short-term project or event, does not justify the cost of a fiber installation, which potentially needs to be deconstructed again. Such a use case is the EPFLoop, a research project at EPFL to develop innovative solutions targeting energy-efficient and autonomous capsules via operational-driven design of the hyperloop system [97]. For the purpose of a demonstration and validation of the mmWave bridge, we have conducted a measurement campaign to provide a 5G cell signal from an existing nearby mobile network site to the hyperloop site and to supply network connectivity inside the tube.

### 5.2.1 Measurement Environment and Setup

A reduced-scale circular test track (tube) with a diameter of 40 m has been built for EPFLoop next to the EPFL campus [98]. A dedicated 5G NR standalone (SA) cell that provides a low latency is required to control the hyperloop pod driving inside the tube and to stream telemetry data from the pod to the control center in real-time. The closest mobile network site where cellular infrastructure connected to fiber is already available is located on the “Odyssey” building, around 140 m away (visible in the middle of Fig. 5.4a). For practical reasons, an Amarisoft Callbox Classic [89] was employed as gNB to provide the dedicated 5G NR SA cell with 100 MHz of bandwidth in the 3.6 GHz frequency band and a TDD pattern with 74.3 % DL allocation. The gNB and mmWave bridge donor node were installed on the 4th floor of the Odyssey building. The mmWave bridge service node was installed next to the hyperloop tube at a distance of 140 m from the donor node. An RF shielded Faraday box was used to

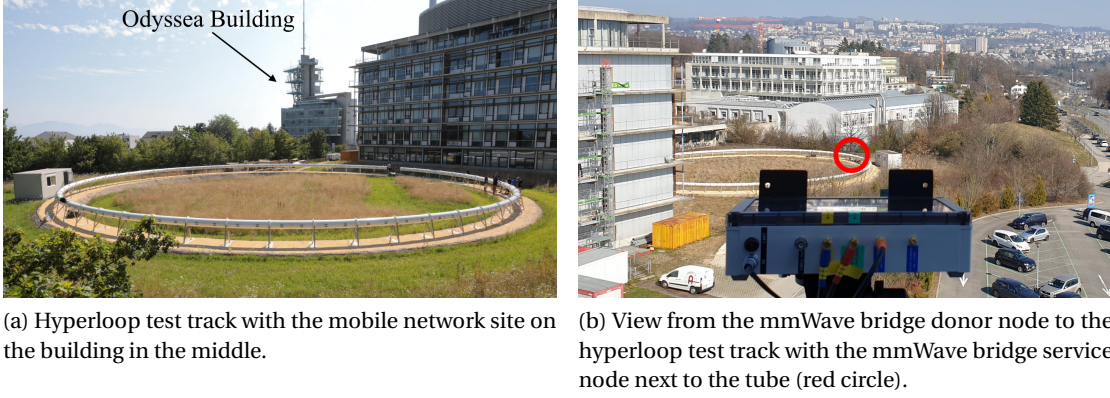


Figure 5.4: EPFLoop hyperloop site where we conducted a measurement campaign to demonstrate the potential of our mmWave bridge for the fronthaul of a small cell [98].

accommodate the UE because antennas were not yet installed inside the tube. According to the test license from the Swiss OFCOM, the carrier frequency for the fronthaul link was configured to 39.75 GHz. The measurements took place in March 2022.

### 5.2.2 Measurement Results

Multiple measurements were conducted to characterize the FWA communication link. First, the high-gain horn antennas of the donor and service node were adjusted, then path loss measurements were conducted. Finally, the 5G link was established, and throughput measurements were performed.

#### 5.2.2.1 Path Loss and Link Budget

The path loss for the 140 m fronthaul donor link was measured first as a reference after aligning the horn antennas. A CW signal at 39.75 GHz with a transmit power of 21.5 dBm EIRP was available on the donor node side, taking into account the cable loss (3.5 dB) and the horn antenna gain (25 dBi  $\pm$  2 dB). On the service node side, a power of  $-83.8$  dBm was measured, again considering the cable loss (4 dB) and horn antenna gain (20 dBi  $\pm$  2 dB). Therefore, the measured FSPL results in 105.3 dB, which is 2 dB below the calculated path loss, according to Friis. The deviation is explained with the tolerance of  $\pm 2$  dB for the horn antennas. In the next step, the end-to-end mmWave bridge link was measured, and the available signal power at the service node DL output port at 3.65 GHz was  $-4.0$  dBm, deviating 0.8 dB from the theory shown in the link budget in Table 5.1. The TX and RX gains are taken from Fig. 4.7 for the frequencies used. The noise power at the mmWave bridge service node is given as  $-42$  dBm in Table 4.3, yielding a calculated expected SNR of 37.2 dB.

Additionally, an EVM measurement was done in the same way as described in Section 4.2.4.

Table 5.1: Calculated link budget for the FWA link to the hyperloop site.

Stage:	DL power in [dBm]	TX gain [dB]	TX ant. [dBi]	Path loss [dB]	RX ant. [dBi]	RX gain [dB]	DL power out [dBm]
Signal	-1.5	17	25	107.3	25	37	<b>-4.8</b>

The resulting EVM for the link was  $-32.6$  dB which translates to an SNR of  $28.33$  dB for 256-QAM using (4.2) and (4.3).

### 5.2.2.2 5G Throughput Measurements

For the 5G measurements, we connected the Amarisoft gNB to the mmWave bridge donor node and the Faraday box to the service node. Inside the Faraday box, we placed a COTS 5G mobile router that supports the 5G NR SA standard (Huawei 5G CPE Pro 2) as a UE. Basic metrics such as RSRP and SINR could be logged with a laptop computer connected over the Ethernet interface into the Faraday box and the router. The throughput tests were performed with iPerf3 and five parallel connections to ensure full buffers.

The UE constantly reported an RSRP of  $-77$  dBm or  $-78$  dBm and an SINR of  $28$  dB to  $29$  dB without data traffic. During the iPerf3 throughput test running for ten minutes, the reported SINR varied between  $26$  dB and  $27$  dB, and the gNB showed that the UE reported a channel quality indicator (CQI) of 14, which is the second-highest CQI value [99]. Furthermore, the gNB used an MCS of 22 to 24 on the DL, showing that 256-QAM was used with a coding rate of 0.74, 0.78, and 0.82, respectively [99]. Considering the TDD DL/UL pattern, a peak throughput of 385 Mbps could be expected. However, the measured maximum throughput was around 21 % lower (304 Mbps), as shown in Fig. 5.5. Retransmissions due to decoding errors only accounted for around 1 %. Validation measurements in the controlled environment of the lab showed the same maximum throughput of around 304 Mbps, also with the UE directly connected to the gNB. The peak throughput is only achieved when scheduling dummy data on all 273 physical resource blocks (PRBs) with a test command on the gNB. We could also confirm this limitation with other configurations, which did not exist in the previous software release of the gNB. Therefore, we conclude that the mmWave bridge for the hyperloop use case works because the same throughput measured in the field can also be achieved in the lab with and without the mmWave bridge. Clearly, the consistent SNR measurements support the peak 5G cell capacity. Finally, the minimum measured latency for the 5G SA TDD cell over the mmWave bridge was 7.8 ms.

## 5.3 Summary

We have conducted two measurement campaigns that show that the mmWave bridge concept works. COTS smartphones and mobile routers can connect to a 4G or 5G cell that is displaced

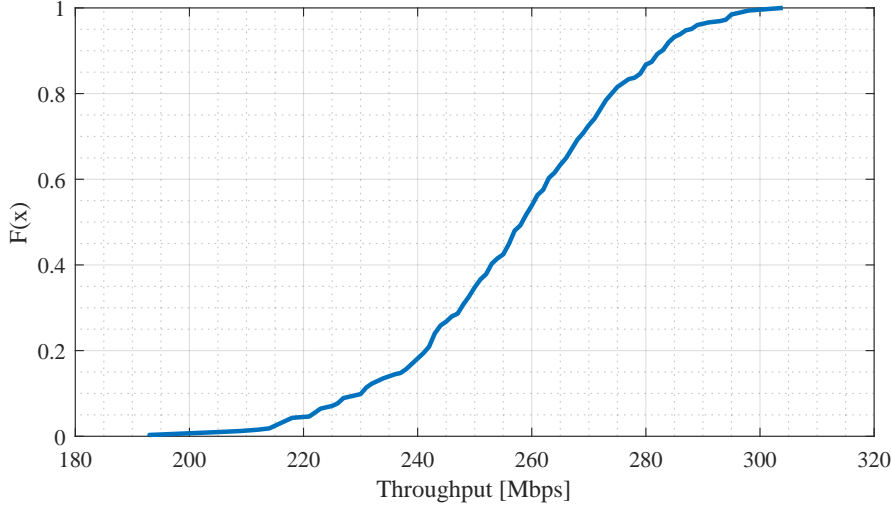


Figure 5.5: ECDF of the measured throughput for a 5G SA cell fronthauled over the mmWave bridge to the hyperloop track.

by the mmWave bridge by several 100 m. Moreover, the measurements demonstrate the operation with FDD and TDD in real-world scenarios.

Using a 20 MHz 4G LTE FDD cell and a transmit power of only 30 dBm EIRP, a donor link fronthaul distance of up to 800 m was achieved while providing the peak throughput with 64-QAM. The authors in [92] roughly estimate a distance of 10 km for roof-top antennas providing LOS links and 500 m with wall-mounted antennas and some clutter, based on simulations of a 200 MHz 2×2 MIMO cell at 28 GHz and 50 dBm EIRP. If we translate their result to our parameters (our prototype provides a power density that is approximately 17 dB lower, and we have around 3 dB increased path loss at 39 GHz, resulting in a distance scaling factor of around 1/10), we obtain a distance of 1000 m for LOS and 50 m for a link with clutter in-between. Although we did not measure the achievable distance with clutter (more details are needed for a comparison), we note that our LOS measurements tend to agree with the estimates based on simulations in [92].

Besides providing FWA service to buildings, another use case is to provide a (temporary) small cell if a fiber backhauled installation is not justified or impossible. In particular, we demonstrated that a 100 MHz 5G SA TDD cell could provide more than 200 Mbps over the 140 m fronthaul donor link distance for the EPFLoop [97] prototype.

## 6 mmWave Bridge for Cellular Corridors for Railways

With the ubiquitous availability of mobile broadband, people got used to surfing the Internet, streaming media, and using cloud services even while commuting or traveling on trains. As the worldwide consumed and generated mobile data traffic still grows [1], the demand for high-capacity mobile connectivity is also increasing for passengers traveling on railways. Therefore, mobile network operators continuously have to upgrade their wireless infrastructure to provide sufficient data capacity and prevent data congestion also along railway tracks. However, regular macro networks around railway lines cannot provide the required data capacity. The solution is a dedicated *cellular corridor* providing long linear cells along the tracks [52, 54].

An inter-city double-deck train can carry around 1400 passengers during rush hour. With only 10 percent of the passengers using the cellular network at an average throughput of 5 Mbps [52, 100], a total capacity of 700 Mbps must be provided. Even with a 100 MHz cell bandwidth available with 5G NR, a significant spectral efficiency of  $>7$  bit/s/Hz is required for such high data rates, which in turn demands a high SNR [101]. Unfortunately, modern railway carriages with their thermally insulating Low-E windows act as Faraday cages making it hard to use the cellular network inside. Several solutions to the attenuation problem exist. However, most of them require the installation of onboard equipment, such as repeaters or cellular WLAN routers. Regular upgrades on the train onboard equipment due to changes and extensions in the RAN are hard or sometimes even impossible to execute, causing conflicts between the long life cycles of the railway industry and the fast evolution in telecommunications [54]. A first step to address the problem is to replace the train windows with laser-treated Low-E windows (FSS) with a transmission loss that is close to that of regular windows while maintaining a high thermal insulation [36, 37]. The additional cost for laser-treated Low-E windows is a fraction of the cost for onboard repeaters. Additionally, cellular sites are built along the railway tracks to create a dedicated RF corridor—a long linear cell. Multiple measurement campaigns have been conducted to study the characteristics of such corridors [102, 103] and maximize the capacity provided into the train. With such measures, a throughput of 1.2 Gbps has been achieved on a train traveling at around 140 km/h in 2020 [104]. However, many macro-type cell sites are needed at an inter-site distance (ISD) of 500–1500 m, depending on the environment and the railway track geometry.

In this chapter, we propose a method to solve the railway RF corridor implementation problem using the mmWave bridge, consisting of low-power out-of-band repeater nodes operating on mmWave frequencies. The innovative use of the mmWave bridge allows increasing the ISD of the dedicated macro sites along the railway tracks, significantly reducing the overall deployment cost. The mmWave frequencies are used for the fronthaul and prevent interference to existing sub-6 GHz cells in the vicinity of the railway tracks. The mmWave bridge prototype described in Chapter 4 has been installed at a commercial railway line to conduct a measurement campaign and quantify the achievable ISD extension.

In addition to the cost benefits, our mmWave bridge solution can also significantly lower the high energy consumption of linear cells deployed along railway tracks. We effectively reduce the number of high-power remote radio heads along the tracks without compromising cell capacity. Based on detailed power consumption models and a calibrated model of the wireless link capacity, the system is optimized for energy efficiency while maintaining the same average data capacity as a conventional deployment. Furthermore, we exploit the network transparency of the mmWave bridge to introduce a smart switching mechanism that allows powering the service nodes with photovoltaic (PV) cells. We show that the mmWave bridge can cut the average energy consumption by 50 % to 79 % compared to the conventional deployment with only high-power sites.

In Section 6.1, we first explain how the railway track coverage is improved with the help of mmWave bridges. Next, the cellular corridor trial installation and the measurement setup are described, together with how the measurements have been performed and processed. The results and improvements in received power due to the presence of the mmWave bridge service nodes are discussed. Subsequently, Section 6.2 describes how our low-power bridge solution increases the energy efficiency of the railway track coverage infrastructure. The model and its calibration to estimate the wireless link capacity are explained. Moreover, we describe the power model used for cellular base stations and the power consumption of the prototype implementation for a low-power bridge node parameterized according to the same model. The power model is extended to fully solar-powered bridge nodes. Finally, the results from numerical evaluations of example deployments are presented and discussed.

### 6.1 Improving Railway Track Coverage

For a data capacity-optimized deployment of macro sites, these need to be placed a few 100 m away from the railway tracks to ensure a small incidence angle<sup>1</sup> to the train windows over an extended track segment. However, building these new macro sites implies a lengthy process that requires civil construction permissions from all involved landowners who provide the space for the macro sites and from those affected by the optical fiber and power cable installation. A simplification of this process is to install all new macro sites for the RF corridor

---

<sup>1</sup>The incidence angle is defined as the horizontal angle between the incident RF signal and a line normal to the windowpane of a train wagon at the point of incidence.

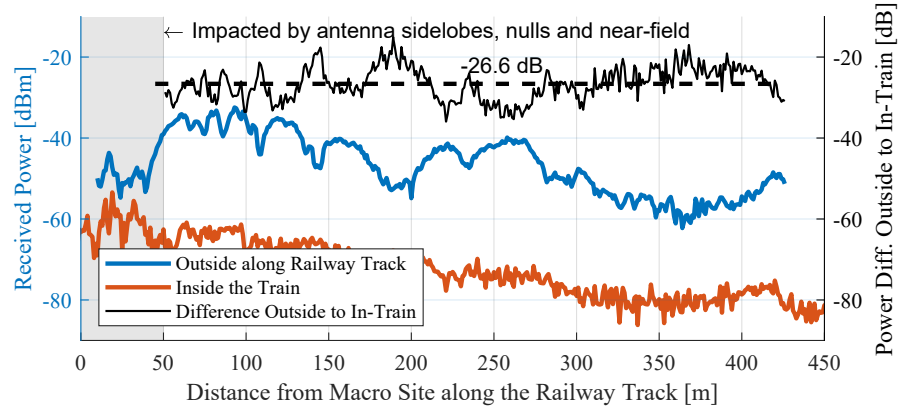


Figure 6.1: Measured signal power outside and inside the train and the resulting penetration attenuation (power difference).

on the property of the railway company just next to the railway tracks. Unfortunately, the proximity to the tracks causes wide incidence angles for the electromagnetic waves between the macro antenna and the train windowpane. Furthermore, with the strict EMF exposure regulations in Switzerland, the macro sites need an ISD of as low as 500 m to guarantee a sufficiently high signal power and capacity inside the train. With a cost of US\$ 175,000 per macro site [74] and considering the length of the railway network with close to 1000 km of tracks in Switzerland to be equipped, the cost is prohibitive.

To solve the issue of a large number of costly macro sites on railway corridors, we strive to increase the ISD. Railway tracks for high speeds are often mostly straight and must have curves with large radii. Masts for the railway overhead catenary wire exist every 50 m. Two conditions attenuate the link between the high-gain pencil beam macro antenna and a UE inside a train. First, the wide incidence angle to the train windowpane results in a narrow windowpane cross-section. Second, the catenary masts and the catenary overhead bars block the LOS between the macro antenna and the train windowpane. These angles and blockages cause an extra attenuation of 20 dB to 30 dB for the considered railway track section and used railway carriage, as illustrated in Fig. 6.1.

The attenuation issue can be solved by installing additional small antennas along the railway tracks to form a DAS, which maintains the received power levels inside the train at an increased macro ISD. The cell signals for the DAS can be fronthauled between the macro site and DAS nodes by an optical fiber. However, civil work constitutes 60-80 % of the total cost for antenna sites [74], and laying fiber to all nodes is costly; therefore, a wireless fronthaul can contribute to further savings as electrical power is often already available (or solar panels can be used). Finally, no permission for the antenna installation is required if the total effective radiated power (ERP) per antenna location is below 6 W, as it fulfills the condition for the EMF exposure limit of the general public [105, 106].

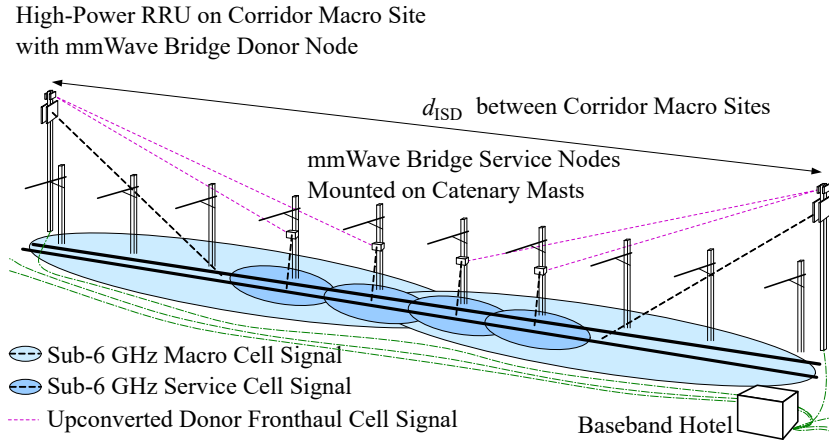


Figure 6.2: Cellular corridor with macro sites along a railway track providing the linear cell enhanced by mmWave bridge nodes in between.

### 6.1.1 mmWave Bridge for Cellular Railway Corridors

A long linear cell along a railway track has been referred to as a cellular RF corridor [54]. Such a corridor implemented with highly directive antennas on the masts along and in the vicinity of the track is called an *antenna corridor* [103]. The typical deployment of a cellular corridor along a modern railway track is illustrated in Fig. 6.2, with the masts for the cellular macro sites along the track. Each mast is equipped with two cross-polarized pencil-beam antennas supporting two transceivers, mounted back-to-back covering the railway tracks. Each antenna is fed by a remote radio unit (RRU) connected via optical fiber (green dash-dotted lines) to a baseband hotel<sup>2</sup>. For efficiency reasons, a single cell from a BBU is already shared by multiple RRUs along a railway track segment of several kilometers. A typical deployment of this form requires high-power RRUs every 500 m to 1000 m to maintain the maximum data capacity provided by 5G NR inside trains.

To reduce the number of costly macro sites along the cellular corridor, we must extend the ISD of the corridor macro sites while maintaining the system capacity. For indoor wireless networks, it is well known that the coverage of wireless cells can be extended with signal repeaters. However, in-band repeaters require high isolation between the antenna directed at the donor cell (e.g., macro site) and the antenna for the service cell (serving the users). Hence, in-band repeaters are rarely considered for outdoor scenarios like the railway track deployments considered here. Out-of-band repeaters are an attractive option for solving the isolation issue by mixing the received signal to another carrier frequency before transmitting the amplified signal. The issue with out-of-band repeaters is that they occupy additional frequency resources, which is again prohibitive in outdoor deployments with precious licensed frequency spectrum. We solve this problem by using readily available mmWave frequency bands for the donor fronthaul link that forwards the cell signal from the donor node to the service node, as proposed in Chapter 3. Thus, fewer costly macro sites are needed while

<sup>2</sup>A baseband hotel is a place where many baseband units (BBUs) for multiple cell sites are pooled together.

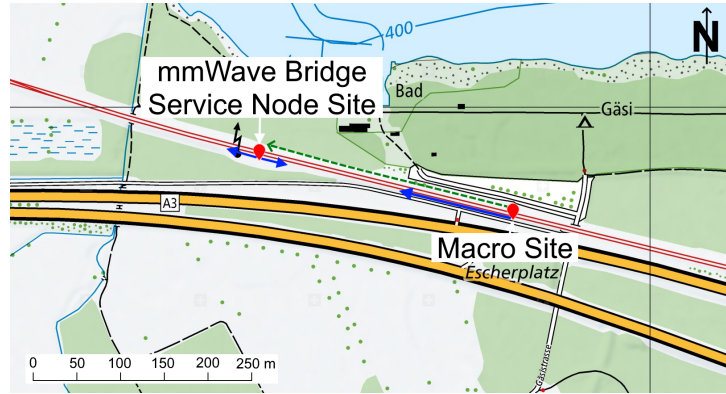


Figure 6.3: Antenna locations and their azimuth directions along the railway tracks (Source: Swisstopo [107]).

maintaining the same network capacity. A donor node installed on the macro site mast mixes the downlink cell signal to a higher carrier frequency for the wireless fronthaul to the service node, see Fig. 6.2. Then, the mmWave bridge service nodes mix the signal back to its original carrier frequency. The uplink signal is treated similarly but in the reverse direction. For ease of deployment, the compact bridge service nodes can be installed on existing catenary masts that are generally available every 50 m.

### 6.1.2 Trial Infrastructure

A railway track in the eastern part of Switzerland near lake Walensee [107] and partially shown on the map in Fig. 6.3 was selected to build and measure an antenna corridor. Several macro sites with RRUs and high-gain (25 dBi) pencil-beam antennas were built next to the two-lane railway track [103]. For this work, the corridor macro site deployment was extended with a mmWave bridge.

#### 6.1.2.1 Macro Site

The macro site used for the measurement campaign hosts the 5G NR RUs and macro antennas. The pencil-beam antenna for 3.6 GHz was installed at a height of 8.6 m above the railway track, with a transverse distance to the train windowpane of 3 m. The azimuth tuning of the main beam is aligned with the direction of the railway track towards the west (blue arrow at “Macro Site” in Fig. 6.3), and the elevation tuning angle was  $0^\circ$ . Furthermore, the polarization  $+45^\circ$  (up towards the railway track) was used for the measurements reported here, indicated with arrows in Fig. 6.4. A signal generator was installed to provide a CW signal at 3.59 GHz fed to a 3 dB power divider. The first output was connected to a power amplifier for the macro site antenna. This branch gave a signal power of 24.2 dBm at the port of the pencil-beam antenna resulting in an EIRP of 47.1 dBm. The second output of the power divider was connected to the mmWave bridge donor node input.

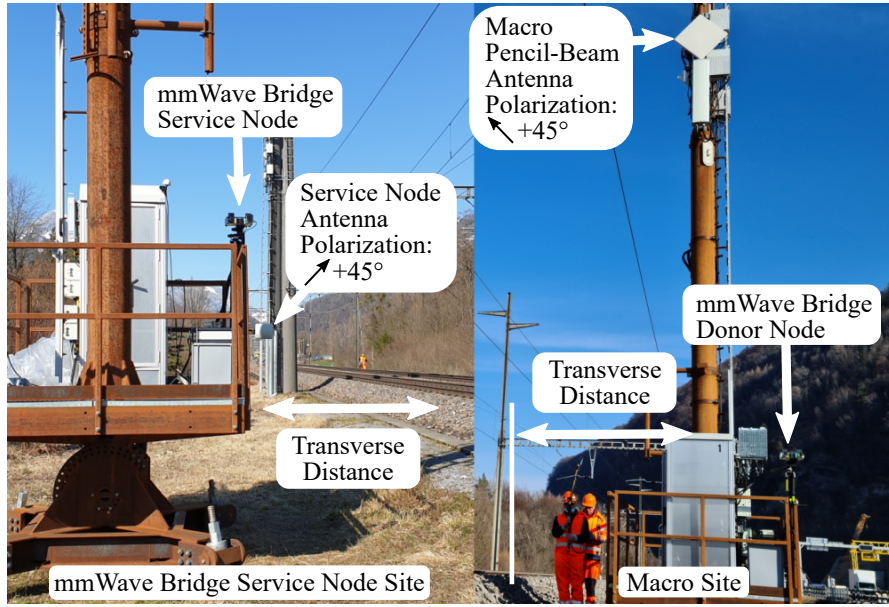


Figure 6.4: The macro antenna with the mmWave bridge donor node on the right and the service node on the left.

### 6.1.2.2 mmWave Bridge Installation

The mmWave bridge donor node was installed at the macro site. A directional coupler at the RF port of a macro cell RU feeds a fraction of the sub-6 GHz cell power to the mmWave bridge donor node, which is upconverted to a mmWave frequency and fronthauled to the mmWave bridge service node, see Fig. 6.5. The frequency downconversion in the service node translates the cell signal back to the original sub-6 GHz carrier frequency, and the antenna emits the amplified cell signal. Horn antennas with 25 dBi gain were used for the mmWave donor link on both nodes for such a static installation. Based on a test license from the Swiss OFCOM [94], the carrier frequency was configured to 39.75 GHz.

The mmWave bridge service node was installed on an existing platform at a distance of 292 m from the macro site, as shown in Fig. 6.3. At the mmWave bridge service node, the received and downconverted signal was connected to a power amplifier and a 3 dB power divider connecting to the service antennas, see Fig. 6.5. Two 5.9 dBi gain Huber + Suhner antennas were mounted at the height of the train window in a back-to-back configuration, i.e., one antenna covering the railway track westwards and one covering the railway track eastwards at a transverse distance of 4.7 m to the train windowpane, see Fig. 6.4. The 3.6 GHz service antennas provided an EIRP of 32.8 dBm and 32.5 dBm, respectively. Again, the same polarization of  $+45^\circ$  (up towards the railway track) was used as shown in Fig. 6.4. For the mmWave donor link, the Friis FSPL results in a 113.7 dB loss. We obtained 116.3 dB based on the measured power levels, which is within the tolerance of the TX and RX antenna gains ( $\pm 2$  dB).

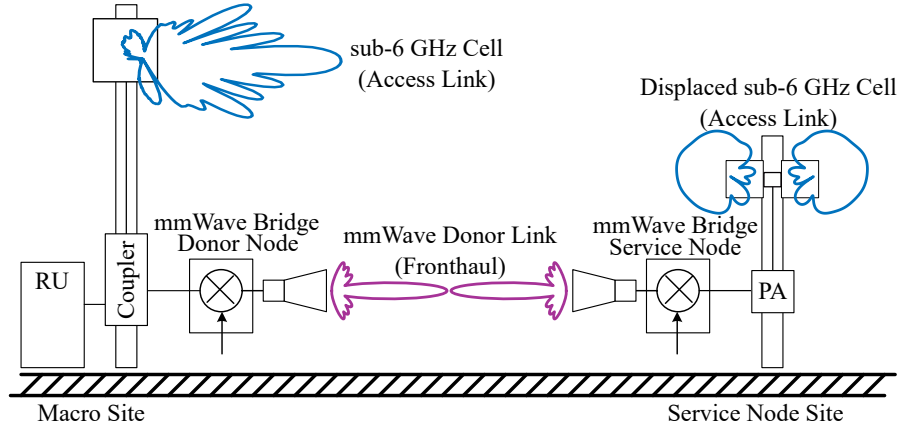


Figure 6.5: Schematic of the macro site and the mmWave bridge donor and service nodes.

### 6.1.3 Measurement Methodology

The trains used for the measurements were single-deck low-floor regional trains, as shown in Fig. 6.6a, equipped with laser-treated Low-E windowpanes (FSS).

A Rohde & Schwarz FSH8 spectrum analyzer was used for the measurements outside along the railway track. The FSH8 was configured to conduct time-domain measurements. A sweep time of 1 s was set for sufficient resolution in the distance, and a resolution bandwidth (RBW) of 30 kHz was configured. In order to continuously measure the signal, the FSH8 was set in spectrogram mode. During each sweep, 631 power samples were captured and registered by the FSH8. A wideband dipole antenna from Huber + Suhner was connected to the FSH8 through a 2-meter cable of 1.8 dB loss. The antenna was held up at 2.5 m above ground, and the persons performing the measurements were walking at almost a constant speed on the cable duct along the railway track. Simultaneously, the GPS location was recorded.

A Rohde & Schwarz FSW spectrum analyzer was used for the measurements inside the train. The same dipole antenna was installed in a seat compartment on a tripod at 0.4 m from the windowpane at a height of 1.1 m above the floor, as shown in Fig. 6.6b. The FSW was configured to record the complex baseband signal with a sample rate of 10 kHz. Cable losses have been calibrated in the measurements.

According to Lee's sampling criterion [34], fast fading effects have been mitigated by averaging the measured power samples in the linear domain over a distance of  $40\lambda$ .

### 6.1.4 Results and Discussion

Measurements of only the macro antenna have been conducted first to obtain a baseline scenario for reference. Then, the mmWave bridge was installed with the donor node at the macro site and the service node at a distance of 292 m. Accordingly, the previous measurements



(a) A typical single-deck low-floor regional train in which measurements were conducted.



(b) Measurement equipment on the train (note that only one of the dipole antennas was connected to the visible instrument).

Figure 6.6: Pictures of the type of train used for measurements and how the equipment was installed inside.

have been repeated as a second scenario with the mmWave bridge in operation in addition to the macro antenna. For each scenario, multiple train runs in both directions have been considered for more samples and better convergent results. As an indicator of uncertainty in our measurements, the average standard deviation was computed among all measurement runs. A standard deviation of 3.1 dB is obtained for the baseline scenario (macro site only) and 2.6 dB for the scenario with the mmWave bridge.

### 6.1.4.1 Coverage for Macro Antenna (Baseline)

For the baseline reference scenario with only the macro antenna, the measured power levels inside the train are shown with red and orange lines in Fig. 6.7. The horizontal axis represents the distance along the railway track segment west of the macro site in Fig. 6.3. Four measurement runs, two in opposite directions, have been averaged in linear domain and used to fit the power, modeled with the FSPL, and shown with a thick dark orange line. The upper and lower borders indicate the range depending on the transversal distance of the track. The resulting

path loss with the calibration  $L_{M,calib} = 32.67$  dB is given according to

$$L_M(d_l) = \left(d_l \frac{4\pi}{\lambda}\right)^2 \cdot L_{M,calib} \quad \text{for } |d_l| \geq d_F, \quad (6.1)$$

where  $d_l$  represents the longitudinal distance on the railway track. The path loss is approximated as a constant for longitudinal distances below the Fraunhofer distance  $d_F = \frac{2D^2}{\lambda} = 17.2$  m defining the near-/far-field border of the pencil-beam antenna, with  $D$  being the largest linear dimension encircling the whole antenna.  $\lambda$  represents the wavelength of the carrier frequency. Note that the difference between the phase center<sup>3</sup> of the macro antenna and the center of the railway carriage's middle windowpane in height and transversal distance is neglected, accepting an inaccuracy of 1 dB for  $|d_l| < d_F$  in the studied configuration. The modeled power matches the measurements with an RMSE of 3.1 dB.

In Fig. 6.7, we note that for the first 200 m, there is a power difference of up to around 10 dB between the two parallel railway tracks (one for each direction) for the macro-only scenario. This difference can be explained by the two railway tracks having a transverse distance difference of 3.8 m, resulting in slightly different angles and windowpane cross-sections with the pencil-beam macro antenna. Due to the sidelobes in the antenna pattern, this results in a deviating antenna gain. Further, the blockage of the LOS by catenary masts is notably different for the nearer railway track (with a shorter transverse distance) compared to the farther one. Finally, the measured power levels from the macro antenna are considerably higher between 50 m and 200 m than the FSPL model suggests. These higher power levels can be explained by the antenna pattern and the two-ray ground reflection model, which are shown as a thin black line in Fig. 6.7.

### 6.1.4.2 mmWave Bridge Coverage Increase

The measured power with both the macro antenna *and* the mmWave bridge in operation is shown with green and blue lines in Fig. 6.7. Again, measurements from four runs, two in opposite directions, have been averaged in linear domain to fit the power with the FSPL model for the macro antenna and service node combined, depicted with a thick blue line. The upper and lower borders (for the farther and closer railway track, respectively) also indicate the range depending on the transversal distance of the track. The light blue dashed line represents the power only from the service node, based on the free space path loss model, adapted with the calibration  $L_{S,calib} = 18.75$  dB as

$$L_{S,n}(d_l) = \left[ d_{tv,S,n}^2 + (d_l - d_{l,S,n})^2 \right] \left( \frac{4\pi}{\lambda} \right)^2 \cdot L_{S,calib}. \quad (6.2)$$

The equation in (6.2) is a general model for an arbitrary number of service nodes, while we only used one service node in our measurements. Because the service node antennas are installed

---

<sup>3</sup>The phase center of an antenna represents the apparent source of radiation.

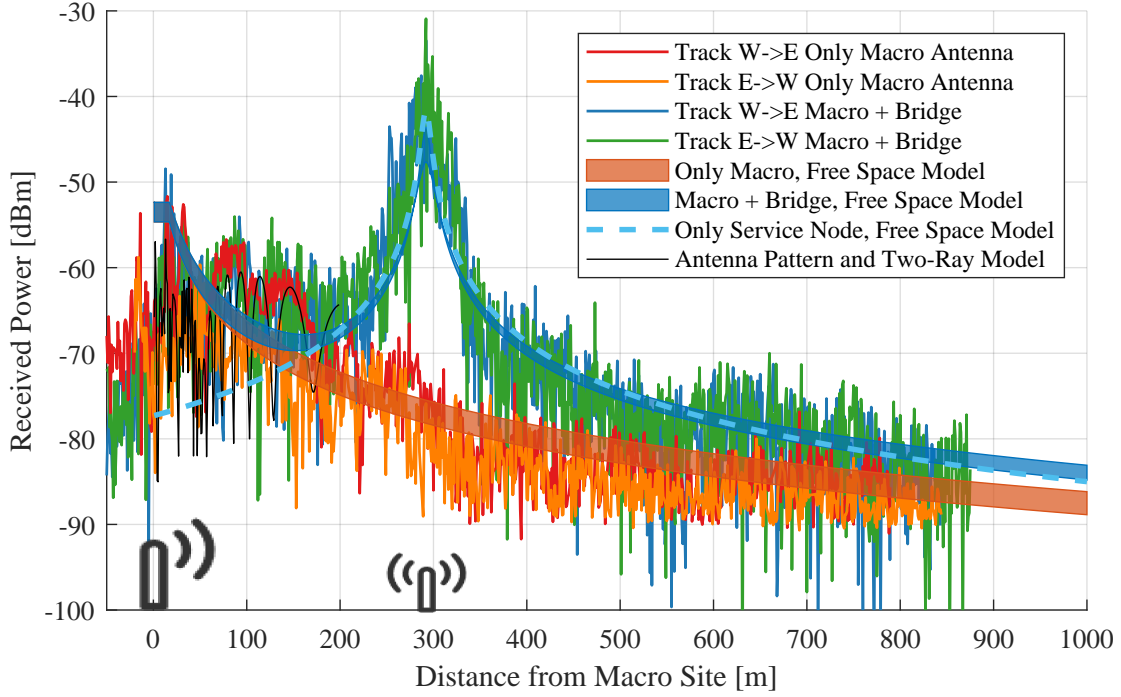


Figure 6.7: Measured signal power inside the train for only the macro antenna as a baseline and the macro antenna enhanced with the mmWave bridge at 292 m. The macro antenna transmit power was 47.1 dBm EIRP, the mmWave bridge transmit power was 32.5 dBm EIRP.

at the height of the railway carriage windowpane, the height difference can be neglected. However, the transversal distance of the  $n$ th service node antenna to the windowpane is represented with  $d_{tv,S,n}$ . The position of the  $n$ th service node along the longitudinal distance of the railway track is considered with  $d_{l,S,n}$ . The Fraunhofer distance is irrelevant due to the small dimension ( $D = 0.25$  m) of the service node antenna. The RMSE of the modeled power compared with the measured power is 4.9 dB.

Comparing the two scenarios with and without the mmWave bridge, Fig. 6.7 shows that the mmWave bridge service node provides a substantial increase in power starting at around 150 m. Even beyond 500 m up to 800 m, the service node lifts the power by 5-8 dB.

The difference between the high-gain macro antenna and the low-gain service node antennas can be analyzed by comparing the measured power levels outside and inside the railway carriage, see Fig. 6.8. The macro pencil-beam antenna with the 25 dBi gain creates a focused beam along the railway track, causing less scattering around the railway tracks to reflect power through the windowpanes into the carriage. This reduced scattering results in a carriage penetration gain of  $-26.6$  dB (Fig. 6.1 with a  $5^\circ$  overshooting antenna) and  $-23.3$  dB for the measurements with the mmWave bridge (Fig. 6.8). The service antennas with a lower gain of 5.9 dBi selected for a shorter coverage range with a DAS supported by our mmWave bridge, therefore, bring several advantages over a high-gain pencil beam antenna applied in the context of a high-power corridor with only macro cells:

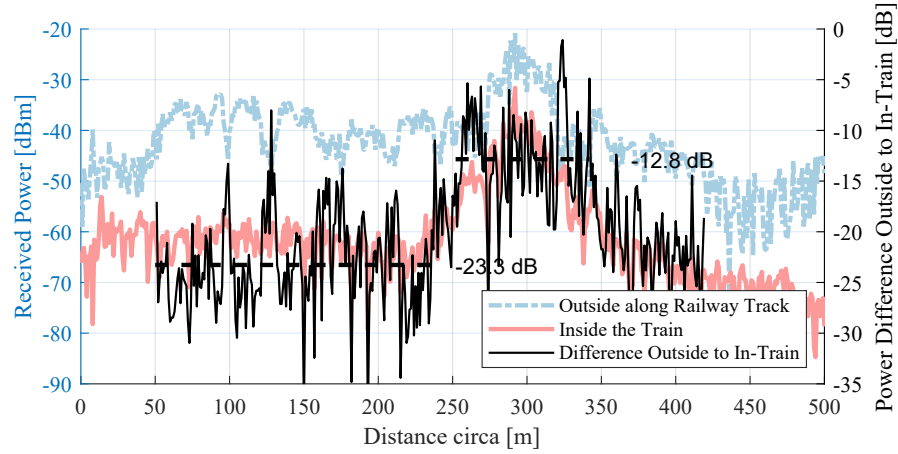


Figure 6.8: Signal power and difference for the macro and service node antennas outside and inside the train.

1. The lower directivity allows for more power passing in LOS through the cross-section of the windowpane into the carriage.
2. There is a reduced blockage of the LOS due to catenary masts and the height difference to the carriage windowpane.
3. There are no sidelobes and nulls in the antenna pattern.
4. They create a richer channel allowing for more reflections into the train resulting in a wagon penetration gain of  $-12.8$  dB for the 50 m before and after the antenna.
5. The antenna dimensions result in a significantly shorter near-field distance.

The disadvantage of the lower gain is the more substantial power decrease in the longitudinal distance compared to the high-gain antenna, requiring shorter antenna installation intervals.

Finally, for each scenario, all measurement runs for both tracks have been combined to calculate the ECDF presented in Fig. 6.9. The additional mmWave bridge service node can increase the median power by 10.5 dB for the 1000 m railway track segment under study. 5G NR throughput measurements have been done in the antenna corridor with only macro antennas. Based on these measurements, the linear regression for the throughput versus the RSRP gave a slope of 13.65 Mbps/dB for a 100 MHz 5G NR cell. Hence, with an RSRP increase of 10.5 dB, an additional 143 Mbps can be achieved over the 1000 m track segment if the throughput is not saturating at the theoretical peak data rate.

While the presented measurement results are specific to the type of railway carriage, our further measurements suggest that these results are also applicable within 2–3 dB to other modern railway carriages. An impact on the signal attenuation from the mmWave bridge service node to the railway carriage is expected when two trains pass in opposite directions. However, the impact only lasts for a few seconds at high velocities and does not lead to an outage.

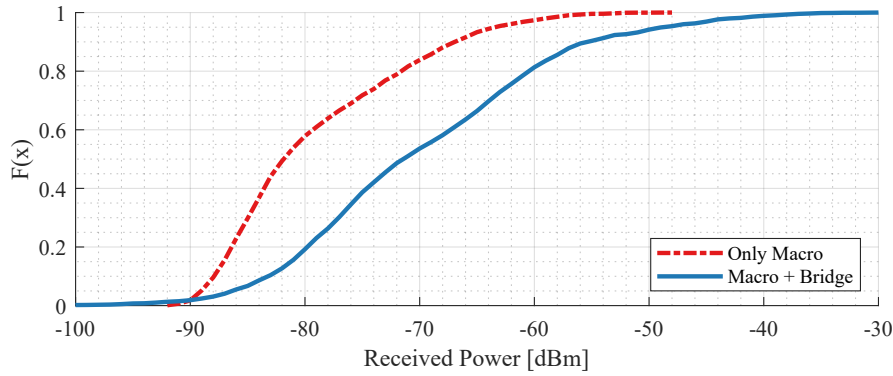


Figure 6.9: ECDF of all measurements taken in trains for comparison over the 1000 m track segment west of the macro site.

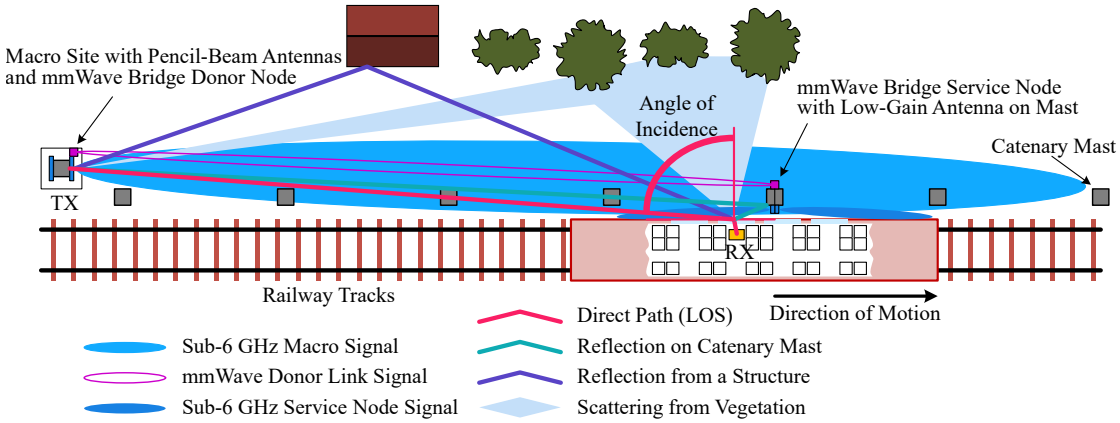


Figure 6.10: Direct and indirect signal paths discussed for the Doppler measurements.

### 6.1.4.3 Doppler Measurements

For wireless vehicular communications, the effect of Doppler is relevant. It is even more severe for an antenna corridor concept due to the wide incident angles between the LOS component and railway carriage windowpanes over a considerable portion of the corridor path length, as shown in Fig. 6.10. The Doppler effect is dependent on the relative velocity and the angle between the velocity vectors of TX and RX antennas weighted by their far-field radiation functions<sup>4</sup>. An overview of the dominant signal paths discussed here is provided in Fig. 6.10. The end-to-end Doppler profile of the channel is given by the velocity of the train, the direct path (LOS) from the cellular corridor antennas to the railway carriage window, the indirect NLOS paths from reflections and scattering by catenary masts and surrounding structures and vegetation, and the transmission loss of the windowpane<sup>5</sup> [109].

<sup>4</sup>E.g., a high antenna directivity (small HPBW) results in less scattering around the vicinity of the antenna.

<sup>5</sup>Note that the windowpane transmission loss depends on the angle of incidence [108, Fig. 1] and impacts the weighting (magnitude) of Doppler components from different angles.

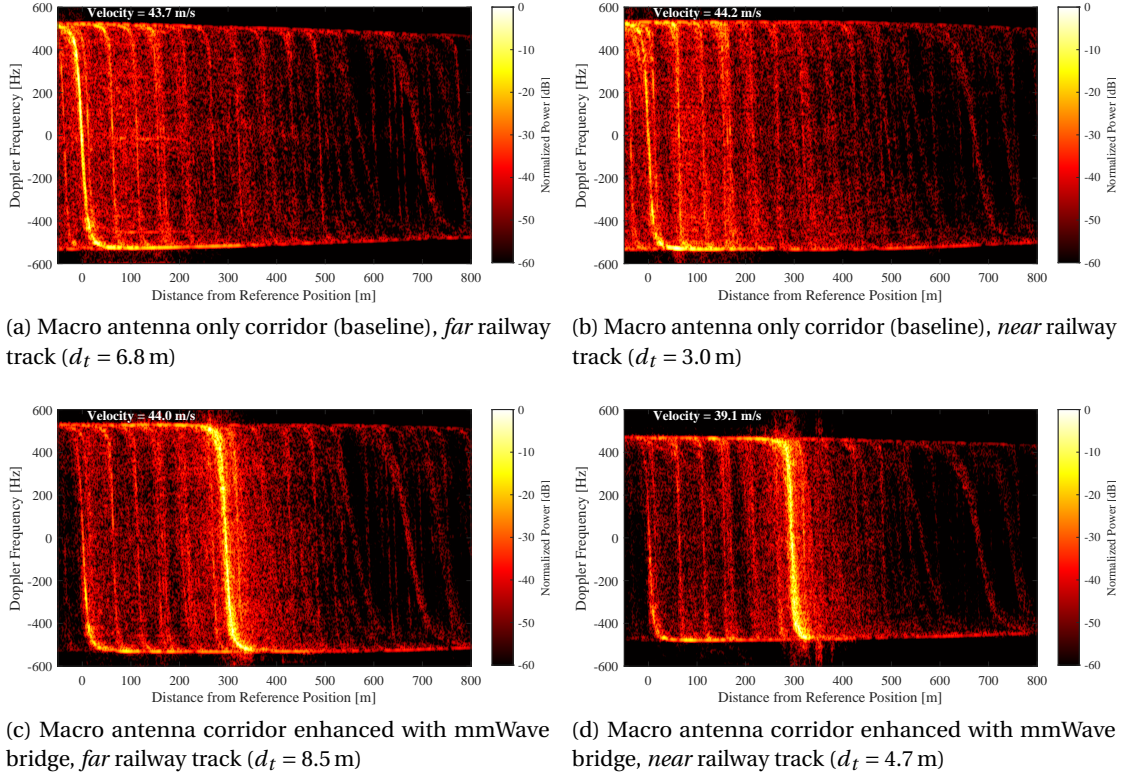


Figure 6.11: Doppler spectrum for only the macro antenna corridor (baseline) and the macro antenna enhanced with the mmWave bridge on two different railway tracks (*far*, *near*), resulting in different transverse distances between the corridor antennas and the train windowpane.

The Doppler spectrum measurement at 3590 MHz is presented in Fig. 6.11 for the macro antenna corridor as a baseline (top) and the macro antenna corridor enhanced with a mmWave bridge (bottom). The left and right results represent two different transverse distances (*far* and *near* railway tracks). All figures show the result of a train driving from east to west in Fig. 6.3 and illustrated in Fig. 6.10.

The measurements in Fig. 6.11a and Fig. 6.11b show the dominant LOS component from the macro pencil-beam antenna for the first 200 m, which are also shown with red and orange lines in Fig. 6.7. Additionally, the reflections of catenary masts every 50 m are also clearly visible. In Fig. 6.11c and Fig. 6.11d, the mmWave bridge at 292 m is distinctly visible as in Fig. 6.7 with the green and blue lines.

The short transverse distances of the antennas to the railway tracks lead to a severe reduction of the cross-section between the windowpane and the antenna radiation pattern as the train moves away from the corridor antenna. As a result, the indirect paths from catenary masts and the surroundings are measured for longer distances for the highly directive macro antennas compared to the low-gain service antennas of the mmWave bridge. Furthermore, the obtained results of the received signal power around 0 Hz Doppler frequency can be used to approximate

the distribution of the angle of incidence at the railway carriage windows and serve as an indication of reflected and scattered power in the vicinity of the window (e.g., see Fig. 6.11a at 0 Hz  $\pm$  50 Hz).

A comparison of the Doppler spectra in Fig. 6.11 also proves that the lower gain service antenna results in richer multipath through reflections and scattering around the antenna site than the high-gain macro antenna. Thus, a macro antenna corridor enhanced with mmWave bridge nodes may also support a higher channel rank from the service nodes.

### 6.1.4.4 Stretching the Macro Inter-Site Distance

Since the ultimate goal is the extension of the railway corridor macro ISD, a simple model is created according to (6.3) using the antennas' powers  $P_M^{\text{RSTP}}$  for the macro antennas and  $P_{S,n}^{\text{RSTP}}$  for the  $N$  service node antennas, with the calibrated FSPL models in (6.1) and (6.2), respectively.  $d_{\text{ISD}}$  denotes the macro ISD.

$$P_{\text{UE}}^{\text{RSRP}}(d_l) = \frac{P_M^{\text{RSTP}}}{L_M(d_l)} + \frac{P_M^{\text{RSTP}}}{L_M(d_{\text{ISD}} - d_l)} + \sum_{n=1}^N \frac{P_{S,n}^{\text{RSTP}}}{L_{S,n}(d_l)} \quad (6.3)$$

For orthogonal frequency division multiple access (OFDMA) based communications technologies such as 4G LTE and 5G NR, the composite signal power (total power over the whole cell signal bandwidth available) varies depending on the number of used PRBs. The maximum transmit power allowed by EMF regulations is only used if all PRBs are allocated and the entire bandwidth is used. Therefore, it is common to know and compare power levels per subcarrier, represented by the RSRP. For this more intuitive interpretation, the power levels are offset by  $10 \log_{10}(1/3300) = -35.2$  dB to reflect the difference between the maximum transmit power of a 100 MHz bandwidth cell and one subcarrier. In a typical example configuration for the numerical analysis here, the macro ISD is 1000 m with a macro antenna power of 600 W ERP, resulting in a reference signal transmit power (RSTP) of  $P_M^{\text{RSTP}} = 181.8$  mW (22.6 dBm). Five mmWave bridge service nodes have been placed with a 100 m inter-node spacing centered between two macro sites. Moreover, each service node has an RSTP of  $P_{S,n}^{\text{RSTP}} = 1.82$  mW (2.6 dBm), just at the Swiss EMF exposure limit of 6 W ERP [105] for small cells in the general public.

The numerical evaluation of (6.3) for the 5G NR RSRP inside the train is shown in Fig. 6.12. A scalar metric is used to compare different scenarios. For example, the measured power can be averaged over the distance if a train travels along the antenna corridor at a constant velocity. The resulting average RSRP is shown with dashed lines for the scenario with only the macro sites (orange lines) and the scenario with additional service nodes (blue lines), resulting in a 10.1 dB RSRP increase compared to only the macro antenna corridor.

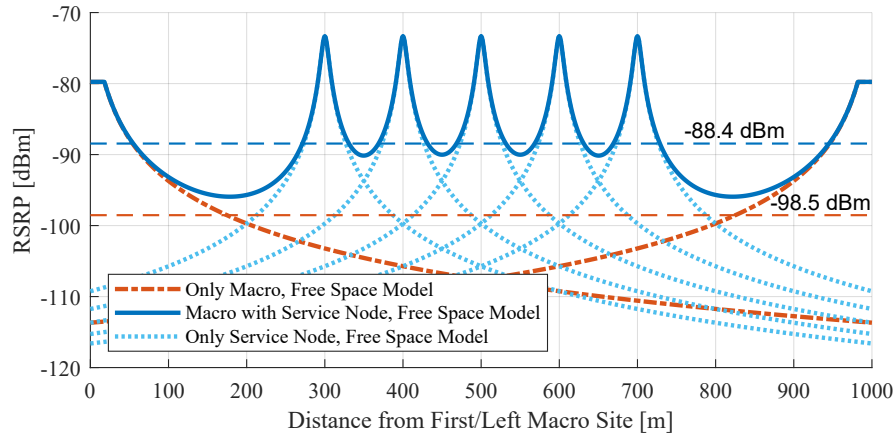


Figure 6.12: Example of a macro ISD of 1000 m with a transmit power of 600 W ERP and five mmWave bridge service nodes with a transmit power of 6 W ERP each. The average RSRP is shown with dashed lines.

Measurements have shown that 5G UEs can cope with power profiles shown in Fig. 6.12 and variations of even 30 dB as frequently as every 50 m. For example, a UE inside a train with a velocity of 200 km/h moves by 28 mm per 5G NR slot of 0.5 ms and, based on the FSPL model, only experiences a power change of maximum 0.025 dB per slot. Fast fading effects have a more substantial impact on the received signal than the power changes from many antennas along the railway track.

The above model in (6.3) is used for the numerical evaluation of various configurations. At first, a baseline configuration with only macro antennas every 500 m is assumed. This baseline is then compared to configurations with the macro antennas with a longer ISD and additional mmWave bridge service nodes installed in between. Because it is envisaged to install the mmWave bridge service nodes on the existing catenary masts, the available inter-node distance is limited to a multiple of 50 m. For our evaluation, inter-node distances of {100,200,300} m were chosen. A maximum of six mmWave bridge service nodes are placed between the macro sites. Each macro site would feed a maximum of three mmWave bridge service nodes per side. By numerical evaluation of these configurations for a range of ISDs, the maximum macro ISD that can still provide at least the same average RSRP inside the train as the baseline configuration can be found, as shown in Fig. 6.13.

With six mmWave bridge service nodes and an inter-node distance of 300 m, the same average RSRP can be achieved at a macro ISD of 2350 m as with a macro ISD of 500 m without using mmWave bridge service nodes. Such an increase in ISD corresponds to a significant reduction in infrastructure costs. The farthest mmWave donor link would result in 1025 m which is still feasible under LOS, as the measurements in Section 5.1 have shown. Also, high-speed railway tracks are relatively straight, with large radii in curves, and the geological topography along the railway tracks often supports LOS at the height of train windowpanes for such distances.

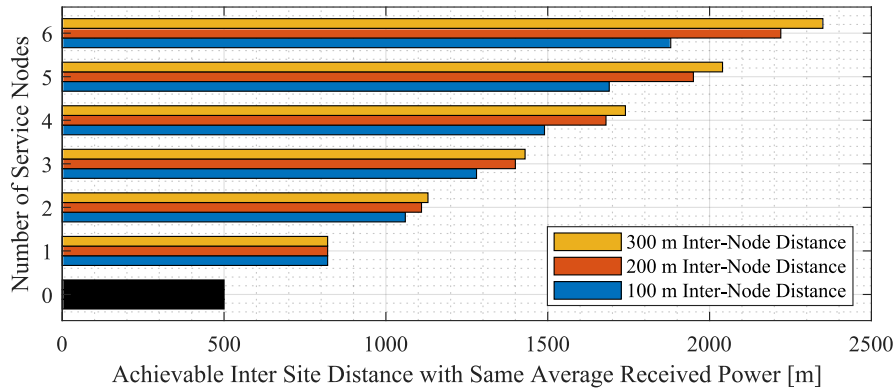


Figure 6.13: Numerical evaluation of average power in a train for a given number of mmWave bridge service nodes at a given inter-node distance.

## 6.2 Increasing Cellular Network Energy Efficiency

A regular macro cell site consumes an average power of 3200 W [110]. Because more and more cell sites are needed, people are working on optimizing the mobile network energy efficiency [57–59]. While such optimizations are essential and needed in the long term, they are difficult because of multiple constraints and the heterogeneous structure and topography of cellular networks. An essential and more structured part of the network is the infrastructure dedicated to providing cellular capacity to railways with a cellular corridor [52, 54]. Unfortunately, deploying this type of coverage to the 118,000 km of electrified railway tracks in Europe adds up to an energy consumption of 1.24 TWh per year.

In a cellular corridor, antennas are fed by RRUs connected to a baseband hotel via optical fiber. Considering higher frequency bands used by 5G and the stringent EMF limits enforced in certain countries (e.g., Canada, Italy, Poland, Switzerland, China, Russia) [111], ISDs of a few 100's of meters up to 1000 m are necessary to provide the required data capacity. While short ISDs are common in dense urban areas and are needed to provide sufficient cells for the capacity demand, the particular railway scenario does not need such a high cell density. Furthermore, because trains must maintain a minimum distance between each other for safety reasons, only up to one train is present in a given railway track segment at most. Therefore, a mobile cell can be linearly stretched along the railway tracks with the help of a DAS and multiple RRUs, reducing the number of required BBUs. Still, one high-power RRU can consume up to 300 W, and with two RRUs required per site and an ISD of 500 m, the power consumption rises to 1200 W per kilometer of installation. Nevertheless, ISDs of, e.g., 500 m or more, are only possible with penetration loss optimized railway carriages. Because modern railway carriages significantly dampen the wireless signals [102, 112], which dramatically reduces capacity, onboard relays have been used to overcome the high signal attenuation. However, active relays also consume power (650 W for five frequency bands) and increase the required cooling energy. Therefore, structured Low-E windows, also known as FSS [102, 113, 114], have become state-of-the-art.



Figure 6.14: Low-power mmWave bridge node prototype during measurements.

### 6.2.1 System Architecture for Low Power Consumption

To reduce the power consumption of the cellular corridor, we extend the ISD of the high-power macro sites. The average data capacity along the cellular antenna corridor is maintained with low-power repeater nodes (mmWave bridge service nodes) between the macro sites, as already shown in Fig. 6.2. We have conducted several measurements with our mmWave bridge prototype described in Chapter 4 and shown in Fig. 6.14 to calibrate the port-to-port attenuation, also considering the railway carriage penetration loss. Based on this attenuation model, the SNR can be computed, which is used for the data capacity estimation. By numerical evaluation, considering the high-power macro ISD and the number of intermediate low-power service nodes, the maximum ISD is determined with which a given average data capacity is supported. Finally, using a model for the power consumption of the high-power RRU and the low-power service node, the total power consumption is computed and normalized to a distance of 1 km.

#### 6.2.1.1 Railway Track Capacity Model with Bridge Nodes

When reducing the number of high-power macro sites while adding new low-power bridge nodes, the capacity of the system must be recalculated with a model to adjust the number of nodes to maintain the original cell capacity along the railway track. To this end, we adapt the basic model from the corridor measurements in Section 6.1 to a slightly more complex and comprehensive model.

The RSRP along the railway track at distance  $d$  is computed based on the high-power (HP) RRU with a maximum transmit power of 1500 W ERP and the low-power (LP) bridge node with a maximum transmit power of 6 W ERP. Note that the total signal power must be divided by the number of subcarriers to obtain the RSTP or RSRP. Here, we consider a 5G NR carrier of 100 MHz with 3300 subcarriers resulting in  $P_{\text{HPRSTP}} = 26.6$  dBm and  $P_{\text{LPRSTP}} = 2.6$  dBm. To obtain the RSRP for  $P_{\text{HP}}(d) = P_{\text{HPRSTP}}/L_{\text{HP}}(d)$  and  $P_{\text{LP},n}(d) = P_{\text{LPRSTP}}/L_{\text{LP},n}(d)$ , we introduce the port-to-port attenuation  $L_{\text{HP}}$  and  $L_{\text{LP}}$  based on Friis with a calibration factor of  $L_{\text{HP,calib}} = 33$  dB and  $L_{\text{LP,calib}} = 20$  dB to account for antenna dependent losses into railway carriages,

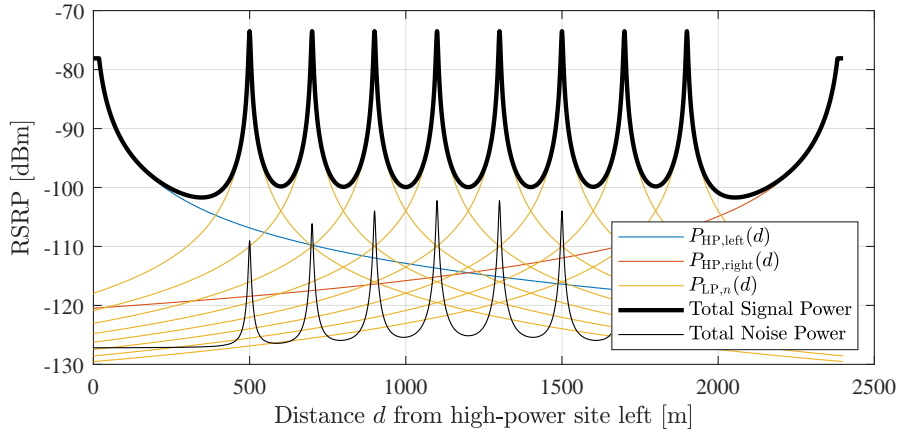


Figure 6.15: An example of the signal and noise power profiles for a maximum transmit power of 1500 W ERP for the high-power sites (left and right,  $d_{\text{ISD}} = 2400$  m) and 6 W ERP for the  $N = 8$  low-power mmWave bridge service nodes in between.

which are in line with the measurements in [103] and [9]:

$$L_a(d) = (d - d_a)^2 \left( \frac{4\pi}{\lambda} \right)^2 \cdot L_{\{\text{HP,LP}\}, \text{calib}} \quad \text{for } |d - d_a| \geq d_F. \quad (6.4)$$

The positions of the high-power sites and the  $N$  low-power bridge service nodes are denoted with  $d_a$ , where  $a \in \{\text{HP, left}, \text{HP, right}, \text{LP}, n | n = 1 \dots N\}$ ,  $\lambda$  represents the wavelength. The received signal power at position  $d$  from the high-power site on the left  $P_{\text{HP, left}}(d) = P_{\text{HP}}(d)$  and from the high-power site on the right  $P_{\text{HP, right}}(d) = P_{\text{HP}}(d_{\text{ISD}} - d)$ .  $d_{\text{ISD}}$  denotes the inter-site distance between two high-power sites, and the path loss is approximated as a constant for distances below the Fraunhofer distance  $d_F$ , analog to (6.1). For illustration, we repeat Fig. 6.12, but with a different exemplary configuration shown in Fig. 6.15. The power levels from the high-power sites are now shown with blue and orange lines. The received signal power from the  $n$ th low-power bridge service node at position  $d$  is denoted by  $P_{\text{LP}, n}(d)$ , and shown in Fig. 6.15 (yellow lines).

The SNR at position  $d$  along the railway track between two high-power sites is calculated according to

$$\text{SNR}(d) = \frac{P_{\text{HP, left}}(d) + P_{\text{HP, right}}(d) + \sum_{n=1}^N P_{\text{LP}, n}(d)}{N_{\text{RSRP}} \cdot \text{NF}_{\text{UE}} + \sum_{n=1}^N N_{\text{LP}, n}(d)}. \quad (6.5)$$

The thermal noise floor per subcarrier is obtained by  $N_{\text{RSRP}} = 10 \log_{10}(kTB) = -132$  dBm, with  $k = 1.38 \cdot 10^{-23}$  J/K denoting the Boltzman constant,  $T = 290$  K the temperature, and the bandwidth  $B = 15$  kHz. The total noise power consists of the thermal noise floor per subcarrier  $N_{\text{RSRP}}$  multiplied by the noise figure of a typical UE  $\text{NF}_{\text{UE}} = 5$  dB and the received noise power from all  $N$  low-power bridge service nodes  $N_{\text{LP}, n}(d)$ . The noise of a service node at distance  $d$  is obtained by  $N_{\text{LP}, n}(d) = N_{\text{RSRP}} \text{NF}_{\text{LP}} / L_{\text{LP}, n}(d)$ , where  $\text{NF}_{\text{LP}} = 8$  dB represents

the noise figure of the low-power bridge node. The numerator (total signal power) of (6.5) and the denominator (total noise power) are both also depicted in Fig. 6.15 with black lines. If a train travels along a cellular corridor, e.g., from left to right in Fig. 6.15, a UE inside that train would see the decreasing cell signal power from the high-power site at 0 m (blue line), which drops below  $-100$  dBm after around 250 m. In a conventional cellular corridor, the following high-power site would be located at 500 m and starts serving the user after 250 m with increasing power until 500 m. With the low-power bridge nodes added instead (yellow lines), the following high-power site can be moved to, e.g., 2400 m. Still, the signal power can be kept above  $-100$  dBm, and the UE experiences a peak for each low-power repeater node before the next serving high-power site dominates.

Finally, the data capacity along the railway track can be estimated based on the calculated SNR above. The equation in [95, Sec. A.2] is used to represent a calibrated model based on the Shannon bound, an attenuation factor  $\alpha = 0.6$ , and the maximum spectral efficiency of 5G NR  $\text{Thr}_{\text{MAX}} = 5.84$  bps/Hz.

### 6.2.1.2 Radio Unit Power Model

A power consumption model for cellular infrastructure equipment has been developed in the context of the EARTH project of the European Union 7th Framework Program. This parameterized model provides a simplified estimate of the average power consumption of cellular infrastructure equipment as a linear function of the data traffic load [115]. The power for BBU, RRU, and complete base stations, or various forms of small cells or repeaters can be approximated with the simplified equation (6.6), where  $P_{\text{in}}$  is the consumed power.

$$P_{\text{in}} = \begin{cases} P_0 + \Delta_p P_{\text{max}} \chi, & 0 < \chi \leq 1 \\ P_{\text{sleep}}, & \chi = 0 \end{cases} \quad (6.6)$$

The constant  $P_0$  represents the baseline power consumption from, e.g., power supply, oscillators, and cooling.  $\Delta_p$  denotes the slope of the load-dependent power consumption,  $\chi = [0, 1]$  denotes the load as a fraction of the maximum possible load, and  $P_{\text{max}}$  is the maximum RF output power. Finally,  $P_{\text{sleep}}$  represents the constant power consumption when the equipment is in sleep mode when no data traffic is present. The transition time between the active state and the sleep mode is assumed to be in the order of a few hundred milliseconds.

The energy consumption of cellular equipment can be calculated based on parameters from the literature [57, 60–63, 115, 116] modeled based on actual products. Thus, with the parameters in [115], also listed in Table 6.2, a high-power site with two RRUs consumes a power of 560 W under full traffic load for a mast with two sectors, 336 W under no load, and 224 W in sleep mode, also shown in Fig. 6.16.

The power consumption for the low-power bridge node is based on the sub-components used for our prototype hardware and listed in Table 6.1 for common, DL, and UL functions. A GNSS

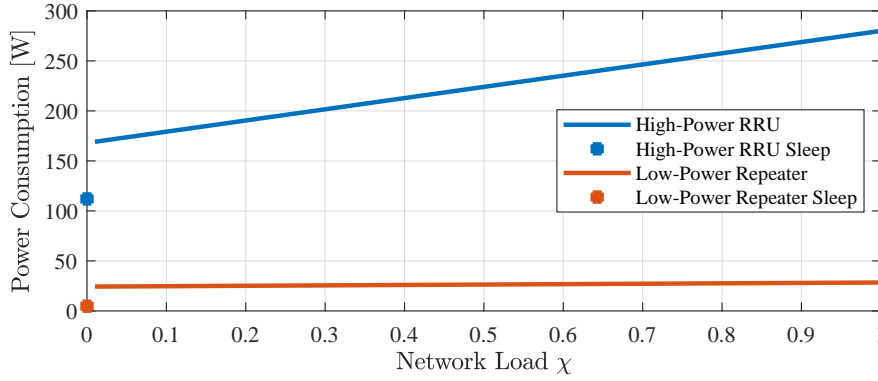


Figure 6.16: Network traffic load-dependent power consumption of a high-power RRU and a low-power bridge node based on (6.6) and the parameters in Table 6.2.

Table 6.1: Low-power mmWave bridge node power consumption.

Parameter	Common [W]	DL [W]	UL [W]	Sleep [W]
Controller	2	-	-	2
GNSS DOXO	2.22	-	-	2.22
Local Oscillator	5	-	-	0.5
Frequency Doubler	0.35	-	-	0
RF Switches	0.195	-	-	0
RX LNA	-	0.27	-	0
TX PA	-	5	-	0
RX LNA	-	-	0.462	0
Second RX LNA	-	-	0.335	0
TX PA	-	-	5	0
Number of Path	1	2	2	-
Total Power	28.38			4.72

DOXO is used to maintain a stable reference clock. On the RX side, LNAs and on the TX side, PAs are employed. For the operation under full data traffic load, the total power consumption amounts to 28.4 W. If there is no data traffic, the amplifiers consume less power. However, all sub-components would still be in operation, resulting in a power consumption of 24.3 W. Note that the power consumption of the low-power bridge node is based on a prototype, and even better savings may be obtained with a fully integrated product.

### 6.2.2 Energy Autonomous Bridge Nodes

While the low-power bridge nodes already consume only a fraction of a high-power RRU, the energy consumption can be further reduced by smartly switching on and off specific sub-components. Both the low-power controller and the GNSS disciplined oven-controlled crystal

Table 6.2: Power model parameters for the RRU and mmWave bridge node.

Node Type	$P_{\max}$ [W]	$P_0$ [W]	$\Delta_p$	$P_{\text{sleep}}$ [W]
High-Power RRU	40	168	2.8	112
Low-Power Bridge Node	1	24.26	4.0	4.72

oscillator (OCXO) operate continuously to control the mmWave bridge node and maintain a stable reference for the LO. The used LO offers a sleep mode that keeps locking onto the reference clock but has its output drivers shut off to enable low standby power with rapid on/off transitions. All other sub-components of the bridge node are not powered in this sleep mode. The resulting power consumption is also listed in the last column in Table 6.1, and the parameters for the model in (6.6) are listed in Table 6.2. In this application for a cellular corridor, the sleep mode will be the primary mode of operation. A passing train is detected using, e.g., a photoelectric barrier, and the bridge node will switch to full operation during that time duration.

### 6.2.2.1 Solar Power Model

With the intelligent sleep mode, the design and dimensioning of an off-grid PV powering system are straightforward. The solar radiation energy captured by a PV module installed at given angles can be calculated based on equations and models documented in the literature (e.g., [117]). Several models exist for the solar radiation available at a given geographical location, either based on local measurements or estimation methods. For our study, we use PVGIS [118] belonging to the latter. The accuracy of PVGIS has been validated in several papers [119–121] and delivers robust results. PVGIS is a free online tool (<https://ec.europa.eu/jrc/en/pvgis>) providing several calculations and databases. It can also be used to calculate the performance of an off-grid PV system as it would be used for a bridge node. Multiple statistics are calculated based on a solar radiation database, a geographical location, the peak power of the PV module and its azimuth and tilt angle, the battery capacity, and the expected daily energy consumption.

### 6.2.2.2 Geographical Setting

In our study, we consider the following examples: high-speed railway corridors in Madrid (Spain), Lyon (France), Vienna (Austria), Berlin (Germany), and the railway test track near Weesen (Switzerland) mentioned in Section 6.1. Standard PV modules with around 0.6 m width and 1.4 m height providing a peak power<sup>6</sup> of 180 W<sub>p</sub> are considered, which can be vertically installed on the existing catenary masts. Three modules easily fit vertically on regular masts with a height of 7 m to 9 m. The following parameters were used for PVGIS (version 5.1):

<sup>6</sup>The maximum output power of PV modules is expressed in Watt-peak (W<sub>p</sub>).

- Solar radiation database: PVGIS-COSMO
- Installed peak PV power: 540 W<sub>p</sub>
- Battery capacity: 720 Wh
- Discharge cutoff limit: 40 %
- Tilt/slope angle: 90°
- Azimuth angle: 0°

### 6.2.3 Numerical Results and Discussion

Before we can calculate the energy advantages of our solution, we first need to evaluate how much the ISD of high-power masts can be extended with how many low-power bridge nodes. Based on the path loss and capacity models in Section 6.2.1.1, the throughput can be calculated for every scenario (ISD in 50 m steps, number of low-power bridge nodes  $\{0, \dots, 10\}$ ). For each number of nodes, the maximum ISD for which an SNR > 29 dB (to guarantee the peak throughput of 5G NR) is registered. Each high-power RRU and antenna is assumed to transmit with 2500 W EIRP (64 dBm), while the low-power bridge nodes transmit with a maximum of 10 W EIRP (40 dBm). The resulting maximum ISDs for one to ten nodes are: {1250, 1450, 1600, 1800, 1950, 2100, 2250, 2400, 2500, 2650} m.

#### 6.2.3.1 Grid Powered Operation

We assume that high-power RRUs deployed for the specific use case of a cellular corridor along railway tracks employ power-saving functions when there is no data traffic. Specifically, the RRU is only operating with full data traffic load for the time that a train needs to pass the coverage section of the mast. The resulting average energy consumption is calculated according to Section 6.2.1.2 and shown in Fig. 6.17 for different cases. In the first case (“Continuous Operation”), we keep the low-power bridge nodes operating continuously while only the RRU is switched to sleep mode if there is no traffic on any of the associated bridge nodes. Given the parameters in Table 6.3, the RRUs are in full load operation on a 24-hour average for 2.85 % of the time at a 500 m high-power RRU ISD and 9.66 % at a 2650 m high-power RRU ISD. The use of at least three low-power bridge nodes extends the high-power ISD to a minimum of 1600 m. The resulting average energy consumption per hour and kilometer is reduced to below 50 % of a conventional deployment with only high-power RRUs (left/blue columns in Fig. 6.17). Note that an additional low-power donor node is considered for one service node, and two low-power donor nodes are considered for two or more service nodes (see Fig. 6.2).

Using the method described earlier to reduce further the low-power bridge node energy consumption, even more significant energy savings can be achieved. One low-power mmWave bridge node then only consumes an average power of 5.17 W (124.1 Wh per day). According to Fig. 6.17 (middle/orange columns), a single bridge node allows extending the high-power ISD to 1250 m which yields energy savings of 57 %. With ten low-power bridge nodes, an ISD of 2650 m is achieved, resulting in a 74 % energy reduction.

Table 6.3: Parameters for average energy consumption calculations.

Parameter	Value
Number of trains/h	8
Operation under full load per train	16 s - 55 s
Hours per night without passenger railway traffic	5 h
Length of a train	400 m
LP bridge node spacing	200 m
Velocity of a train	200 km/h
Power for HP RRU under full load	560 W
Power for HP RRU in sleep mode	224 W
Power for LP bridge node under full load	28.4 W
Power for LP bridge node no load	24.3 W
Power for LP bridge node in sleep mode	4.7 W

Table 6.4: PVGIS results at the four exemplary regions for one year.

Parameter	Madrid	Lyon	Vienna	Berlin	Weesen
Required peak PV power [Wp]	540	540	540	600	540
Required battery capacity [Wh]	720	720	1440	1440	720
Days with full battery [%]	98.13	95.15	93.73	88.0	95.94

### 6.2.3.2 Energy-Autonomous Bridge Operation

If the average power consumption is small enough (i.e., roughly a single-digit Watt number), off-grid powering by a battery-backed solar PV system is feasible. As described in Section 6.2.2.1, up to three standard PV modules can be mounted vertically on the railway catenary masts. The captured solar power is stored in a battery that supplies power to the low-power bridge nodes.

To evaluate the potential and stability of such an energy-autonomous setup, we assume the parameters in Table 6.3 and set the hourly energy consumption profile for PVGIS to 5 h per night continuously in sleep mode while the low-power bridge nodes operate in a mix of sleep mode and full load for the remaining 19 h per day. With PVGIS and the parameters listed in Section 6.2.2.2 for high-speed railway corridors in the four exemplary regions, the performance of the autonomous PV system can be analyzed in terms of the battery charging state, given the peak PV power of the modules. More specifically, PVGIS estimates the power production of the PV modules, the battery performance based on the charging and capacity state, and the probability of the battery charge state at the end of the day.

With the standard system dimensions listed in Section 6.2.2.2, the monthly solar radiation prediction data showed that the PV system in Vienna and Berlin might lead to insufficient energy capacity in winter. Therefore, the requirement of zero-day downtime dictates an

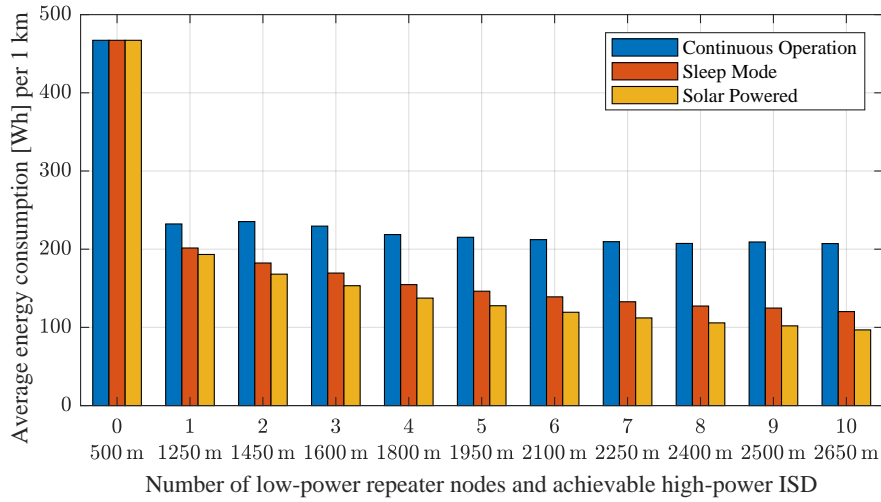


Figure 6.17: Average energy consumption normalized to 1 km for the conventional cellular corridor on the very left and 1 to 10 low-power bridge nodes placed in between high-power masts (always using energy-saving techniques) to extend their ISD while maintaining the peak throughput for users.

adaptation. By doubling the battery capacity in Vienna and Berlin, and slightly larger PV modules for Berlin, continuous operation even in winter can be achieved. As shown in Table 6.4, the other three locations function well with the default configuration.

If all low-power bridge nodes are solar-powered, the overall energy consumption from the grid is further reduced because only the high-power RRUs at extended ISDs remain grid powered. For example, with just one intermediate low-power bridge node, 59 % less energy is consumed, and with ten low-power bridge nodes between two high-power sites, 79 % less energy is consumed compared to the conventional deployment with only high-power RRUs (right/yellow column in Fig. 6.17).

### 6.3 Summary

A cellular antenna corridor is a solution to ensure a high SNR and bring a high data capacity into trains. Unfortunately, the installation of high-power macro sites in short intervals along the railway tracks is expensive. With our mmWave bridge nodes, multiple low-power service nodes can be installed between high-power macro sites. No additional interference is created with the other networks on sub-6 GHz frequencies. The increased power levels allow stretching the macro site distance intervals, thereby lowering the cost. Measurements on a commercial railway line demonstrate the feasibility and show even a median power increase of 10.5 dB for one service node with 14.6 dB less transmit power than the macro site. Calibrated path loss models were used to numerically evaluate several configurations and estimate the possible macro site distance increase.

Further to the cost reduction, we find that the use of low-power mmWave bridge nodes also has the potential to significantly improve the energy efficiency of a cellular corridor for railways. Because an RRU consumes several hundred Watts in power, we propose to reduce the number of RRUs with intermediate mmWave bridge nodes while maintaining the same data capacity. The local increase in cell signal power allows extending the high-power site distances, thus requiring fewer sites and lowering the overall energy consumption. Moreover, adding sleep modes to the low-power bridge nodes ultimately allows for energy-autonomous operation. With only the high-power RRUs grid-powered and with longer inter-site distances (mmWave bridges are PV-powered), an energy saving of 79 % can be achieved, and the overall system cost is further reduced (no need for grid power connections to the bridge nodes).



## 7 Beam Control for Layer-1 Repeaters

In Chapter 2, we saw that wireless networks in the mid-band spectrum (3–6 GHz) and certainly in the mmWave frequency range (above 24 GHz) do not adequately cover the inside of buildings and vehicles. Densifying the existing mobile network with additional sites takes time and is costly because of the site acquisition, obtaining the construction permissions, and the civil infrastructure construction itself. The mmWave bridge introduced in Chapter 3 is a solution that can also be deployed rapidly without construction work. For this chapter, we generalize the mmWave bridge regarding the carrier frequency to an amplify-and-forward (AF) repeater node. Such AF repeaters wirelessly fronthaul the cell signal and extend mobile data capacity into buildings or vehicles (land, sea, air) where the limited cell power otherwise does not provide a sufficiently high SNR. High-gain analog beamforming antennas are used to minimize the path loss between the base station and the repeater. Besides increasing the communication link signal power, the inter-cell interference (ICI) is reduced, which translates into an increased SINR and, thus, into higher network capacity. While AF repeaters operate on the physical layer, they are simple and RAT agnostic. However, the issue of this simplicity is that the necessary beam adjustment must be performed without information from and without coordination with the underlying RAT and without significant impact on throughput.

In this chapter, we address the issue of beam measurement and control for a wide range of transparent AF repeaters. First, the repeater setup with an analog beamforming antenna and the associated measurement and control mechanisms are explained in Section 7.1. Next, the cell search and establishment of an initial link are described in Section 7.2. Then, we explain how to measure new beams with minimal distortion of the communication and quantify the impact on the achievable data throughput with measurements using a 4G/5G prototype in Section 7.3. Finally, Section 7.4 describes the beam management used for tracking a remote node and evaluates several beam subset selection and beam tracking methods.

The real-world beamforming antenna data used in this chapter was obtained from the measurement campaigns described in Section 2.1 and is made publicly available under: <https://c4science.ch/source/bfmeasdata3500mhz/>.

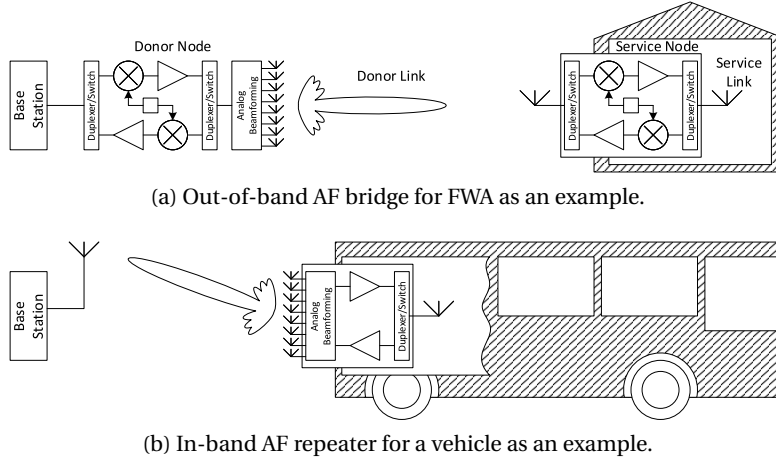


Figure 7.1: System block diagrams embedded in two example use cases.

## 7.1 System Overview

An important advantage of AF repeaters is the transparency towards the conveyed RAT signals. Although our focus is on 4G and 5G mobile networks, other RATs may also be used. We consider two variants, in- and out-of-band repeater operation, for which use cases are described in the following to provide a cellular signal to an area with poor to no coverage.

### 7.1.1 Out-of-Band Repeater

The first use case is a typical FWA scenario, similar to what has been presented in Chapter 3. An out-of-band AF repeater/bridge consists of a donor node and a service node, as shown by the high-level block diagram in Fig. 7.1a. The bridge donor node is installed at the base station and mixes the DL signal to a given donor link carrier frequency for the wireless fronthaul to the bridge service node. There, the DL signal is mixed down to the original cell carrier frequency, amplified, and retransmitted as the service signal. The UL signal is treated similarly in the reverse direction. Such an out-of-band AF repeater has the advantage that it does not require a high RF isolation between the donor-facing antenna and the service antenna. In contrast to the bridge proposed in Chapter 3 that operates at mmWave frequencies, we do not specify the donor link frequency and generalize the AF repeater bridge to use any available frequency.

### 7.1.2 In-Band Repeater

The second use case is an in-band AF repeater, as shown in Fig. 7.1b. Such systems can be installed on moving vehicles like buses, trains, and boats. Due to the high RF entry loss of the vehicle hull, the RF isolation between the outside donor link antenna and the inside service link antenna is sufficiently high, and an in-band repeater (without the frequency mixing components) can be employed.

### 7.1.3 Beamforming Antenna and Control

In line with the signal transparency, the beamforming antennas are fully analog regarding the RF signals, but digital control circuits are used for switching the active serving beam. Furthermore, we consider the beamforming antenna as a module either installed on the base station side (donor node) for the out-of-band repeater bridge use case or on the in-band repeater, e.g., installed on a moving vehicle. In any case, an initial link needs to be established after a power-on or loss of communication link. Beams must then be continuously scanned during operation to determine if another beam provides a higher signal power. In the out-of-band repeater bridge use case, the bridge service node intermittently transmits a pilot signal synchronized with the beam scanning interval on the bridge donor node to allow beam power measurements. For the beamforming antenna that is installed with the in-band repeater on the mobile side, the DL cell broadcast signals of the RAT, which are periodically sent in many RATs (e.g., during  $143 \mu\text{s}$  every 20 ms for 5G [39]), can be used to measure the beam power.

## 7.2 Cell-Search and Initial Access Link

After powering up a bridge or repeater, the location of the bridge service node or the repeater is unknown. A bridge service node starts transmitting a pilot signal to allow the bridge donor node to identify its counterpart by scanning the beams. The donor node beam scanning can be done exhaustively or optimized with prior information. Because a repeater node is used in a more mobile scenario than the bridge, and its orientation may continuously change, an exhaustive systematic scan of all beams may be the default strategy. After successfully identifying a bridge service node pilot or cell broadcast signal, the initial access procedure is completed, and a beam tracking procedure is entered.

### 7.2.1 Systematic Scan

The repeater or bridge donor node continuously scans all available beams until a pilot signal can be received. The exhaustive scanning of  $M$  beams with each single beam measurement taking  $T_{\text{bm}}$  seconds allows for a beam scan cycle period of  $MT_{\text{bm}}$  seconds. However, if, for example, the periodically transmitted broadcast signal of a 5G cell is used for the beam power measurement, the beam scanning period has to match the cell broadcast signal interval of, e.g.,  $T_{\text{BC,int}} = 20 \text{ ms}$ , thus extending the beam scan cycle period to  $MT_{\text{BC,int}}$ , if one beam power measurement is performed on each broadcast signal. Hence, for beamforming antennas with many beams (the mmWave beamforming antenna used in the bridge prototype described in Chapter 4 features over 1300 beams), a strategy is needed to reduce the number of beam scans to a subset of all available beams.

### 7.2.2 Scan with Prior Information

In many real-world scenarios, the locations where users need the data capacity (i.e., the location of bridge service nodes or repeaters) relative to the donor node or base station are not uniformly distributed. Therefore, it is possible to consider these locations to determine which beams (i.e., beam angles) are necessary to cover the relevant area and thus, reduce the number of required beams for scanning. Location data can be obtained in several ways: based on maps or derived from vehicular traffic density maps or measurements. However, to use the location data for selecting beams, the obtained three-dimensional location data first needs to be transformed into the two-dimensional beam-angle space, taking into account the installation orientation of the beamforming antenna. The equations for the coordinate transformation of GPS location data into beam azimuth  $\phi_{\text{user}}$  and elevation  $\theta_{\text{user}}$  angles are given in the Appendix A.1.2.

With only a reduced set of beams, we want to carefully select the beams under consideration to minimize the probability of missing a service node. To this end, location data is transformed and used to derive a discretized location PDF in azimuth angles  $\phi_j$  and elevation angles  $\theta_k$  (see Fig. 7.2):

$$\mathbf{P}_{\text{user}}(\phi_j, \theta_k) = f(\phi_{\text{user}}, \theta_{\text{user}}). \quad (7.1)$$

Furthermore, the beam pattern of the beamforming antenna is required in the form of an antenna gain matrix  $\mathbf{G}(i, \phi_j, \theta_k)$  with elements  $G_{ijk}$  [dBi], where  $i = 1 \dots M$  is the active beam index and  $\phi_j = \phi_{\min} \dots \phi_{\max}$  and  $\theta_k = \theta_{\min} \dots \theta_{\max}$  are the discrete azimuth and elevation angle ranges of the antenna pattern, respectively. We further define  $G_{\min}$  as a minimum antenna gain required to establish a communication link of sufficient quality.  $M$  denotes the number of available beams of the antenna, and  $K \leq M$  is the number of selected beams to scan. Accordingly, the following sets are defined:

- $\mathbf{B}_M$  is the set of all available beams,  $|\mathbf{B}_M| = M$
- $\mathbf{B}_K \subseteq \mathbf{B}_M$  is a subset of  $K$  selected beams from all  $M$  possible beams, where  $\mathbf{B}_K = \{j : j \in \mathbb{N}, 1 < j \leq M\}$  and  $|\mathbf{B}_K| = K$

Next, the gain matrix is converted to a mask with the help of an indicator function:

$$\begin{aligned} \tilde{\mathbf{G}}(i, \phi_j, \theta_k) &= \mathbf{1}_{[G_{ijk} < G_{\min}]} \\ &= \begin{cases} 1, & \text{if } \mathbf{G}(i, \phi_j, \theta_k) < G_{\min} \\ 0, & \text{otherwise.} \end{cases} \end{aligned} \quad (7.2)$$

Then, the probability of missing a node, given the chosen beam subset  $\mathbf{B}_K$ , the discrete antenna gain mask matrix  $\tilde{\mathbf{G}}$ , and a discrete user or node location PDF  $\mathbf{P}_{\text{user}}$ , is given by:

$$P_{\text{miss}}(\mathbf{B}_K, \tilde{\mathbf{G}}, \mathbf{P}_{\text{user}}) = \sum_{\theta_k} \sum_{\phi_j} f(\phi_j, \theta_k) \prod_{i \in \mathbf{B}_K} \tilde{\mathbf{G}}(i, \phi_j, \theta_k). \quad (7.3)$$

Finally, with

$$\mathbf{B}_K = \underset{\mathbf{B}_K \subseteq \mathbf{B}_M}{\operatorname{argmin}} P_{\text{miss}}(\mathbf{B}_K, \bar{\mathbf{G}}, \mathbf{P}_{\text{user}}) \quad (7.4)$$

we minimize the probability of missing a node when scanning a set of  $K$  out of  $M$  beams. In the next section, we show how (7.4) is solved in practice.

### 7.2.3 Results Using Outdoor Measurements

For the numerical evaluation, we use measurements from multiple campaigns in three exemplary scenarios; further details are provided in Section 2.1.3. Measurement samples close to the base station have been filtered out because of artifacts from beam sidelobes. The location and orientation of the base station antenna and the measurement positions are transformed with (A.1)-(A.7) to obtain the beam azimuth and elevation angles for each measurement sample. A two-dimensional histogram is created and normalized to the sum over both axes, which results in the discrete node location PDF in (7.1); see Fig. 7.2 for visualization. The representation of such location data in the beam-angle space also allows to easily identify which beams are necessary and which ones may not be needed.

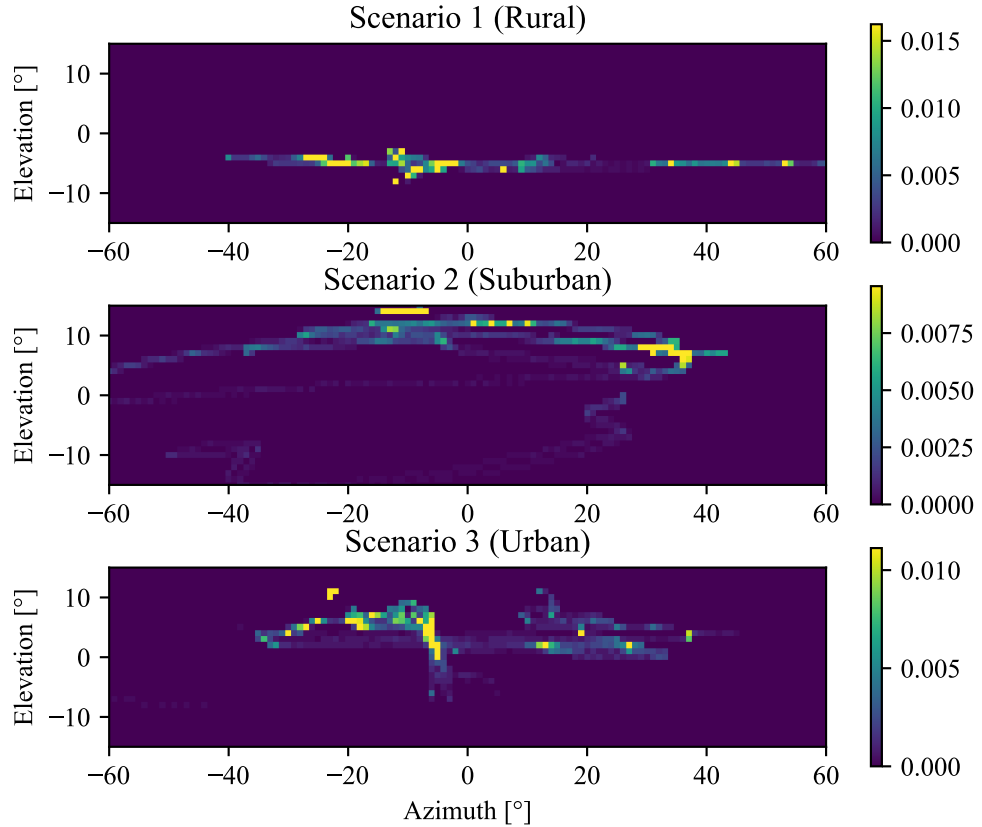
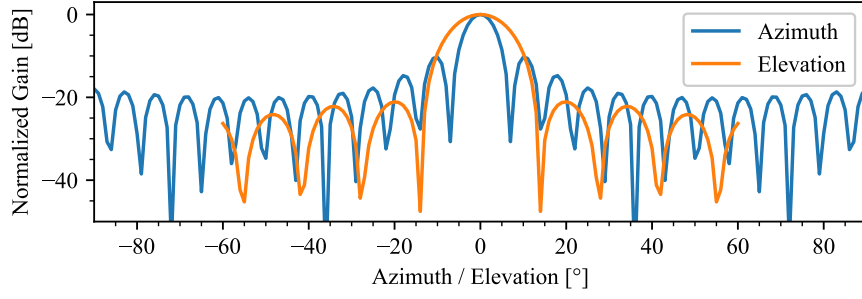
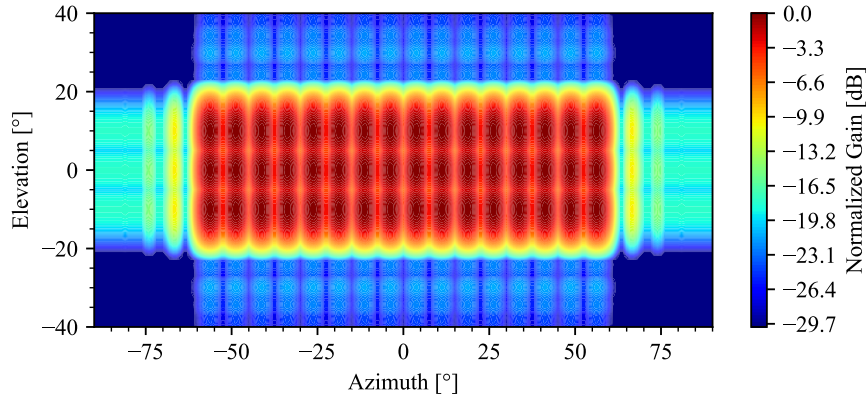


Figure 7.2: The location probability distribution for three measurement locations.



(a) Generic azimuth and elevation pattern of a single beam.



(b) Combined envelope pattern of a grid-of-beams antenna.

Figure 7.3: Synthesized combined envelope beam pattern of a grid-of-beams antenna used in the numerical evaluation.

Table 7.1: The probability of missing a node depending on the number of beams ( $K$ ) to scan.

$K$	Scenario 1	Scenario 2	Scenario 3
5	0.0913	0.0534	0.0479
6	0.0672	0.0294	0.0292
7	0.0524	0.0171	0.0165
8	0.0391	0.0102	0.0098
9	0.0264	0.0052	0.0051
10	0.0152	0.0006	0.0016
11	0.0089	0.0000	0.0006
12	0.0063	-	0.0000
13	0.0038	-	-
14	0.0019	-	-
15	0.0013	-	-
16	0.0006	-	-
17	0.0002	-	-
18	0.0000	-	-

With a generic beam pattern with a horizontal HPBW of  $6^\circ$  and a vertical HPBW of  $12^\circ$ , a grid-of-beams antenna with 16 azimuth angles and three elevation angles (total of 48 beams) is emulated, as shown in Fig. 7.3b.

To solve (7.4), we used Python with the multi-objective optimization module pymoo [122]. The optimization has been run for an increasing number of  $K \geq 5$  beams to find the set  $\mathbf{B}_K$  of beams that minimizes  $P_{\text{miss}}$  according to (7.4). The results are listed in Table 7.1 and show that the rural scenario requires the most beams to cover the area with a low risk of missing any node (18 versus 11 and 12 for suburban and urban, respectively). If, for example, a 0.1 % probability of missing a node is tolerated, 16, 10, and 11 beams of the 48 available beams are required for the rural, suburban, and urban environments, respectively.

### 7.3 Beam Measurement Process and Impact

Due to the transparent operation, the repeater or bridge nodes cannot access and control RAT-specific in-band signaling and beam reference signals. Nonetheless, the bridge donor nodes still need to probe various beams to find one providing a higher received power than the current serving beam. Because the repeater bridge provides a cellular signal to places with poor to no capacity, a minor degradation in capacity can be sacrificed for beam tracking and optimization if the provided capacity is still significantly higher than without a repeater. For the intermittent beam scanning, a subset of all possible beams is probed, and the measured received power for each beam is registered. The serving beam may subsequently be adjusted based on the updated beam measurements.

#### 7.3.1 3GPP Link Failure Protocol Mechanism

The intermittent beam measurements cause impairments in the RF signal (e.g., signal outage or transients in phase and magnitude) and may corrupt data transmitted in the DL or UL. While momentary impairments may be similar to natural variations in the physical layer signal, the higher radio resource control (RRC) layer may also notice a degradation in the communication link. Such events then have a more significant impact. The 4G and 5G standards define the following process for the UE [123]: if the DL control channel cannot be successfully decoded during a 200 ms interval, an out-of-sync indication is triggered, see Fig. 7.4. The parameter N310 defines the number of consecutive out-of-sync events after which a timer (T310) starts. If the timer elapses according to the configured duration, the UE triggers a radio link failure (RLF) and terminates the link by moving to the state RRC\_IDLE or initiates an RRC connection reestablishment/reconfiguration. Successful decoding of the DL control channel block during a 100 ms interval results in an in-sync indication. If the UE counts N311 consecutive in-sync indications before the timer T310 has elapsed, the timer is stopped, and no action is taken. Additionally, the base station can request DL measurements from the UE with the RRC reconfiguration message, e.g., in case (too many) irregularities are detected on the communication link.

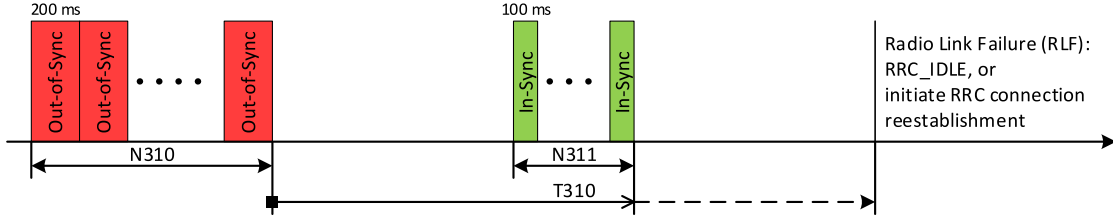


Figure 7.4: RRC events and timers for 4G and 5G.

### 7.3.2 Beam Measurement Impact Results

It is evident that the beam measurements shall not cause a radio link failure, nor should they cause the base station to trigger RRC reconfiguration messages. Extensive lab measurements have been performed to test the impact of the beam measurements on the communication link. The bridge donor node was connected to a commercial radio unit providing a standard 4G cell. The parameters N310, N311, and T310 were set to 20, 1, and 2000 ms, respectively. The bridge service node was installed across the room and was connected to an RF shielded box with antennas inside to provide the service cell signal to a commercial smartphone. Full buffer DL data traffic was generated with an application (iPerf3) on the smartphone. Physical link parameters, the medium access control (MAC) data throughput, and RRC messages were logged with monitoring software on a laptop computer connected to the smartphone. Two scenarios were measured:

**Beam Switching:** the donor node beam is periodically reconfigured to other beams for a given duration resulting in 10 dB more path loss between the donor and service node.

**Beam Blanking:** the donor node beam is periodically reconfigured to a heavily misaligned beam that leads to a complete signal outage for a given duration.

To analyze the impact of beam measurements on the resulting MAC throughput, we define the *beam measurement ratio*

$$\eta = \frac{nT_{\text{bm}}}{T_{\text{int}}} \quad (7.5)$$

as the beam measurement *duration*  $nT_{\text{bm}}$  (time duration while  $n$  beams are sequentially measured, each taking  $T_{\text{bm}}$  seconds) over the beam measurement *interval*  $T_{\text{int}}$  (time interval when beam measurements are triggered). The maximum achievable throughput over an ideal channel (considering the minimum outage required for scanning) is denoted with  $\text{Tput}_{\text{max}}$ . The ratio  $\eta$  also defines the minimum throughput reduction  $\text{Tput}_{\text{loss}} = \eta \text{Tput}_{\text{max}}$  because the transients occurring in the RF signal during the beam measurements may render the DL or UL signals erroneous. The number of beams that can be scanned per second is obtained by:

$$N_{\text{b}} = \frac{n}{T_{\text{int}}} = \frac{\eta}{T_{\text{bm}}} \quad (7.6)$$

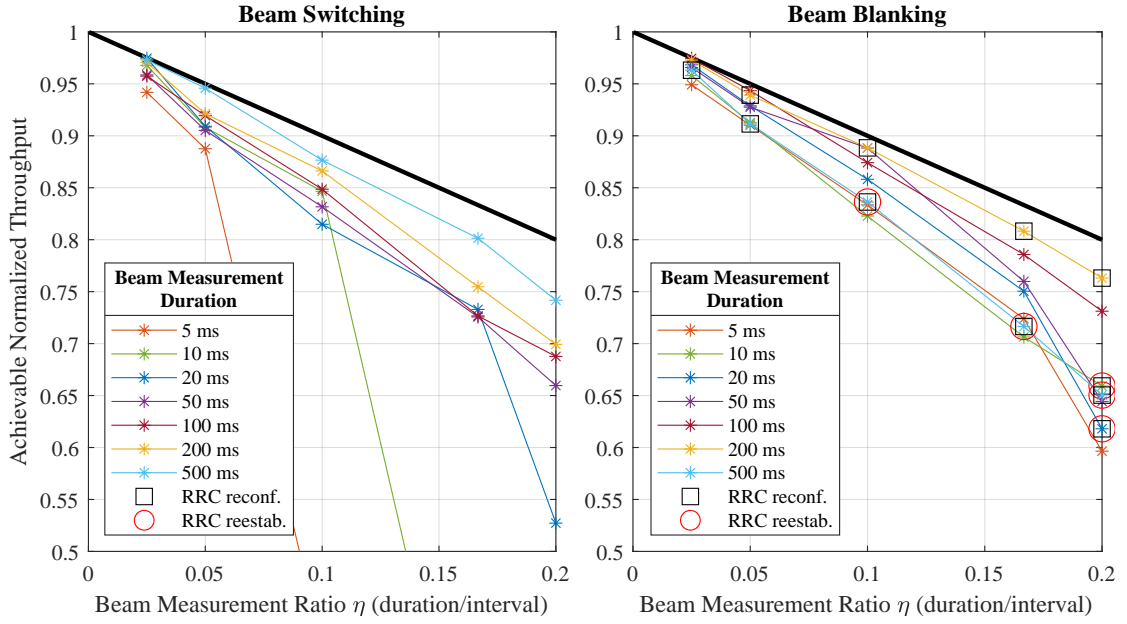


Figure 7.5: Resulting normalized throughput and RRC events for link interruptions with different durations and intervals when switching to a beam providing 10 dB less signal power (left) and switching to a beam leading to a signal outage (right).

Assuming a beam measurement period of  $T_{bm} = 100 \mu s$ , the five beam measurement ratios in Fig. 7.5 allow for  $n = \{250, 500, 1000, 1666, 2000\}$  beam measurements per second.

Note that the intervals for the measurements were slightly offset by 0.2 ms to prevent a perfect alignment with the subframe timing of the cell signal and to obtain a steady drift to ensure that all parts of a radio frame are impacted. Each configuration set was logged for 4 minutes, and the results are shown in Fig. 7.5. The solid black lines indicate the ideal minimum throughput reduction  $T_{put,loss}$ . For the beam switching scenario, neither the UE nor the base station noticed a significant impact that required the RRC to act. However, in the beam blanking scenario (right plot in Fig. 7.5), the base station triggered UE-side measurements with RRC reconfiguration messages for the beam measurement durations of 200 ms and 500 ms (box markers). The UE even triggered RRC connection reestablishment processes for 14 %, 12.5 %, and 4 % of the actions with a beam measurement duration of 500 ms and a beam measurement interval of 5 s, 3 s, and 2.5 s, respectively.

From Fig. 7.5, we note that a beam measurement duration of up to 100 ms and a beam measurement ratio  $\eta < 0.2$  is beneficial because no RRC messages are triggered. To interpret the results, we show the beam switching measurements in Fig. 7.6 as colored dot markers. The color corresponds to the fractional throughput reduction, which cannot be smaller than the beam measurement ratio shown with the background color gradient and the contour lines. Clearly, the shorter the beam measurement duration, the fewer beams can be scanned, and the smaller the impact on the data throughput reduction. Similarly, the less frequent beams

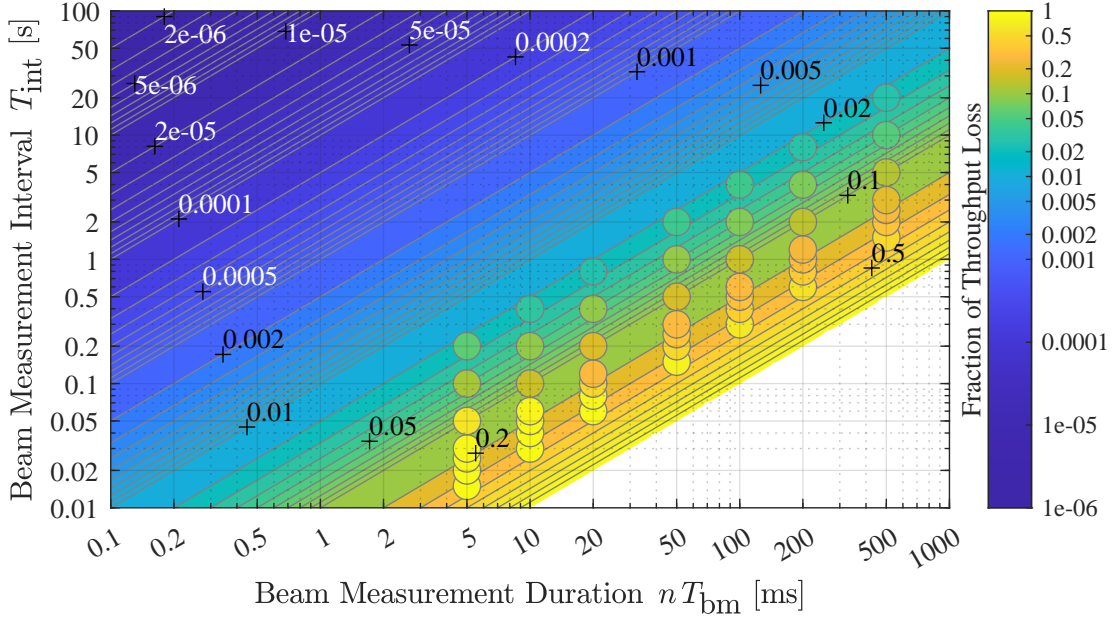


Figure 7.6: The background color represents the minimal theoretical throughput reduction (fraction) with respect to the beam measurement duration and beam measurement interval. Colored dots show the measured throughput reduction.

are measured (longer beam measurement interval), the smaller the impact on the throughput. Depending on the optimization criteria, Fig. 7.6 can be used to find the best configuration, given requirements on either the tolerable throughput loss, the number of beams, or the beam measurement interval (update rate).

## 7.4 Beam Management and Tracking

Because the beam scanning interval and the number of beams to scan have an adverse effect on the link capacity, the number of beams to be scanned must be kept low and wisely selected. We evaluated several options for selecting a beam subset  $\mathbf{B}_K$  that is scanned and used for adjusting the serving beam. Without any strategy, choosing  $K$  out of  $M$  beams results in  $\binom{M}{K}$  possible combinations that quickly grow to large numbers, especially with dozens or hundreds of beams. The process of selecting  $K$  out of  $M$  beams and measuring the respective signal powers can be formulated as a single-state Markov decision process (MDP) for which the multi-armed bandit (MAB) approach with non-stationary rewards is employed. More generally, the process of measuring and selecting the beams is formulated in Algorithm 1.

### 7.4.1 Algorithm Choices for Beam Tracking

The computational complexity for beam tracking has to be kept small because the computing resources in a bridge or repeater node are limited due to the size, weight, power consumption,

---

**Algorithm 1** Beam measurement and selection

---

```

1: define the  $\mathbf{B}_K$  beams for initial access
2: loop
3:   measure beams in  $\mathbf{B}_K$ 
4:   RUNSELECTIONALGORITHM(...)
      evaluate beam measurement result (rewards)
      define next  $\mathbf{B}_K$  beams to be measured
5:   update main beam for communication link based on reward
6: end loop

```

---

and cost (SWaP-C). Out of a large variety of MAB algorithms, we describe and compare the two that performed best against randomly selecting beams and the nearest neighbor selection. The following algorithms are called in line 4 in Algorithm 1 of our simulation.

#### 7.4.1.1 Random Beam Selection

The best beam and  $K - 1$  random beams are used for each beam measurement iteration (line 4 in Algorithm 1). Then, the measured beam with the maximum signal power is selected as the serving beam until the next iteration (line 5 in Algorithm 1). The computational complexity for the random selection is low and scales with the number of beams:  $\mathcal{O}(K)$ .

#### 7.4.1.2 Nearest Neighbor Selection

As a baseline and simple form for tracking, the serving beam and  $K - 1$  neighboring beams with the smallest angular separation to the currently used beam are selected and measured at each iteration on line 4 in Algorithm 1. Based on the measurements, the serving beam is adjusted to the one providing the maximum signal power. Such a table lookup has a very low computational complexity:  $\mathcal{O}(1)$ .

#### 7.4.1.3 Simple Multi-Armed Bandit

The simplest form of an  $\epsilon$ -greedy MAB is described in [124, Chapter 2.5], where  $\epsilon$  is the exploration probability. Our adaptation of the algorithm to the beam selection is listed in Algorithm 2. For each beam measurement iteration  $n$ , the rewards are used to update the action estimate according to  $Q_{n+1} \doteq Q_n + \alpha [R_n - Q_n]$ , where  $\alpha$  is the constant step-size parameter. The  $\lfloor (1 - \epsilon)K \rfloor$  most significant values in  $Q_n(i)$  determine the exploitation beams, and  $\lfloor \epsilon K \rfloor$  exploration beams are randomly picked from the remaining available beams. After the measurements,  $\arg\max_i Q_{n+1}(i)$  provides the beam with index  $i$ , selected as the new serving beam. The computational complexity is  $\mathcal{O}(K \log K)$  [125].

---

### Algorithm 2 Simple multi-armed bandit

---

```

1: function SIMPLEMAB( $R, Q, \alpha, \epsilon, K, \mathbf{B}_K$ )           ▷ meas. result stored as reward in  $R$ 
2:    $Q \leftarrow Q + \alpha [R - Q]$                        ▷ update action-value estimate
3:    $\mathbf{B}_K \leftarrow \{ \lfloor (1 - \epsilon)K \rfloor \text{ indices } i \text{ of largest values from } Q, \quad \triangleright \text{compose new set of beams}$ 
       $\lfloor \epsilon K \rfloor \text{ random indices } i \text{ from remaining set } \}$ 
4:   define main beam index  $i$  from  $\arg\max_i Q(i)$ 
5: end function

```

---

#### 7.4.1.4 Contextual Bandit with Nearest Neighbor Selection

This beam selection algorithm is similar to the simple MAB in Algorithm 2, but with an adaptation to the exploitation. The best serving beam is often gradually changing to neighboring beams in outdoor scenarios. Therefore, for each beam, we can define a list of neighboring beams with increasing angular distances. Then, at each beam measurement iteration, the  $\lfloor (1 - \epsilon)K \rfloor$  closest beams to the current serving beam are selected for exploitation (line 3 in Algorithm 3), and  $\lfloor \epsilon K \rfloor$  beams are randomly picked from the remaining available beams for exploration. After the measurements, again,  $\arg\max_i Q_{n+1}(i)$  defines the beam index  $i$  as the new serving beam. This algorithm has the same computational complexity as the simple MAB.

---

### Algorithm 3 Contextual multi-armed bandit

---

```

1: function CONTEXTUALMAB( $R, Q, \alpha, \epsilon, K, \mathbf{B}_K$ )           ▷ meas. result stored as reward in  $R$ 
2:    $Q \leftarrow Q + \alpha [R - Q]$                        ▷ update action-value estimate
3:    $\mathbf{B}_K \leftarrow \{ \lfloor (1 - \epsilon)K \rfloor \text{ indices } i \text{ of beams closest to beam } \arg\max_i Q(i),$ 
       $\lfloor \epsilon K \rfloor \text{ random indices } i \text{ from remaining set } \}$ 
4:   define main beam index  $i$  from  $\arg\max_i Q(i)$ 
5: end function

```

---

#### 7.4.2 Performance Evaluation with Measurements

For the performance evaluation of the adaptive beam subset selection, the measurement data from the beamforming testbed and measurement campaigns described in Section 2.1.3 are again used. These measurement datasets provide RSRP values for all beams and various UE locations at three base station sites. Samples were taken continuously during drive tests and are therefore correlated over time. Note that some beam tracking algorithms considered here exploit the correlation between subsequent samples (locations) in time. The constant step-size parameter  $\alpha$  and the greedy exploration parameter  $\epsilon$  have been selected to provide the best results for both MAB algorithms. The parameter  $\alpha$  has been set to 0.999 to weigh the newest reward strongly without completely neglecting older rewards. Similarly, with an  $\epsilon = 0.5$ , half of the  $K$  beams are used for exploration. The beam selection algorithms are run on all samples for all datasets 100 times to average out the random selection.  $K$  beams are checked for each sample, and the beam index for the beam providing the highest power is registered. By comparing the maximum possible beam power with the highest measured beam power, a beam power adjustment error (BPAE) is obtained. For example, the BPAEs for one run with  $K = 18$  over all dataset samples are shown in Fig. 7.7.

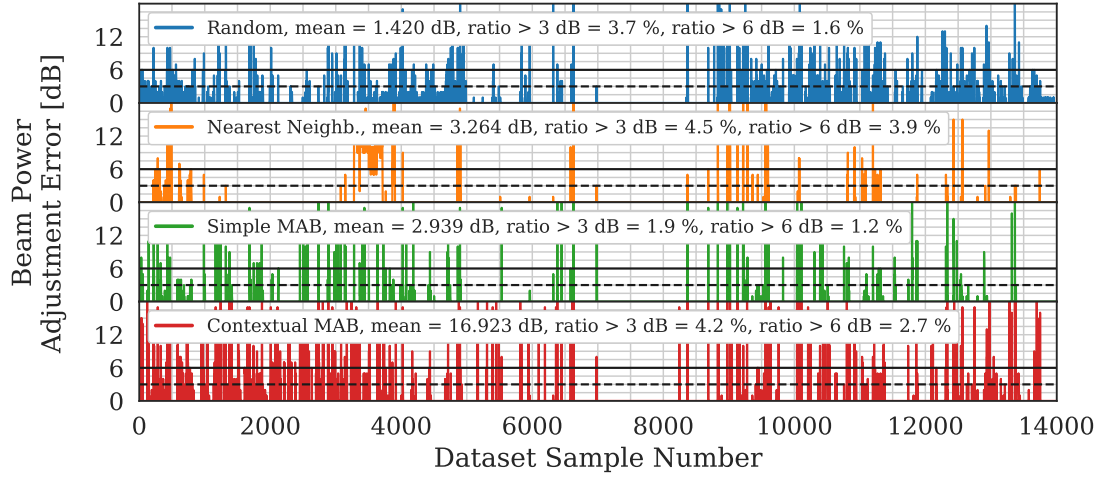


Figure 7.7: Beam power adjustment error for the evaluated algorithms.

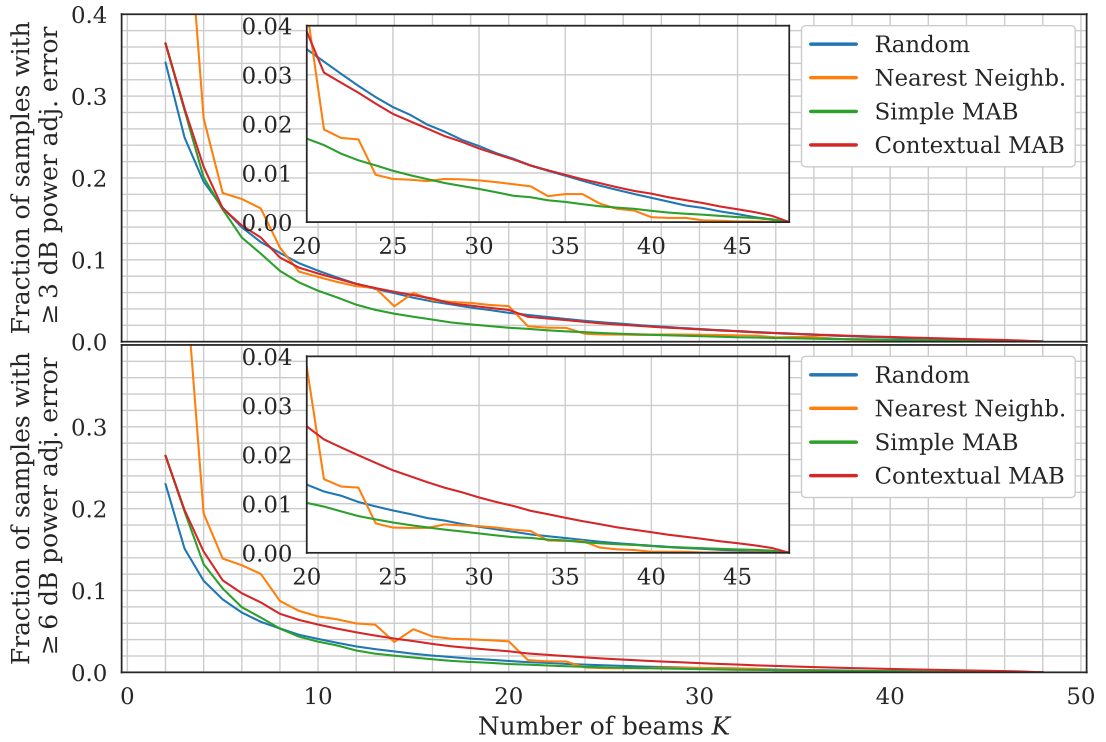


Figure 7.8: Fraction of samples exceeding a certain beam power adjustment error versus the number of scanned beams per measurement sample for different models.

A small BPAE of a few dB can often be tolerated if the RF link budget is not at its limits. Also, a few occasional larger BPAEs can be tolerated by the RAT. However, if the beam management is not converging rapidly to the best beam, many samples have a BPAE. Therefore, the evaluation criteria for the algorithm performance is the fraction of samples that exceed a given BPAE threshold that is chosen based on application requirements. In Fig. 7.8, the average of 50 runs is shown. Undoubtedly, the more measured beams (the higher  $K$ ), the smaller the errors, and the fewer samples exceed the threshold. The highest beam power can always be found with all  $K = M = 48$  beams scanned, resulting in zero error. While the random selection often results in a BPAE  $> 0$  (see Fig. 7.7), its average BPAE can be smaller compared to the other algorithms, especially for  $K < 5$ . For a higher number up to around 36 beams, the simple MAB outperforms all other schemes. The contextual MAB only has an advantage over the nearest neighbor algorithm and only up to  $K = 20$ . Beyond that, its performance is similar to or even worse than the random selection. MABs build up an estimate of the action values for each beam that helps in tracking and quicker converging to the best beam. The nearest neighbor algorithm converges slower because it does not track any state. For more than 20 beams, the simple MAB performs somewhat similarly to the nearest neighbor algorithm in line with Table 7.1, where we saw that all dataset sample locations could be covered with only 18 beams. Therefore, if the correct 18 beams are selected, convergence to the best beam is possible. If we tolerate a BPAE of  $\geq 6$  dB for, e.g., 1 % of the samples, 20 beams are required for scanning. By consulting Fig. 7.6 and assuming that the beam measurement period is 1 ms and 2 % throughput loss is tolerated, we note that a complete beam scan can be done every 1 s (20 beam measurements per second).

### 7.5 Summary

Amplify-and-forward repeaters are a simple solution to provide mobile network data capacity to areas with limited or no network coverage. Thanks to the shorter wavelength at higher frequencies ( $> 3$  GHz), beamforming antennas with many antenna elements can be constructed with practical sizes. RAT transparent repeaters also benefit from the higher directivity and gain of analog beamforming antennas. However, with dozens or even hundreds of possible beams, it is impractical, and in the case of a moving user device, impossible to measure all beams to determine the best serving beam. Therefore, a method for optimizing the number of beams to scan based on prior location information is presented and validated with measurements for the initial access. Furthermore, we have presented a method to perform intermittent beam measurements during active communication without having access to in-band beam control. The impact on the achievable data throughput has been measured for the example of a 4G LTE link, and it has been found that intermittent beam measurements are possible without coordination with the RAT and without significant throughput degradation. Finally, several algorithms for beam tracking based on a reduced subset have been evaluated using measurement datasets. To conclude, the presented methods allow a transparent amplify-and-forward repeater with analog beamforming antennas to operate also in a dynamic environment with changing locations.

## 8 Conclusion and Outlook

The topic of this thesis is the question of how the data capacity potential of cellular networks such as 4G and 5G can be brought into buildings or other shielded structures such as trains. Mobile network operators (MNOs) deploy their cellular networks primarily outdoors to cover as large areas as the regulatory defined transmit power allows. However, a significant ratio of the mobile network traffic is consumed or originates indoors, but also while commuting or traveling by train. Moreover, the increase in buildings and modern railway carriages equipped with thermally insulating coated windows, which also strongly attenuate cellular signals, is detrimental to the mobile network capacity. While the continued densification of cell sites is necessary to address these and other issues, it is also costly and takes time. To this end, fiber optical links to buildings allow for high broadband Internet speeds and the installation of indoor cellular equipment. Nevertheless, there are still buildings and places where fiber deployment is not feasible for economic reasons, unduly effort (e.g., temporary installations), or simply impossible due to the geology (e.g., mountainous terrain) or the use case scenario of vehicles and railways. An established solution to provide a higher data capacity for railways is a cellular antenna corridor along the railway tracks with many high-power macro sites with short inter-site distances (ISDs), e.g., every 500 m to 1000 m.

We have started the work by analyzing the coverage and capacity of 5G in the mid-band spectrum (3.6 GHz) with a pre-commercial 5G testbed that was lent to us. Extensive measurement campaigns conducted in rural, suburban, and urban environments are described in Chapter 2. We analyzed the results and compared the measured path losses with empirical path loss models used in the industry. We found that the models generally overpredict the path loss and that the group of models from the 3rd Generation Partnership Project (3GPP), on average, have the lowest prediction error (rural 14.9 dB, suburban 3.8 dB, urban 2.1 dB). Under the same regulatory effective radiated power limitations also used for previous mobile network generations, the higher carrier frequencies and wider bandwidths of 5G cells in the mid-band spectrum cause a lower power density on the receiver side. For example, a 100 MHz cell at 3.6 GHz results in a 10.4 dB lower reference signal received power (RSRP) compared to a 20 MHz cell at 1.8 GHz with the same total transmit power. In addition, the high building entry

loss (BEL) of modern buildings results in a meager signal-to-noise ratio (SNR) and, thus, a low cellular capacity and inefficient use of cellular resources.

Consequently, we have analyzed state-of-the-art solutions to increase the cellular capacity inside buildings or underserved areas, for example, along railway tracks. If a fiber backhaul is unavailable or too costly to deploy, layer-1 repeater or layer-2/-3 relays are employed. However, these solutions rely on the outdoor cellular network and diminish the available outdoor capacity. In the case of a cellular corridor along railway tracks, layer-2/-3 relays cannot be used to reduce the number of required macro cell sites because of the inherent delay in the cell signal. Moreover, in-band repeaters require costly full-duplex suppression because of the low isolation between the donor and service link antenna.

In Chapter 3, we propose a mmWave bridge as a solution to provide additional wireless capacity inside buildings or to remote places and along railway tracks. Our mmWave bridge is an out-of-band amplify-and-forward repeater system with a donor node at, e.g., an existing cell site and a service node—the customer premises equipment (CPE)—installed at a building. Without impacting the existing outdoor mobile network, the radio frequency (RF) signal of an additional (small) cell on the existing site is connected to the donor node instead of an antenna. The cell signal is upconverted to a mmWave carrier frequency and fronthauled to the service node. An outdoor antenna is installed, e.g., at the building, to minimize the path loss and is connected to the service node. The service node itself downconverts the fronthauled cell signal and retransmits it on its original carrier frequency inside the building or the desired place where the capacity is needed. Uplink signals are treated the same but in the reverse direction. Our mmWave bridge consists of a simple hardware architecture with analog RF circuits for low signal delays. The transparent operation works independently of the radio access technology (RAT) and is backward and forward-compatible. Hence, existing mobile infrastructure and user equipment (UE) readily work with the mmWave bridge. No interference to the existing outdoor mobile network is added by using the newly available mmWave spectrum. Highly directive mmWave beamforming antennas are used for spatially multiplexing many links, and the large available bandwidth in the mmWave spectrum can be used for multiplexing links on different frequencies.

Detailed link budget models have been developed to compare the mmWave bridge with the four solutions: (1) the outdoor macro network as a baseline; (2) a small cell with wired backhaul; (3) a layer-3 relay; (4) a layer-1 repeater. Based on Monte Carlo simulations, we found that the mmWave bridge provides a similar capacity as layer-1 repeaters and layer-3 relays for a single link. However, the mmWave bridge adds additional capacity independent of the outdoor network. Additionally, significant cell sector capacity gains are possible with the mmWave bridge thanks to the spatial and frequency multiplexing of links, where we calculated an 11-fold increase compared to layer-1 repeaters.

In Chapter 4, we describe a prototype of the mmWave bridge that we have developed. The prototype consists of two almost identical nodes used as a donor and a service node. The local

---

oscillator for the up- and downconversion of the cell signal is one of the most critical elements because its phase noise directly impacts the achievable link SNR. With the prototype, we can now fronthaul a cellular single input single output (SISO) signal and have validated 4G and 5G signals in frequency division multiplexing (FDD) as well as time division multiplexing (TDD). The measured error vector magnitude (EVM) is in the range of  $-32.6$  dB to  $-24.9$  dB, which is low enough to support 256-QAM. Furthermore, digitally controllable mmWave beamforming antennas are used, allowing up to 1313 different beam directions.

For the use case of providing fixed wireless access (FWA) service to buildings or concealed areas, outdoor measurements were conducted to prove the mmWave bridge concept works and to measure its performance. Chapter 5 first describes a campaign where we measured the SNR and 4G throughput versus the fronthaul distance in line-of-sight (LOS). The peak capacity of the cell could be maintained for an FWA link of up to 800 m. Next, we demonstrated that a 5G cell with 100 MHz of bandwidth can be fronthauled from a macro cell site to a location where a dedicated cell in an RF-shielded area is needed. An example is the test tube for the hyperloop research project at EPFL (EPFLoop), where the measurements took place. The measured SNR was around 27 dB, and a stable connection was maintained for at least ten minutes. More extended measurements were performed in the lab, where a UE remained connected over the mmWave bridge for 24 hours running continuous throughput tests.

We have further explored the use of our mmWave bridge in Chapter 6 for the cellular antenna corridor along railway tracks. A mmWave bridge donor node is installed on every macro cell site, and intermediate low-power mmWave bridge service nodes are installed on catenary masts. This installation allows the extension of the macro ISD, resulting in lower roll-out costs and considerable energy reduction while maintaining the capacity. In a measurement campaign to measure the impact of the enhanced signal inside trains, we measured a median power increase of 10.5 dB for one service node and the given railway track segment. We numerically evaluated several configurations based on calibrated path loss models to estimate the number of required mmWave bridge service nodes and the possible macro ISD increase. Furthermore, we studied the energy efficiency of a cellular corridor and found that the use of low-power bridge nodes with correspondingly enlarged ISDs indeed substantially lowers the overall energy consumption. Additionally, if the low-power bridge nodes are optimized with a sleep mode enabled when no trains pass, they can even be autonomously powered by a battery-backed PV system. As a result, even better savings are achieved, lowering the energy consumption by 79 % compared to the conventional macro site cellular antenna corridor.

Finally, in Chapter 7, we generalized the mmWave bridge regarding the fronthaul carrier frequency to discuss transparent amplify-and-forward (AF) repeaters with beamforming antennas. Because layer-1 AF repeaters are agnostic to the cellular signals, there is no possibility for an in-band control for the beam steering. We propose a method to perform beam measurements with a minimal impact on the user throughput. With measurements based on 4G, we could estimate the impact and derive a guideline for choosing the number of beam measurements versus the impact on the 4G throughput. For the initial link establishment,

we describe the probability of missing a user and optimize the number of beams to measure with the help of a genetic algorithm. In the studied examples, only 23 % to 37 % of all the possible beams need to be scanned not to miss a user. Furthermore, we evaluated several reinforcement learning algorithms to reduce the number of measurements for beam tracking with moving users such as a vehicle. A multi-armed bandit (MAB) with non-stationary rewards outperforms the compared algorithms.

### Outlook

The mmWave bridge prototype proves the feasibility that 4G and 5G cells in sub-6 GHz frequencies can be fronthauled over mmWave frequencies and provide the cell capacity to commercial off-the-shelf (COTS) UEs on the original frequencies of the cells. Furthermore, the prototype can be used for demonstrations and field measurements. However, plenty of work is left to turn the prototype into a product. Because 4G and 5G cells operate with two multiple input multiple output (MIMO) layers by default, the bridge must be extended with two downlink and uplink paths and cross-polarized antennas for  $2 \times 2$  MIMO operation. In addition, it should be investigated how to support a higher order of MIMO layers. Furthermore, the frontend hardware based on COTS connectorized RF modules and components needs to be converted to a higher integrated RF circuit board. Moreover, a low phase noise local oscillator should be integrated on the board with a carefully chosen trade-off between quality and cost. Additionally, alternative methods for the synchronization among the LOs of the bridge nodes can be studied, e.g., as proposed in [126].

Globally, the advances and momentum of Open RAN, an initiative to disaggregate the radio access network (RAN) based on open interfaces, are increasing. Consequently, the newly specified fronthaul interface can be implemented, e.g., on a field programmable gate array (FPGA) in the donor node, to facilitate the interfacing and integration of the mmWave bridge. In this case, the donor node serves as the radio unit (RU) connecting to the distributed unit (DU), e.g., with the O-RAN split 7.2x. Such an arrangement offers more flexibility concerning the intermediate frequency for the up- and downconversion in the donor node because it does not need to be identical to the actual carrier frequency of the cell signal. However, the service node may remain unchanged.

Finally, considering the future evolution of mobile networks, there is tremendous potential with cell-free networks. The mmWave bridge readily integrates with such cell-free networks because it virtually creates a path that can be seen as a strong link in a multipath propagation environment. However, the impact of such links in cell-free networks needs to be investigated in detail.

# A Appendix

## A.1 Coordinate Transformation to Beam Angles

Base station antennas installed in the field are fixed at a given position and orientation. To achieve the best coverage of a certain area, these angles need to be wisely adjusted for passive antennas with a specified fixed beam pattern. However, for beamforming antennas with an electronically steerable beam, certain flexibility is allowed. The equations here are based on [127] and can be used to simply transform a position of a user to the relative beam angle in case of line-of-sight between the user and the antenna.

### A.1.1 Coordinate Frames

Latitude, longitude, and height coordinates from a map or from Global Positioning System (GPS) are often expressed with reference to the World Geodetic System 1984 (WGS84), based on a reference ellipsoid, a standard coordinate system, and altitude. However, a base station antenna is installed at a certain position on the Earth, with a given azimuth angle (horizontal angle measured clockwise from north) and tilt angle (angular shift in elevation). Several coordinate frames are necessary to perform the transformation.

#### A.1.1.1 Earth-Centered Earth-Fixed Frame (ECEF, $e$ -frame)

This frame has its origin at the center of mass of the Earth and rotates with it, Fig. A.1. The  $z$ -axis is parallel to the mean spin axis of the Earth, the  $x$ -axis points to the reference meridian and the  $y$ -axis completes the right-handed orthogonal frame.

#### A.1.1.2 Local Tangent Plane/Frame ( $t$ -frame)

The local tangent plane has its origin coinciding with the position of the base station antenna on the Earth, see Fig. A.1. Its  $x$ -axis points towards the geodetic north, the  $z$ -axis towards the

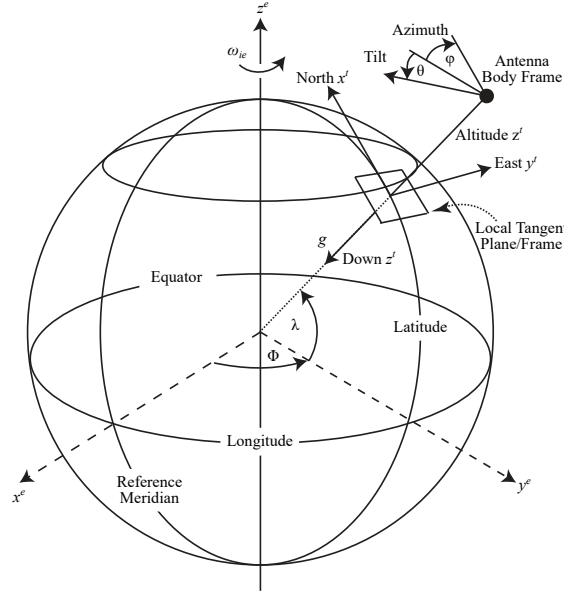


Figure A.1: Relations between ECEF frame ( $e$ ), local tangent-frame ( $t$ ), and body frame ( $b$ ) [127].

origin of the  $e$ -frame, and the  $y$ -axis completes the right-handed orthogonal frame on the geodetic reference ellipse. This coordinate frame is also referred to as the North-East-Down (NED) system.

#### A.1.1.3 Body Frame ( $b$ -frame)

A base station antenna has a given azimuth and tilt angle with respect to the  $t$ -frame, see Fig. A.1. The origin of the body frame is located at the center of the antenna, with its  $x$ -axis pointing in the broadside direction, the  $z$ -axis down to the center of the Earth, and the  $y$ -axis completes the right-handed orthogonal system.

#### A.1.2 Transformation from Coordinates to Beam Angles

To transform the location data as WGS84 GPS coordinates in latitude  $\lambda$ , longitude  $\Phi$ , and altitude  $h$  to beam azimuth and elevation angles from the base station or beamforming antenna point of view, several steps are necessary. First, the coordinates are transformed to the Earth-Centered Earth-Fixed (ECEF) frame ( $e$ -frame) according to [128]

$$\begin{aligned} x^e &= (h + N) \cos \lambda \cos \Phi \\ y^e &= (h + N) \cos \lambda \sin \Phi \\ z^e &= (h + (1 - e^2)N) \sin \lambda \end{aligned} \tag{A.1}$$

with  $N(\lambda) = a / \sqrt{1 - e^2 \sin^2(\lambda)}$  and  $e = 8.1819191 \times 10^{-2}$ .

The direct cosine matrix (DCM) is a commonly used transformation method between coordinate systems. An arbitrary vector written in terms of the orthogonal unit vector  $\{\mathbf{1}_x^a, \mathbf{1}_y^a, \mathbf{1}_z^a\}$  can be written as

$$\mathbf{p}^m = x^m \mathbf{1}_x^m + y^m \mathbf{1}_y^m + z^m \mathbf{1}_z^m \quad (\text{A.2})$$

To transform one vector  $\mathbf{p}^m$  in the coordinate system  $m$  to a vector  $\mathbf{p}^n$  in the coordinate system  $n$  that uses the same origin, the following DCM matrix multiplication can be used:

$$\mathbf{p}^n = \mathbf{R}_m^n \mathbf{p}^m. \quad (\text{A.3})$$

According to [128], the transformation DCM from the  $e$ - to the local tangent ( $t$ -frame) reads

$$\mathbf{R}_e^t = \begin{bmatrix} -\sin(\Phi) & \cos(\Phi) & 0 \\ -\sin(\lambda) \cos(\Phi) & -\sin(\lambda) \sin(\Phi) & \cos(\lambda) \\ \cos(\lambda) \cos(\Phi) & \cos(\lambda) \sin(\Phi) & \sin(\lambda) \end{bmatrix}. \quad (\text{A.4})$$

The installed (beamforming) antenna has a given azimuth  $\varphi$  and tilt  $\theta$ , which defines the body frame ( $b$ -frame). The coordinates from the  $t$ -frame can finally be transformed to the antenna's  $b$ -frame with

$$\mathbf{R}_t^b = \begin{bmatrix} \cos(\varphi) & \sin(\varphi) & 0 \\ -\sin(\varphi) \cos(\theta) & \cos(\varphi) \cos(\theta) & \sin(\theta) \\ \sin(\varphi) \sin(\theta) & -\cos(\varphi) \sin(\theta) & \cos(\theta) \end{bmatrix}. \quad (\text{A.5})$$

The two transformation matrices  $\mathbf{R}_e^t$  and  $\mathbf{R}_t^b$  can be combined into one DCM that reads

$$\mathbf{R}_e^b = \mathbf{R}_t^b \mathbf{R}_e^t. \quad (\text{A.6})$$

The base station (BS) or bridge donor node antenna coordinates and the locations of users or bridge service nodes in WGS84 format are converted into ECEF coordinates with (A.1), resulting in  $\mathbf{p}_{\text{BS}}^e$  and  $\mathbf{p}_{\text{user}}^e$ , respectively. Subsequently, the ECEF coordinates are transformed to the beamforming antenna body frame with  $\mathbf{p}_{\text{user}}^b = \mathbf{R}_e^b (\mathbf{p}_{\text{user}}^e - \mathbf{p}_{\text{BS}}^e)$ . Finally, the azimuth and elevation angles relative to the beamforming antenna corresponding to beam boresight angles are obtained from  $\mathbf{p}_{\text{user}}^b$  with

$$\begin{aligned} \phi_{\text{user}} = az &= \arctan2(x_{\text{user}}^b, y_{\text{user}}^b) \\ \theta_{\text{user}} = el &= \arctan2(\sqrt{x_{\text{user}}^b{}^2 + y_{\text{user}}^b{}^2}, z_{\text{user}}^b). \end{aligned} \quad (\text{A.7})$$



# Bibliography

- [1] “Ericsson Mobility Report November 2021,” Ericsson AB, White Paper, Nov. 2021. [Online]. Available: <https://www.ericsson.com/4ad7e9/assets/local/reports-papers/mobility-report/documents/2021/ericsson-mobility-report-november-2021.pdf>
- [2] ABI Research, “ABI Research Anticipates In-Building Mobile Data Traffic to Grow by More Than 600% by 2020,” Jan. 2016. [Online]. Available: <https://www.abiresearch.com/press/abi-research-anticipates-building-mobile-data-traf/>
- [3] “Ericsson Mobility Report June 2020,” Ericsson AB, White Paper, Jun. 2020. [Online]. Available: <https://www.ericsson.com/en/mobility-report/reports/june-2020>
- [4] ITU-R, “Compilation of measurement data relating to building entry loss,” ITU-R, Tech. Rep. Report P.2346-2, Mar. 2017. [Online]. Available: <https://www.itu.int/pub/R-REP-P2346>
- [5] Larry Greenstein, “One Hundred Years of Radio,” Red Bank, NJ, Sep. 1999. [Online]. Available: <http://www.winlab.rutgers.edu/archive/Marconi%20Day/Greenstein.pdf>
- [6] A. Schumacher, R. Merz, and A. Burg, “3.5 GHz Coverage Assessment with a 5G Testbed,” in *2019 IEEE 89th Vehicular Technology Conference (VTC2019-Spring)*, Apr. 2019, pp. 1–6. [Online]. Available: <https://doi.org/10.1109/VTCSpring.2019.8746551>
- [7] —, “A mmWave Bridge Concept to Solve the Cellular Outdoor-to-Indoor Challenge,” in *2020 IEEE 91st Vehicular Technology Conference (VTC2020-Spring)*, May 2020, pp. 1–6. [Online]. Available: <https://doi.org/10.1109/VTC2020-Spring48590.2020.9128458>
- [8] —, “Adding Indoor Capacity without Fiber Backhaul: An mmWave Bridge Prototype,” *IEEE Communications Magazine*, vol. 59, no. 4, pp. 110–115, May 2021. [Online]. Available: <https://doi.org/10.1109/MCOM.001.2000722>
- [9] A. Schumacher, N. Jamaly, R. Merz, and A. Burg, “Improving railway track coverage with mmWave bridges: A Measurement Campaign,” in *Proceedings of the 1st Workshop on 5G Measurements, Modeling, and Use Cases*. New York, NY, USA: Association for Computing Machinery, Aug. 2021, pp. 8–13. [Online]. Available: <https://doi.org/10.1145/3472771.3472774>

- [10] A. Schumacher, R. Merz, and A. Burg, "Increasing Cellular Network Energy Efficiency for Railway Corridors," in *2022 Design, Automation & Test in Europe Conference (DATE2022)*, Mar. 2022, pp. 1103–1106. [Online]. Available: <https://doi.org/10.23919/DATE54114.2022.9774757>
- [11] —, "Beam Selection and Tracking for Amplify-and-Forward Repeaters," in *2022 IEEE 95th Vehicular Technology Conference (VTC2022-Spring)*, Jun. 2022, pp. 1–7.
- [12] B. Bertenyi, "5G Evolution: What's Next?" *IEEE Wireless Communications*, vol. 28, no. 1, pp. 4–8, Feb. 2021.
- [13] G. Interdonato, E. Björnson, H. Quoc Ngo, P. Frenger, and E. G. Larsson, "Ubiquitous cell-free Massive MIMO communications," *EURASIP Journal on Wireless Communications and Networking*, vol. 2019, no. 1, p. 197, Aug. 2019. [Online]. Available: <https://doi.org/10.1186/s13638-019-1507-0>
- [14] 3GPP, "UMTS-LTE 3500 MHz Work Item Technical Report," 3rd Generation Partnership Project (3GPP), Technical Report (TR) 37.801, Oct. 2011. [Online]. Available: <http://www.3gpp.org/ftp/Specs/html-info/37801.htm>
- [15] B. Clerckx and C. Oestges, *MIMO Wireless Networks: Channels, Techniques and Standards for Multi-Antenna, Multi-User and Multi-Cell Systems*. Academic Press, Jan. 2013.
- [16] V. S. Abhayawardhana, I. J. Wassell, D. Crosby, M. P. Sellars, and M. G. Brown, "Comparison of empirical propagation path loss models for fixed wireless access systems," in *2005 IEEE 61st Vehicular Technology Conference*, vol. 1, May 2005, pp. 73–77 Vol. 1.
- [17] M. C. Walden and F. J. Rowsell, "Urban propagation measurements and statistical path loss model at 3.5 GHz," in *2005 IEEE Antennas and Propagation Society International Symposium*, vol. 1A, Jul. 2005, pp. 363–366 Vol. 1A.
- [18] W. Joseph, L. Roelens, and L. Martens, "Path Loss Model for Wireless Applications at 3500 MHz," in *2006 IEEE Antennas and Propagation Society International Symposium*, Jul. 2006, pp. 4751–4754.
- [19] P. Imperatore, E. Salvadori, and I. Chlamtac, "Path Loss Measurements at 3.5 GHz: A Trial Test WiMAX Based in Rural Environment," in *2007 3rd International Conference on Testbeds and Research Infrastructure for the Development of Networks and Communities*, May 2007, pp. 1–8.
- [20] S. Kun, W. Ping, and L. Yingze, "Path loss models for suburban scenario at 2.3GHz, 2.6GHz and 3.5GHz," in *2008 8th International Symposium on Antennas, Propagation and EM Theory*, Nov. 2008, pp. 438–441.
- [21] M. Riback, J. Medbo, J. Berg, F. Harrysson, and H. Asplund, "Carrier Frequency Effects on Path Loss," in *2006 IEEE 63rd Vehicular Technology Conference*, vol. 6, May 2006, pp. 2717–2721.

- [22] I. Rodriguez, H. C. Nguyen, N. T. K. Jørgensen, T. B. Sørensen, J. Elling, M. B. Gentsch, and P. Mogensen, "Path loss validation for urban micro cell scenarios at 3.5 GHz compared to 1.9 GHz," in *2013 IEEE Global Communications Conference (GLOBECOM)*, Dec. 2013, pp. 3942–3947.
- [23] K. L. Chee, A. Anggraini, T. Kaiser, and T. Kürner, "Outdoor-to-indoor propagation loss measurements for broadband wireless access in rural areas," in *Proceedings of the 5th European Conference on Antennas and Propagation (EUCAP)*, Apr. 2011, pp. 1376–1380.
- [24] B. Halvarsson, A. Simonsson, A. Elgcrona, R. Chana, P. Machado, and H. Asplund, "5G NR Testbed 3.5 GHz Coverage Results," in *2018 IEEE 87th Vehicular Technology Conference (VTC Spring)*, Jun. 2018, pp. 1–5.
- [25] M. Hata, "Empirical formula for propagation loss in land mobile radio services," *IEEE Transactions on Vehicular Technology*, vol. 29, no. 3, pp. 317–325, Aug. 1980.
- [26] European Commission, "COST Action 231: Digital mobile radio towards future generation systems: Final Report." European Commission, Brussels, Belgium, Tech. Rep. EUR 18957, Apr. 1999. [Online]. Available: <https://publications.europa.eu/en/publication-detail/-/publication/f2f42003-4028-4496-af95-beaa38fd475f/language-en>
- [27] V. Erceg, L. J. Greenstein, S. Y. Tjandra, S. R. Parkoff, A. Gupta, B. Kulic, A. A. Julius, and R. Bianchi, "An empirically based path loss model for wireless channels in suburban environments," *IEEE Journal on Selected Areas in Communications*, vol. 17, no. 7, pp. 1205–1211, Jul. 1999.
- [28] IEEE, "Channel Models for Fixed Wireless Applications," IEEE, Tech. Rep. IEEE 802.16.3c-01/29r4, Jul. 2001. [Online]. Available: [http://www.ieee802.org/16/tg3/contrib/802163c-01\\_29r4.pdf](http://www.ieee802.org/16/tg3/contrib/802163c-01_29r4.pdf)
- [29] ECC, "The analysis of the coexistence of FWA cells in the 3.4 - 3.8 GHz band," Electronic Communication Committee (ECC) within the European Conference of Postal and Telecommunications Administration (CEPT), Tech. Rep. ECC Report 33, May 2003.
- [30] Pekka Kyösti, Juha Meinilä, Lassi Hentilä, Xiongwen Zhao, Tommi Jämsä, Christian Schneider, Milan Narandzić, Marko Milojević, Aihua Hong, Juha Ylitalo, Veli-Matti Holappa, Mikko Alatossava, Robert Bultitude, Yvo de Jong, and Terhi Rautiainen, "WINNER II Channel Models," European Commission, Tech. Rep. D1.1.2 V1.2, IST-4-027756 WINNER II Deliverable, Feb. 2008. [Online]. Available: <https://www.cept.org/files/8339/winner2%20-%20final%20report.pdf>
- [31] ITU-R, "Propagation data and prediction methods for the planning of short-range outdoor radiocommunication systems and radio local area networks in the frequency range 300 MHz to 100 GHz," ITU-R, Tech. Rep. Recommendation P.1411-9, Jun. 2017. [Online]. Available: <https://www.itu.int/rec/R-REC-P.1411-9-201706-I/en>

- [32] 3GPP, "Study on channel model for frequencies from 0.5 to 100 GHz," 3rd Generation Partnership Project (3GPP), Technical Report (TR) 38.901, 06 2018, version 15.0.0.
- [33] ITU-R, "Prediction of Building Entry Loss," ITU-R, Tech. Rep. Recommendation P.2109, Jun. 2017. [Online]. Available: <https://www.itu.int/rec/R-REC-P2109/en>
- [34] W. C. Y. Lee and Y.-S. Yeh, "On the Estimation of the Second-Order Statistics of Log Normal Fading in Mobile Radio Environment," *IEEE Transactions on Communications*, vol. 22, no. 6, pp. 869–873, Jun. 1974.
- [35] A. Goldsmith, *Wireless Communications*. Cambridge: Cambridge University Press, 2005. [Online]. Available: <http://ebooks.cambridge.org/ref/id/CBO9780511841224>
- [36] O. Bouvard, M. Lanini, L. Burnier, R. Witte, B. Cuttat, A. Salvadè, and A. Schüller, "Mobile communication through insulating windows: A new type of low emissivity coating," *Energy Procedia*, vol. 122, pp. 781–786, Sep. 2017. [Online]. Available: <https://linkinghub.elsevier.com/retrieve/pii/S187661021733000X>
- [37] L. Burnier, M. Lanini, O. Bouvard, D. Scanferla, A. Varathan, C. Genoud, A. Marguerit, B. Cuttat, N. Dury, R. Witte, A. Salvadè, and A. Schüller, "Energy saving glazing with a wide band-pass FSS allowing mobile communication: Up-scaling and characterisation," *IET Microwaves, Antennas & Propagation*, vol. 11, no. 10, pp. 1449–1455, Aug. 2017. [Online]. Available: <https://digital-library.theiet.org/content/journals/10.1049/iet-map.2016.0685>
- [38] Mikio Iwamura, Hideaki Takahashi, and Satoshi Nagata, "Relay Technology in LTE-Advanced," *NTT DOCOMO Technical Journal*, vol. 12, no. 2, pp. 29–36, Sep. 2010. [Online]. Available: [https://www.nttdocomo.co.jp/english/binary/pdf/corporate/technology/rd/technical\\_journal/bn/vol12\\_2/vol12\\_2\\_029en.pdf](https://www.nttdocomo.co.jp/english/binary/pdf/corporate/technology/rd/technical_journal/bn/vol12_2/vol12_2_029en.pdf)
- [39] E. Dahlman, S. Parkvall, and J. Sköld, *5G NR: The Next Generation Wireless Access Technology*, 1st ed. Academic Press, Aug. 2018.
- [40] O. Teyeb, A. Muhammad, G. Mildh, E. Dahlman, F. Barac, and B. Makki, "Integrated Access Backhauled Networks," in *2019 IEEE 90th Vehicular Technology Conference (VTC2019-Fall)*, Sep. 2019, pp. 1–5.
- [41] M. Cudak, A. Ghosh, A. Ghosh, and J. Andrews, "Integrated Access and Backhaul: A Key Enabler for 5G Millimeter-Wave Deployments," *IEEE Communications Magazine*, vol. 59, no. 4, pp. 88–94, Apr. 2021.
- [42] E. Basar, M. Di Renzo, J. De Rosny, M. Debbah, M.-S. Alouini, and R. Zhang, "Wireless Communications Through Reconfigurable Intelligent Surfaces," *IEEE Access*, vol. 7, pp. 116 753–116 773, 2019.
- [43] Ö. Özdoğan, E. Björnson, and E. G. Larsson, "Intelligent Reflecting Surfaces: Physics, Propagation, and Pathloss Modeling," *IEEE Wireless Communications Letters*, vol. 9, no. 5, pp. 581–585, May 2020.

- 
- [44] Q. Wu and R. Zhang, "Towards Smart and Reconfigurable Environment: Intelligent Reflecting Surface Aided Wireless Network," *IEEE Communications Magazine*, vol. 58, no. 1, pp. 106–112, Jan. 2020.
- [45] G. Larson, "Deployment Options for Providing Indoor Coverage in High Frequency Bands," Master's thesis, KTH Royal Institute of Technology, Stockholm, 2015. [Online]. Available: <http://urn.kb.se/resolve?urn=urn:nbn:se:kth:diva-177597>
- [46] V. Venkatkumar, T. Haustein, and M. Faulkner, "Relaying results for indoor coverage in long-term evolution and beyond," *European Transactions on Telecommunications*, vol. 21, no. 8, pp. 770–779, 2010. [Online]. Available: <https://onlinelibrary.wiley.com/doi/abs/10.1002/ett.1450>
- [47] S. Biswas, S. Vuppala, J. Xue, and T. Ratnarajah, "On the Performance of Relay Aided Millimeter Wave Networks," *IEEE Journal of Selected Topics in Signal Processing*, vol. 10, no. 3, pp. 576–588, Apr. 2016.
- [48] T. Wirth, L. Thiele, T. Haustein, O. Braz, and J. Stefanik, "LTE Amplify and Forward Relaying for Indoor Coverage Extension," in *2010 IEEE 72nd Vehicular Technology Conference - Fall*, Sep. 2010, pp. 1–5.
- [49] K. Hiltunen, "Using RF Repeaters to Improve WCDMA HSDPA Coverage and Capacity Inside Buildings," in *2006 IEEE 17th International Symposium on Personal, Indoor and Mobile Radio Communications*, Sep. 2006, pp. 1–5.
- [50] M. Breiling, D. W. K. Ng, C. Rohde, F. Burkhardt, R. Schober, and T. Heyn, "UE-Side Virtual MIMO Using mm-Wave for 5G," Fraunhofer IIS, White Paper, Aug. 2014.
- [51] R. Zhu, Y. E. Wang, Q. Xu, Y. Liu, and Y. D. Li, "Millimeter-wave to microwave MIMO relays (M4R) for 5G building penetration communications," in *2018 IEEE Radio and Wireless Symposium (RWS)*, Jan. 2018, pp. 206–208.
- [52] B. Lannoo, D. Colle, M. Pickavet, and P. Demeester, "Radio-over-fiber-based solution to provide broadband internet access to train passengers [Topics in Optical Communications]," *IEEE Communications Magazine*, vol. 45, no. 2, pp. 56–62, Feb. 2007.
- [53] J. Wang, H. Zhu, and N. J. Gomes, "Distributed Antenna Systems for Mobile Communications in High Speed Trains," *IEEE Journal on Selected Areas in Communications*, vol. 30, no. 4, pp. 675–683, May 2012.
- [54] N. Jamaly, S. Maunon, R. Merz, A. Schumacher, and D. Wenger, "Delivering Gigabit Capacities to Passenger Trains: Tales from an Operator on the Road to 5G," *IEEE Communications Magazine*, vol. 57, no. 9, pp. 18–23, Sep. 2019.
- [55] A. Kanno, P. T. Dat, N. Yamamoto, and T. Kawanishi, "Millimeter-Wave Radio-Over-Fiber Network for Linear Cell Systems," *Journal of Lightwave Technology*, vol. 36, no. 2, pp. 533–540, Jan. 2018.

## Bibliography

---

- [56] P. T. Dat, A. Kanno, N. Yamamoto, and T. Kawanishi, "WDM RoF-MMW and linearly located distributed antenna system for future high-speed railway communications," *IEEE Communications Magazine*, vol. 53, no. 10, pp. 86–94, Oct. 2015.
- [57] L. Falconetti, P. Frenger, H. Kallin, and T. Rindhagen, "Energy efficiency in heterogeneous networks," in *2012 IEEE Online Conference on Green Communications (GreenCom)*, Sep. 2012, pp. 98–103.
- [58] S. Tombaz, K. W. Sung, and J. Zander, "Impact of densification on energy efficiency in wireless access networks," in *2012 IEEE Globecom Workshops*, Dec. 2012, pp. 57–62.
- [59] A. Arbi and T. O'Farrell, "Energy efficiency in 5G access networks: Small cell densification and high order sectorisation," in *2015 IEEE International Conference on Communication Workshop (ICCW)*, Jun. 2015, pp. 2806–2811.
- [60] G. Auer, V. Giannini, I. Godor, P. Skillermark, M. Olsson, M. A. Imran, D. Sabella, M. J. Gonzalez, C. Desset, and O. Blume, "Cellular Energy Efficiency Evaluation Framework," in *2011 IEEE 73rd Vehicular Technology Conference (VTC Spring)*, May 2011, pp. 1–6.
- [61] H. Holtkamp, G. Auer, V. Giannini, and H. Haas, "A Parameterized Base Station Power Model," *IEEE Communications Letters*, vol. 17, no. 11, pp. 2033–2035, Nov. 2013.
- [62] Y.-N. R. Li, M. Chen, J. Xu, L. Tian, and K. Huang, "Power Saving Techniques for 5G and Beyond," *IEEE Access*, vol. 8, pp. 108 675–108 690, 2020.
- [63] B. Debaillie, C. Desset, and F. Louagie, "A Flexible and Future-Proof Power Model for Cellular Base Stations," in *2015 IEEE 81st Vehicular Technology Conference (VTC Spring)*, May 2015, pp. 1–7.
- [64] W. B. Abbas and M. Zorzi, "Context information based initial cell search for millimeter wave 5G cellular networks," in *2016 European Conference on Networks and Communications (EuCNC)*, Jun. 2016, pp. 111–116.
- [65] A. Capone, I. Filippini, and V. Sciancalepore, "Context Information for Fast Cell Discovery in mm-wave 5G Networks," in *Proceedings of European Wireless 2015; 21th European Wireless Conference*, May 2015, pp. 1–6.
- [66] T. Nitsche, A. B. Flores, E. W. Knightly, and J. Widmer, "Steering with eyes closed: Mm-Wave beam steering without in-band measurement," in *2015 IEEE Conference on Computer Communications (INFOCOM)*, Apr. 2015, pp. 2416–2424.
- [67] T. S. Cousik, V. K. Shah, J. H. Reed, T. Erpek, and Y. E. Sagduyu, "Fast Initial Access with Deep Learning for Beam Prediction in 5G mmWave Networks," *arXiv:2006.12653 [cs, eess]*, Jun. 2020. [Online]. Available: <http://arxiv.org/abs/2006.12653>
- [68] H. Hassanieh, O. Abari, M. Rodriguez, M. Abdelghany, D. Katabi, and P. Indyk, "Fast millimeter wave beam alignment," in *Proceedings of the 2018 Conference of*

- the ACM Special Interest Group on Data Communication*. New York, NY, USA: Association for Computing Machinery, Aug. 2018, pp. 432–445. [Online]. Available: <https://doi.org/10.1145/3230543.3230581>
- [69] M. Hashemi, A. Sabharwal, C. E. Koksal, and N. B. Shroff, “Efficient Beam Alignment in Millimeter Wave Systems Using Contextual Bandits,” in *IEEE INFOCOM 2018 - IEEE Conference on Computer Communications*, Apr. 2018, pp. 2393–2401.
  - [70] ITU-R, “Final Acts WRC-19,” ITU-R, Sharm El-Sheikh, Egypt, Tech. Rep., 2019. [Online]. Available: <https://www.itu.int/en/ITU-R/conferences/wrc/2019/Pages/default.aspx>
  - [71] Swisstopo, “Mobile Coverage Map Lausanne/Vaud,” Lausanne, Vaud, Switzerland, Feb. 2022. [Online]. Available: <https://s.geo.admin.ch/95ea8f1eb2>
  - [72] Z. Pi and F. Khan, “An introduction to millimeter-wave mobile broadband systems,” *IEEE Communications Magazine*, vol. 49, no. 6, pp. 101–107, Jun. 2011.
  - [73] G. Smail and J. Weijia, “Techno-economic analysis and prediction for the deployment of 5G mobile network,” in *2017 20th Conference on Innovations in Clouds, Internet and Networks (ICIN)*, Mar. 2017, pp. 9–16.
  - [74] W. Guo and T. O’Farrell, “Capacity-Energy-Cost Tradeoff in Small Cell Networks,” in *2012 IEEE 75th Vehicular Technology Conference (VTC Spring)*, Yokohama, Japan, May 2012, pp. 1–5.
  - [75] V. Chandrasekhar, J. G. Andrews, and A. Gatherer, “Femtocell networks: A survey,” *IEEE Communications Magazine*, vol. 46, no. 9, pp. 59–67, Sep. 2008.
  - [76] W. Xie, N. Mao, and K. Rundberget, “Cost Comparisons of Backhaul Transport Technologies for 5G Fixed Wireless Access,” in *2018 IEEE 5G World Forum (5GWF)*, Jul. 2018, pp. 159–163.
  - [77] T. S. Rappaport, *Wireless Communications: Principles and Practice*. Prentice Hall PTR, 1996.
  - [78] G. F. Riley and T. R. Henderson, “The ns-3 Network Simulator,” in *Modeling and Tools for Network Simulation*, 1st ed., K. Wehrle, M. Güneş, and J. Gross, Eds. Berlin, Heidelberg: Springer, 2010, pp. 15–34. [Online]. Available: [https://doi.org/10.1007/978-3-642-12331-3\\_2](https://doi.org/10.1007/978-3-642-12331-3_2)
  - [79] L. Råde and B. Westergren, *Mathematics Handbook for Science and Engineering*. Studentlitteratur, 1998.
  - [80] 3GPP, “Study on new radio access technology: Radio Frequency (RF) and co-existence aspects,” 3rd Generation Partnership Project (3GPP), Technical Report (TR) 38.803, 09 2017, version 14.2.0.

## Bibliography

---

- [81] —, “NR; User Equipment (UE) radio access capabilities,” 3rd Generation Partnership Project (3GPP), Technical Specification (TS) 38.306, 06 2019, version 15.6.0.
- [82] L. Laughlin, C. Zhang, M. A. Beach, K. A. Morris, and J. L. Haine, “Minimum Downlink Band Duplex Isolation Requirements for LTE User Equipment,” in *2019 IEEE International Conference on Communications Workshops (ICC Workshops)*, May 2019, pp. 1–6.
- [83] Eric J. Black, “Holographic Beamforming and MIMO,” Pivotal Commware, White Paper, Dec. 2017. [Online]. Available: <https://pivotalcommware.com/wp-content/uploads/2017/12/Holographic-Beamforming-WP-v.6C-FINAL.pdf>
- [84] Pat Hindle, “Comprehensive Survey of Commercial mmWave Phased Array Companies | Microwave Journal,” Jan. 2020. [Online]. Available: <https://www.microwavejournal.com/articles/33357-comprehensive-survey-of-commercial-mmwave-phased-array-companies>
- [85] R. W. Stewart, L. Crockett, C. Ramsay, J. Goldsmith, D. Northcote, and K. Barlee, “Software Defined Radio With RFSoc & PYNQ,” San Jose, CA, USA, Jun. 2018. [Online]. Available: [https://www.xilinx.com/support/documentation/university/XDF\\_2018/XDF\\_2018\\_Posters\\_ALL%2033.pdf](https://www.xilinx.com/support/documentation/university/XDF_2018/XDF_2018_Posters_ALL%2033.pdf)
- [86] R. A. Shafik, M. S. Rahman, and A. R. Islam, “On the Extended Relationships Among EVM, BER and SNR as Performance Metrics,” in *2006 International Conference on Electrical and Computer Engineering*, Dec. 2006, pp. 408–411.
- [87] M. Vigilante, E. McCune, and P. Reynaert, “To EVM or Two EVMs?: An Answer to the Question,” *IEEE Solid-State Circuits Magazine*, vol. 9, no. 3, pp. 36–39, 2017.
- [88] A. K. Thyagarajan, P. Balasubramanian, V. D, and K. M, “SNR-CQI Mapping for 5G Downlink Network,” in *2021 IEEE Asia Pacific Conference on Wireless and Mobile (APWiMob)*, Apr. 2021, pp. 173–177.
- [89] Amarisoft, “AMARI Callbox.” [Online]. Available: <https://www.amarisoft.com/products/test-measurements/amari-lte-callbox/>
- [90] Federal Office of Communications OFCOM, “Higher internet speeds as part of the universal service,” Oct. 2021. [Online]. Available: <https://www.admin.ch/gov/en/start/documentation/media-releases.msg-id-86370.html>
- [91] Ookla, “Speedtest Global Index – Internet Speed around the world.” [Online]. Available: <https://www.speedtest.net/global-index>
- [92] K. Laraqui, S. Tombaz, A. Furuskär, B. Skubic, A. Nazari, and E. Trojer, “Fixed Wireless Access: On a Massive Scale with 5G,” *Ericsson Technology Review*, vol. 94, no. #01 2017, pp. 52–65, Dec. 2016. [Online]. Available: <https://www.ericsson.com/en/reports-and-papers/ericsson-technology-review/articles/fixed-wireless-access-on-a-massive-scale-with-5g>

- 
- [93] B. Skubic, M. Fiorani, S. Tombaz, A. Furuskär, J. Mårtensson, and P. Monti, "Optical Transport Solutions for 5G Fixed Wireless Access [Invited]," *Journal of Optical Communications and Networking*, vol. 9, no. 9, p. D10, Sep. 2017. [Online]. Available: <https://opg.optica.org/abstract.cfm?URI=jocn-9-9-D10>
- [94] OFCOM, "Federal Office of Communications (OFCom)." [Online]. Available: <https://www.bakom.admin.ch/bakom/en/home.html>
- [95] 3GPP, "Evolved Universal Terrestrial Radio Access (E-UTRA); Radio Frequency (RF) system scenarios," 3rd Generation Partnership Project (3GPP), Technical Report (TR) 36.942, 07 2018, version 15.0.0.
- [96] Swisstopo, "Rural mmWave Measurement Location," Schüpfen, Switzerland, Nov. 2020. [Online]. Available: <https://s.geo.admin.ch/964d75c47f>
- [97] EPFLoop, "EPFLoop - Pushing the boundaries of transportation," Mar. 2022. [Online]. Available: <https://epfloop.ch/>
- [98] Swisstopo, "EPFL Hyperloop Site," Ecublens, Switzerland, Mar. 2022. [Online]. Available: <https://s.geo.admin.ch/9684fd6cc9>
- [99] 3GPP, "NR; Physical layer procedures for data," 3rd Generation Partnership Project (3GPP), Technical Specification (TS) 38.214, 06 2019, version 15.6.0.
- [100] D. Raca, D. Leahy, C. J. Sreenan, and J. J. Quinlan, "Beyond throughput, the next generation: A 5G dataset with channel and context metrics," in *Proceedings of the 11th ACM Multimedia Systems Conference*. New York, NY, USA: Association for Computing Machinery, May 2020, pp. 303–308. [Online]. Available: <https://doi.org/10.1145/3339825.3394938>
- [101] R. Merz, D. Wenger, D. Scanferla, and S. Mauron, "Performance of LTE in a High-velocity Environment: A Measurement Study," in *Proceedings of the 4th Workshop on All Things Cellular: Operations, Applications, & Challenges*. New York, NY, USA: ACM, 2014, pp. 47–52. [Online]. Available: <http://doi.acm.org/10.1145/2627585.2627589>
- [102] N. Jamaly, D. Scanferla, C. Genoud, and H. Lehmann, "Analysis and Measurement of Penetration Loss for Train Wagons with Coated vs Uncoated Windows," in *2018 12th European Conference on Antennas and Propagation (EuCAP)*, London, UK, Apr. 2018, p. 610 (5 pp.). [Online]. Available: <http://digital-library.theiet.org/content/conferences/10.1049/cp.2018.0969>
- [103] N. Jamaly, D. Wenger, R. Schoch, M. Rohrer, and R. Jegerlehner, "Measurement of Pathloss for Train Passengers in an Antenna Corridor," in *2021 15th European Conference on Antennas and Propagation (EuCAP)*, Düsseldorf, Germany, Apr. 2021, pp. 1–5.
- [104] Swisscom, "Greater bandwidth in trains," Oct. 2020. [Online]. Available: <https://www.swisscom.ch/en/about/news/2020/10/21-mehr-bandbreite-im-zug.html>

## Bibliography

---

- [105] Swiss Federal Council, “SR 814.710 - Verordnung über den Schutz vor nichtionisierender Strahlung (NISV),” Jun. 2019. [Online]. Available: [https://www.fedlex.admin.ch/eli/cc/2000/38/de#annex\\_1/lvl\\_d1087e41/lvl\\_6/lvl\\_61](https://www.fedlex.admin.ch/eli/cc/2000/38/de#annex_1/lvl_d1087e41/lvl_6/lvl_61)
- [106] GSMA, “Improving wireless connectivity through small cell deployment,” GSMA, Research Report Booklet, Dec. 2016. [Online]. Available: [https://www.gsma.com/publicpolicy/wp-content/uploads/2016/12/GSMA\\_Small\\_Cell\\_Deployment\\_Booklet.pdf](https://www.gsma.com/publicpolicy/wp-content/uploads/2016/12/GSMA_Small_Cell_Deployment_Booklet.pdf)
- [107] Swisstopo, “Walensee Trial Railway Track,” Weesen, Switzerland, May 2021. [Online]. Available: <https://map.geo.admin.ch/?E=2726503&N=1220956&zoom=10>
- [108] N. Jamaly, S. Maunon, and A. Kishk, “Application of Reflecting Panels in Realisation of Antenna Corridor for Train Communications,” in *2019 13th European Conference on Antennas and Propagation (EuCAP)*, Krakow, Poland, Mar. 2019, pp. 1–5.
- [109] N. Jamaly, A. Schumacher, and D. Wenger, “Micro versus Macro Antenna Corridor for Trains Equipped with FSS Windowpanes,” in *2022 16th European Conference on Antennas and Propagation (EuCAP)*, Madrid, Spain, Mar. 2022, pp. 1–5.
- [110] J. Rowley, “Mobile Communication Networks: Energy Efficiency & Green Power,” GSM Association, Presentation, 2010. [Online]. Available: [https://www.itu.int/dms\\_pub/itu-t/oth/3C/02/T3C020000330001PDFE.pdf](https://www.itu.int/dms_pub/itu-t/oth/3C/02/T3C020000330001PDFE.pdf)
- [111] L. Chiaraviglio, A. S. Cacciapuoti, G. D. Martino, M. Fiore, M. Montesano, D. Trucchi, and N. B. Melazzi, “Planning 5G Networks Under EMF Constraints: State of the Art and Vision,” *IEEE Access*, vol. 6, pp. 51 021–51 037, 2018.
- [112] M. Lerch, P. Svoboda, S. Ojak, M. Rupp, and C. Mecklenbraeuer, “Distributed Measurements of the Penetration Loss of Railroad Cars,” in *2017 IEEE 86th Vehicular Technology Conference (VTC-Fall)*, Toronto, ON, Sep. 2017, pp. 1–5. [Online]. Available: <http://ieeexplore.ieee.org/document/8287899/>
- [113] T. Berisha and C. F. Mecklenbräuer, “Smartphone-based Measurements on-board FSS-aided Railway Vehicles,” in *2019 13th European Conference on Antennas and Propagation (EuCAP)*, Mar. 2019, pp. 1–5.
- [114] O. S. Trindade, T. Berisha, P. Svoboda, E. Bura, and C. F. Mecklenbräuer, “Assessment of Treatment Influence in Mobile Network Coverage on Board High-Speed Trains,” *IEEE Access*, vol. 8, pp. 162 945–162 960, 2020.
- [115] W. M. Wajda, G. Auer, P. Skillernmark, Y. Jading, Oliver Blume, Vito Giannini, Istvan Godor, Muhammad Ali Imran, Efstathios Katranaras, Magnus Olsson, and Dario Sabella, “EARTH Deliverable D 2.3 Energy efficiency analysis of the reference systems, areas of improvements and target breakdown,” Tech. Rep. INFSO-ICT-247733, Jan. 2012. [Online]. Available: <https://www.semanticscholar.org/>

- paper/INFSO-ICT-247733-EARTH-Deliverable-D-2-.3-Energy-%2C-Wajda-Auer/79ed35658478c4124a3b55120cef7f33c9c01bf6
- [116] NTT DOCOMO, Alcatel-Lucent, Alcatel-Lucent Shanghai Bell, Ericsson, and Telecom Italia, “Base Station Power Model,” 3GPP, Tech. Rep. R1-114336, Nov. 2011.
  - [117] E. Calabrò, “An Algorithm to Determine the Optimum Tilt Angle of a Solar Panel from Global Horizontal Solar Radiation,” *Journal of Renewable Energy*, vol. 2013, p. e307547, Apr. 2013. [Online]. Available: <https://www.hindawi.com/journals/jre/2013/307547/>
  - [118] T. Huld, R. Müller, and A. Gambardella, “A new solar radiation database for estimating PV performance in Europe and Africa,” *Solar Energy*, vol. 86, no. 6, pp. 1803–1815, Jun. 2012. [Online]. Available: <https://www.sciencedirect.com/science/article/pii/S0038092X12001119>
  - [119] Ana María Gracia and Thomas Huld, “Performance comparison of different models for the estimation of global irradiance on inclined surfaces: Validation of the model implemented in PVGIS.” European Commission, Joint Research Centre, Institute for Energy and Transport, LU, Tech. Rep., 2013. [Online]. Available: <https://data.europa.eu/doi/10.2790/91554>
  - [120] M. A. Kallioğlu, A. Durmuş, H. Karakaya, and A. Yılmaz, “Empirical calculation of the optimal tilt angle for solar collectors in northern hemisphere,” *Energy Sources, Part A: Recovery, Utilization, and Environmental Effects*, vol. 42, no. 11, pp. 1335–1358, Jun. 2020. [Online]. Available: <https://doi.org/10.1080/15567036.2019.1663315>
  - [121] D. González-Peña, I. García-Ruiz, M. Díez-Mediavilla, M. I. Dieste-Velasco, and C. Alonso-Tristán, “Photovoltaic Prediction Software: Evaluation with Real Data from Northern Spain,” *Applied Sciences*, vol. 11, no. 11, p. 5025, Jan. 2021. [Online]. Available: <https://www.mdpi.com/2076-3417/11/11/5025>
  - [122] J. Blank and K. Deb, “Pymoo: Multi-Objective Optimization in Python,” *IEEE Access*, vol. 8, pp. 89 497–89 509, 2020.
  - [123] 3GPP, “Evolved Universal Terrestrial Radio Access (E-UTRA); Radio Resource Control (RRC); Protocol specification,” 3rd Generation Partnership Project (3GPP), Technical Specification (TS) 36.331, 06 2019, version 15.6.0.
  - [124] R. S. Sutton and A. G. Barto, *Reinforcement Learning: An Introduction*, 2nd ed. Cambridge, MA, USA: MIT Press, Nov. 2018. [Online]. Available: <https://mitpress.ubli.sh.com/ereader/2351/?preview#page/Cover>
  - [125] E. Even-Dar, S. Mannor, and Y. Mansour, “PAC Bounds for Multi-armed Bandit and Markov Decision Processes,” in *Computational Learning Theory*, J. Kivinen and R. H. Sloan, Eds. Berlin, Heidelberg: Springer, 2002, pp. 255–270.

## Bibliography

---

- [126] A. Ghasempour and S. K. Jayaweera, "Data synchronization for throughput maximization in distributed transmit beamforming," in *2017 Cognitive Communications for Aerospace Applications Workshop (CCAA)*, Jun. 2017, pp. 1–4.
- [127] A. Schumacher, "Integration of a GPS aided Strapdown Inertial Navigation System for Land Vehicles," Master's thesis, KTH Royal Institute of Technology, Stockholm, Sweden, Mar. 2006.
- [128] J. A. Farrell, *The Global Positioning System & Inertial Navigation*. McGraw Hill Professional, Jan. 1999.

## List of Acronyms

<b>3G</b>	3rd Generation of Mobile Networks
<b>3GPP</b>	3rd Generation Partnership Project
<b>4G</b>	4th Generation of Mobile Networks
<b>5G</b>	5th Generation of Mobile Networks
<b>6G</b>	6th Generation of Mobile Networks
<b>AAS</b>	Active Antenna System
<b>AF</b>	Amplify-and-Forward
<b>AWGN</b>	Additive White Gaussian Noise
<b>BBU</b>	Baseband Unit
<b>BEL</b>	Building Entry Loss
<b>BPAAE</b>	Beam Power Adjustment Error
<b>BS</b>	Base Station
<b>C-RAN</b>	Centralized/Cloud-RAN
<b>CAPEX</b>	Capital Expenditure
<b>COTS</b>	Commercial Off-The-Shelf
<b>CP</b>	Cyclic Prefix
<b>CPE</b>	Customer Premises Equipment
<b>CQI</b>	Channel Quality Indicator
<b>CW</b>	Continuous Wave
<b>DAS</b>	Distributed Antenna System
<b>DCM</b>	Direct Cosine Matrix
<b>DF</b>	Decode-and-Forward
<b>DL</b>	Downlink
<b>DOCXO</b>	Disciplined Oven-Controlled Crystal Oscillator
<b>DU</b>	Distributed Unit
<b>ECDF</b>	Empirical Cumulative Distribution Function
<b>ECEF</b>	Earth-Centered Earth-Fixed
<b>EIRP</b>	Effective Isotropic Radiated Power
<b>EMF</b>	Electromagnetic Field
<b>ERP</b>	Effective Radiated Power
<b>EVM</b>	Error Vector Magnitude

## List of Acronyms

---

<b>FDD</b>	Frequency Division Multiplexing
<b>FDMA</b>	Frequency Division Multiple Access
<b>FPGA</b>	Field Programmable Gate Array
<b>FR1</b>	NR Frequency Range 1 (410 MHz - 7.125 GHz)
<b>FR2</b>	NR Frequency Range 2 (24.25 GHz - 52.6 GHz)
<b>FSPL</b>	Free Space Path Loss
<b>FSS</b>	Frequency Selective Surface
<b>FTTH</b>	Fiber to the Home
<b>FWA</b>	Fixed Wireless Access
<b>Gbps</b>	Gigabits per Second
<b>GMT</b>	Greenwich Mean Time
<b>gNB</b>	5th Generation Node B
<b>GNSS</b>	Global Navigation Satellite System
<b>GPS</b>	Global Positioning System
<b>HBF</b>	Holographic Beam Forming
<b>HP</b>	High-Power
<b>HPBW</b>	Half Power Beamwidth
<b>IAB</b>	Integrated Access and Backhaul
<b>ICI</b>	Inter-Cell Interference
<b>IF</b>	Intermediate Frequency
<b>IMT</b>	International Mobile Telecommunications
<b>IoT</b>	Internet of Things
<b>ISD</b>	Inter-Site Distance
<b>ISI</b>	Intersymbol Interference
<b>ITU-R</b>	International Telecommunication Union Radiocommunication Sector
<b>LNA</b>	Low Noise Amplifier
<b>LO</b>	Local Oscillator
<b>LOS</b>	Line-of-Sight
<b>Low-E</b>	Low-Emissivity
<b>LP</b>	Low-Power
<b>LS</b>	Least Squares
<b>LTE</b>	Long Term Evolution, 4th Generation Radio Access Technology from 3GPP
<b>MAB</b>	Multi-Armed Bandit
<b>MAC</b>	Medium Access Control
<b>Mbps</b>	Megabits per Second
<b>MCS</b>	Modulation and Coding Scheme
<b>MDP</b>	Markov Decision Process
<b>MIMO</b>	Multiple Input Multiple Output
<b>mmWave</b>	Millimeter Wave
<b>MNO</b>	Mobile Network Operator

<b>MRS</b>	Mobility Reference Signal
<b>MRSRP</b>	Mobility Reference Signal Received Power
<b>MS</b>	Mobile Station
<b>MTC</b>	Machine-Type Communication
<b>mTRP</b>	Multiple Transmission and Reception Point
<b>MU-MIMO</b>	Multi-User MIMO
<b>NED</b>	North-East-Down
<b>NIR</b>	Non-Ionizing Radiation
<b>NLOS</b>	Non-Line-of-Sight
<b>NR</b>	New Radio, 5th Generation Radio Access Technology from 3GPP
<b>NSA</b>	Non-Standalone
<b>O-RAN</b>	Open RAN Alliance
<b>OCXO</b>	Oven-Controlled Crystal Oscillator
<b>OFCOM</b>	Federal Office of Communications
<b>OFDM</b>	Orthogonal Frequency Division Multiplexing
<b>OFDMA</b>	Orthogonal Frequency Division Multiple Access
<b>P1dB</b>	1 dB Gain Compression Point
<b>PA</b>	Power Amplifier
<b>PAPR</b>	Peak-to-Average Power Ratio
<b>PDF</b>	Probability Density Function
<b>PRB</b>	Physical Resource Block
<b>PV</b>	Photovoltaic
<b>QAM</b>	Quadrature Amplitude Modulation
<b>QPSK</b>	Quadrature Phase Shift Keying
<b>RAN</b>	Radio Access Network
<b>RAT</b>	Radio Access Technology
<b>RAU</b>	Remote Antenna Unit
<b>RBW</b>	Resolution Bandwidth
<b>RF</b>	Radio Frequency
<b>RFSoc</b>	Radio Frequency System-on-Chip
<b>RIS</b>	Reconfigurable Intelligent Surface
<b>RLF</b>	Radio Link Failure
<b>RMS</b>	Root Mean Square
<b>RMSE</b>	Root Mean Square Error
<b>RRC</b>	Radio Resource Control
<b>RRU</b>	Remote Radio Unit
<b>RSRP</b>	Reference Signal Received Power
<b>RSTP</b>	Reference Signal Transmit Power
<b>RU</b>	Radio Unit
<b>RX</b>	Reception

## List of Acronyms

---

<b>SA</b>	Standalone
<b>SDMA</b>	Spatial Division Multiple Access
<b>SINR</b>	Signal-to-Interference-and-Noise Ratio
<b>SISO</b>	Single Input Single Output
<b>SME</b>	Small and Medium-Sized Enterprise
<b>SNR</b>	Signal-to-Noise Ratio
<b>sub-6 GHz</b>	Carrier Frequencies Below 6 GHz
<b>SWaP-C</b>	Size, Weight, Power, and Cost
<b>TCP</b>	Transmission Control Protocol
<b>TDD</b>	Time Division Multiplexing
<b>TX</b>	Transmission
<b>UE</b>	User Equipment
<b>UL</b>	Uplink
<b>UMTS</b>	Universal Mobile Telecommunications System, 3rd Generation Radio Access Technology from 3GPP
<b>WGS84</b>	World Geodetic System 1984
<b>WiMAX</b>	Worldwide Interoperability for Microwave Access
<b>WLAN</b>	Wireless Local Area Network

# List of Figures

1.1	Monthly mobile data traffic development since the year 2017 and prediction until the year 2027 [1]. . . . .	1
1.2	Frequency allocation for fixed and mobile use (grey shades). Licensed frequency bands in use for mobile communications in Switzerland (dark blue), frequency bands for mmWave mobile communications (light blue). (Source: Swiss OFCOM) . . . . .	2
2.1	5G NR frequency ranges (FR) and harmonized frequency allocations (light gray). FR1 and FR2 are supported with the first release of 5G NR (Rel. 15). . . . .	7
2.2	(a) Shows the 5G testbed AAS on a mast and the UE in the field, (b) the map of the rural deployment with a red star indicating the AAS location with the 120° sector, and the LOS/NLOS classification. Similarly, (c) and (d) show the map of the suburban and urban deployments, respectively. . . . .	13
2.3	Antenna patterns used for the macro antennas (conventional sector and AAS). . . . .	14
2.4	Measurement van with a UE inside and its antennas installed at the back on the roof. A second UE on wheels is shown behind the van. . . . .	15
2.5	The installation of the base station rack (left picture) and the AAS on the live macro site mast (right picture). . . . .	16
2.6	View of a part of the suburban measurement area from the AAS. . . . .	17
2.7	Rural environment measurements compared to models. . . . .	19
2.8	Distribution of the measured shadow fading components. The solid curve represents the Gaussian fit for each distribution and is an indication if the shadow fading has a log-normal distribution. . . . .	20
2.9	Path loss for 3.5 GHz vs. 800 MHz and 2.1 GHz in the rural and suburban measurement area; validating the theory of 12.8 dB and 4.4 dB path loss difference. . . . .	20

## List of Figures

---

2.10 Suburban environment measurements compared to models. . . . .	21
2.11 Urban environment measurements compared to models. . . . .	21
2.12 Outdoor-to-indoor penetration loss shown as ECDF of the received power difference from indoor compared to outdoor. . . . .	23
2.13 Methods to increase indoor data capacity. . . . .	25
2.14 Base station transmitting to mobile stations inside buildings. Direct signal path in green, relayed/repeated signal path in blue. . . . .	27
3.1 Exemplary mobile coverage map showing mobile sites from all MNOs as circles and the availability of 3G, 4G, and 5G service with transparent tiles. (Source: Swisstopo [71]). . . . .	34
3.2 Two sub-6 GHz cells (B and C) are upconverted to mmWave, transmitted to buildings where they are downconverted, and re-transmitted inside on their original carrier frequency. Indoor users are offloaded from the legacy outdoor cell A to either cell B or C. . . . .	35
3.3 Deployment examples for a mmWave bridge for FWA service to houses (a) or large buildings (b) and as a fronthaul for an RF corridor along a railway track (c). . . . .	37
3.4 Multiple indoor cells (blue) fronthauled over mmWave bridges (mmWB) in the coverage area of a macro cell (large green circle). . . . .	38
3.5 Block diagram of the mmWave bridge donor node and service node. The serving antenna for the user access link is placed indoors. . . . .	39
3.6 Simulation block diagram: multiple scenarios can be configured and run. . . . .	41
3.7 Examples of scenario environments that can be generated. . . . .	42
3.8 Abstracted signal path from a base station to an indoor mobile station. . . . .	42
3.9 Block diagrams of the simulation models for the four active equipment. The added noise components depend on the noise figures of the active sub-components of the respective signal path and the thermal noise. . . . .	44
3.10 Indoor SINR coverage estimation for the outdoor-to-indoor macro network baseline (left plots) and with the mmWave bridge fronthauled cell with rooftop CPE antennas (right plots). . . . .	50
3.11 Single link SISO capacity comparison for the five discussed methods in two frequency bands, where applicable. The boxes show the 5%ile and 95%ile, the median (horizontal red line inside the box), and the mean value (+ marker) . . .	51

3.12 Cell capacity comparison based on simultaneously scheduled single SISO links (bar segments in different color shades) for the five discussed methods in two frequency bands, where applicable . . . . .	52
4.1 Block diagram of one mmWave bridge node (common for donor and service node)	56
4.2 Picture of one frontend with the mmWave HBF antennas and the control and signal processing board. . . . .	57
4.3 Schematic diagram of one mmWave bridge node frontend. . . . .	57
4.4 A multicarrier IF signal mixed with an LO with a given phase noise characteristic and the resulting mixer RF output signal as a combination of the IF and LO signals.	59
4.5 NR TDD DL signal (C1, yellow) and the DL/UL switch timing (C3, blue). . . . .	60
4.6 Pivotal Commware HBF antenna for 39 GHz . . . . .	60
4.7 Measured transmission S21 of the respective paths. . . . .	63
4.8 Measured phase noise at 18 GHz of three signal generators in comparison. . . . .	63
4.9 Measured constellation for the EVM calculation. . . . .	64
4.10 Angular RF power spectrum from a beam scan at the donor node in an outdoor scenario with LOS to the service node (maximum at 2° azimuth and 0° elevation).	66
4.11 Angular RF power spectrum from a beam scan at the donor node in an indoor scenario with NLOS to the service node (maximum at -6° azimuth and 0° elevation). . . . .	66
4.12 Estimated maximum link distance for the prototype at an output power of 30 dBm EIRP. . . . .	67
5.1 Map of the rural measurement location and weather condition on one of the measurement days (Map source: Swisstopo [96]). . . . .	71
5.2 RSRP measurement agrees with the FSPL model, and variations come from two-ray ground reflections on the mmWave donor link. . . . .	72
5.3 Measurement results for 50 m up to 1300 m and calculated results up to 3000 m for the UE connected over the mmWave bridge and, for comparison, directly to the sub-6 GHz cell. . . . .	72

## List of Figures

---

5.4	EPFLoop hyperloop site where we conducted a measurement campaign to demonstrate the potential of our mmWave bridge for the fronthaul of a small cell [98]. . . . .	74
5.5	ECDF of the measured throughput for a 5G SA cell fronthauled over the mmWave bridge to the hyperloop track. . . . .	76
6.1	Measured signal power outside and inside the train and the resulting penetration attenuation (power difference). . . . .	79
6.2	Cellular corridor with macro sites along a railway track providing the linear cell enhanced by mmWave bridge nodes in between. . . . .	80
6.3	Antenna locations and their azimuth directions along the railway tracks (Source: Swisstopo [107]). . . . .	81
6.4	The macro antenna with the mmWave bridge donor node on the right and the service node on the left. . . . .	82
6.5	Schematic of the macro site and the mmWave bridge donor and service nodes. . . . .	83
6.6	Pictures of the type of train used for measurements and how the equipment was installed inside. . . . .	84
6.7	Measured signal power inside the train for only the macro antenna as a baseline and the macro antenna enhanced with the mmWave bridge at 292 m. The macro antenna transmit power was 47.1 dBm EIRP, the mmWave bridge transmit power was 32.5 dBm EIRP. . . . .	86
6.8	Signal power and difference for the macro and service node antennas outside and inside the train. . . . .	87
6.9	ECDF of all measurements taken in trains for comparison over the 1000 m track segment west of the macro site. . . . .	88
6.10	Direct and indirect signal paths discussed for the Doppler measurements. . . . .	88
6.11	Doppler spectrum for only the macro antenna corridor (baseline) and the macro antenna enhanced with the mmWave bridge on two different railway tracks ( <i>far</i> , <i>near</i> ), resulting in different transverse distances between the corridor antennas and the train windowpane. . . . .	89
6.12	Example of a macro ISD of 1000 m with a transmit power of 600 W ERP and five mmWave bridge service nodes with a transmit power of 6 W ERP each. The average RSRP is shown with dashed lines. . . . .	91

6.13 Numerical evaluation of average power in a train for a given number of mmWave bridge service nodes at a given inter-node distance. . . . .	92
6.14 Low-power mmWave bridge node prototype during measurements. . . . .	93
6.15 An example of the signal and noise power profiles for a maximum transmit power of 1500 W ERP for the high-power sites (left and right, $d_{\text{ISD}} = 2400$ m) and 6 W ERP for the $N = 8$ low-power mmWave bridge service nodes in between. . . . .	94
6.16 Network traffic load-dependent power consumption of a high-power RRU and a low-power bridge node based on (6.6) and the parameters in Table 6.2. . . . .	96
6.17 Average energy consumption normalized to 1 km for the conventional cellular corridor on the very left and 1 to 10 low-power bridge nodes placed in between high-power masts (always using energy-saving techniques) to extend their ISD while maintaining the peak throughput for users. . . . .	100
7.1 System block diagrams embedded in two example use cases. . . . .	104
7.2 The location probability distribution for three measurement locations. . . . .	107
7.3 Synthesized combined envelope beam pattern of a grid-of-beams antenna used in the numerical evaluation. . . . .	108
7.4 RRC events and timers for 4G and 5G. . . . .	110
7.5 Resulting normalized throughput and RRC events for link interruptions with different durations and intervals when switching to a beam providing 10 dB less signal power (left) and switching to a beam leading to a signal outage (right). . . . .	111
7.6 The background color represents the minimal theoretical throughput reduction (fraction) with respect to the beam measurement duration and beam measurement interval. Colored dots show the measured throughput reduction. . . . .	112
7.7 Beam power adjustment error for the evaluated algorithms. . . . .	115
7.8 Fraction of samples exceeding a certain beam power adjustment error versus the number of scanned beams per measurement sample for different models. . . . .	115
A.1 Relations between ECEF frame ( $e$ ), local tangent-frame ( $t$ ), and body frame ( $b$ ) [127]. . . . .	122



## List of Tables

2.1	Comparison of path loss parameters for (2.1) at 3.5 GHz . . . . .	10
2.2	Selected empirical path loss models . . . . .	11
2.3	Estimated Path Loss Model Parameters for (2.1) . . . . .	18
2.4	Path loss model prediction error statistics . . . . .	22
2.5	Outdoor-to-indoor comparison at 3.5 GHz . . . . .	22
3.1	Simulation parameters and example values . . . . .	49
4.1	Part list for one mmWave bridge node frontend in Fig. 4.3. . . . .	57
4.2	Measured mmWave bridge node prototype power and gain . . . . .	62
4.3	mmWave bridge link budget for a 100 MHz 5G NR signal at the sub-component stages referenced in Fig. 4.3 for a nominal LOS distance of 500 m. . . . .	62
5.1	Calculated link budget for the FWA link to the hyperloop site. . . . .	75
6.1	Low-power mmWave bridge node power consumption. . . . .	96
6.2	Power model parameters for the RRU and mmWave bridge node. . . . .	97
6.3	Parameters for average energy consumption calculations. . . . .	99
6.4	PVGIS results at the four exemplary regions for one year. . . . .	99
7.1	The probability of missing a node depending on the number of beams ( $K$ ) to scan.	108



# Adrian SCHUMACHER

## PERSONAL INFORMATION

---

Date of Birth: 27 June 1979

Email: aschumacher@ieee.org

Place of Birth: Bern, CH

Membership: IEEE Senior Member

Nationality: Swiss

Languages: German, English, French, Swedish

## EDUCATION

---

06.2018 – 06.2022 **Ph.D.** in El. Eng., École polytechnique fédérale de Lausanne, Lausanne, CH

08.2004 – 03.2006 **M.Sc.** in El. Eng., KTH Royal Institute of Technology, Stockholm, SE

10.2000 – 01.2004 **B.Sc.** in El. Eng., University of Applied Sciences Bern, Burgdorf, CH

08.1996 – 07.2000 **Federal Diploma of Vocational Education**, certified electronics technician,  
GIB Bern (Securiton AG), Bern, CH

## PROFESSIONAL EXPERIENCE

---

10.2013 – current **Swisscom (Switzerland) Ltd.**, Ittigen, CH  
*Senior Wireless Engineer* in the Infrastructure and Innovation departments.

04.2010 – 09.2013 **Rohde & Schwarz GmbH & Co. KG**, Munich, DE  
*System Architect DSP* in the Test & Measurement Division.

01.2009 – 03.2010 **Rohde & Schwarz North America Inc.**, Beaverton, OR, USA  
*Senior Development Engineer DSP* in the Test & Measurement Division.

04.2006 – 12.2008 **Rohde & Schwarz GmbH & Co. KG**, Munich, DE  
*Development Engineer DSP* in the Test & Measurement Division.

02.2004 – 07.2004 **Rohde & Schwarz GmbH & Co. KG**, Munich, DE  
*Trainee* in the Radiomonitoring and Radiolocation Division.

08.2000 – 05.2003 **Securiton AG**, Zollikofen, CH and **Triadem Solutions AG**, Biel, CH  
*Electronic Technician*, hard- and software development, part time jobs during studies.

08.1996 – 07.2000 **Securiton AG**, Zollikofen, CH  
*Vocational Electronic Technician Student*, hard- and software development.

## PATENTS

---

- **A. Schumacher** (Swisscom), “Methods and Systems for Bridging for Mobile Communications Systems”, US2021368583A1/EP3917278A1, published 2021-12-01.
- **A. Schumacher** (Swisscom), “Multi-Pane Glazing Unit”, EP3767062A1, published 2021-01-20.
- **A. Schumacher**, H. Scheidig, G. Bacor, R. Durai (Rohde & Schwarz), “Measuring Device and Measuring Method for Detecting Errors in Signals”, WO2014139600A1, published 2014-09-18.
- **A. Schumacher** (Rohde & Schwarz), “Method and Device for Determining the Number of Uncorrelated Transmission Channels in a MIMO Transmission System”, WO2014040611A1, published 2014-03-20.
- **A. Schumacher**, A. Michl (Rohde & Schwarz), “Mobilfunkgerät mit Signalqualitätsanzeige und entsprechendes Betriebsverfahren”, DE102011087778B4, published 2013-06-06, granted 2015-05-07.
- **A. Schumacher** (Rohde & Schwarz), “Messvorrichtung und Messverfahren zur Vermessung einer Backoff-Zeitspanne”, DE102011082597B4, published 2013-03-14, granted 2019-05-16.
- **A. Schumacher** (Rohde & Schwarz), “Method and System for Measuring Mobile Stations in Communications Networks with Virtual Antenna Arrays”, WO2011085759A1/US8818289B2, published 2011-07-21, granted 2014-08-26.
- **A. Schumacher** (Rohde & Schwarz), “Test equipment and mobile radio device and a method for testing a mobile radio device”, US8509700B2, published 2010-09-30, granted 2013-08-13.
- **A. Schumacher**, H. Gerlach (Rohde & Schwarz), “Method and System for Bandwidth Detection”, WO2009106116A1/ES2378731T3, published 2009-09-03, granted 2012-04-17.
- **A. Schumacher** (Rohde & Schwarz), “Circuit for Producing Polyphase Sequences”, WO2009100746A1/EP2243236B1/US8533247B2, published 2009-08-20, granted 2012-11-14.
- **A. Schumacher** (Rohde & Schwarz), “Test Device, Mobile Radio Device and Method for Testing a Mobile Radio Device”, WO2008116516/US8509700B2 published 2008-10-02, granted 2013-08-13.
- A. Michl, **A. Schumacher** (Rohde & Schwarz), “Method and Measuring System for Measuring and Testing a Mobile Radio Terminal”, WO2008049498/EP2095656B1, published 2008-05-02, granted 2012-11-14.
- **A. Schumacher** (Rohde & Schwarz), “Optimized Fourier Transform for Non-Radix-2 DFT Length”, EP1909190A1, published 2008-04-09.

# List of Publications

## Journal Papers

**A. Schumacher**, R. Merz, and A. Burg, “Adding Indoor Capacity without Fiber Backhaul: An mmWave Bridge Prototype,” *IEEE Communications Magazine*, vol. 59, no. 4, p. 110–115, May 2021. DOI: 10.1109/MCOM.001.2000722

## Conference Papers

**A. Schumacher**, R. Merz, and A. Burg, “Beam Selection and Tracking for Amplify-and-Forward Repeaters,” in *2022 IEEE 95th Vehicular Technology Conference (VTC2022-Spring)*, June 2022, pp. 1–6. [accepted]

**A. Schumacher**, R. Merz, and A. Burg, “Increasing Cellular Network Energy Efficiency for Railway Corridors,” in *2022 Design, Automation & Test in Europe Conference (DATE2022)*, Mar. 2022, pp. 1103-1106. DOI: 10.23919/DATE54114.2022.9774757

**A. Schumacher**, N. Jamaly, R. Merz, and A. Burg, “Improving railway track coverage with mmWave bridges: A Measurement Campaign,” in *Proceedings of the 1st Workshop on 5G Measurements, Modeling, and Use Cases*, New York, NY, USA, Aug. 2021, pp. 8–13. DOI: 10.1145/3472771.3472774

**A. Schumacher**, R. Merz, and A. Burg, “A mmWave Bridge Concept to Solve the Cellular Outdoor-to-Indoor Challenge,” in *2020 IEEE 91st Vehicular Technology Conference (VTC2020-Spring)*, May 2020, pp. 1–6. DOI: 10.1109/VTC2020-Spring48590.2020.9128458

**A. Schumacher**, R. Merz, and A. Burg, “3.5 GHz Coverage Assessment with a 5G Testbed,” in *2019 IEEE 89th Vehicular Technology Conference (VTC2019-Spring)*, Apr. 2019, pp. 1–6. DOI: 10.1109/VTCSpring.2019.8746551

## Outside the Scope of this Thesis

N. Jamaly, **A. Schumacher**, D. Wenger, “Micro versus Macro Antenna Corridor for Trains Equipped with FSS Windowpanes,” in *2022 16th European Conference on Antennas and Propagation (EuCAP)*, Mar. 2022, pp. 1–5. Available: <https://ieeexplore.ieee.org/document/9769673>

## List of Publications

---

- N. Xu, S. Li, C. S. Charollais, A. Burg, and **A. Schumacher**, “Machine Learning Based Outdoor Localization using the RSSI of Multibeam Antennas,” in *2020 IEEE Workshop on Signal Processing Systems (SiPS)*, Oct. 2020, pp. 1–5. DOI: 10.1109/SiPS50750.2020.9195235
- N. Jamaly, S. Mauron, R. Merz, **A. Schumacher**, and D. Wenger, “Delivering Gigabit Capacities to Passenger Trains: Tales from an Operator on the Road to 5G,” *IEEE Communications Magazine*, vol. 57, no. 9, pp. 18–23, Sept. 2019. DOI: 10.1109/MCOM.2019.1800949
- N. Jamaly, R. Merz, **A. Schumacher**, D. Scanferla, and D. Wenger, “MIMO capacity enhancement beyond that of the ideal rayleigh multipath by virtue of a leaky feeder cable,” in *2016 10th European Conference on Antennas and Propagation (EuCAP)*, Apr. 2016, pp. 1–5. DOI: 10.1109/EuCAP2016.7481985
- R. Merz, **A. Schumacher**, N. Jamaly, D. Wenger, and S. Mauron, “A Measurement Study of MIMO Support with Radiating Cables in Passenger Rail Cars,” in *2015 IEEE 81st Vehicular Technology Conference (VTC Spring)*, May 2015, pp. 1–5. DOI: 10.1109/VTCSpring.2015.7145620
- I. Skog, **A. Schumacher**, and P. Händel, “A Versatile PC-Based Platform For Inertial Navigation,” in *Proceedings of the 7th Nordic Signal Processing Symposium - NORSIG 2006*, June 2006, pp. 262–265. DOI: 10.1109/NORSIG.2006.275238